UNIVERSITY OF CALIFORNIA
Santa Barbara

Fermi Level Engineering of the Perovskite and Electron Transport Layer Interface through Charge Transfer Doping

A dissertation submitted in partial satisfaction
of the requirements for the degree

Doctor of Philosophy in
Materials

by

Erin Elizabeth Perry

Committee in charge:

Professor Michael Chabinyc, Chair
Professor Ram Seshadri
Professor Stephen Wilson
Professor Jon Schuller

September 2018

The dissertation of Erin Elizabeth Perry is approved.

_____
Ram Seshadri

_____
Stephen Wilson

_____
Jon Schuller

_____
Michael Chabinyc, Committee Chair

August 2018

Fermi Level Engineering of the Perovskite and Electron Transport Layer Interface Through Charge Transfer Doping

ACKNOWLEDGEMENTS

I would first like to extend my utmost gratitude to my advisor, Prof. Michael Chabinyc for his academic guidance throughout my time at UC Santa Barbara. I would also like to thank Prof. Ram Seshadri who at times functioned like my second advisor and was always willing to help with obstacles I was facing. Additionally, thank you to Stephen Wilson and Jon Schuller for their time and effort on my dissertation committee. I would gratefully acknowledge my financial support that enabled me to pursue this research, as well as for funding to participate in academic conferences: DOE under Grant Award Number DE-SC-0012541, AFOSR MURI program under Grant Award Number FA9550–12–1–0002, NSF under Grant Award Number DMR-1305247, and the MC-CAM Program at UCSB sponsored by Mitsubishi Chemical Corporation (Japan).

I would also like to thank all the administrative staff of the Materials Department and MRL, who kept everything running smoothly and made sure all the lab supplies kept showing up. Thank you to the technical staff for their valuable expertise in instrument training, measurement acquisition and analysis. The assistance of Tom Mates in performing Ultraviolet Photoelectron Spectroscopy was particularly important for this research.

I would like to thank my mentor John Labram who taught me about device physics and provided comradery. I am also grateful to other members of the Chabinyc Group who trained me, helped with measurements and also tried to make sure that the lab didn't burn down. I would not have made it through graduate school without the emotional support of my friends and family. I would particularly like to thank my best friend Colin Stewart who always stuck by me.

Curriculum Vitæ Erin Elizabeth Perry

EDUCATION

2013-2018 Doctor of Philosophy (Ph.D.) in Materials
University of California, Santa Barbara (UCSB)
2009-2013 Bachelor of Science (B.S.) in Materials Science and Engineering
Massachusetts Institute of Technology (MIT)

RESEARCH

2013-2018 **Graduate Student Researcher**, Chabinyc Research Group
Materials Department, UC Santa Barbara
2012-2013 **Undergraduate Researcher,** Strano Research Group
Department of Chemical Engineering, MIT
2010-2012 **Undergraduate Researcher**, Electrochemical Energy Lab
Department of Mechanical Engineering, MIT

TEACHING

Research Mentor, UC Santa Barbara
Robert Johnstone (High School Teacher, Ventura School District)
Gabriel Lopez (Undergraduate, University of Texas El Paso)
Teaching Assistant
Structure and Properties I, MATRL 100A
Introductory Undergraduate Level Course, Materials, UC Santa Barbara
Laboratory Instructor
Materials in the Human Experience, 3.094
Undergraduate Level Course, Archaeology and Materials, MIT

PUBLICATIONS

- Labram, J.G.; **Perry, E.E.**; Venkatesan, N.; Chabinyc, M.L. Intensity-Dependent Charge-Carrier Diffusion Lengths in Methylammonium Lead Iodide at < 1 Sun. Accepted to *Appl. Phys. Lett.*
- **Perry, E.E.**; Labram J.G.; Venkatesan, N.; Nakayama, H.; Chabinyc, M.L. N-type Surface Doping of $MAPbI_3$ via Charge Transfer from a Small Molecule. *Adv. Electron. Mater. 2018, 4* (7), 1800087.
- **Perry, E. E.**; Chiu, C.-Y.; Moudgil, K.; Schlitz, R. A.; Takacs, C. J.; O'Hara, K. A.; Labram, J. G.; Glaudell, A. M.; Sherman, J. B.; Barlow, S.; Hawker, C. J.; Marder, S. R.; Chabinyc, M. L. High Conductivity in a Nonplanar N-Doped Ambipolar Semiconducting Polymer. *Chem. Mater.* 2017. (7)
- Labram, J. G.; Venkatesan, N. R.; Takacs, C. J.; Evans, H. A.; **Perry, E. E.**; Wudl, F.; Chabinyc, M. L. Charge Transport in a Two-Dimensional Hybrid Metal Halide Thiocyanate Compound. *J. Mater. Chem. C* 2017, *5* (24), 5930–5938.

- Russ, B.; Robb, M. J.; Popere, B. C.; **Perry, E. E.**; Mai, C.-K.; Fronk, S. L.; Patel, S. N.; Mates, T. E.; Bazan, G. C.; Urban, J. J.; Chabinyc, M. L.; Hawker, C. J.; Segalman, R. A. Tethered Tertiary Amines as Solid-State N-Type Dopants for Solution-Processable Organic Semiconductors. *Chem Sci* 2016.
- Lehner, A. J.; Wang, H.; Fabini, D. H.; Liman, C. D.; Hébert, C.-A.; **Perry, E. E.**; Wang, M.; Bazan, G. C.; Chabinyc, M. L.; Seshadri, R. Electronic Structure and Photovoltaic Application of BiI_3. *Appl. Phys. Lett.* 2015, *107* (13), 131109.
- Labram, J. G.; Fabini, D. H.; **Perry, E. E.**; Lehner, A. J.; Wang, H.; Glaudell, A. M.; Wu, G.; Evans, H.; Buck, D.; Cotta, R.; Echegoyen, L.; Wudl, F.; Seshadri, R.; Chabinyc, M. L. Temperature-Dependent Polarization in Field-Effect Transport and Photovoltaic Measurements of Methylammonium Lead Iodide. *J. Phys. Chem. Lett.* 2015, *6* (18), 3565–3571.
- Russ, B.; Robb, M. J.; Brunetti, F. G.; Miller, P. L.; **Perry, E. E.**; Patel, S. N.; Ho, V.; Chang, W. B.; Urban, J. J.; Chabinyc, M. L.; Hawker, C. J.; Segalman, R. A. Power Factor Enhancement in Solution-Processed Organic N-Type Thermoelectrics Through Molecular Design. *Adv. Mater.* 2014, *26* (21), 3473–3477.
- Suntivich, J.; **Perry, E. E.**; Gasteiger, H. A.; Shao-Horn, Y. The Influence of the Cation on the Oxygen Reduction and Evolution Activities of Oxide Surfaces in Alkaline Electrolyte. *Electrocatalysis* 2013, *4* (1), 49–55.
- Lee, Y.; Suntivich, J.; May, K. J.; **Perry, E. E.**; Shao-Horn, Y. Synthesis and Activities of Rutile IrO_2 and RuO_2 Nanoparticles for Oxygen Evolution in Acid and Alkaline Solutions. *J. Phys. Chem. Lett.* 2012, *3* (3), 399–404.

AWARDS

- Honorable Mention, National Science Foundation Graduate Research Fellowship
- Chancellor's Fellowship, UC Santa Barbara, 2013

ABSTRACT

Fermi Level Engineering of the Perovskite and Electron Transport Layer Interface Through Charge Transfer Doping

by

Erin Elizabeth Perry

Perovskite solar cells (PSCs) have captured the focus of the photovoltaic field due to their ease of fabrication and high power conversion efficiencies of ~22%.[1] In PSCs, the perovskite active material is sandwiched between electron and hole transport layers that serve to extract photogenerated charge carriers and avoid direct contact between the perovskite layer and metal electrodes in order to prevent degradation.[2–4] There is a variety of electron and hole transport materials that result in high efficiency devices. However, organic semiconductors are the most attractive from an industrial standpoint because of their low temperature processing and scalability.[5] The major obstacle to use of organic semiconductors in PSCs is their low carrier mobility and carrier concentration, which hinder their ability to effectively transport photogenerated carriers to electrodes and may cause them to act as resistors in the device series. These issues are especially prevalent in thicker transport layers, which would likely be the case for industrial roll-to-roll processing.[6] In order to overcome transport issues, doping of organic transport layers is performed to passivate trap sites and increase the concentration of free carriers.

To date, there have been few reports on understanding how the presence of small molecule dopants can influence the perovskite active layer. Due to the similarity in energy levels, small molecule dopants that have been developed to dope organic semiconductors are

also likely to be effective candidates for charge transfer to $MAPbI_3$.[7,8] In addition, $MAPbI_3$ has a low density of surface states which is typical of ionic semiconductors.[9] The subject of this dissertation is to understand the impacts of charge transfer from small molecules or doped organic semiconductors to the surface of $MAPbI_3$. In order to improve understanding of what occurs at the interface of $MAPbI_3$ and electron transport layers (ETLs), this work is segmented into three components: doping of *n*-type polymers, surface *n*-type doping of $MAPbI_3$ and doping of the ETL in PSCs. The major implication of this dissertation is that doping of ETLs likely impacts carrier recombination at the $MAPbI_3$ surface. The surface doping study was used as a model system to provide a means to understand the more complex heterointerface of doped organic blends at perovskite surfaces. In literature there have been numerous reports of a deep electron trap level roughly around mid-gap.[10–14] Surface doping indicates that at moderate degrees of doping, the Fermi level shift will passivate this recombination center, resulting in higher photoconductivity and steady-state photoluminescent intensity. At high degrees of doping, there is an overabundance of charge beyond what is necessary to passivate surface traps, creating an additional pathway for bimolecular recombination. In addition, excessive charge leads to degradation of $MAPbI_3$'s surface, a phenomenon likely enhanced by $MAPbI_3$ character as an ionic crystal. The third study of this dissertation examines the effect of dopant concentration in the ETL on solar cell performance. Variations of several orders of magnitude were utilized to illustrate the potential impacts of doping. The choice of the ETL for this study utilized design principles for polymer structure that promotes polymer: dopant miscibility. Solar cell performance experienced a rise and fall in performance with ETL doping concentration, consistent with observations from surface doping. Evidence of trap passivation was observed by higher open circuit voltages (V_{OC}) and longer carrier

lifetimes for moderate doping concentrations. Numerous studies in literature on the impact of doping ETLs on PSCs have identified a range of factors influencing performance, including changes to carrier mobility, electrical conductivity, energy level alignment, and morphology.[15] This dissertation recommends that charge transfer to the perovskite surface should be added to this list of considerations.

TABLE OF CONTENTS

LIST OF FIGURES

in increasing and decreasing directions in order to characterize reversibility of temperature.

Figure S4.20 Power law ($\sigma_{PC} \propto G^{\alpha}$) fits to extract the light exponent factor α from photoconductivity versus photoexcitation density G of neat $MAPbI_3$. The extracted light exponent factor α is ≈0.8, indicating bimolecular and monomolecular decay.

Figure S4.21 Photoconductivity of (left) neat $MAPbI_3$ and (right) 0.5 mg/mL doped $MAPbI_3$ over a period of 90 min constant illumination of 525 nm light with a photon flux of 5.8×10^{17} photons cm^{-2} s^{-1}.

Figure S5.1 The 2D GIWAXS of neat PDI-2T indicates that it is a glassy polymer due to the diffuse scattering features. GIWAXS patterns given include (a) 2D images and (b) 1D linecuts.

Figure S5.2 Steady-state photoluminescence (SS-PL) of thin film samples, including (a) PDI-2T on quartz and (b) PDI-2T/$MAPbI_3$ bilayers. PDI-2T on quartz shows PL intensity due to the perylene-diimide unit, which is quenched upon doping. For PDI-2T/$MAPbI_3$ bilayers, there is a red-shift relative to $MAPbI_3$ for neat/low doping concentrations. Other studies on the passivation effect of PCBM on $MAPbI_3$ reported a blue-shift (from 782 to 775) that was attributed to passivation of trap states the lead to radiative recombination. In contrast, no shift was observed in $MAPbI_3$ films passivated with the Lewis base pyridine. This inconsistency may be a result of the mechanism for surface passivation: PCBM is believed to be adsorbing onto Pb-I antistite defective grain boundary, and Lewis bases are passivating dangling Pb atoms through coordination or bond formation. The black dashed line indicates the wavelength (770 nm) that transients were collected at in time-resolved photoluminescence (TR-PL). There is PL signal for PDI-2T that is quenched upon doping at this wavelength, which was relevant to analysis of the fast decay component of TR-PL.

Figure S5.3 Solution steady-state photoluminescence of PDI-2T (neat) versus PDI-2T (1 wt% dopant). The lower PL intensity of PDI-2T (1 wt% dopant) indicates that the charge transfer mechanism of $(2\text{-Cyc-DMBI})_2$ to PDI-2T occurs in solution.

Figure S5.4 Optical absorption of (a) PDI-2T on quartz and (b) on $MAPbI_3$ and (c) an overlay of PDI-2T (10 wt% dopant) on quartz and $MAPbI_3$. For PDI-2T on quartz, the optical gap is around ~1.6 eV. At low doping concentration there a neutral polymer transition at ~2.0 eV with limited bleaching upon doping for 0.1 wt% and 1 wt%. For 10 wt%, the neutral polymer peak has been completely bleached and a new transition has emerged at ~1.6 eV, which is the result of heavy doping. The emergence of this transition may also be present at 1 wt%. For PDI-2T/$MAPbI_3$ bilayers, optical absorption indicates that there is no degradation of the bulk with ETL deposition. This observation is most relevant

Figure S5.19 Cross-sectional SEM images of 0.5 mg/mL loading of PDI-2T (1 wt% dopant) on the $MAPbI_3$ surface. Low solution loadings result in patchy coverage of the perovskite surface, allowing Pb and I orbitals still be accessible to XPS (probes top ~10 nm of the film) in some areas of the film.

Figure S5.20 XPS core level shifts of (a) Pb 4f and (b) I 3d orbital peak positions. Upon doping, a shift of ~0.2 eV toward high binding energy occurs, indicating downward band bending at the $MAPbI_3$ surface.

Figure S5.21 Biexponential fits of the time-resolved photoluminescence decay of (a) PDI-2T (neat)/$MAPbI_3$, (b) PDI-2T (0.1 wt% dopant)/$MAPbI_3$, (c) PDI-2T (1 wt% dopant)/$MAPbI_3$, (d) PDI-2T (10 wt% dopant)/$MAPbI_3$, (e) bare $MAPbI_3$, and (f) PDI-2T (neat) on quartz. Biexponential fitting incorporates a fast decay time lifetime τ_1 associated with recombination behavior at the surface, and a slow decay lifetime τ_2 associated with recombination in the bulk. The fast decay component of PDI-2T (neat)/$MAPbI_3$ and PDI-2T (0.1 wt% dopant)/$MAPbI_3$ is dominated by the decay of PDI-2T, consequently information about surface recombination lifetimes in $MAPbI_3$ for these samples are masked. TR-PL spectra were collected using a pulse energy density of 0.15 uJ/cm^2, which corresponds to a charge density of 6.9×10^{15} cm^{-3}.

Figure S5.22 Time-resolved photoluminescence spectra of PDI-2T/$MAPbI_3$ bilayers, showing (left) the full TR-PL spectra and (right) the spectra around the fast decay component. Spectra correspond to bilayers according to: (a) & (b) PDI-2T (neat)/$MAPbI_3$, (c) & (d) PDI-2T (0.1 wt% dopant)/$MAPbI_3$, (e) & (f) PDI-2T (1 wt% dopant)/$MAPbI_3$, and (g) & (h) PDI-2T (10 wt% dopant)/$MAPbI_3$. Time-resolved PL decays were measured using a 410 nm excitation and three pulse energy densities: 0.15 uJ/cm^2, 0.05 uJ/cm^2, and 0.015 uJ/cm^2, which correspond to charge densities of 6.9×10^{15}, 2.3×10^{15}, and 6.9×10^{14} cm^{-3}.

Figure S5.23 Time-resolved photoluminescence spectra of (a) & (b) bare $MAPbI_3$ on quartz and (c) PDI-2T (neat) on quartz, showing (left) the full TR-PL spectra and (right) the spectra around the fast decay component. PDI-2T on quartz was measured as a control to account for the photoluminescence of PDI-2T (perylene-diimide unit) in bilayer samples such as PDI-2T (neat)/$MAPbI_3$ and PDI-2T (0.1 wt% dopant)/$MAPbI_3$. By PDI-2T (1 wt% dopant) the time-resolved photoluminescence no longer has intensity. Time-resolved PL decays were measured using a 410 nm excitation and three pulse energy densities: 0.15 uJ/cm^2, 0.05 uJ/cm^2, and 0.015 uJ/cm^2, which correspond to charge densities of 6.9×10^{15}, 2.3×10^{15}, and 6.9×10^{14} cm^{-3}.

LIST OF TABLES

Chapter 1

Introduction

Perovskite solar cells (PSCs) have captured the focus of the photovoltaic field due to their ease of fabrication and high power conversion efficiencies of ~22%.[18] In PSCs, the perovskite active material is sandwiched between electron and hole transport layers that serve to extract photogenerated carriers from the perovskite and transport these charges to electrodes.[5] Hole transport layers are typically composed of organic semiconductors such as spiro-OMeTAD (2,20,7,70-tetrakis-(N,N0-di-p-methoxyphenylamine)-9,90-spirobifluorene)), PEDOT:PSS (poly(3,4-ethylenedioxythiophene) polystyrene sulfonate) or PTAA **(**Poly (triaryl amine))**.**[19] In contrast, there is a variety of electron transport layers (ETLs) that result in high efficiency devices, including inorganic materials such as ITO (indium tin oxide), FTO (fluorine-doped tin oxide), TiO_2 (titanium dioxide), and ZnO (zinc oxide).[20] However, ETLs composed of organic semiconductors are more attractive from an industrial standpoint because of their low temperature processing and scalability.[5] The major obstacle to use of organic semiconductors in ETLs is their low carrier mobility and carrier concentration, which

hinder their ability to effectively transport photogenerated carriers to electrodes and may cause them to act as resistors in the device series. These issues are especially prevalent in thicker transport layers, which would likely be the case for industrial roll-to-roll processing which is limited to organic layers of 100 to 300 nm.[6] In order to overcome transport issues, doping of organic transport layers is performed to passivate trap sites and increase the concentration of free carriers. Doping of the organic transport layer has numerous impacts on PSC performance, which several studies attribute to improvements in carrier transport.[21] The subject of this dissertation is to understand the additional impacts of interfacial passivation and bimolecular recombination as a result of the charge transfer to the surface of $MAPbI_3$ from either the electron transport layer or the small molecule dopant itself. The context for this work is provided in this introductory chapter. To introduce this dissertation's investigation of the interface between $MAPbI_3$ and organic semiconductors, topics covered will include a relevant background of both systems, as well as the known impacts of using these materials jointly in a device. Topics include (1) an introduction to PSCs, (2) a description of perovskite solar cell devices, focusing on the role of the electron transport layer, (3) an overview of interfacial passivation outlining the surface characteristics of $MAPbI_3$ and known passivation techniques, (4) a review of semiconductors that are known to be able to be surface doped using small molecule dopants, and (5) a background of *n*-type doping of organic semiconductors.

1.1 Introduction to Perovskite Solar Cells

1.1.1 Motivation for Solar as an Alternative Energy Source

There is a growing need to develop renewable energy sources in order to meet increased global consumption while limiting the release of greenhouse gases into the atmosphere. Potential alternative energy sources include solar, nuclear, hydropower, geothermal, wind, wave, tidal and biomass. Aside from nuclear power, these energy sources are tied to geographic locations and are likely to all play a role in the transition away from fossil fuels. Solar energy is a promising candidate for widespread deployment as there is unrestricted capacity for energy collection from photovoltaics. Current power generation and potentials of the most common forms of renewable energies are summarized in Table 1.1.[17] Several conclusions can be drawn regarding the potential for solar energy: (1) even with deployment in limited land area, photovoltaics alone could produce substantially more energy than current need and (2) compared to other renewable sources, solar radiation is by far the largest potential source of energy.[22] It is therefore likely that a sustainable global energy system based on renewable sources will depend on solar energy as a major source. An important benefit to photovoltaics is that it can be used as the electricity supply in many rural and remote areas where power grids are not economically feasible, which is especially important in the developing world where people are still seeking a higher standard of living.[23] A primary consideration for widespread deployment will be developing technologies that can become economically competitive with fossil fuels.

Table 1.1 Current generation and potentials of selected renewable energy sources.[17] The current global energy demand is ~17.7 Terrawatts (terra is 10^{12}, and giga is 10^{9}).

Power Source	Current Generation [GW]	Technical Potential [GW]	Theoretical Potential [GW]
Hydropower	1,064	1,585	4,660
Biomass Energy	1,585	>8,750	92,000
Solar Energy	227	>49,900	1.23×10^{8}
Wind Energy	433	20,300	190,000

1.1.2 Introduction to Solar Cell Devices

Solar irradiance on a semiconductor results in an absorbed photon exciting an electron from the valence band to the conduction band, leaving behind a hole.[22] The basis of solar cell devices is that electron-hole pairs can be separated by a semiconductor diode structure, resulting in the collection of charge carriers on opposite sides of a device in the form of electrical energy. A semiconductor diode is composed of a *p*-*n* junction connected to two electrodes. Before photon absorption, the concentration gradient of free carriers in a *p*-*n* junction will result in holes diffusing from the *p*-type region into the *n*-type region, and electrons diffusing from the *n*-type region into the *p*-type region. This leaves behind ionized donor or acceptor atoms that are no longer screened, creating a depletion region with an electric field. Upon absorption of photons in the depletion region, electrons in the conduction band move in the opposite direction of the electric field (towards the *n*-type region) and holes in the valence band move in the same direction of the electric field (towards the *p*-type region).[22] Consequently, electron-hole pairs are separated and move towards opposite ends of the device where they are collected.

Design of efficient solar cell devices aims for (1) maximization of the absorption of photons through control over the bandgap (optimum is 1.1 eV) and (2) minimization of recombination of photogenerated electron-hole pairs in the device.[22] There are several potential recombination mechanisms that can occur: recombination through traps (defects) in the band gap (first order), radiative (band-to-band) recombination (second order), and Auger recombination (third order).[24] An illustration of these recombination pathways is given in Figure 1.1.[22] Trap-assisted recombination can occur both in the semiconductor bulk and at the surface. The concentration of surface traps is particularly high due to defects that occur as

a result of the abrupt termination of the crystal lattice.[22] As a result, passivation of surfaces/interfaces in solar cells is often key to achieving high device performance. Radiative recombination, in which electron and holes recombine, is simply the reverse of photon absorption and is the basis for devices such as lasers and light emitting diodes (LEDs). Auger recombination also results in the recombination of an electron-hole pair, but instead of reemitting a photon, the energy is transferred to third carrier. After excitation, the third carrier will relax thermally and release excess energy and momentum in the form of a phonon.[22]

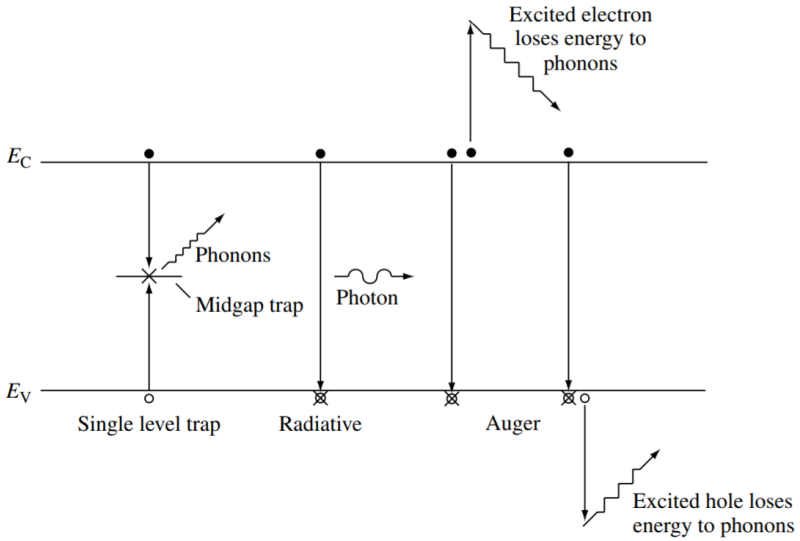

Figure 1.1 Carrier recombination process in solar cells: trap-assisted recombination, radiative recombination and Auger recombination. (From [22])

Quantification of solar cell performance is based on several figures of merit, namely the open-circuit voltage, V_{OC}; the short-circuit current, I_{SC}; the fill factor, FF; and the power conversion efficiency, PCE. It is also common to report the I_{SC} normalized for area, or J_{SC}. Figure 1.2 gives an example current-voltage curve showing how V_{OC}, I_{SC} and FF are defined.[22] An efficient solar cell will have a high V_{OC}, a high I_{SC}, and a FF as close as possible to 1. The FF is a measure of the squareness of the I–V curve and is defined as the ratio of the

maximum achieved power to the to the product of the V_{OC} and I_{SC}, which is always less than one.[22]

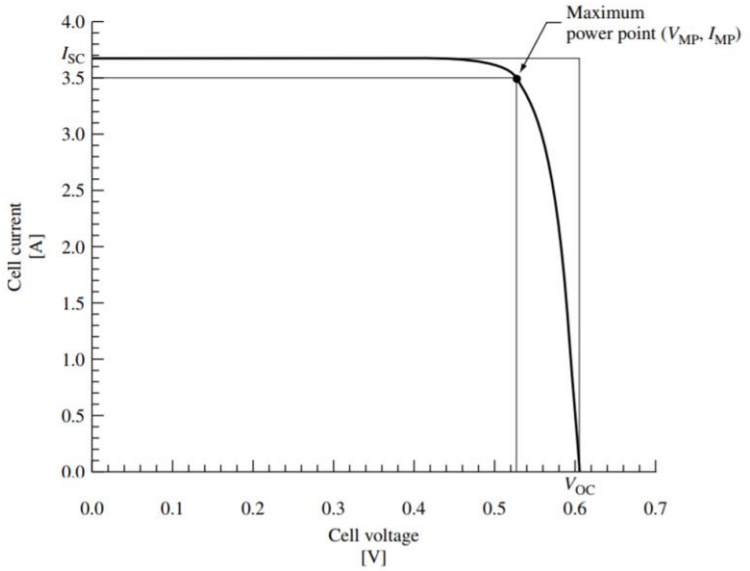

Figure 1.2 Current-Voltage (I-V) curve of a solar cell showing how I_{SC}, V_{OC} and FF are defined. Fill factor is the ratio of the maximum achieved power to the product of the V_{OC} and I_{SC}, and is always <1. (From [22])

1.1.3 Potential for Perovskites in Photovoltaics

While silicon solar cells are widely commercialized, alternative photovoltaic technologies are of interest due to their potential to reduce costs and/or increase efficiency. Silicon solar cells have power conversion efficiencies (PCE)s up to 26%,[25] benefit from long lifetimes of ~20 years,[26] and continue to drop in price due to mass production.[27] However, there is still room for improvement in the photovoltaic industry. The manufacturing process of silicon is very energy intensive, and usually uses rare and toxic materials like cadmium telluride, copper indium selenide, cadmium indium gallium di-selenide and silicon tetrachloride.[28] Additionally, the indirect band gap of silicon also makes it a non-ideal candidate for solar cell applications.

In the past decade, a new solar cell technology has emerged that shows a great deal of promise called perovskites. The first perovskite $CaTiO_3$ was discovered in 1839, and was named after Russian mineralogist Count Lev Perovski. Collectively, perovskites are termed all compounds that adopt the crystal structure of $CaTiO_3$,[29] although in recent years "perovskite" is commonly assumed to refer to the photovoltaic subset of these compounds. In 2009, Tsutomu Miyasaka of Toin University in Japan fabricated a new type of solar cell made of the organometal halide perovskite $CH_3NH_3PbI_3$ (or frequently abbreviated $MAPbI_3$) with a conversion efficiency of 3.8%.[30] Currently the highest efficiency PSCs approach 22%,[18] which is similar to the performance of commercial silicon cells. In addition to attaining similar performance levels (albeit in a laboratory environment), perovskites could offer several advantages over silicon: processing occurs close to room temperature, successive layers of the device stack are deposited using easily scalable methods, and the composition consists of earth abundant materials. Furthermore, it may be desirable to create tandem solar cells of silicon and perovskites to more efficiently harvest higher energy photons.[31] This is a result of the differing band gaps of silicon and $MAPbI_3$, which are 1.1 and 1.6 eV respectively.

1.1.2 Semiconductor Properties of $MAPbI_3$

Hybrid halide perovskites have the chemical composition of ABX_3, where the A site is a monovalent, non-coordinating cation (methylammonium (CH_3NH_3 or "MA"), formamidinium ($HC(NH_2)_2$ or "FA") or Cs), the B site is a bivalent p-block metal (typically Pb, Sn and Ge), and the X site is a halide anion (iodide (I^-), chloride (Cl^-), or bromide (Br^-)), which coordinates to the metal.[29] The perovskite composition that has received the most attention in recent years is $MAPbI_3$ (Figure 1.3),[32] although many compositional variations

have been investigated to improve performance, stability, or environmental compatibility. The crystal structure of halide perovskites consists of corner sharing [BX_6] octahedra, with an A cation occupying the central cuboctahedral cavity.[29] The crystal structure of 3D perovskites has a very high lattice stabilization energy,[33] which allows it to form even with variation in processing conditions and precursor concentrations.

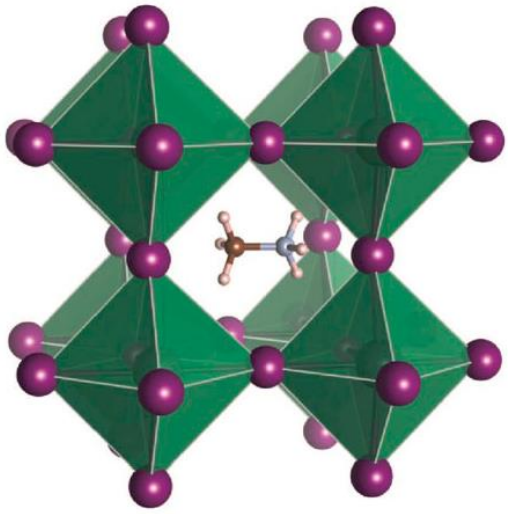

Figure 1.3 Crystal structure of cubic metal halide perovskites with the generic chemical formula ABX_3. Organic or inorganic cations occupy center position A (depicted is MA) whereas metal cations and halides occupy the B (grey) and X (purple) positions respectively. (From [32])

$MAPbI_3$ has proven to be a remarkable candidate for photovoltaic applications due to semiconductor properties such as a direct bandgap which is responsible for very strong optical absorption ($\alpha \approx 10^5$ cm^{-1}),[17] very low trap densities (~10^{10} cm^{-3}),[34] high 3D mobility (>100 $cm^2V^{-1}s^{-1}$) due to a corner connected network of octahedra[35] and small effective masses of charge carriers,[36] large exciton diffusion lengths (150 μm),[35] and photon recycling following radiative recombination.[37]

As part of its character as an ionic semiconductor, vacancy defects play a major role in perovskite devices. This results in a diode structure of *p-i-n* formed in $MAPbI_3$ solar cells. *P-*

type doping is created by the presence of lead and methylammonium vacancies; *N*-type doping is created by the presence of iodine vacancies.[38] Under an applied electric field, as occurs in photovoltaic operation, vacancies drift to the corresponding electrodes and create a *p*-*i*-*n* structure,[38] where "*i*" is an intrinsic (undoped) layer between the *p*- and *n*-type layers. It is not unprecedented in solar cells devices to use a *p*-*i*-*n* diode rather than a conventional *p*-*n* diode. *P*-*i*-*n* structures can be desirable in solar cells when charge carriers have low mobilities and thus are unlikely to encounter one another, because charge carrier creation is enhanced by the built in electric field extending over a larger absorption width. However, in systems with high mobility charge carriers, *p*-*i*-*n* structures lead to a high recombination rate of electrons and holes due to the region where recombination occurs (i.e. $n \approx p$ or intrinsic) is larger. Consequently, it is likely that perovskite solar cells would have higher performance if a *p*-*n* structure could be engineered.

In comparison to other high performance semiconductors, there is a lack of knowledge about how to dope perovskite systems. For perovskites to be a candidate for a wider range semiconductor applications, it is essential to understand how to manipulate the Fermi level and increase the number of charge carriers. Doping has proved challenging as a result of the complex crystal structure of $MAPbI_3$, making it difficult to find substitutional atoms with the correct charge within the tolerance factor of the lattice. Currently, the only published method of controlling the charge carrier concentration is to vary the ratio of MAI and PbI_2 in the precursor solution in order to create vacancies.[39,40] There have been several other reports of doping in literature, but these studies are controversial.[41–44] Criticisms include that improvements in electrical performance may be the result of dopants changing the crystallization process.[21] In contrast to traditional doping via introducing impurity atoms, the

surface transfer doping technique investigated in this thesis is analogous to modulation doping. Modulation doping is used in conventional semiconductor systems such as GaAs when very high carrier mobilities are desired.[45] Modulation doping is performed by successive deposition of different semiconductor materials in which free carriers from a doped layer enter an intrinsic layer, which serves to create free carriers that are spatially separated from impurity donors. Thus, modulation doping avoids introducing impurity atoms that would act as donor-carrier scattering centers in the semiconductor layer of interest.

1.2 Perovskite Solar Cell Devices

1.2.1 Architectures of Perovskite Solar Cells

In PSCs, the perovskite absorber material is sandwiched between an electron transport layer (ETL) and hole transport layer (HTL), which serve to transport charge carriers to electrodes. The remarkable performances of PSCs is not limited to any specific device architecture (*n-i-p* or *p-i-n*) or choice of material of the transport layers. The three most common solar cell architectures are mesoscopic, conventional planar, and inverted planar, which are depicted in Figure 1.4.[5] The mesoscopic device architecture (*n-i-p*) is the most commonly reported and is typically composed of a stack of a transparent conducting substrate (e.g. FTO), an electron-transport layer (ETL) composed of compact TiO_2, a mesoporous scaffold layer , a perovskite layer, a hole transport layer (HTL), and a high-work-function (WF) electrode.[5] In some devices, the mesoporous TiO_2 scaffold is coated with PCBM ([6,6]-Phenyl C_{61} butyric acid methyl ester) to create a bilayered ETL in order to take advantage of PCBM passivation of oxygen defects that are present on the TiO_2 surface.[46] Planar device architectures (*n-i-p*) have a similar stack structure, but lack the mesoporous scaffold.[5] Their electron transport layers

are composed of compact metal oxides such as TiO_2, ZnO or SnO_2.[5] The downside to these device architectures is that the use of metal oxides as the ETL requires high annealing temperatures (<450°C), which can be an obstacle to commercialization and would lead to degradation of substrates in flexible devices. Another alternative structure is the inverted planar device structure (*p-i-n*), which employs a transparent conducting substrate (e.g., ITO), an HTL, a perovskite layer, an ETL, and a low-WF metal electrode.[5] In this structure, typically organic semiconductors are used as both the HTL and ETL, which allows for low temperature fabrication (<150°C). PCBM has an added advantage as an ETL because it provides more efficient charge extraction from perovskites than metal oxide layers do.[47]

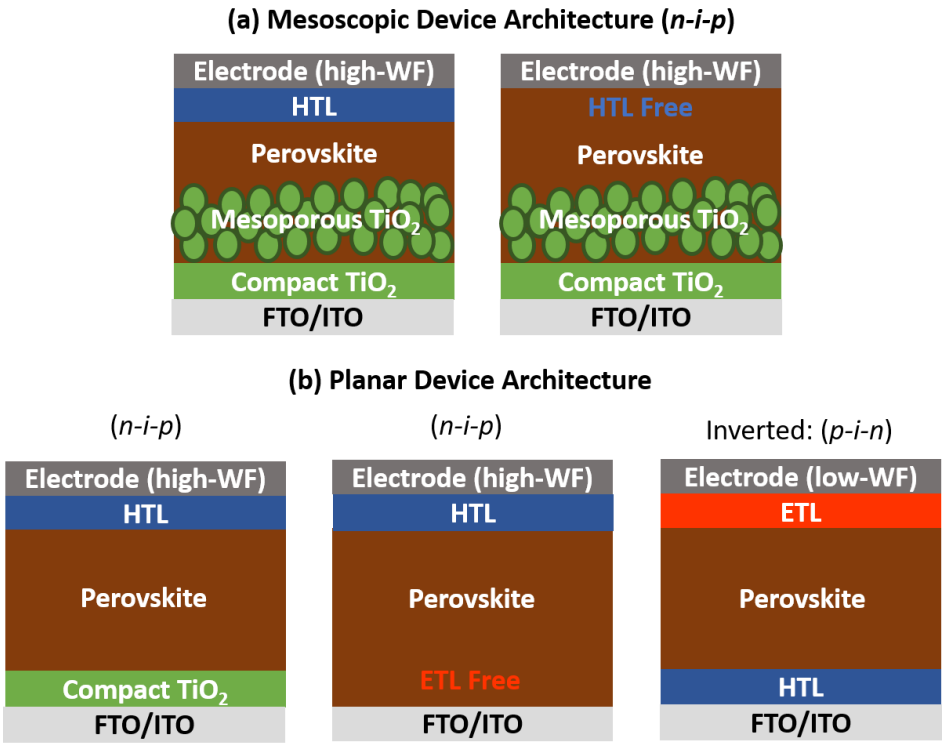

Figure 1.4 Structure diagram of perovskite solar cell device architectures. (a) Mesoscopic PSCs, which can include: (left) conventional mesoscopic and (right) hole transport layer-free architectures. (b) Planar PSCs, which can include: (left) conventional planar, (middle) compact layer-free and (right) inverted planar architectures.

1.2.2 Role of Electron Transport Layers

The presence of transport layers in PSCs is necessary to prevent contact between $MAPbI_3$ and metal electrodes, which may react and lead to degradation of the perovskite.[2–4] ETLs serve to extract and transport photo generated electrons and act as a blocking layer for holes to suppress charge recombination.[5] There are numerous characteristics to consider for the choice of an ETL: energy level alignment, electron mobility, passivation of surface trap sites, and morphological contact to the perovskite surface.[22] These factors determine charge extraction, transfer and recombination at the interface, which play important roles in determining device performance. The impact of these factors can be summarized as follows:

- Energy level alignment between the ETL and perovskite facilitates electron extraction,[15] which impacts the V_{OC}. The V_{OC} is also influenced by the energy difference between the Fermi levels of the ETL and HTL.
- Carrier mobility should be high in order for electrons to be efficiently transported through the ETL and collected at the electrodes, which impacts the I_{SC}.
- Trap sites at the perovskite surface and grain boundaries can lead to carrier recombination, which will impact the $V_{OC.}$ Some ETLs, such as PCBM, have been shown to be able to passivate defect sites.[48]
- Morphology is important since good contact between the perovskite and ETL is necessary for efficient charge extraction. This is often cited as the cause for poor performance in heavily doped organic ETLs because dopant aggregates disrupt contact of the ETL with the perovskite surface.[49,50]

1.3 Passivation of Interfaces in $MAPbI_3$ Solar Cells

Surface and interface passivation is one of the most commonly used strategies to improve the photovoltaic performance of PSCs.[51] Reports have shown that the interfaces between various functional layers are essential to the performance of a device.[52,53] Typical PSCs in the inverted device structure contain six main interfaces, including (1) the interface between the transparent conductive oxide and hole transport layer (HTL); (2) the interface between the hole transport material and perovskite; (3) interfaces at perovskite grain boundaries; (4) the interface between the perovskite and electron transport layer (ETL); (5) the interface between the electron transport layer and electrode, and (6) the interface between the electrode material and atmospheric environment.[51] Charge recombination processes usually take place at the interfaces due to the high concentration of defects that occur at the surface termination of crystal lattices. In recent years, there have been numerous approaches developed to accomplish interfacial passivation; this section will outline approaches related to organic transport layers.

1.3.1 Surface Characteristics of $MAPbI_3$

Crucial to insight of how to develop passivation techniques is a fundamental understanding of the types and densities of defects that form at surfaces. The bulk and surface trap density of $MAPbI_3$ have been reported as 5×10^{16} cm^{-3} and 1.6×10^{17} cm^{-3} respectively measured with time-resolved photoluminescence.[54] The surface trap density of $MAPbI_3$ is low compared to conventional covalent semiconductors. This can be illustrated by the fact that $MAPbI_3$ thin films have reported surface and grain boundary recombination velocities of ≈150 cm/s and ≈7 cm/s respectively,[9] which are several orders of magnitude smaller than the surface recombination velocity of unpassivated silicon ~10^6 cm/s.[55]

There have been numerous studies on the chemical composition of the surface termination of $MAPbI_3$. Theoretical studies of $MAPbI_3$ indicate that formation energies of MAI-terminated slabs are much lower than those of PbI_2-terminated slabs.[56] This can be attributed to two causes: (1) the MAI-terminated slab has a lower density of surface dangling bonds, and (2) the MA-I bond is weaker than the Pb-I bond, which typically results in lower surface energy.[56] Despite energetic considerations, processing outcomes are likely to be the decisive factor in determining surface termination. The low thermodynamic stability of $MAPbI_3$ and higher volatility of methylammonium (MA) and iodide relative to lead, can cause these species to be sublimed during the annealing process following spin-coating,[57,58] resulting in under-coordinated Pb^{2+} atoms at the crystal surface.[59] Theoretical and experimental studies have shown that these under-coordinated Pb^{2+} atoms can act as electronic trap states within the perovskite material.[40,60] Therefore, the purpose of some passivation routes is to use the net charge of Pb^{2+} atoms to create coordination, or bond formation with electron donating or sharing species.[59,61,62]

Another consideration is the energetic position of recombination centers within the bandgap. The low surface and grain boundary velocities of $MAPbI_3$ thin films indicate that the density of these recombination centers is relatively low, albeit still existent.[9] In many computational and experimental studies, trap-assisted recombination is identified as the dominant recombination pathway, primarily caused by the presence of electron traps near the center of the band gap.[10–14] Consequently, a second route for passivation could be to shift the position of the Fermi level such that the recombination center becomes passivated.

Both the surface termination and Fermi level position were considered in the passivation technique outlined in this dissertation. *N*-type doping of the surface of $MAPbI_3$ via electron

transfer from the ETL is energetically favorable due to the positive charge on the Pb^{2+} terminated surface. In addition, *n*-type doping also results in a Fermi level shift towards the conduction band, which would passivate mid-gap recombination centers. The most common forms of surface passivation reported in literature to date are also described below. These studies were used as a guide for developing design principles and identifying the type of techniques used to determine if surface passivation was achieved.

1.3.2 Surface Passivation by PCBM and Fullerene Derivatives

Employment of PCBM and other fullerene derivatives as the ETL is a commonly used method to passivate the surface of perovskites. This effect was first reported by the Huang Group, who showed that annealing of a PCBM/perovskite stack resulted in the fullerene's diffusion into grain boundaries and surface defects.[48] Passivation of surface traps was confirmed by the significant increase in the photocurrent response speed (Figure 1.5(a)), and a substantial increase in PL intensity (Figure 1.5(b) & (c)).[48] PCBM passivation leads to higher device performance by improving various electrical properties: reduced charge carrier recombination at the interface, longer charge carrier lifetime, and higher mobility in the ETL. Other fullerene derivatives, such as intrinsic fullerene (C_{60}) or $IC_{60}BA$ have also been reported to have a similar effect.[63] It is believed that the mechanism behind the fullerene passivation is a result of PCBM adsorbing onto the Pb-I antistite defective grain boundary (Figure 1.5(d).[64]

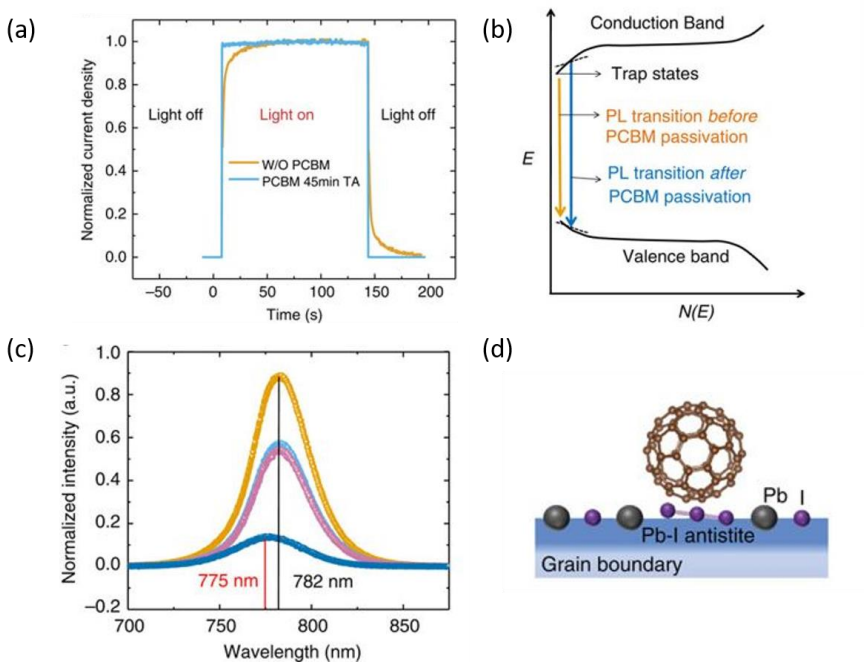

Figure 1.5 Evidence of PCBM passivation of the $MAPbI_3$ surface. (a) Photocurrent upon turning on and turning off the incident light for the devices with and without PCBM. (b) Schematic of the blue-shift of the PL peaks due to the passivation effect. (c) The PL spectra of perovskite films measured with PCBM from the air side (dark blue), from the ITO side (pink), and perovskite films without a PCBM layer from the air side (orange), and from the ITO side (sky blue). (d) Passivation schematic of PCBM adsorbing onto Pb-I antistite defective grain boundary which acts as a deep trap. (From [48] and [64])

1.3.3 Surface Passivation by Lewis Bases

Snaith et al. developed a surface passivation method by coating the perovskite surface with the Lewis bases thiophene, pyridine, and iodopentafluorobenzene (IPFB).[59,65] Lewis base treatment resulted in PCE increases from 13% for the untreated solar cells to 15.3% and 16.5% for the thiophene and pyridine-treated solar cells respectively.[59] This performance improvement originated from reduced non-radiative electron–hole recombination, which led to an increase in carrier lifetimes by nearly an order of magnitude (up to 2 μs) (Figure 1.6(a)), as measured by time-resolved photoluminescence.[59] The proposed mechanism for this increase is that Lewis bases bind to and screen the electrostatic charge of under-coordinated

Pb^{2+} atoms at the film's surface that would otherwise act as trap sites.[59] A carton of this mechanism is given in Figure 1.6(b) & (c).[59]

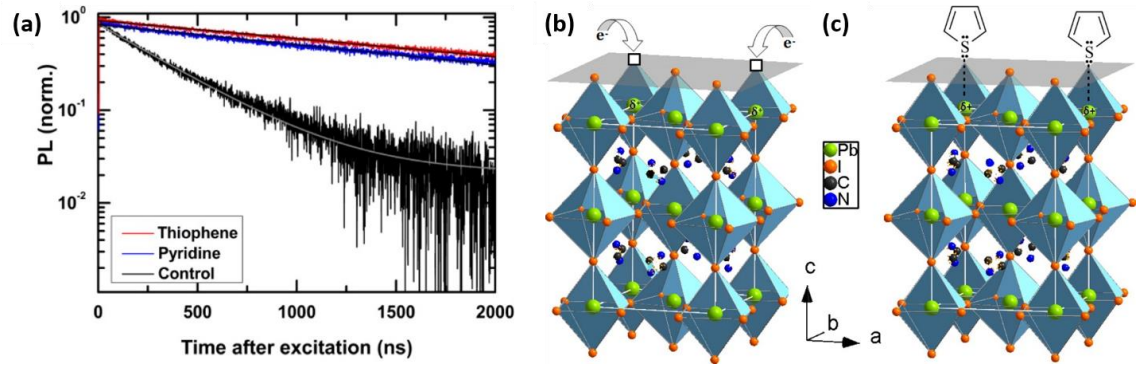

Figure 1.6 Evidence and mechanism for Lewis base passivation of the $MAPbI_3$ surface. (a) Time-resolved photoluminescence of thiophene- and pyridine-passivated perovskite surfaces as compared to a bare perovskite surface following a 507 nm pulsed excitation. (b) Sublimation of iodine at the surface of the perovskite leads to vacancy sites (depicted as hollow boxes) and a net 2+ charge on Pb atoms (shown in green). The surface net positive charge acts as a Coulombic trap for photo generated electrons. (b) Thiophene or pyridine molecules can donate electron density to Pb atoms by formation of a covalent bond, effectively neutralizing the excess surface positive charge. (From [59] "Reprinted (adapted) with permission from (Noel, N. K.; Abate, A.; Stranks, S. D.; Parrott, E. S.; Burlakov, V. M.; Goriely, A.; Snaith, H. J. Enhanced Photoluminescence and Solar Cell Performance via Lewis Base Passivation of Organic–Inorganic Lead Halide Perovskites. *ACS Nano* 2014, *8* (10), 9815–9821). Copyright (2014) American Chemical Society.")

1.4 Surface Transfer Doping

An intrinsic semiconductor is a pure semiconductor without any dopant species present, resulting in a Fermi level that is positioned in the center of the band gap. However, for many applications, semiconductors are doped to increase the concentration of free carriers, leading to increased electrical conductivity and a shift in the Fermi level position. Conventional doping is usually achieved by ion implantation via bombarding the semiconductor with energetic ions (dopants) followed by thermal annealing. This incorporates external impurity atoms into the host lattice of the semiconductor. Depending on the relative number of valence

electrons, the dopants can either donate excess electrons as negative free charge carriers to the conduction band (*n*-type doping), or can accept additional electrons from surrounding atoms, leaving positively charged holes as free charge carriers in the valence band (*p*-type doping). While this method of doping is well established, there are some classes of semiconductors and applications for which it is unsuitable which require the development of doping techniques that are less structurally disruptive.[66]

Nanostructured materials such as one-dimensional (1D) nanowires and two-dimensional (2D) nanosheets experience severe crystal damage as a result of bombardment with dopant ions. Consequently, developing new strategies to effectively dope nanostructured semiconductors has recently been of interest. For carbon and phosphorus based semiconductors such as carbon nanotubes (CNTs), graphene, phosphorene and organic semiconductors, a nondestructive method of doping can be performed by electron transfer between the semiconductor and molecular dopants on its surface.[67] The prerequisites for surface doping for these semiconductors are based on energetics: the LUMO of the molecular dopant must be close to or below the Valence Band Maximum (VBM) of the semiconductor for *p*-type doping, or the HOMO of the dopant must lie close to or above the Conduction Band Minimum (CBM) of the semiconductor for *n*-type doping. The additional prerequisite of a lack of surface states is not relevant for low dimensional semiconductors.

Surface doping has been illustrated for several three dimensional semiconductors, such as silicon and diamond.[68,69] For bulk semiconductors, this doping method results in a free carrier distribution that is localized near the surface, due to the electric field created by the interfacial charge separation.[66] However, localization still allows charge carriers to freely move parallel to the surface. This technique is thus not suitable for bulk doping but is of

interest for surface/interface engineering. For charge transfer to occur, surface treatment must be carried out for covalent semiconductors that have surface reconstructions from the bulk or oxide layers. The surface treatment (e.g. hydrogenation for diamond and alkylation for silicon)[68,69] induces surface passivation by removing interfering surface states from the gap and lowering the ionization energy sufficiently to facilitate electron transfer.[70] Charge transfer from small molecule dopants to semiconductor surfaces is not a universal occurrence as the reaction is highly dependent on the nature/quantity of surface states.

Surface transfer doping involves significant interfacial charge transfer that results in band-bending of the surface.[66] When the semiconductor and small molecule dopant come into contact, the Fermi levels equilibrate by driving electrons from the valence band of the semiconductor to the empty acceptor levels of the dopant (*p*-type), or from the full donor level of the dopant to the conduction band of the semiconductor (*n*-type). Fermi level equilibration can also occur between semiconductors in contact. As a result of the interfacial charge transfer, free carriers are created near the semiconductor surface, leaving behind charged dopant molecules. Together this builds up a space-charge layer that induces band bending of the semiconductor surface. Band bending can be so drastic that the Fermi level of the semiconductor can be in the degenerate regime.[66]

1.5 N-type doping of Organic Semiconductors

1.5.1 Molecular Doping Overview

Doping of inorganic and organic semiconductors is achieved via two distinct strategies. For inorganic semiconductors, doping is accomplished by substitution of an atom or addition of an interstitial atom within the crystalline matrix. These impurity atoms either add electrons

to donor states near the conduction band edge (*n*-type doping), or provide empty acceptor states near the valence band edge (*p*-type doping). In contrast, doping in organic semiconductors is accomplished by blending with small molecules that either accept or donate electrons.[71,72] It is possible to dope organic semiconductors with single atoms, however this route leads to dopant diffusion that causes poor device performances and lifetimes.[71,72] Molecular doping circumvents diffusion issues by controlling the molecule's size or shape to create bulkiness. This poses an additional challenge for incorporating high dopant concentrations that don't disrupt the structural quality of organic semiconductors.

The driving force for small molecules to dope organic semiconductors is based on their relative energy level positions. For effective charge transfer, the ionization energy, I.E., (the HOMO level) of the small molecule must lie close or above the electron affinity, E.A., (the

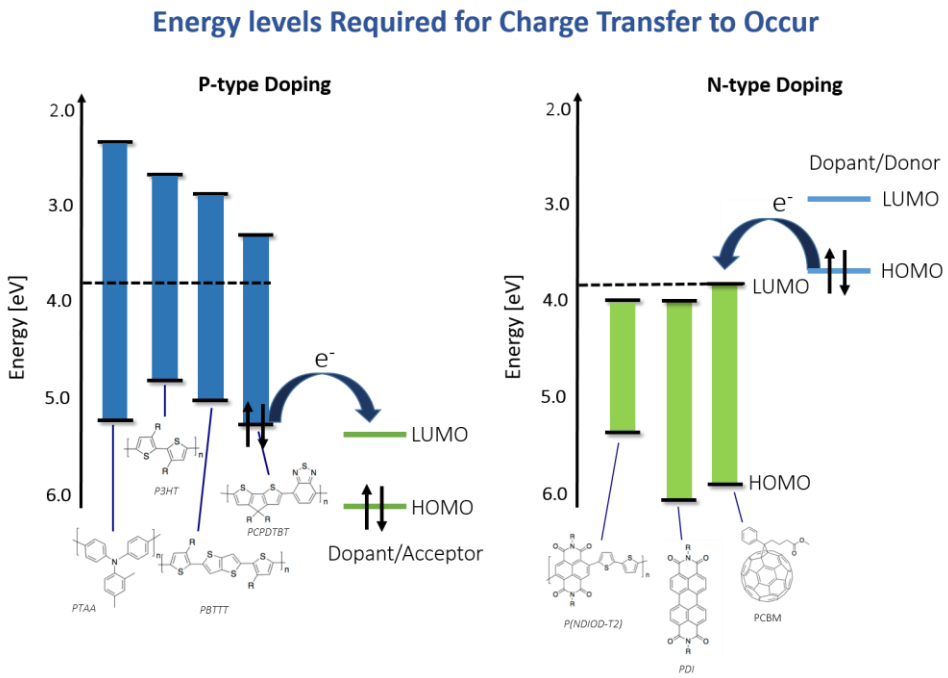

Figure 1.7 Scheme of *p*-type doping (left) and *n*-type doping (right) of organic semiconductors. In *p*-type doping the dopant molecule acts as an electron accepter. In *n*-type doping the dopant molecule acts as an electron donor.

LUMO level) of the semiconductor for *n*-type doping, or the electron affinity, (the LUMO level) of the small molecule must lie close or below the ionization potential (the HOMO level) of the semiconductor for *p*-type doping (Figure 1.7). In some instances, activation energy in the form of light or heat is necessary for charge transfer to occur and to dissociate the electron transfer complex into free carriers (carriers not bound to the now ionized dopant molecule).[73]

1.5.1 Classes of Molecular N-type Dopants

The electrical performance of *n*-type organic semiconductors has lagged behind that of *p*-type semiconductors. The highest reported conductivities for stable *p*-doped polymers are ~1000 S/cm for materials such as PEDOT:PSS and solution-processed poly(alkyl-thiophene) derivatives. [74–77] In contrast, the highest conductivities for *n*-doped polymers reach ~1 to 10 S/cm[78–80] with only unstable alkali-metal-doped polyacetylene reaching 1500 S/cm.[81] Doping of *n*-type organic semiconductors has proved challenging due to their relatively shallow electron affinities (EA) of -3.5 to -4.5 eV which make them prone to dedoping when exposed to the ambient atmosphere. Accordingly, much of the work to develop new *n*-dopants has focused on enhancing the air-stability of either the precursor dopant or the doped charge transfer state.[71] Strategies for *n*-type doping generally fall into three different categories: (1) Alkali metals, (2) molecular compounds with very high HOMOs, and (3) air-stable dopant precursors that can donate electrons upon incorporation into a film. Alkali metals can come in the form of elemental dopants (such as Li, Na, K, and Cs), or inorganic solids (such as oxy metal salts of the general form X_2CO_3 where X = Li, Na, K, Rb, Cs, as well as Cs_3PO_4, Cs_3VO_4, CsN_3, and Li_3N).[72] Alkali metal dopants have diffusion issues due to their small size, consequently they will not be discussed further in this section. A brief overview of

molecular dopant classes will be described below. To accompany this description, Figure 1.8 gives the chemical structure of the classes of molecular dopants with examples.

Strategy 2: Molecular compounds with very high HOMO levels

- This class of dopants has a simple charge transfer mechanism due to their low ionization energies. As a consequence, dopants are sensitive to air and must be stored in a nitrogen environment, making them less appealing for industrial applications. There is a variety of examples within this dopant class, including tetrathiafulvalene (TTF) and its derivatives,[82] tetrathianaphthacene (TTN),[83] metal complexes such as $[Ru(terpy)_2]^0$, $[Cr(bpy)_3]^0$, and $[Cr(TMB)_3]^0$,[84] and dimetal complexes such as $Cr_2(hpp)_4$ and $W_2(hpp)_4$.[85–87] Additionally, cobaltocene and decamethylcobaltocene (DMC) are also part of this class of dopants, and were utilized in part of this dissertation. Cobaltocene and decamethylcobaltocene result in strong *n*-type doping as a result of their solid-state ionization energies of -4.07 and -3.30 eV respectively.[88,89]

Strategy 3: Air-stable precursor molecules that can donate an electron

- Hydrides: This class of dopants couples a chemical reaction to the electron transfer process. The dopant donates a hydride atom to the organic semiconductor, which is followed by electron transfer. The exact mechanism for this reaction likely varies for the specific dopant/organic semiconductor system. The doping mechanism for this class of dopants is distinct from others with solely electron transfer, so the energetic prerequisites for electron transfer are not entirely determined by the alignment of the dopant HOMO and the organic semiconductor LUMO. Rather, the effectiveness of doping depends on the free energy of electron transfer from dopant radical to the organic semiconductor and on the difference in the strengths of the dopant–H bond and the organic semiconductor C−H

bond formed as a result of hydride transfer.[72] The most well-known dopant of this class is N-DMBI (4-(1,3- dimethyl-2,3-dihydro-1H-benzoimidazol-2-yl)phenyl)- dimethyl amine).[90]

- Anion Doping: This class of dopants is composed of soluble Lewis base anions that will electron transfer to an electron-deficient π system (π-acid) with a positive quadrupole (a distribution of electric charge consisting of four equal monopoles) moment.[91] Design of organic semiconductors for anion doping requires the molecular core to have high strength π-acidity. In addition, the standard prerequisite for the dopant, that the HOMO of the dopant must be higher than the LUMO of the organic semiconductor, must also be met for efficient electron transfer. Examples of demonstrated anion dopants are TBAX salts (X− = F−, Br−, I−, AcO−, HO−).[92]

- Cationic Dyes: This class of dopants uses precursors that donate an electron to organic semiconductors by being activated by heat and/or illumination. Cationic dyes such as pyronin B chloride,[93] crystal violet,[94] and halide salts such as o-MeO-DMBI-I (2-(2-methoxyphenyl)-1,3-dimethyl 1H-benzoimidazol-3-ium iodide)[95,96] consist of an organic cation and an inorganic counter ion.[72] Upon evaporation, the inorganic counter ion is lost and the remaining neutral radical becomes volatile and has strong electron donor characteristics. A leuco radical can also form during evaporation, which has weaker electron donating abilities than the neutral radical. The mechanism for electron transfer from the leuco radical requires light activation, which excites an electron from the HOMO to LUMO level of the dye. Subsequently, electron transfer occurs to the LUMO of the organic semiconductor. The *n*-doping effect becomes permanent by the stabilization of the positive charge on the dopant by hydride transfer to the organic semiconductor.[71,97]

- Dimers: This class of dopants is based on the concept that an air-sensitive dopant radical can be stabilized by dimerization through a weak central C−C σ bond. The doping mechanism can either proceed by electron transfer followed by cleavage of the dimer or cleavage of the dimer followed by electron transfer.[98] There are several advantages to this class of dopants: (1) dopant precursors that are stable in air, (2) dopants can be both solution and vacuum processed, and (3) the size of the dopant cation is tunable to enable some control over ion diffusivity, deposition rate and morphological effects.[72] Currently, most dimer *n*-dopants are synthesized by alkali metal reductions, which presents a barrier to their widespread use. Dimers of 19-electron metallocenes were first reported as *n*-dopants by the Marder and Kahn groups.[98,99] In addition, dimers of DMBI compounds have also been developed by the Bao and Marder groups.[100]

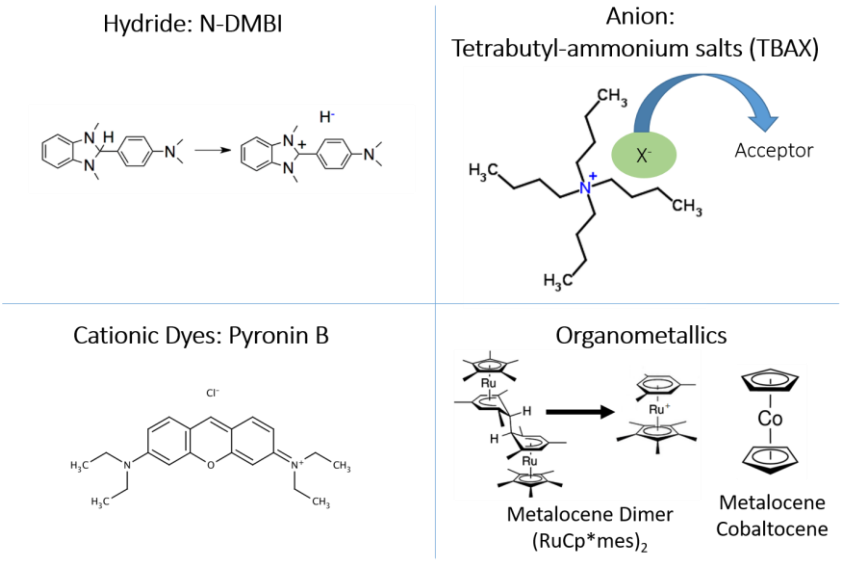

Figure 1.8 Several molecular dopant classes with illustrations of examples dopants, including N-DMBI (hydride transfer dopant), TBAX (anion dopant), pyronin B (cationic dye dopant), $(RuCp^*mes)_2$ (dimer dopant) and cobaltocene (high HOMO dopant).

1.5.2 Structural Considerations for the Organic Semiconductor

From a design standpoint, the structure of *n*-type organic semiconductors will vary based on the desired application. One common application is thin film transistors (TFTs), which are designed to be highly crystalline in order to promote high carrier mobility. The effectiveness of doping a common *n*-type polymer designed for this application was studied by Schlitz et al.[101] In this study, P(NDIOD-2T) (Poly{[N,N'-bis(2-octyldodecyl)naphthalene-1,4,5,8-bis(dicarboximide)-2,6-diyl]-alt-5,5'-(2,2'-bithiophene)}) (reported mobility of 0.85 cm^2/Vs)[102,103] was doped with the *n*-type dopant N-DMBI (Figure 1.9(a)&(b)). Maximum conductivities of ~10^{-3} S/cm were achieved for a doping concentration of a repeat unit: dopant ratio of 10:1. An estimation based on the conductivity equation $\sigma = n \times q \times \mu$ and measurement of mobility (μ) based on field effect transistors indicated that the corresponding carrier concentration (n) is ~10^{17} cm^{-3}.[101] This implies that only 1% of the dopant molecules introduced into solution were active and create free carriers. Typically, heavily doped systems with a 1:1 polymer repeat unit: dopant ratio have carrier concentrations between ~10^{20} to 10^{21} cm^{-3}. [104] To determine why so few dopants were active, the film morphology was characterized using atomic force microscopy (AFM), transmission electron microscopy (TEM) and grazing incidence wide angle scattering (GIWAXS). AFM indicated that large dopant aggregates were present on the film surface (Figure 1.9(c)&(d)). TEM (Figure 1.9(e)) and GIWAXS (Figure 1.9(f)&(g)) indicated that P(NDIOD-2T) was highly ordered and the structure was not significantly perturbed upon doping. These observations were used to conclude that there is poor dopant/polymer miscibility due to the high crystallinity of P(NDIOD-2T), which results in dopant aggregation on the surface while the polymer matrix remains unchanged. This study provided inspiration for design considerations to create polymer structures that would promote dopant/polymer miscibility. In this dissertation,

doping of organic semiconductors with glassy ordering are investigated because they promote free space for dopants to pack. Development of high conductivity systems is relevant to applications such as organic thermoelectrics and integrated circuits. Additionally, having

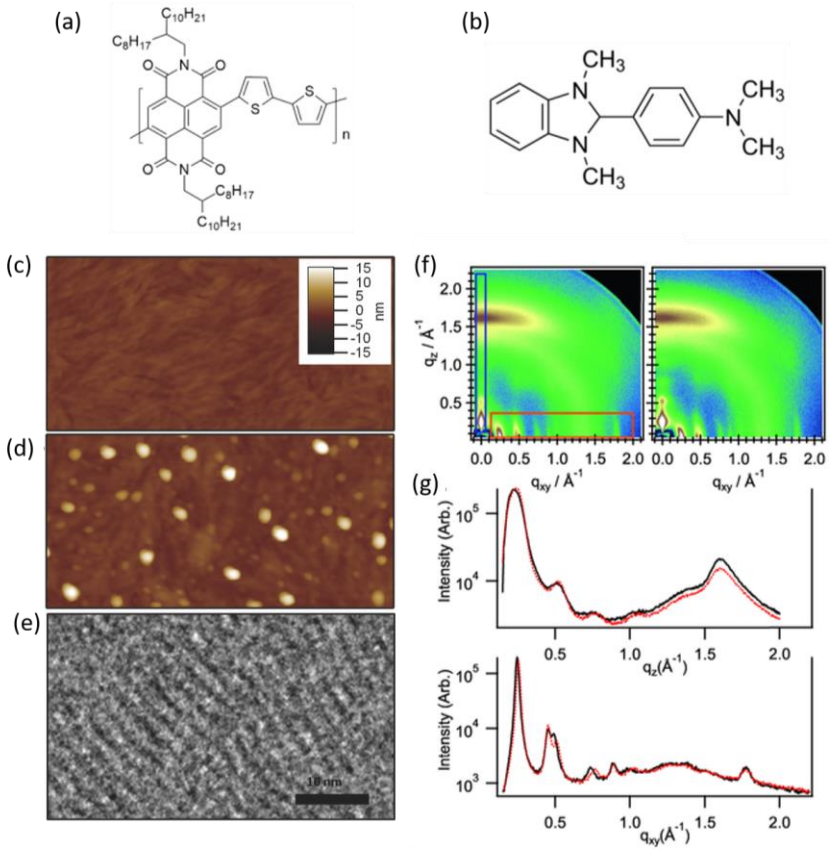

Figure 1.9 Summary of study of polymer: dopant miscibility in a highly crystalline polymer by Schlitz et al. Chemical structures of (a) the semiconducting polymer P(NDIOD-T2) and (b) *n*-type dopant N-DMBI. Atomic force microscopy (AFM) images of (c) neat P(NDIOD-T2) and (d) P(NDIOD-T2) doped at 9 mol.% N-DMBI showing dopant aggregate formation on the surface. (e) Transmission electron microscopy (TEM) reveals the highly ordered structure of N-DMBI doped P(DNIOD-T2) illustrated by clear reflections from the polymer backbone. (f) Grazing incidence X-ray diffraction detector images for (left) P(NDIOD-T2) annealed at 150 °C for 6 hours and (right) P(NDIOD-T2) doped at 25 mol.% N-DMBI and annealed at 150 °C for 45 minutes. The detector images are qualitatively indistinguishable for both processing conditions. (g) Accompanying line cuts along the q_z (top) and q_{xy} (bottom) directions. (From [101])

control over the dopant concentration in PSC ETLs is essential to understanding the effects of charge transfer.

1.5.4 Known Impacts of Doping Organic Electron Transport Layers

The rise of PSCs has created an additional application for doped organic semiconductors, which requires investigation of design principles for high performance. Organic semiconductors are limited in their use as transport layers for PSCs by their low mobility and electrical conductivity, which are detrimental to their ability to efficiently transport electrons to electrodes and may cause the ETL to act as a resistor in the device series. In order to overcome this issue, doping can be used to passivate trap sites and increase the concentration of free carriers through electron transfer.[30,36–38] The impact of doping has a complicated interaction between the ETL and the perovskite surface, leading to changes in solar cell performance by varying doping concentration. There have been several attempts in literature to try to understand this relationship.

Liao et al recently performed a detailed study of doping PCBM with decamethylcobaltocene (DMC) and characterized the impact on various properties that dictate the performance of ETLs.[15] This study was performed using the mesoporous bilayer device architecture in which the TiO_2 scaffold was coated with PCBM (Figure 1.10(a)). Doping resulted in the desired adjustments in electrical properties of PCBM films, with an increase in conductivity of ~10^{-7} S/cm to ~10^{-4} S/cm and an increase in mobility of ~10^{-5} cm^2/Vs to ~10^{-4} cm^2/Vs upon doping (Figure 1.10(b)). Doping resulted in induced shifts in the LUMO level of PCBM from -3.87 eV (neat) to -4.04 eV (0.1 wt% doping), illustrating that doping can be used to tune the interfacial energetic barriers at the PCBM/$MAPbI_3$ interface in order to

achieve better alignment (Figure 1.10 (c)). Time-resolved photoluminescence was used to confirm improved interfacial energy alignment; a reduced carrier lifetime was measured for doped PCBM as compared to neat, suggesting efficient extraction of photogenerated carriers from the perovskite active layer. Doping PCBM also improved the wettability of GBL (γ-Butyrolactone) and DMSO (dimethyl sulfoxide) on the surface of the TiO_2/PCBM bilayered ETL. This resulted in the average grain size of perovskite films increasing from 100 to 300 nm upon doping at 0.1 wt%. Another morphological effect that occurred upon doping PCBM was reduced surface roughness on TiO_2, which was believed to lead to better interfacial contact with the perovskite active layer. These effects would only be a consideration in conventional planar (*n-i-p*) devices. Additionally, doping PCBM was shown to alter the trap density of states (tDOS) of the underlying TiO_2 layer, by reducing the shallow trap density of states from 0.25 to 0.3 eV by two orders of magnitude, which was attributed to improved contact of doped PCBM passivating interfacial traps (Figure 1.10 (d)). This technique was not also used to study the tDOS of $MAPbI_3$ when in contact with doped PCBM. Solar cell performance (including FF, V_{OC} and J_{SC}) initially increases with doping concentration and then decreases (Figure 1.10(e)). Improvement of the V_{OC} upon doping is attributed to better energy level alignment at the interface of PCBM/$MAPbI_3$. Improvement of the J_{SC} is attributed to larger grains in the $MAPbI_3$ film as well as enhanced transport of photogenerated carriers in PCBM as a result of higher mobility. Improvement in FF is attributed to good interfacial contact of doped PCBM with $MAPbI_3$ as well as reduced series resistance, which was confirmed using impedance spectroscopy. Hysteresis was also observed to be reduced for doped PCBM, which was identified as being the result of better interfacial contact.[15] Additionally, trap states in the perovskite layer were also identified as a potential cause for

hysteresis, but the effects of $MAPbI_3$ contact with a doped ETL layer were not investigated. Additional evidence of $MAPbI_3$ surface passivation could be present in the results of this study as there was a substantial increase in steady-state photoluminescent intensity for the ETL/$MAPbI_3$ device stack for doped PCBM (Figure 1.10 (f)).[15]

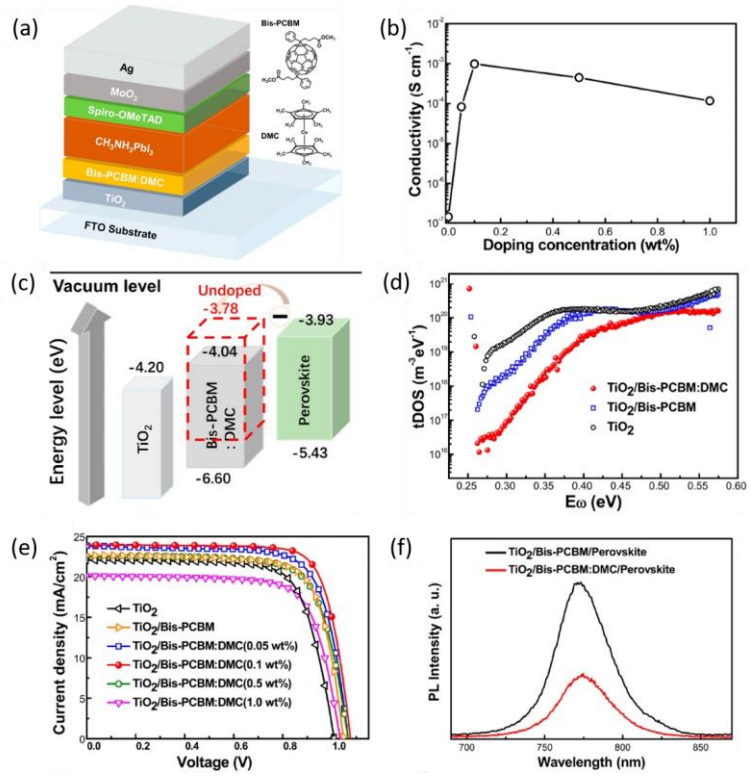

Figure 1.10 Summary of study of ETL performance reported by Liao et al on the effect of doping PCBM with DMC. (a) A diagram of the *n-i-p* device structure utilizing a bilayered TiO_2/ PCBM:DMC ETL. Also depicted are the chemical structures of PCBM and DMC. (b) Conductivity of DMC doped PCBM films with varying dopant concentration. (c) Schematic of energy levels determined by UPS for TiO_2, PCBM (before and after doping), and $MAPbI_3$. (d) tDOS distribution for TiO_2, TiO_2/PCBM and TiO_2/PCBM:DMC showing passivation of shallow traps of TiO_2 when PCBM is doped. (e) J-V cures of solar cells utilizing ETLs of TiO_2, TiO_2/PCBM and TiO_2/PCBM:DMC with varying dopant concentrations. Maximum PCEs are obtained for 0.1 wt% DMC. (f) PL spectra of $MAPbI_3$ deposited on top of TiO_2/PCBM and TiO_2/PCBM:DMC bilayers. (From [15] "Reprinted (adapted) with permission from (Ye, Q.-Q.; Wang, Z.-K.; Li, M.; Zhang, C.-C.; Hu, K.-H.; Liao, L.-S. N-Type Doping of Fullerenes for Planar Perovskite Solar Cells. *ACS Energy Lett.* 2018, *3* (4), 875–882). Copyright (YEAR) American Chemical Society.")

There have also been numerous reports in literature that explore doping concentration in organic ETLs in the inverted planar device structure (*p*-*i*-*n*), which was the architecture used in this dissertation to investigate solar cell performance. Several of these studies have focused on PCBM: solution cast with N-DMBI (4-(2,3-Dihydro-1,3-dimethyl-1*H*-benzimidazol-2-yl)-*N*,*N*-dimethylbenzenamine) (1, 3, 5 wt%),[21,49] sequentially cast with N-DMBI (0.4, 0.7 and 1 wt%)[50], and solution cast with decamethylcobaltocene (DMC) (0.05, 0.1, 0.5, 1 wt%).[15] Other studies have focused on several other organic semiconductor/dopant systems: di-perylene diimide (diPDI) doped with DMBI (0.5, 1, 3, 5 wt%)[105], C_{60} doped with (*N*-DPBI) (4-(1,3-dime-thyl-2,3-dihydro-1H-benzimidazol -2-yl)-N,N-diphenylaniline) (0, 0.5, 1, 5, 10 wt%)[106], and *c*- HATNA doped with Et3N (1, 3, 5 wt%).[107] It is a common theme in these studies that fill factor, V_{OC} and J_{SC} all initially increase with doping concentration and then decrease. The increase is attributed to improved electron mobility and conductivity, leading to better carrier transport in the ETL. The decrease is attributed to degraded morphology as a result of aggregate formation due to heavy doping, leading to lower mobility and poor charge transfer at the interface. To date, there has not been a study focusing on the impact of charge transfer on recombination at the interface of a doped ETL/ $MAPbI_3$.

Chapter 2

Selected Techniques Used to Characterize the Impact of Charge Transfer Doping

The electronic and structural effects of charge transfer doping on organic semiconductors and the surface of $MAPbI_3$ was characterized with a wide variety of experimental techniques. In this dissertation, an experimental emphasis is placed on quantifying the number of free carriers created as a result of charge transfer. The techniques used in this pursuit were electron paramagnetic resonance (EPR) and Ultraviolet Photoelectron Spectroscopy (UPS). EPR was used to characterize the number of charge carriers in doped organic semiconductors by quantifying the concentration of organic radicals. UPS was used to characterize the changes in energy levels that occur upon doping, such as the shift of the Fermi level position within the bandgap. Detailed below is a background on the theory and experimental approach to performing EPR and UPS for the material systems of interest in this dissertation.

2.1 Quantitative Measurement of Carrier Concentration in Organic Semiconductors Using EPR

Electron Paramagnetic Resonance (EPR), sometimes also referred to as Electron Spin Resonance (ESR), is a spectroscopy technique that relies on the absorption of electromagnetic radiation in order to characterize spin-carrying particles. EPR is very similar to Nuclear Magnetic Resonance (NMR), but measures the transitions of unpaired electrons rather than nuclear transitions. The foundation of this type of spectroscopy is the Zeeman Effect, which describes the interaction of unpaired electrons with a magnetic field produced by an EPR apparatus.[108] Like protons, electrons have spin giving them a magnetic moment, which causes them to act like compasses when placed in a magnetic field. Electrons have two potential spin states; in the absence of a magnetic field these two spin states are equal in energy. However, when an external magnetic field is supplied, the paramagnetic electrons can either orient in a direction parallel (lower energy) or antiparallel (higher energy) to the direction of the magnetic field (Figure 2.1(a)).[108,109]

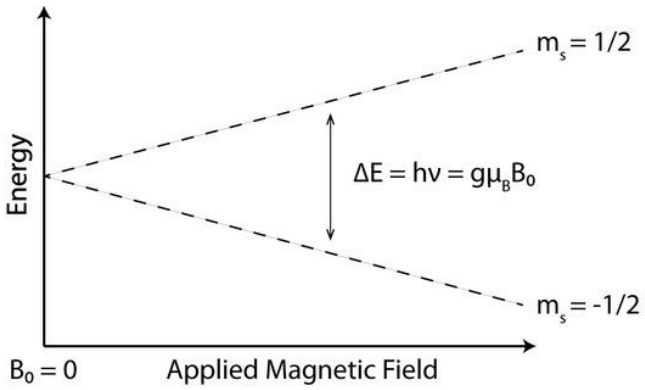

Figure 2.1 (a) Energy levels for an electron spin ($M_S = \pm 1/2$) in an applied magnetic field B. Spins will transition between energy levels as a result of absorption of electromagnetic energy. (From [109])

Initially, there will be more electrons in the lower energy level (i.e., parallel to the field) than in the higher energy level (antiparallel).[108] In a magnetic field, the absorption of energy will cause a transition from the lower energy electron spin state to the higher energy electron spin state (Figure 2.1(b)).[108] According to Plank's Law, energy will be absorbed if $\Delta E = h\nu$, where ΔE is the energy difference upon absorption, h is Plank's constant and ν is the frequency of radiation. In EPR operation, the electromagnetic frequency ν is kept constant, and the magnetic field in scanned for the resulting changes in absorption. The measured absorption will depend linearly on the magnetic field. Peak absorption occurs upon resonance, which is when the magnetic field is tuned such that the energy difference between spin states matches the energy of radiation. The EPR spectrum is typically reported as the first derivative of absorption (Figure 2.1).[108,110]

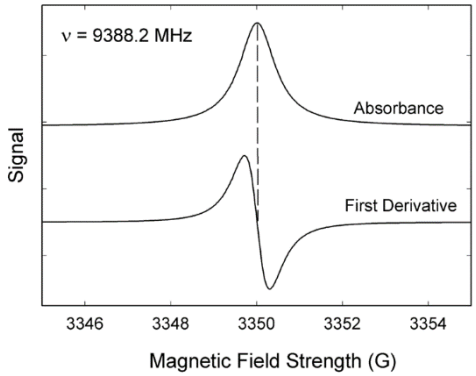

Figure 2.2 EPR spectrum is typically reported as the first derivative of absorption. (From [110])

There is a wide range of materials that have unpaired electrons, including free radicals, organic radicals, numerous transition metal ions, and defects in materials. EPR spectral features that occur as a result of these potential sources can be distinguished using the g-factor, which provides information about the local spin environment. The g-factor is used as scaling

factor to account for the coupling of orbital and spin angular momentum.[108] Under resonance conditions, the g-factor can be solved for using the following equation:

$$h\nu = g\,\mu_B\,B_0 \qquad 2.1$$

where $h\nu$ is the quantum of electromagnetic wave energy, μ_B is the Bohr magneton, and B_0 is the magnetic induction of the external magnetic field. Experimentally, this value is extracted by recording the frequency for resonance and the magnetic field for which there is peak absorbance (or where the first derivative for absorbance crosses Intensity = 0).[108] The g-factor of a free radical is 2.0023 ± .003. For an organic radical (such as a polaron in a doped organic semiconductor), the g-factor is very close to this value and typically falls within the range of 1.99 to 2.01. However for transition metal ions, the g-factor can vary wildly between 1.4 to 3.0 as a result of the spin-orbit coupling and zero-field splitting.[111] For the case of Pb, paramagnetic ions are Pb^{+} and Pb^{3+} which have g factors of ~2 and 1 to 1.7 respectively. Pb^{2+} is diamagnetic and is therefore EPR silent.[112]

The integrated intensity of absorption curve of the EPR signal provides information about the concentration of EPR active species in a sample.[108] The integrated intensity may also be affected by the microwave power. In the correct range of microwave power, the signal intensity will grow at the square root of the power. However, saturation will occur if too much power is used, resulting in the EPR signal diminishing and broadening.[108] In order to avoid saturation, a power sweep should be performed in order to determine the correct range (linear regime); here we measured power attenuations of 18, 24, 30, 36, 42 and 48 dB.

In order to obtain a quantitative measurement of concentration, the integrated intensity of a sample may be compared to that of a reference sample with a known number of spins.[108,113] The reference sample used here was a mixture of DPPH (α-α- diphenyl-fl-picryl

hydrazyl) [EPR active material with a g factor of 2.0036] and KBr (Potassium Bromide) [filler material]. The filler material was used such that the reference mimics the geometry of thin film samples in order to have a similar quality factor of the cavity. Varying ratios of the concentration of DPPH: KBr were made in order to determine which results in the widest range of potential attenuation values in the linear regime. Typically, a total mass of ~0.15 mg of DPPH diluted to fit the necessary volume produced good results. When calculating carrier concentration based on a reference, the EPR spectrum should be collected using the same microwave power.

A well-defined sample volume is necessary to obtain an accurate value of carriers/cm^3. Here, thin films were spun onto microscope cover quartz substrates and subsequently broken using a diamond scribe into rectangles with approximate dimensions of 2.5 × 15 mm. The primary source of error in a quantitative EPR measurement is likely measurement of the sample volume. The dimensions (width × length) of the rectangular films can be determined using a micrometer or a photograph of the sample next to a scale bar and extracting the area using ImageJ. In order to determine the sample height, the thickness of a sample may be taken by scratching the film and measuring the height profile in several locations using either a profilometer (Dektak) or an AFM depending on film mechanical strength.

2.2 Measurement of Energy Levels Using Ultraviolet Photoelectron Spectroscopy

Ultraviolet photoelectron spectroscopy (UPS) is a surface sensitive technique that allows for characterization of the electronic structure of interfaces. Photoelectron spectroscopy is

based on Einstein's photoelectric effect. A photon will remove an electron from a material if the photon's energy is greater than that of the electron's binding energy. Any excess energy will be carried away by the photoelectron in the form of kinetic energy, which can be measured using a spectrometer.[114] This can be described using equation

$$IE = h\nu + KE \qquad 2.2$$

Where I.E. is the ionization energy, hν is the energy of the photon, and KE is the kinetic energy of the photoelectron. Photoemission is described using a three step process: 1) incoming photons are absorbed by electrons; 2) the electrons ejected by photons travel to the sample surface, during which process the majority of the generated electrons suffer inelastic collisions, and lose some of their kinetic energy; 3) the electrons are ejected into the vacuum, and their kinetic energies are measured by the detector.[115] The photoemission spectra consist of two principal components: primary electrons, referring to electrons which do not suffer inelastic collisions; and secondary electrons, which represent those electrons that lose varying amounts of energy by interacting with other electrons on their way through the solid.[116] In the photoemission spectra, primary electrons result in distinct spectral features and peaks which mirror the density of states (DOS) of the sample near the valence band edge. Whereas,

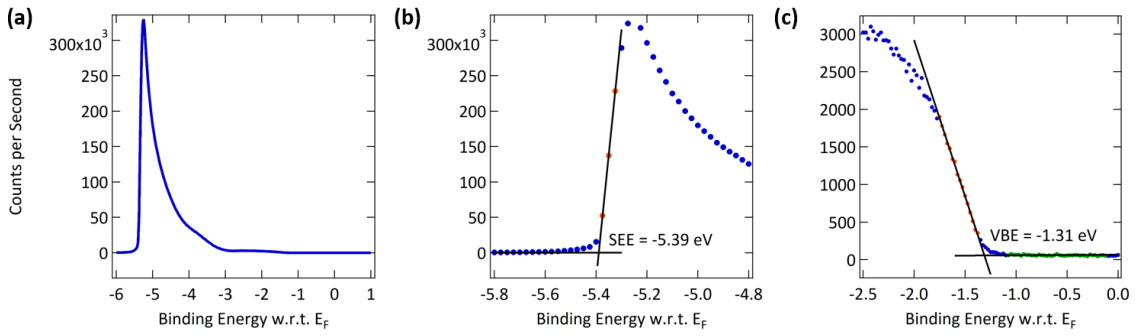

Figure 2.3 Example UPS spectra taken using an H Lyman-α source (10.2 eV). (a) Full UPS spectra that mirrors the DOS of the material, (b) assignment of the SEE, and (c) assignment of the VBE.

secondary electrons give a continuous background that is superimposed with the distinct features given by the primary electrons. The onset of the signal stemming from the secondary electrons is used to calculate the work function of the material. Figure 2.3 provides an example UPS spectra showing (a) a full UPS spectra, (b) assignment of the secondary electron edge (SEE) and (c) assignment of the valence band edge (VBE). Using extracted values of the SEE and VBE, the energy levels (ionization potential (IP), work function (WF), electron affinity (EA)) can be extracted using the following equations. Here, hν is the energy of the photon source.

$$IP = h\nu - |E_{SEE} - E_{VBE}| \quad (2.3)$$

$$WF = h\nu - E_{SEE} \quad (2.4)$$

$$EA = WF - (\text{Band Gap} - |E_{VBE}|) \quad (2.5)$$

The energy of the incident photons determines what type of orbitals are probed. UPS utilizes photons with low energy (21.2 eV from ionization source He(I) or 10.2 eV from an ionization source of H Lyman-α),[117,118] such that only valence electrons are ionized. Whereas in X-ray photoelectron spectroscopy (XPS), photons have sufficient energy (higher than 1000 eV) to excite core level electrons whose orbital energies can be used to determine atomic composition.[119] Both techniques may be necessary to develop an understanding of surface energetics. UPS provides information about ionization energy (I.E.), work function (WF) and Fermi Level (E_F).[10] However, UPS cannot be used to determine the band gap, and thus the conduction/LUMO level of a material (electron affinity (EA)). The electron affinity is determined using Inverse Photoelectron Spectroscopy (IPES). When this technique is not available, the band gap can be approximated using the optical gap from UV-Visible Spectroscopy (UV-Vis).[120] Figure 2.4(a) shows a flat band energy level diagram of these

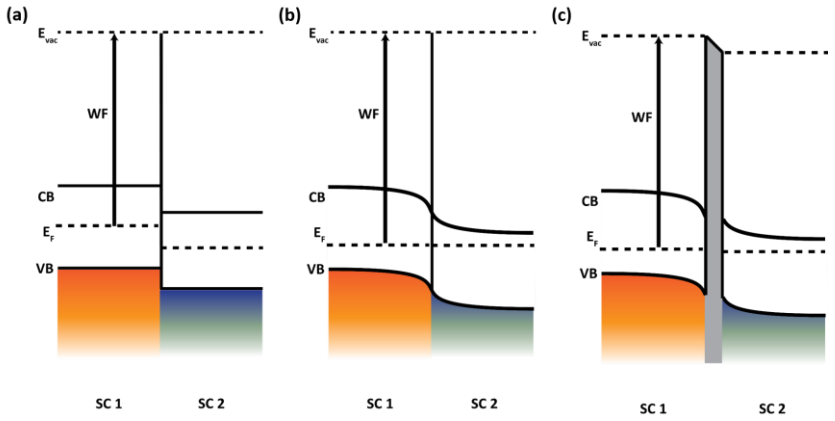

Figure 2.4 Schematic of energy level diagram when two semiconductors are placed in contact for (a) flat band condition, (b) presence of interfacial band bending and (c) presence of interface dipole. Band edges (E_{CB} and E_{VB}), vacuum level E_{VAC}, and work function WF are defined.

parameters.[121] Depending on the system studied, it may be necessary to develop a more complex model that includes band bending and/or interface dipoles.[122] Figure 2.4 (b)&(c) gives an example of what an energy diagram look likes when these components are present.[120,122] Changes in the work function upon doping may include both the effects of band bending and interface dipoles. In order to identify the band bending component, binding energy shifts upon doping of certain atomic orbitals may be seen in XPS spectra. When studying a two separate materials in contact, the band bending that occurs at the interface can be studied by obtaining a UPS spectra for varying the thickness of the upper layer. Typically band bending occurs over a range of ~0-30 nm. Figure 2.5 shows an example of this variety of experiment.[123]

The position of the Fermi level can be used to obtain an estimate of carrier concentration in inorganic materials. Initially, it is necessary to determine a value for the quantum concentration of conduction electrons n_c which requires a value for effective electron mass m*.

$$n_c \equiv N_c/V = 2(m_e^* k_b T/2\pi\hbar^2)^{3/2} \qquad 2.6$$

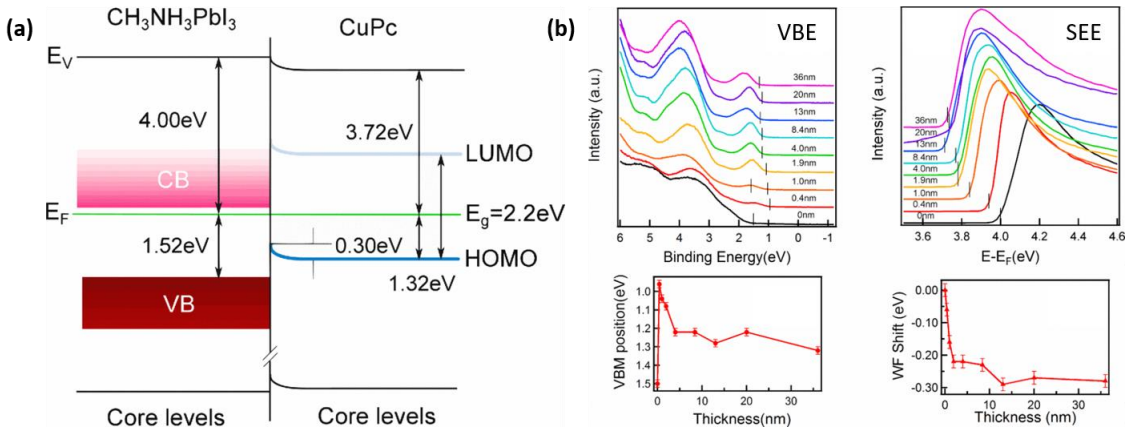

Figure 2.5 Example study of measurement of band bending at the interface of two semiconductor materials (a) Energy level diagram of Perovskite/CuPc interface. (b) Valence band and work function shifts from UPS measurements determined from the valence band edge and secondary electron edge. (From [123])

Where k_b is the Boltzman constant, T is the temperature, and ħ is Plank's constant divided by 2π. Using this term for the quantum concentration of conduction electrons, the conduction electron concentration for *n*-type doping is given by the following equation:

$$n_e = n_c \times \mathrm{Exp}\left[\frac{-(\varepsilon_c - \mu)}{k_b T}\right] \qquad 2.7$$

The difference in energy levels between the conduction band ε_c and the Fermi level μ is determined experimentally by the positions of the Electron Affinity (EA) from IPES and the Valence Band Edge (VBE) from UPS. Since these values are used within an exponential term, small degrees of error can lead to significant variation in conduction electron concentrations. These errors could arise for a variety of sources: (1) an inaccurate value of the band gap as a result of estimating from the optical gap, (2) the resolution of UPS apparatus of ± 0.15 eV, and (3) charge transfer from the underlying substrate, which may seem dramatic if a material has an intrinsically low carrier concentration.

In disordered systems such as organic semiconductors and perovskites, sample degradation is a major consideration when performing photoelectron spectroscopy. The high

incidence of photons can mediate photo-chemical reactions, which can cause bond breakage or cross-linking.[124–129] While degradation is more prevalent for XPS due to the higher energy of its photon source (Kα: 1486 eV), significant degradation can also occur during UPS.[124,125] In addition, the spot size for photoelectron spectroscopy is relatively large >100 μm, so successive UPS and XPS measurement can eventually lead to issues even while changing locations on the sample. In UPS, radiation damage leads to shifts in binding energy or change the DOS shape near the valence band,[124,125] making accurate extraction of energy levels difficult. Typically the effects of sample degradation are mitigated by limiting the dwell time to short periods, however this limits the resolution of the scan and is not suitable for experiments that measure the same film location while a second layer is deposited (i.e. measurement of band bending at an interface). An alternative route to limiting sample degradation can be to use a UPS apparatus with a source that has lower energy photons and lower photon fluxes.[117] Energy level characterization of $MAPbI_3$ in this dissertation was carried out on UPS apparatuses with either a photon source of He (I) (21.22 eV) (Chapter 4) and H Lyman-α (10.2 eV) (Chapter 5). The later UPS setup was designed specifically by Kenneth Graham's Group at University of Kentucky to limit degradation of disordered semiconductors.[117]

There is a wide spread of IEs reported in literature for $MAPbI_3$, ranging from 5.1 to 6.65 eV.[130] Likely part of this uncertainty is the variation in which different studies assign the valence band edge, which can be done either on a linear or semi-logarithmic scale. The latter is done in order to account for the low DOS near the valence band edge.[131] Furthermore, measurement of the onset of the DOS near the valence band edge will depend on the signal to noise ratio and the noise floor of the experimental setup. There is potential for the H Lyman-

α source UPS apparatus to enable better accuracy of assignment of the valence band edge as a result of higher resolution scans from longer dwell times. In this dissertation, characterization of $MAPbI_3$ using two different UPS apparatuses with both He(I) and H Lyman-α sources allows for comparison of extracted energy levels from different experimental setups. Figure 2.6 depicts fitting of the VBE of $MAPbI_3$ on both the linear and semi-logarithmic scales for the two experimental setups. There is extremely close agreement of the VBE for all fits except for the semi-logarithmic fit of the He(I) source, which varies by

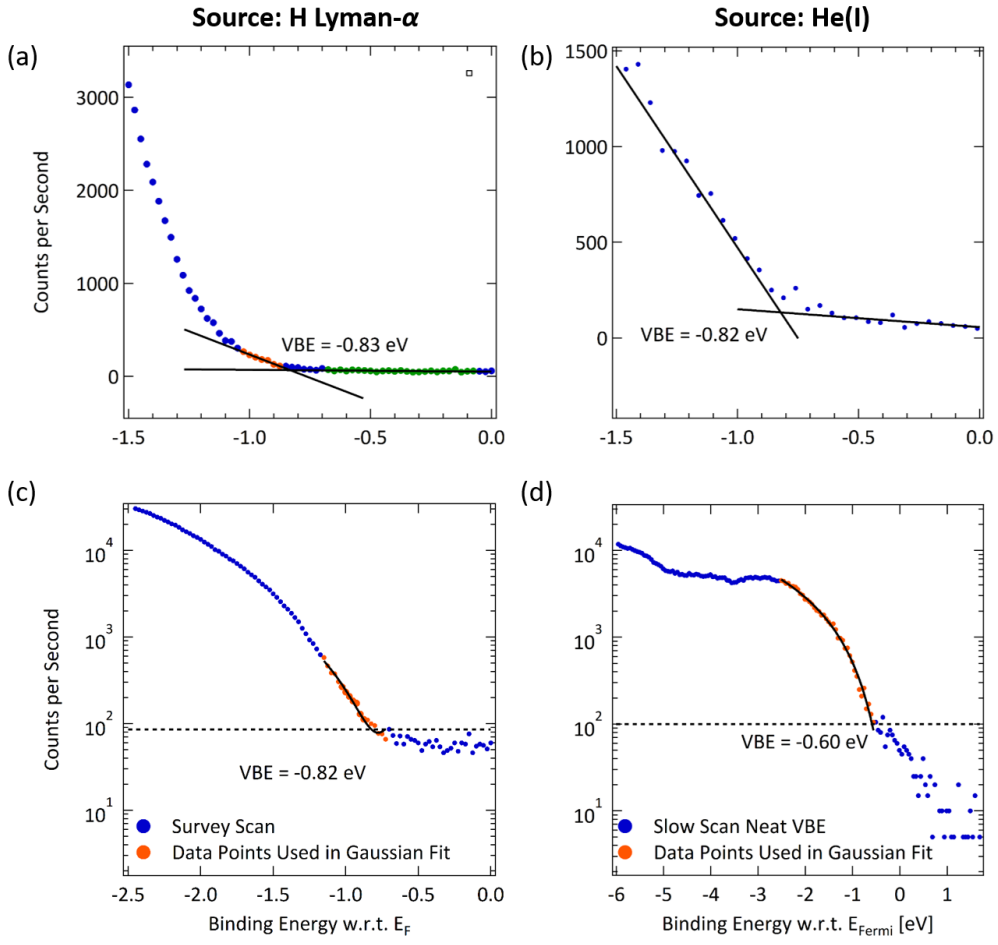

Figure 2.6 Comparison of fits for the VBE of $MAPbI_3$ measured using UPS setups with (left) an H Lyman-α source and (right) a He(I) source. Fits depicted in (a) & (b) were performed on a linear scale. Fits depicted in (c) & d were performed on a semi-logarithmic scale.

~0.2 eV (which would probably still be considered good agreement). Another feature of comparison is the number of intensity counts of the noise floors on the semi-logarithmic scale. The noise floor was used to fit the VBE by finding the intersection of the Gaussian fit of the falling valence edge. The noise floor for the He (I) is higher than the H Lyman-α (~100 counts as opposed to ~85 counts), which could potentially lead to less accurate fitting of the VBE.

Chapter 3

N-doping of a Non-Planar Ambipolar Semiconducting Polymer Illustrating Improved Polymer: Dopant Miscibility

Reprinted with Permission of [132]:

Perry, E. E.; Chiu, C.-Y.; Moudgil, K.; Schlitz, R. A.; Takacs, C. J.; O'Hara, K. A.; Labram, J. G.; Glaudell, A. M.; Sherman, J. B.; Barlow, S.; et al. High Conductivity in a Nonplanar N-Doped Ambipolar Semiconducting Polymer. *Chem. Mater.* 2017.

The major obstacle to use of organic semiconductors in PSCs is their low carrier mobility and carrier concentration, which hinder their ability to effectively transport photo generated carriers to electrodes and may cause them to act as resistors in the device series.[5] In order to overcome transport issues, doping of organic transport layers is performed to passivate trap sites and increase the concentration of free carriers.[133] Consequently, an important consideration for the choice of organic semiconductor is its ability to be doped with high efficiency with limited structural disruption. Previously, it was shown that highly crystalline polymers with planar backbones such as P(NDIOD-2T) have polymer: dopant miscibility

issues that lead to low doping efficiencies and dopant aggregate formation.[101] One of the factors impacting the performance of organic ETLs is its morphology, which requires good contact with the $MAPbI_3$ surface in order for effective extraction of photo generated charge.[49,50] In previous studies of ETL dopant concentration, it was been proposed that dopant aggregate formation leads to diminished solar cell performance as a result of disrupted morphology/interfacial contact.[49,50] A detailed understanding of the relationship between polymer structure and the electrical and structural impacts of doping is important for developing design strategies for high efficiency PSC electron transport layers. Here, the effects of *n*-doping are investigated on a non-planar polymer P(BTP-DPP). The twist in the backbone of P(BTP-DPP) and its glassy ordering creates steric space for dopants to pack, resulting in near 100% doping efficiency of $(RuCp^*mes)_2$ and approximately one charge carrier per polymer repeat unit. This study suggests that exploration of backbone architectures that can improve dopant miscibility could be of interest in developing high performance organic ETLs.

This heavily doped system also provided a means to investigate the nature of *n*-type charge carriers. At low doping concentration, charge carriers take the form of polarons, which are radical-ion pairs. High distortion energies caused by accommodating a significant degree of additional charge can lead to recombination of polarons into bipolarons which are ion-ion pairs. To date there has been limited observation of bipolarons in *n*-type systems. This chapter evaluates spectroscopic signatures that could indicate the presence of bipolarons, which were challenging to identify due to the narrow band gap of the ambipolar polymer used in this study. A model for charge percolation in this system is developed based on the assumption of the coexistence of polaronic and bipolaronic charge carriers.

3.1 Introduction

Organic semiconductors are candidates for use in next-generation light-emitting devices,[134,135] thin-film transistors (TFTs),[136] photovoltaics,[137,138] and thermoelectrics.[101,104,139–142] Many of these devices benefit from electrical doping that can improve the effective carrier mobilities by filling trap states,[143] can enhance electrical conductivity by increasing the density of free charge carriers,[97] and/or can lower barriers to charge-carrier injection or collection at electrodes.[72,97] While high electrical conductivity in *p*-doped materials has been demonstrated, *n*-doped materials have lagged behind. A key challenge for *n*-doping is the development of stable compounds that can reduce organic semiconductors with low electron affinities.[71]

Here we report physical and electrical characterization of *n*-doping of a low-band gap polymer based on a non-planar (*E*)-8,8'-biindeno[2,1-*b*]thiophenylidene unit, P(BTP-DPP) doped with a relatively air stable, yet highly reducing organometallic dopant: ruthenium pentamethylcyclopentadienyl mesitylene dimer, $(RuCp^*mes)_2$. We find that processing conditions are an essential factor for achieving high electrical conductivity. Significantly, sequential processing of the polymer and dopant leads to formation of heavily doped films that may be useful for *n*-type transparent conductive films.

Semiconducting polymers have been reported with high hole and electron mobilities in TFTs, but the electrical conductivities of chemically doped materials differ substantially. Solution-processable ambipolar transistors using donor-acceptor polymers as the active layer have been reported to have electron and hole mobilities in the range of 1 to 10 $cm^2 V^{-1} s^{-1}$.[144–146] When compared to the similar values achievable for electron and hole mobilities, there

are no clear examples of comparable electrical conductivity obtained for the same polymer doped to be *p*-type or *n*-type. The highest reported conductivities for stable *p*-doped polymers are ~1000 S cm^{-1} for materials such as PEDOT:PSS[77] and solution-processed poly(alkyl-thiophene) derivatives.[74–76] In contrast, the highest conductivities for *n*-type polymers[78–80] reach ~1 to 10 S cm^{-1} with only unstable alkali-metal-doped polyacetylene reaching 1500 S/cm.[81] A potential origin for the difference in conductivity values achieved to date is the relatively smaller library of *n*-type dopants compared to *p*-type dopants.

In an attempt to achieve high *n*-type conductivities in organic semiconductors, several promising classes of extrinsic dopants have recently been developed.[72] While dopants with low ionization potentials (IEs) are able to reduce a wide range of organic semiconductors, they are frequently unstable in ambient conditions.[28] To overcome this issue dopants have been developed that use bond cleavage instead of simple electron-transfer reactions; dihydro-1*H*-benzoimidazol-2-yl derivatives such as N-DMBI[147],[148], tetrabutylammonium salts,[149] and highly reducing dimeric organometallic complexes[98] have been used, although some of these dopants lead to formation of side products. While this class of dopants can be stable in ambient conditions in the unreacted form and also in the cationic form after electron transfer, the reduced semiconductor can still suffer from environmental degradation depending on its electron affinity. A relatively high conductivity of 8×10^{-3} S/cm was achieved by doping poly[*N*,*N'*-bis(2-octyl-dodecyl)-1,4,5,8-napthalenedicarboximide-2,6-diyl]-alt-5,5'-(2,2'-bithiophene)] (P(NDI2OD-T2) with DMBI-derivatives.[101] Neutral benzimidazoline-radical dimers $DMBI_2$ (which act in a similar way to dimeric organometallic dopants) have shown conductivities of 3×10^{-3} S/cm with (P(NDI2OD-T2), and 2×10^{-2} S cm^{-1} with PCBM.[100] High *n*-type conductivities of 0.5 S cm^{-1} have also been shown in small-molecule systems

using a self-doping mechanism of tethering amine substituents to perylene diimide (PDI) using alkyl spacers.[104,140] Recently, conductivities as high as 2.4 S cm^{-1} have been shown for the ladder-type polymer polybenzimidazobenzophenanthroline (BBL) vapor doped with tetrakis(dimethylamino) ethylene (TDAE).[79]

The above mentioned organometallic dimers combine air stability and highly reducing character by coupling electron transfer to a bond-breaking reaction.[147] These organometallic dimers, in which each metal has an 18-electron configuration, act as "masked" forms of the corresponding highly reducing 19-electron sandwich compounds. In the case of $(RuCp^*mes)_2$, shown in Figure 3.1, the dimer transfers an electron to an acceptor (a step which may be endergonic) yielding an intermediate radical cation dimer, which quickly cleaves to a stable 18-electron cation and a highly reducing 19-electron species, which itself is quickly oxidized by a second equivalent of an acceptor, as illustrated in Figure 3.1(c).[98] This approach has the advantage in that the dimers can potentially undergo a clean reaction with the electron acceptor to form stable monomer cations and host anions without the formation of other side products.[147]

Modest conductivities have been observed in polymer and small-molecule systems doped with dimeric compounds. When doped with 4 wt% $(RuCp^*mes)_2$, P(NDI2OD-T2) was found to reach conductivities of 4×10^{-3} S/cm, the highest known for this class of dopants.[150] This study was performed using processing via spin casting from a co-solution of dopant:polymer in toluene. Additional conductivity studies of this dopant class include doping P(NDI2OD-T2) with 2 wt% rhodocene dimer $[RhCp_2]_2$, which achieved 5.1×10^{-4} S cm^{-1} and with 7.8×10^{-3} molar ratio $[RhCp^*Cp]_2$, which achieved 1.6×10^{-4} S cm^{-1}.[99,151] These studies were also performed using processing via spin casting from a co-solution of dopant:polymer in

chlorobenzene and toluene respectively. A comparable study of vapor-deposited films of copper phthalocyanine doped with 5 wt% $[RhCp_2]_2$ showed conductivities on the range of ~10^{-6} S cm^{-1}.[147]

Here we investigate the interplay of semiconducting polymer structure and processing conditions, such as casting techniques, on electrical conductivity and the efficiency of carrier formation. We examined extrinsic doping of an ambipolar copolymer poly((*E*)-3-(5-([8,8'-biindeno[2,1-*b*] thiophenylidene]-2-yl)thiophen-2-yl)-2,5-bis(2-octyldodecyl)-6(thiophen-2-yl)pyrrolo[3,4-c]pyrrole-1,4(2*H*,5*H*)-dione) (P(BTP-DPP)) (Figure 3.1(a)).[152–154] P(BTP-DPP) has a relatively narrow optical gap of ≈1.2 eV and is designed to possess twisted repeat units, while still allowing for conjugation along the polymer backbone. The non-planar backbone structure provides a contrast to more widely studied polymers with planar units in the backbone that lead to linearity along the chain direction, such as P(NDI2OD-T2). We studied the impact of processing conditions on the resulting electronic structure of the doped polymer using a combination of methods including photoemission, spin resonance and optical

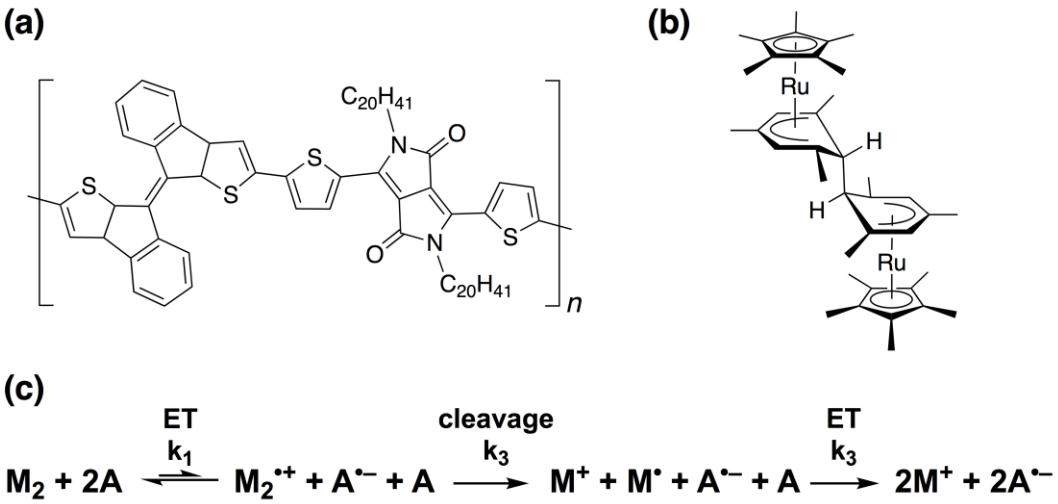

Figure 3.1 Chemical structures of (a) the semiconducting polymer P(BTP-DPP); (b) the organometallic *n*-dopant $(RuCp^*mes)_2$; (c) the reaction mechanism for doping acceptor A (P(BTP-DPP)) with an organometallic dimer M_2 ($(RuCp^*mes)_2$).

spectroscopy and find efficient formation of carriers with $(RuCp^*mes)_2$ as the dopant. The origin of the increase of electrical conductivity (0.45 S cm^{-1}) obtained using a sequential processing method was probed using structural methods such as grazing incidence X-ray scattering and atomic force microscopy. Our results suggest that sequential processing allows for formation of efficient percolation pathways for charge transport relative to casting from a blend of polymer and dopant.

3.2 Experimental Methods

P(BTP-DPP) was synthesized as described in the Supporting Information and in a similar way to previously reported.[152] $(RuCp^*mes)_2$ was synthesized following previously reported procedures.[155,156] P(BTP-DPP) was dissolved in a 50:50 volume percent co-solvent of chlorobenzene and 1,2-dichlorobenzene at 10 mg/mL and heated at 80 °C and stirred for 1 h prior to being filtered with a 1 μm pore sized polytetrafluoroethylene (PTFE) filter. $(RuCp^*mes)_2$ was dissolved in toluene at various concentrations (0.05, 0.1, 0.25, 0.5, 1, 2 and 4 mg/mL) and heated to 80 °C for 1 h without being filtered. Films were spin cast from the solutions described above onto substrates described in the Supporting Information in an N_2 glovebox (<2 ppm O_2). Films were created using sequential casting, with the polymer film deposited first followed by the dopant. Both solutions were deposited with the following spin conditions: 200 rpm for 6 s, 2000 rpm for 60 s, 3000 rpm for 3 s. Following dopant deposition, films were annealed at 80 °C for 10 min. More details of characterization methods can be found in the Supporting Information.

3.3 Results and Discussion

3.3.1 Sequential Casting as a Route to Achieve High Conductivity

The electrical conductivity of semiconducting polymers depends upon the morphology, which is affected by the processing method.[157,158] Two solution-based processes and their effects on electrical properties were examined - blend casting - in which the polymer and dopant are blended together in solution prior to deposition of the film, and sequential casting - in which the polymer and dopant are deposited separately in sequential steps, where the dopant layer is deposited in a semi-orthogonal solvent on top of the polymer layer. Sequential casting is similar to immersion casting in which the polymer film is soaked in a dopant bath.[159],[75] Both methods rely on the solvent of the dopant solution to swell the underlying polymer in order to promote interdiffusion of the dopant.[157] Post-deposition annealing drives the dopant further into the polymer film if required. Sequential deposition has proven successful in forming films of P3HT doped by F_4TCNQ with good uniformity,[157,158] and in forming bulk heterojunctions by interdiffusion of a fullerene acceptor into a polymer.[160] Studies have shown that doped systems processed with sequential casting exhibit higher conductivity and better uniformity than blend cast systems in cases where the dopant and polymer can aggregate in solution.[158] Another significant difference between these casting techniques is that in some systems, sequential casting results in dopant counterions being excluded from crystalline domains, mitigating their negative impact on mobility.[158] In contrast, P(BTP-DPP) is a relatively disordered polymer due its backbone structure and could more readily accommodate counterions. It is still possible, even in this case, that electron transfer in solution could lead to the formation of aggregates that can modify the resulting morphology relative to films cast from the neat polymer.

We examined how sequential casting affected the morphology of doped films of P(BTP-DPP) using atomic force microscopy (AFM) (Figure 3.2). This method of processing appears to create doped films with features that we attribute to the presence of both $(RuCp^*mes)^+$ and $(RuCp^*mes_2)$ dimer aggregates (based on XPS and GIWAXS data, see below) on the film surface. These aggregates become more numerous at higher doping concentrations. The total thickness of the initial films was ≈40 nm. Despite the presence of surface aggregates attributed to the dopant, the films are still relatively smooth after sequential casting (see Supporting Information Figure S3.1 for roughness profiles).

Sequential casting provides the ability to form heavily doped films in P(BTP-DPP), but the concentration of dopant must be determined after infiltration. We determined the level of $(RuCp^*mes)_2$ incorporation upon sequential casting using X-ray photoemission spectroscopy

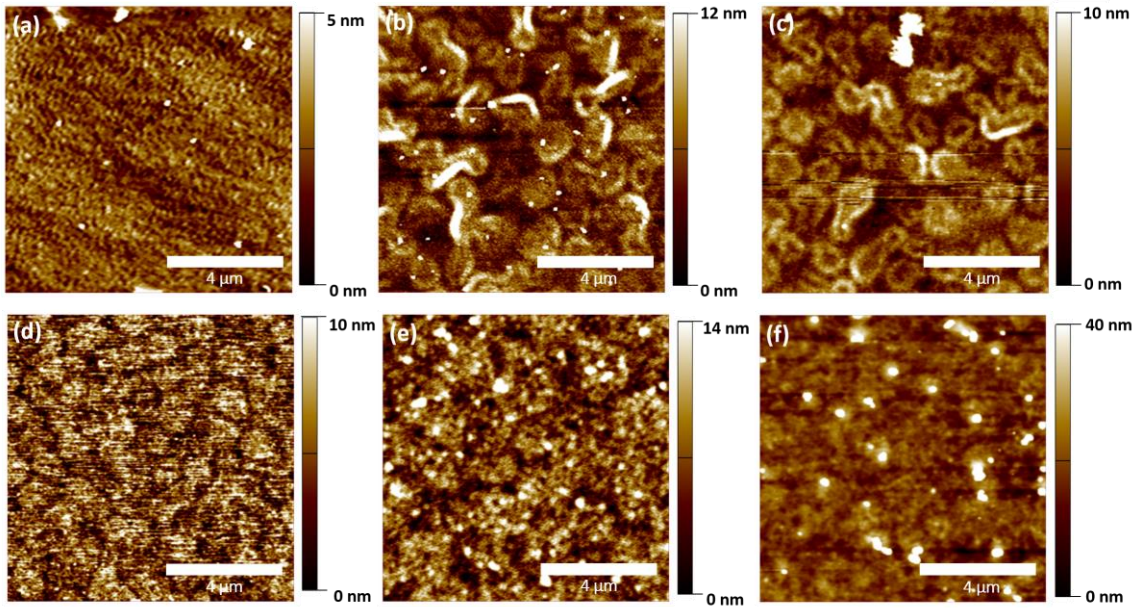

Figure 3.2 Atomic force microscopy topographic images of (a) neat P(BTP-DPP) also processed with toluene and doped P(BTP-DPP) at (b) 0.15 monomeric dopants per repeat unit, (c) 0.37 monomeric dopants per repeat unit, (d) 0.55 monomeric dopants per repeat unit, (e) 0.77 monomeric dopants per repeat unit and (f) 0.92 monomeric dopants per repeat unit.

(XPS). XPS is a surface sensitive technique and probes approximately the first 8 nm of the sample, therefore an assumption in our analysis is that the surface composition reflects the entire film. RuCp*mes aggregates observed by AFM suggest that there will be some difference in the composition measured by XPS and the total film thickness, but the films are still relatively thin (≈40 nm) so we do not expect these differences to be large. We present our data as function of the repeat unit per monomeric dopant so that the concentration of dopant in this system can be more easily compared to other systems where films are cast from a blend of polymer and dopant. The repeat unit per monomeric dopant is reported with respect to RuCp*mes cations instead of $(RuCp^*mes)_2$ dimer (since each dimer contributes two electrons on undergoing the doping reaction). The symmetrical appearance and the binding energy the ruthenium $3d_{5/2}$ peaks in XPS spectra shows that essentially all dopant has reacted at the measured concentrations (Supporting Information Figure S3.2). This observation suggests that unreacted dimer aggregates account for a relatively small fraction of the Ru present. We also assume that ionization of the dopant is solely due to the polymer and that each ionized RuCp*mes cation corresponds to one carrier in the polymer chain. Concentrations of 0.05, 0.1, 0.5 and 1 mg/mL of $(RuCp^*mes)_2$ in the casting solution resulted in repeat unit to monomeric dopant ratios of 1: 6.8, 1: 2.7, 1: 1.3 and 1: 1.1 respectively, i.e. resulting in contributions of up to 0.15, 0.37, 0.77 and 0.92 electrons per monomer unit. This would correspond to weight percentages of 4, 10, 19, and 21 wt% RuCp*mes in doped films. Using these data, we found a logarithmic relationship between composition and concentration that was used to estimate the composition for samples not measured by XPS (Supporting Information Table S3.2 and Figure S3.3).

We observed that sequential casting of P(BTP-DPP) doped with $(RuCp^*mes)_2$ results in measured conductivities nearly an order of magnitude higher (Supporting Information) than films fabricated using blend casting. The electrical conductivity of thin films was measured over a range of compositions (Figure 3.3), with values that reached a plateau at ca. 10^{-1} S cm^{-1} for films sequentially doped with between 0.37 and 0.77 monomeric dopants per repeat unit. A maximum conductivity value of 0.45 S cm^{-1} was achieved at 0.55 monomeric dopants per repeat unit. At this composition, on average there is 1.8 repeat units per monomeric dopant. In contrast, the conductivity for films cast from solutions of blends of the dimer and P(BTP-DPP) only reached ≈0.01 S cm^{-1} at 0.55 monomeric dopants per repeat unit.

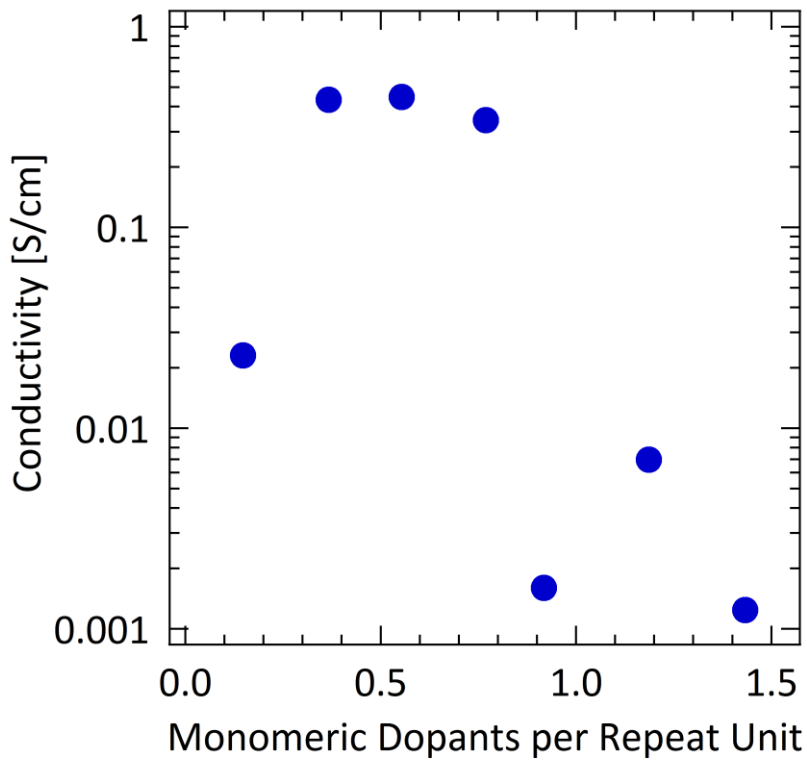

Figure 3.3 Conductivity of sequentially cast films as a function of monomeric dopants per repeat unit present on film surface. See Supporting Information for standard deviations of conductivity values reported.

3.3.2 Nature of Charge Carriers

To understand the nature of the observed electrical conductivity (σ) both the charge carrier density (n) and mobility (μ) should be considered ($\sigma = n\,q\,\mu$ where q is the elementary unit of charge). We do not have a simple independent measure of the carrier concentration and mobility, but the mobility derived from field-effect measurements can be used to estimate n. The electron and hole mobilities of undoped P(BTP-DPP) were found to be $\approx 1 \times 10^{-3}$ and $\approx 3 \times 10^{-3}$ $cm^2\ V^{-1}\ s^{-1}$ respectively (Supporting Information Figure S3.4). The mobility from TFTs provides a value that this representative of the polymer-dielectric interface and is measured at a lower carrier density than the doped samples, but should provide a lower bound for the mobility. If we assume a similar bulk electron mobility, the carrier concentration of the highest conductivity sample would be $1.4 \times 10^{21}/cm^3$. This value is within a factor of three of the number density of monomers of P(BTP-DPP) of 5×10^{20} monomers/cm^3 (Supporting Information) and is consistent with the value of 0.55 monomeric dopants per repeat unit obtained from XPS. The carrier mobility likely depends on dopant concentration; the increased carrier concentration can increase the mobility through trap filling, while the dopant counterions can decrease mobility through disrupting polymer-polymer interactions,[72] but the our data suggests that the mobility from the field-effect measurements are in reasonable agreement with an estimate from the bulk conductivity.

To gain further insight into the observed electrical conductivity, the spin concentration of the system was determined using electron paramagnetic resonance (EPR). Due to strong electron-phonon coupling, charge carriers in organic semiconductors can take the form of either polarons or bipolarons.[161] Polarons are typically the dominant carrier in organic polymeric materials at low carrier concentration and exist as radical-ions, and are thus EPR-

active. As the doping level increases, polarons can potentially combine into bipolarons in order to reduce the distortion energy of the backbone, until bipolarons become the dominant species at high doping levels.[162] Bipolarons exist as either closed-shell dications or dianions, and thus lack paramagnetic spin centers. There is significant discussion currently about the formation of bipolarons in semiconducting polymers and whether a lack of spin centers can be alternately interpreted as spin-interactions between separated polarons.[163] Here, we discuss our data using the long-standing model and point out where the role of electron-electron interactions may impact the interpretation.

As described above, the spin concentrations in heavily doped samples suggest the presence of bipolarons, or at least spin-paired, carriers. While samples with doping levels within the apparent plateau of the conductivity (0.37 to 0.77 monomeric dopants per repeat unit) showed a detectable EPR signal of ~10^{19} spins/cm^3, the signals for samples at other compositions (0.15 and 0.92 monomeric dopants per repeat unit) were below detectable limits (Supporting Information Figure S3.5-3.6). Given that the EPR-silent samples show modest conductivities, this cannot be readily explained by carrier concentrations below the ca. 10^{14} spins/cm^3 threshold of the EPR apparatus. The observable spin concentrations are also low in comparison to other systems displaying similarly high conductivity where carrier densities are often roughly one spin per monomer or 10^{20} to 10^{21} spins/cm^3.[104] An estimation of the carrier concentration based on the weight percentage of dopant incorporated into the film suggests that there should be ~10^{20} carriers/cm^3 which is one order of magnitude higher than the EPR-measured spin concentration. It should be noted that the doping efficiency of $(RuCp^*mes)_2$ is assumed to be close to 100% given the symmetry and binding energy of

ruthenium $3d_{5/2}$ peaks in XPS spectra. Overall these observations suggest the presence of bipolarons or spin-paired species in the doped films.

Optical spectroscopy provided information about the formation of sub-gap states in the doped samples. The changes in optical spectra as the dominant charge carrier transitions from polarons to bipolarons is traditionally understood in terms of a model developed for *p*-type materials such as polythiophene.[164] In this model, doping creates localized charge defects that lead to the formation of sub gap states. In *n*-type systems, the existence of polarons is evidenced by localized electronic levels in the band gap: a doubly occupied state above the valence band edge and a singly occupied antibonding polaron state below the conduction band edge. Upon further doping, the additional electron fills the upper gap state and may cause additional energetic shifts due to the geometric distortion. As mentioned above, electron-electron interactions could further modify the energetics of the states and the resulting optical transitions.[165,166] In either case sub-optical gap transitions from the neutral form are expected.

The positions of sub-gap states were compared to the described model in an attempt to confirm the presence of bipolarons. The optical absorption spectrum (Figure 3.4) show a bleaching of the main transition of the neutral polymer (peak at 1.4 eV) and the growth of an absorption band below the optical transition of the neutral polymer at 0.8 eV (1490 nm) for the sample with 0.37 monomeric dopants per repeat unit and at 0.9 eV (1340 nm) for the sample with 0.77 monomeric dopants per repeat unit. It is notable that aside from the neutral peak at 1.4 eV, which is bleached upon doping at all concentrations, the absorption spectrum in the near-IR region is relatively flat.

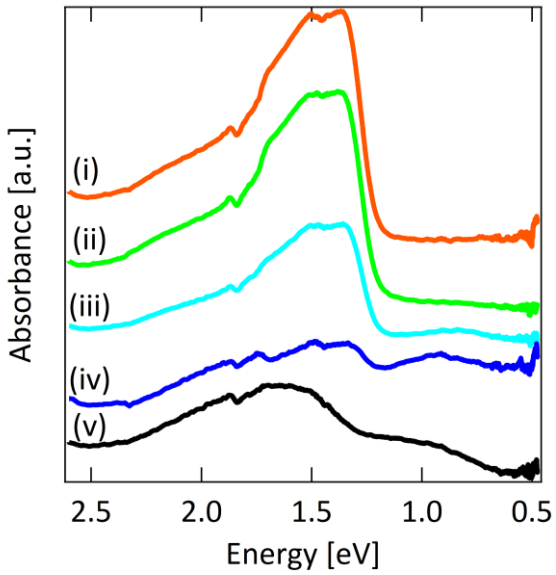

Figure 3.4 UV-VIS absorption spectra of **i)** neat P(BTP-DPP) and P(BTP-DPP) doped with **ii)** 0.15 monomeric dopants per repeat unit **iii)** 0.37 monomeric dopants per repeat unit **iv)** 0.77 monomeric dopants per repeat unit and **v)** 0.92 monomeric dopants per repeat unit.

We performed time-dependent density functional theory (TD-DFT) on a model compound comprising one BTP unit flanked by two thiophene-DPP-thiophene units in an effort to assign the optical transitions (Supporting Information Figure S3.7). This model cannot capture the full electronic structure of the backbone, but does provide an means to investigate the electronic levels in a comparable structure. TD-DFT predicts that the main optical transition of the model compound has a 1st excited state at 1.4 eV. This value is in reasonable agreement with the measured absorption edge in the solid state of 1.2 eV. We then calculated the electronic levels and optical absorption of a monoanion and dianion. The dianion is a closed-shell species and the first optical transition is dominantly from the HOMO to LUMO; here the HOMO orbital is similar to the LUMO of the neutral compound. This transition occurs at 0.9 eV in reasonable agreement with the observed feature in the optical spectra along with a higher lying state predicted at 1.7 eV (Figure 3.4). The monoanion is

necessarily an open-shell species and TD-DFT suggests three transitions at low energy. The first two transitions (at 0.7 and 0.8 eV) have low oscillator strengths, but the third transition, which is relatively strong, is predicted at an energy of 1.0 eV. From these calculations, it is difficult to unambiguously assign the low energy feature to either polarons or bipolarons, because both give sub-optical gap transitions for the charged species. Larger spectral shifts have been observed between anionic and dianionic for polyfluorenes in solution at comparable charge to monomer ratios, but the optical gap of the neutral is much larger (near 3.0 eV).[163]

Changes in the Fermi level of the doped films measured by Ultraviolet photoelectron spectroscopy (UPS) confirm that films have been heavily doped (Figure 3.5 and 3.6). The UPS spectra of the neutral polymer reveals an ionization energy (IE) of 4.9 eV corresponding to the HOMO level (see Supporting Information Figure S3.8-S3.12 for assignment of band edges). The electron affinity can be estimated using the optical gap of 1.21 eV with an uncertainty of the exciton binding energy (~0.3 to 0.5 eV). Upon doping, the spectra shift towards higher binding energy with respect to the Fermi level corresponding to *n*-doping. A vacuum-level shift is also observed, but the dominant change upon doping is the appearance of mid-gap states consistent with observations in other studies of *n*-type doping of organic materials.[100,167] Ultraviolet visible spectroscopy (UV-VIS) did not show an altered optical gap (measured from the onset of the neutral peak to be ~1.21 eV) at low levels of doping (Figure 3.4). Sub-gap states are observed in the UPS spectra and are attributed to the formation of (bi)polaronic species. The presence of sub-gap states is not always observed in the UPS spectra of *n*-doped systems. The failure to observe sub-gap features in previous UPS studies of systems doped with dimeric sandwich compounds is likely due to the lower levels of doping.[168] However, more heavily doped systems do show the emergence of sub-gap states

at higher dopant concentrations, for example, in the cases of copper phthalocyanine n-doped with decamethylcobaltocene (~30 wt%) [169] and of P(NDI2OD-T2) *n*-doped with a $DMBI_2$ dimer (10 molar ratio %).[100] The emergence of negative bipolaronic sub-gap states in polyphenylenevinylene (PPV) systems doped with alkali metals were observed in UPS by the emergence of two separate peaks in accordance with the previously described model for bipolarons.[170],[171] In our system (Figure 3.5), a single sub-gap feature begins to emerge at 0.37 monomeric dopants per repeat unit. The existence of a single feature in the spectrum

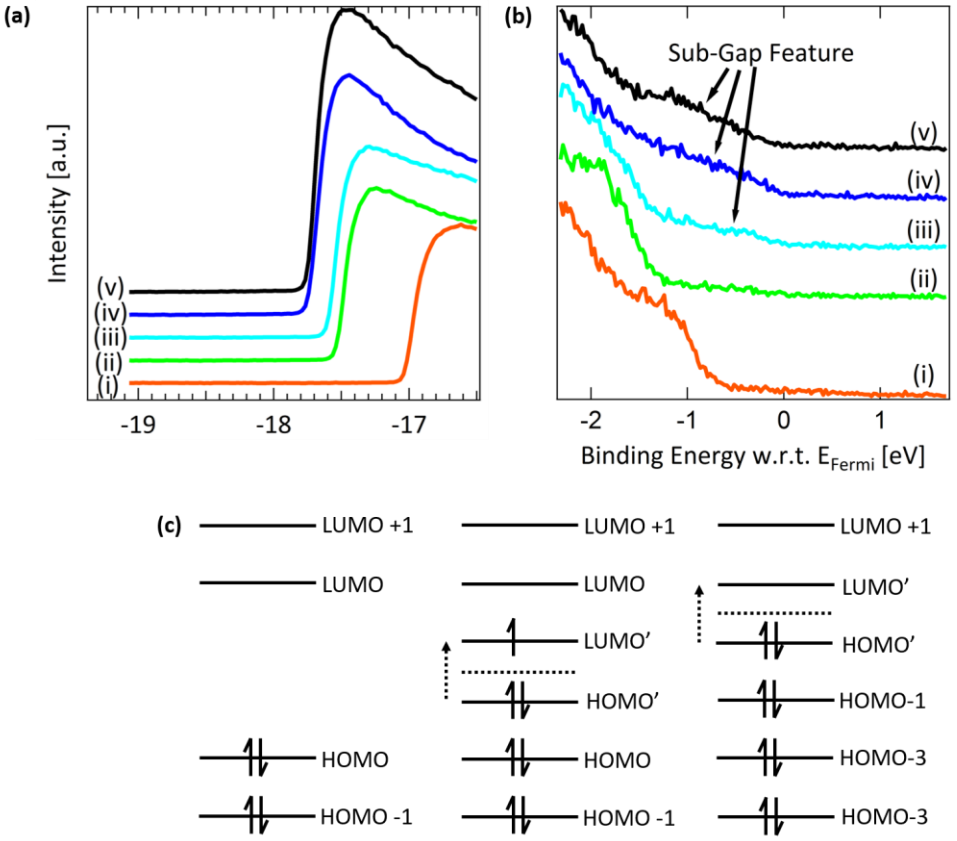

Figure 3.5 UPS spectra around the a) secondary electron edge and b) valence band edge of **i)** neat P(BTP-DPP) and P(BTP-DPP) doped with **ii)** 0.15 monomeric dopants per repeat unit **iii)** 0.37 monomeric dopants per repeat unit per dopant **iv)** 0.77 monomeric dopants per repeat unit and **v)** 0.92 monomeric dopants per repeat unit. A dashed line indicates where the valence band edge has been defined. See Supporting Information Figure S3.8-3.12 for details of fitting. c) Diagram of energy levels depicting how the HOMO and LUMO are redefined as states are filled.

could be the result of it becoming increasingly difficult to resolve independent sub-gap features due to the narrow gap of P(BTP-DPP). The difference in energy of the edge of the sub-gap features and the feature assigned to the HOMO of the neutral polymer is approximately 1 eV, which is consistent with the shift expected from the formation of polaronic levels. More indicative of the nature of the charge carrier is whether there is a finite density of states that exist at the Fermi level.[162] In the case of a very high concentration of bipolarons, the upper sub-gap state will be completely filled and the Fermi level will be located at a higher energy level at which there is a non-existent density of states at E_F. In UPS spectra of doped P(BTP-DPP), the density of states of the sub-gap feature decreases towards

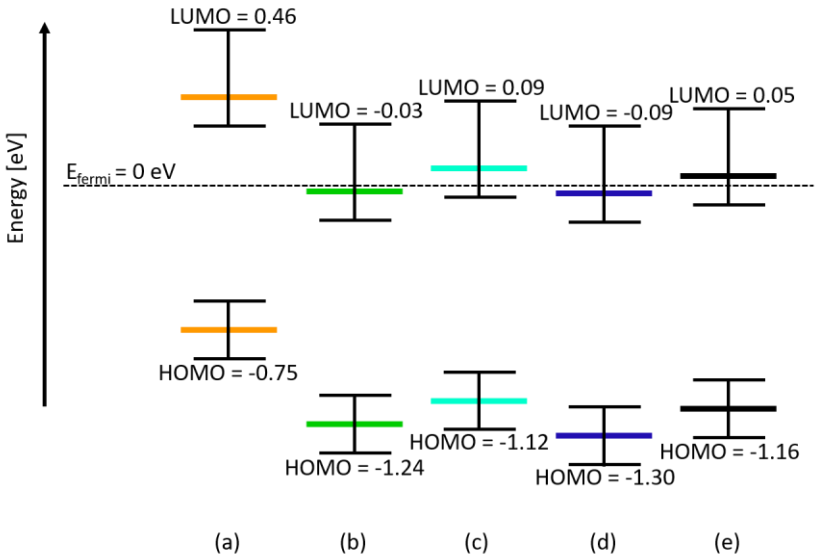

Figure 3.6 The HOMO and LUMO levels realtive to the Fermi level (units of eV) of films as a function of RuCp*mes doping concentration measured by UPS with unoccupied level estimated based on the optical gap for **(a)** neat P(BTP-DPP) and doped P(BTP-DPP) at **(b)** 0.15 monomeric dopant per repeat unit **(c)** 0.37 monomeric dopant per repeat unit **(d)** 0.77 monomeric dopant per repeat unit and **(e)** 0.92 monomeric dopant per repeat unit. The vacuum level relative to the Fermi level is 4.16 eV, 3.66 eV, 3.59 eV, 3.45 eV, and 3.44 eV for neat P(BTP-DPP), and P(BTP-DPP) doped at 0.15, 0.37, 0.77 and 0.92 monomeric dopant per repeat unit respectively. The given error bars are based on the resolution of the UPS apparatus (±0.15 eV), and the error in the unknown exciton binding energy used to estimate the unoccupied levels.

zero at E_F, thus supporting the presence of bipolarons. We cannot, however, rule out other effects such as electron-electron interactions that could strongly modify the DOS without higher level computational studies or additional measurements, e.g. inverse photoemission that could probe the unoccupied states.[165,166]

3.3.3 Morphology and Charge Percolation

The electrical conductivity of a doped semiconducting polymer is a function both of the local and longer range order. Our AFM data shows that the films are relatively uniform and smooth, but do not reveal if the local ordering is impacted by doping. Grazing incidence wide angle X-ray scattering (GIWAXS) was performed in order to characterize how the dopant impacts the local structure and if the features observed in AFM correspond to aggregates of the dopant.

P(BTP-DPP) has glassy order that is not strongly perturbed upon doping. The 2D scattering patterns for the undoped polymer film and for increasing dopant concentrations are shown in Figure 3.7. Analysis of the 2D images through line-cuts in the in-plane and out-of-plane direction are given in Supporting Information Figure S3.13. The 2D GIWAXS of neat P(BTP-DPP) (Figure 3.7(a)) indicates that it is a glassy polymer because of the broader features. We assign the peak at a *q* of 0.3 $Å^{-1}$ (where *q* is the scattering vector), corresponding to a real-space stacking distance of 2.1 nm, as the alkyl stacking between polymer chains. A second order peak is located at 0.6 $Å^{-1}$. There is a broad feature at a *q* of 1.5 $Å^{-1}$ (real-space distance of 4.2 Å) in the out-of-plane direction that we assigned to the spacing between polymer chains, "π-π stacking". The scattering from a neat film of $(RuCp^*mes)_2$ shows rings characteristic of a polycrystalline powder with the most intense features at a q of 0.85 $Å^{-1}$

(Figure 3.7(h)), corresponding to a real-space distance of 7.4 Å. As the fraction of dopant increases, the polymer local packing structure becomes more disordered as evidenced by the broadening of the π-π stacking peak. Figure 3.7(e) shows that scattering features at q~0.85 $Å^{-1}$ become very pronounced below 0.77 monomeric dopants per repeat unit, likely due to unreacted dopant in the dimer form crystallizing and phase separating. This is also seen in the 1D line-cuts (Supporting Information Figure S3.15) where the doped polymer films show a peak emerging at 0.85 $Å^{-1}$ from the dopant which increases in intensity as more dopant is added. XPS shows that the dopant is primarily present in the reacted cationic form given the value of the Ru $3d_{5/2}$ binding energy (Supporting Information Figure S3.3). The AFM images show aggregates that comprise approximately 2% of the surface area of the AFM image of the sample with 0.92 monomeric dopants per repeat unit. At this concentration, we would not expect the peak associated with the neutral dimer to appear as a detectable shoulder on the Ru $3d_{5/2}$ peak in the XPS spectra. However, because of the heavy atom and high crystallinity of the dopant, the X-ray scattering of such aggregates could be prominent relative to the weak scattering from the glassy polymer, explaining why we observe scattering attributable to neutral dopant in more heavily doped samples.

In addition to the processing method, our data suggest that the unique non-planar molecular structure of P(BTP-DPP) also contributes to the high *n*-type electrical conductivity. Previously we have studied *n*-doping of P(NDI2OD-T2), which has a similar LUMO to P(BTP-DPP), with N-DMBI dopants by doping from the casting solution.[101] In order to examine the role of processing, we also attempted doping P(NDI2OD-T2) with $(RuCp^*mes)_2$ via sequential casting at the same dopant solution loading. In contrast to P(BTP-DPP), all P(NDI2OD-T2) doped films were too resistive to measure (<10^{-6} S/cm). The known high

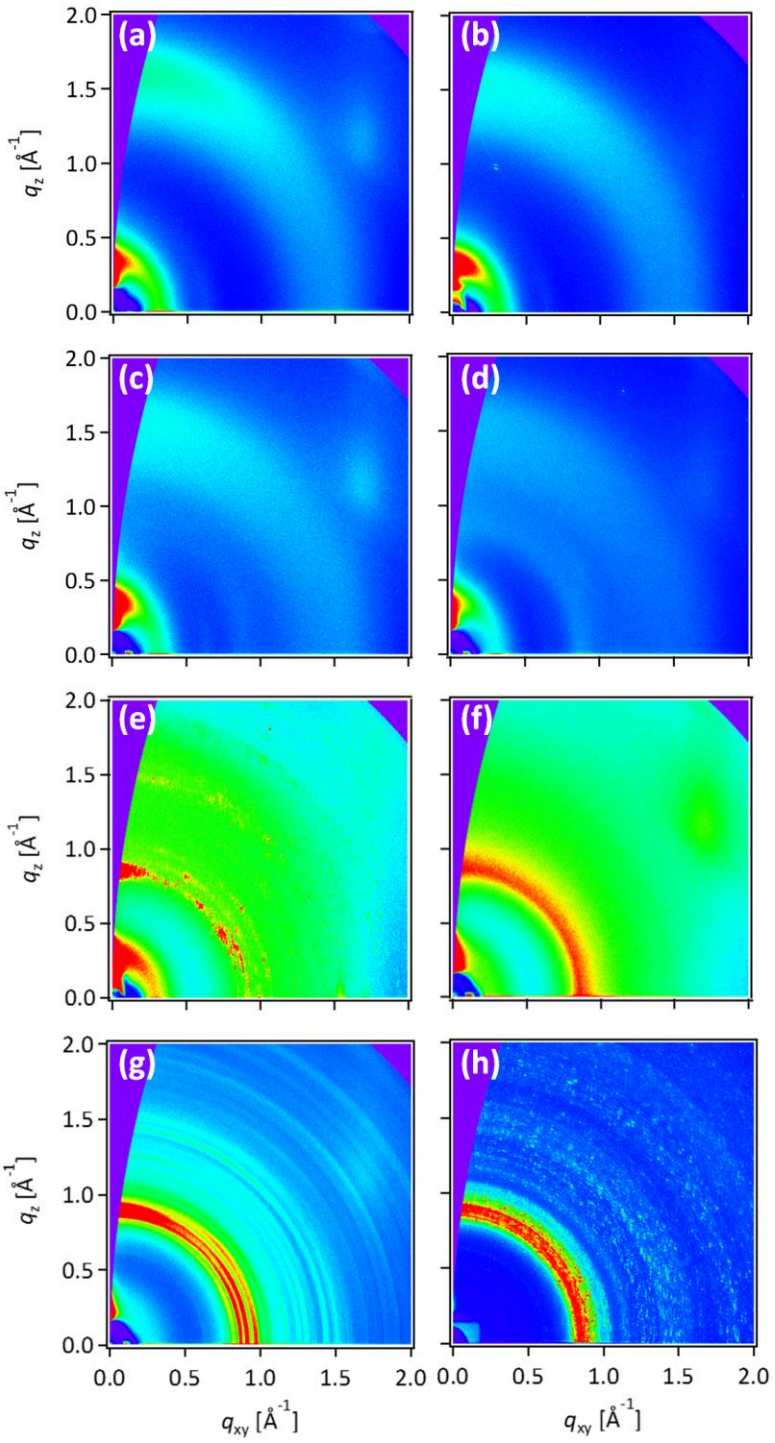

Figure 3.7 GIWAXS patterns for the **(a)** neat polymer (P(BTP-DPP)), **(b)** 0.15 monomeric dopants per repeat unit, **(c)** 0.37 monomeric dopants per repeat unit, **(d)** 0.55 monomeric dopants per repeat unit, **(e)** 0.77 monomeric dopants per repeat unit, **(f)** 0.92 monomeric dopants per repeat unit, **(g)** 1.17 monomeric dopants per repeat unit, and **(h)** neat dopant $(RuCp^*mes)_2$

structural order in P(NDI2OD-T2) may prevent efficient incorporation of the dopant into the film, as previously observed for N-DMBI[101] and also $(RuCp^*mes)_2$.[31] Specifically, the non-planarity of the (*E*)-8,8'-biindeno[2,1-*b*]thiophenylidene unit P(BTP-DPP) structure may allow for a more efficient incorporation of the dopant into the bulk of the film. Models of the backbone conformation for single chains based on geometries from DFT calculations (Figure S3.7) show the significant deviation from linearity of the backbone that likely prevents efficient packing and lead to the glassy ordering observed by GIWAXS.

Given that we suspect the presence of both polarons and bipolarons in samples with highest conductivity, we can now try to develop an explanation for the trends in electrical conductivity and carrier concentration. In the sample with 0.15 monomeric dopants per repeat unit (or 0.05 mg/mL $(RuCp^*mes)_2$ loading), monomeric dopants could concentrate on top of the film creating bipolarons (or other spin-paired species) in that region. We expect that the carriers will be relatively localized because each $(RuCp^*mes)_2$ will split to form two carriers on the polymer in close proximity. These heavily doped film regions create a limited number of charge carrier pathways that lead to a conductivity of $\sim 10^{-2}$ S cm^{-1}. As the doping concentration is increased to 0.37 monomeric dopants per repeat unit (or 0.1 mg/mL $(RuCp^*mes)_2$ loading), the surrounding areas become moderately doped and the increased charge concentration allows polarons to form with a detectable EPR signal of 10^{19} spins/cm^3. The emergence of polarons increases the conductivity to $\sim 10^{-1}$ S cm^{-1} as additional charge-carrier pathways become present. In the 0.55 monomeric dopants per repeat unit sample (or 0.25 mg/mL $(RuCp^*mes)_2$ loading), heavily doped regions have expanded slightly increasing the conductivity. As the doping concentration is increased to 0.77 monomeric dopants per repeat unit (or 0.5 mg/mL $(RuCp^*mes)_2$ loading), the sample is almost homogenously doped

but polaron regions are still present in the film according to the detectable EPR signal. Unreacted dopants, however, begin to aggregate which leads to a small drop off in carrier mobility as carrier pathways become impeded. As a result, no increase in conductivity occurs despite the higher carrier concentration. By 0.92 monomeric dopants per repeat unit (or 1 mg/mL $(RuCp^*mes)_2$ loading) all film regions are heavily doped such that polarons recombine into bipolarons and EPR is again silent. However, neutral dopant crystallites have grown in size and dramatically disrupt carrier mobility likely by extending into the bulk region of the film from the surface. This leads to the drop off in conductivity to ~10^{-3} S cm^{-1}.

3.4 Conclusions

In summary, we have found high *n*-type conductivities of up to 0.45 S cm^{-1} for an ambipolar copolymer, P(BTP-DPP), doped with the organometallic small molecule $(RuCp^*mes)_2$. Sequential casting leads to efficient charge generation and the formation of bipolaronic carriers at high levels of dopant incorporation. Comparison of doping of P(NDI2OD-T2), which comprises planar units and a linear backbone leading to a high mobility in TFTs, to P(BTP-DPP), which has a twisted backbone and lower mobility in TFTs, suggests that the steric space created by the non-planar unit in the polymer backbone and the glassy ordering allows for efficient incorporation of the dopant. Our study suggests that exploration of backbone architectures that can improve the miscibility with a wider range of *n*-dopants could be of interest in developing systems with high *n*-type conductivities. From a design standpoint, the choice of organic semiconductor for developing high conductivity systems may not be the same as for developing high mobility systems for TFT applications.

Such materials have potential use as transparent conductors and electrode layers for organic devices such as TFTs, OLEDs, and TFTs and as thermoelectrics.

Chapter 4

N-type Surface Doping of $MAPbI_3$ via Charge Transfer from Small Molecules

Reprinted with Permission of [172]:

Perry, E.E.; Labram, J.G.; Venkatesan, N. R.; Nakayama, H.; Chabinyc, M. L. N-type Surface Doping of $MAPbI_3$ via Charge Transfer from Small Molecules. *Advanced Electronic Materials 4*(7), 1800087.

Organic hole and electron transport materials are regularly employed as electron- and hole-blocking layers in perovskite thin-film solar cells. In order to optimize charge-extraction in the device, these organic layers can be doped using organic small molecules. However, to date there has been little work carried out on direct doping of perovskite surfaces. In this report, we study the change in electrical properties of thin films of $MAPbI_3$ by surface doping the film with an organic dopant molecule: cobaltocene ($Co(C_5H_5)_2$). By varying the quantity of cobaltocene deposited, the conductivity of $MAPbI_3$ thin films are observed to be tunable over several orders of magnitude. We observe a tunable shift in the Fermi level illustrating

that charge transfer doping enables control over the interfacial energy levels. An increase in photoconductivity is seen at intermediate doping levels, indicating passivation of surface traps confirmed by increased photoluminescence. This model system provides a means to understand more complex heterointerfaces of doped organic blends at perovskite surfaces.

4.1 Introduction

The maximum power conversion efficiencies of lab-scale solar cells based on organic metal halide materials (OMH) have improved from 3.8% to 22.2% in just seven years.[173,174] The ability to manipulate the electronic properties of heterointerfaces enables one to carefully control the efficiency of charge separation and extraction in solar cell devices. Poorly-tuned interfacial energetic barriers at electrode-semiconductor interfaces can greatly limit the charge collection and reduce device efficiencies.[8,123,175] Excessive offsets of the electronic levels between materials can lead to significant charge accumulation at interfaces, influencing charge injection and extraction.[6] The Fermi level of a material controls band alignment at interfaces along with other factors such as the formation of interface states with heterointerfaces.[70] The Fermi level in semiconductors can be tuned by the addition of dopants; however to-date, doping has proven challenging for OMHs[41–44] and there is not yet evidence of the ability to reliably control the profile of doping within a thin film. Little work on directly doping interfaces has been done on methyl ammonium lead iodide ($MAPbI_3$) to see if improvements in efficiencies can be made.[175]

In this report, we study how charge transfer from a molecular dopant occurs at the surface of thin films of $MAPbI_3$. We investigate *n*-type charge transfer doping by directly depositing the organic small molecule cobaltocene ($Co(C_5H_5)_2$) onto thin films of $MAPbI_3$ (Figure 4.1(a))

and by examining the impact on Fermi level position, conductivity and photoconductivity. This model system provides a means to understand more complex heterointerfaces where materials, such as blends of an organic semiconductor and dopant, are in contact with the perovskite active material.

Surface doping of semiconductors induces charge carriers that are dominantly confined within the top few nanometers of the surface by the electric field created by the interfacial charge separation.[66] While this route cannot lead to bulk doping, it has applications for engineering interfacial energy levels by inducing band bending near the surface.[68–70] Doping could potentially improve carrier injection and extraction to $MAPbI_3$ across electron transport layers, such as organic semiconductors, and can help to passivate surface states.[70]

Charge transfer from small molecule dopants has been demonstrated to several inorganic semiconductors: diamond,[68] silicon,[69] carbon nanotubes,[176] graphene[177] and phosphorene.[178] Charge transfer from molecular species to a semiconductor at an interface has several prerequisites.[66] For effective charge transfer, the ionization energy, I.E., (the HOMO level) of the small molecule must lie close or above the conduction band minimum (CBM) of the semiconductor for *n*-type doping, or the electron affinity, E.A., (the LUMO level) of the small molecule must lie close or below the valence band maximum (VBM) of the semiconductor for *p*-type doping. The position of the VBM and CBM of $MAPbI_3$ are ≈5.4 and ≈3.7 eV below the vacuum level respectively, which are similar to the position of the HOMO and LUMO of many organic semiconductors.[7,8] There is some variation in the precise position of the VBM and CBM of $MAPbI_3$ across reports, which is likely a result of preparation conditions, sample treatment and substrate choice.[8,179,180] Based on these reported energy levels, small molecule dopants that have been developed to dope organic

semiconductors are also likely to be effective candidates for charge transfer to $MAPbI_3$.[181] The second prerequisite for charge transfer to occur is for the semiconductor to have an absence of surface states. For covalent semiconductors that may have surface reconstructions from the bulk or have oxide layers, such as diamond and silicon, a surface treatment must be carried out for charge transfer to occur.[68,69] The surface treatment (e.g. hydrogenation for diamond and alkylation for silicon) allows surface passivation by removing interfering surface states from the gap and lowering of the ionization energy sufficient to facilitate electron transfer. [6]

OMH semiconductors such as $MAPbI_3$ present an interesting opportunity for surface doping, since ionic semiconductors normally have a smaller density of surface states in the bandgap than covalent semiconductors.[70] This can be illustrated by the fact that $MAPbI_3$ thin films have reported surface and grain boundary recombination velocities of ≈150 cm/s and ≈7 cm/s respectively,[9] which are several orders of magnitude smaller than values for unpassivated silicon, which has a surface recombination velocity of ~10^6 cm/s.[55] There are, however, defects at the surface of $MAPbI_3$.[182] Due to the low thermodynamic stability of $MAPbI_3$, the annealing process following spin-coating can lead methylammonium (MA) and iodide to be sublimed because of their higher volatility, resulting in under-coordinated Pb atoms at the crystal surface.[183] The under-coordination creates favorable conditions for coordination, or bond formation, with electron rich materials such as Lewis bases that have been pursued to passivate surface traps. [59,61]

4.2 Experimental Methods

Films of $MAPbI_3$ were fabricated using a 1 Molar solution of 1:1 ratio of PbI_2: MAI in a 3:7 ratio (by volume) of DMSO: GBL. The solution was spin-coated onto substrates with the following conditions: 10 seconds at 1000 rpm with 200/s rpm acceleration, followed by 20 seconds at 5000 rpm with a 1000/s rpm acceleration. In the last 4 seconds, an anti-solvent of three drips of chlorobenzene is dropped about the film surface. The film then undergoes an annealing ramp of 40°C for 2 min, 80°C for 2 min, 100°C for 2 min, 110°C for 10 min. Cobaltocene dissolved in toluene at dopant concentrations of 0.1, 0.2, 0.3, 0.5, 1, 5, 10, and 20 mg/mL is spin-coated onto the perovskite surface using the same spin conditions. For electrical device measurements, gold contact pads were evaporated onto the perovskite surface prior to cobaltocene deposition. See Supporting Information for detailed description of experimental methods.

4.3 Results and Discussion

4.3.1 Dopant Surface Coverage of $MAPbI_3$

In order to study the electrical properties of *n*-type surface doped $MAPbI_3$, an interfacial layer of cobaltocene on the perovskite surface was formed by spin coating from toluene solution at various concentrations (See Experimental Methods for details). Cobaltocene acts as an *n*-type dopant (HOMO -4.0 eV) with a simple charge transfer reaction that can occur via solution processing.[88,184] The $MAPbI_3$ surface topography following cobaltocene deposition is shown in SEM and AFM micrographs in Figures 4.1 and S4.1. The cross-sectional height profiles extracted from the AFM images providing the roughness of the films are shown in Figure S4.2. Cobaltocene appears to be deposited with relative uniformity onto the surface, with a surface coverage that depends on the dopant concentration. At low dopant

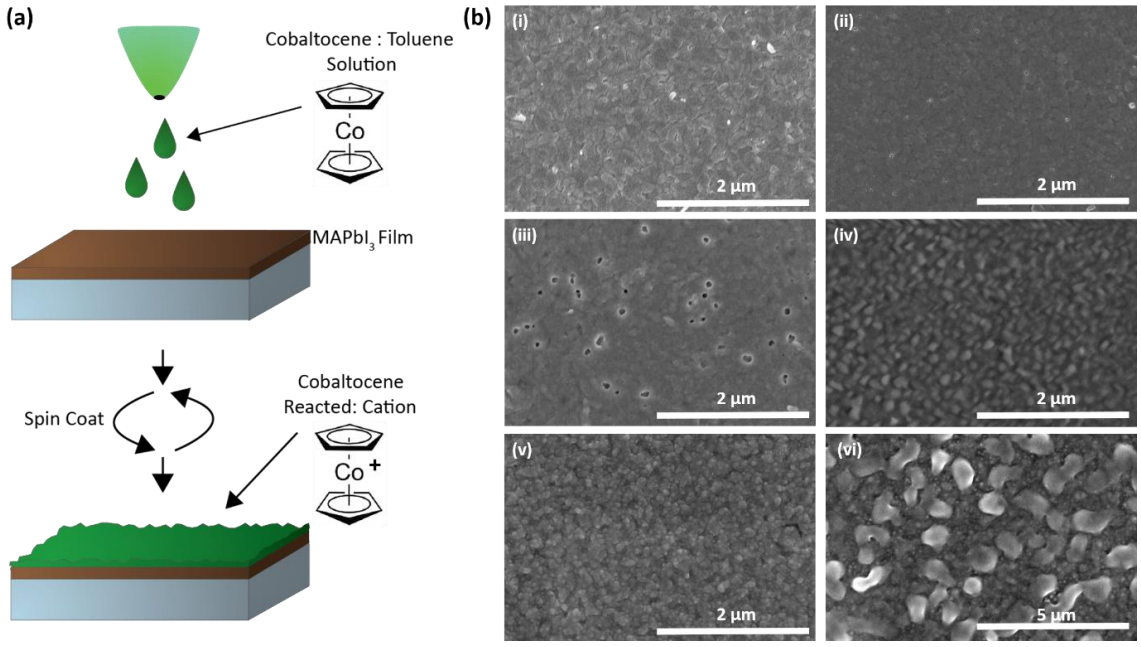

Figure 4.1 (a) Illustration of spin coating cobaltocene: toluene solution onto surface of $MAPbI_3$ films. Dopant solution deposition was done following $MAPbI_3$ annealing and was not used as the anti-solvent. The illustration includes the molecular structure of cobaltocene and its reacted cation form. (b) SEM micrographs of surface of $MAPbI_3$ films (i) neat and with increasing dopant concentration (ii) 0.1 mg/mL, (iii) 0.2 mg/mL, (iv) 0.3 mg/mL, (v) 1 mg/mL, and (vi) 5 mg/mL. Partial surface coverage of cobaltocene is observed at 0.2 mg/mL because of the lack of observable $MAPbI_3$ grains and the texturing of the surface.

concentrations of cobaltocene, such as 0.1 and 0.2 mg/mL, there appears to be texturing corresponding to partial coverage of the dopant. Above a concentration of 0.3 mg/mL, the surface appears to be uniformly coated by cobaltocene, until at a concentration of 5 mg/mL where cobaltocene aggregates are clearly formed on the surface. At this concentration, it is difficult to completely dissolve cobaltocene and aggregates were likely already present in solution. In order to better understand the relationship between dopant concentration and surface coverage, the atomic ratio of Co:I was measured at the surface (~10 nm depth) using X-ray photoelectron spectroscopy (XPS) (Figure S4.3). For dopant concentrations of 0.1, 0.2, 1 and 5 mg/mL, the ratio of Co:I was 0.19, 0.20, 0.28, and 0.77 respectively, which follows a

linear relationship (Figure S4.4 and Table S4.1). While XPS can provide information about atomic percentages of surface composition, it cannot easily distinguish the nature of dopant coverage on the surface (i.e. island growth versus monolayer coverage).

Additionally, atomic ratios collected using XPS were used to determine if there was damage to $MAPbI_3$ upon doping (Figures 4.2(a) and Table S4.1). The atomic ratio of Pb:I at the surface is 1:3, as in $MAPbI_3$, below 1 mg/mL dopant concentration, but above this concentration increasingly more iodine is present at the surface. It is likely that this change is the result of iodide released by chemical damage to the $MAPbI_3$ crystallites in order to act as a counter ion to the reacted cobaltocene cations. Although XPS shows signs of surface degradation at high doping concentrations, techniques such as optical absorption and X-ray

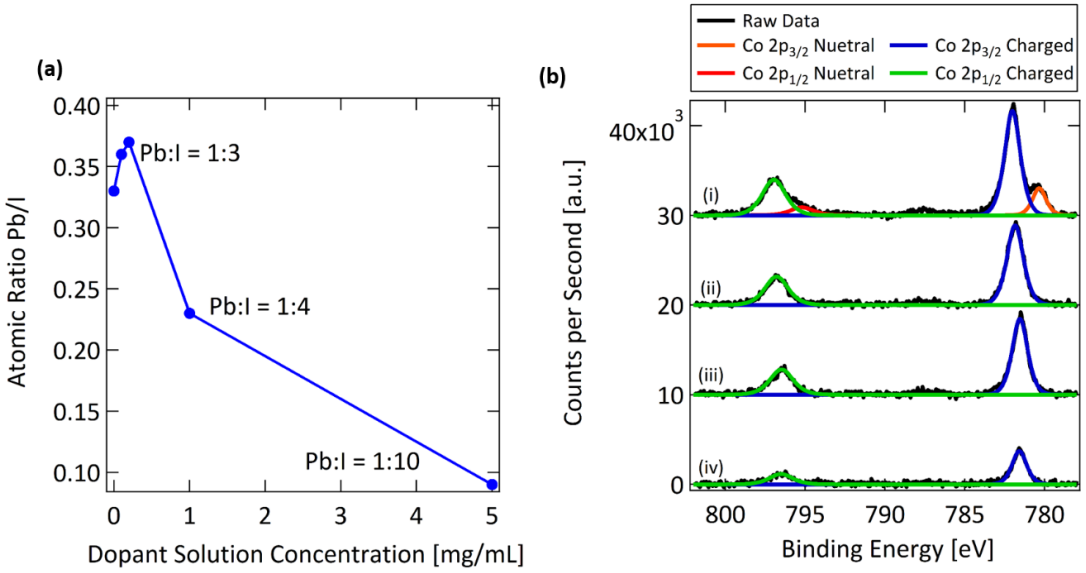

Figure 4.2 XPS of doped $MAPbI_3$ films. (a) Atomic ratio of Pb: I atoms from an XPS survey scan. At low doping concentrations, atomic ratios are 1:3 as expected for $MAPbI_3$. However at increasing dopant concentration less Pb is present, indicating degradation and diffusion of Iodide. (b) Core level spectra of Co $2p_{1/2}$ and $2p_{3/2}$ peaks of $MAPbI_3$ films with the dopant concentrations of (i) 5 mg/mL, (ii) 1 mg/mL, (iii) 0.2 mg/mL and (iv) 0.1 mg/mL. Symmetry of peaks and position of binding energy indicate whether cobaltocene has reacted. At 5 mg/mL ~18% of the cobaltocene is still in the neutral form.

diffraction (XRD) show that a significant portion of the film remains unchanged (Figures S4.5 and S4.6). In addition to degradation from casting at high dopant concentrations, there also appears to be an upper limit to the amount of dopant that reacts with the $MAPbI_3$ surface. At 5 mg/mL dopant concentration, the majority (~82%) of the dopant has reacted, as can be seen by the symmetry and position of the binding energy of cobalt peaks in XPS (Figure 4.2(b)). Dopant aggregates are still in the unreacted form as they make up 16% of the surface area, which matches up well with the amount of unreacted dopant shown in XPS.

4.3.2 Fermi Level Shifts upon Doping

$MAPbI_3$ films show tunable electrical properties as a function of surface coverage. Ultraviolet photoemission spectroscopy (UPS) shows a gradual shift of the VBM away from the Fermi Level, E_F, towards higher binding energy with increasing dopant concentration (Figures 4.3 and S4.7). At high doping concentrations, this shift is so substantial that the surface region is approaching the degenerate limit (E_F within $\approx 3\ k_bT$ of the CBM). Assignment of the valence band edge (VBE) was performed on a linear scale as close to the edge as possible adding some uncertainty to the position due to the low density of states (DOS) near the VBE (Figure S4.8-S4.12).[8,131] The assignment of the VBE was made using high resolution scans measured from -2.5 to 1.6 eV, which we believe allowed for a more precise determination compared to other studies where a linear extrapolation to find the VBE was taken over a wider energy range.[8,179,180] We chose this approach because multiple averages to achieve low noise around the VBE could result in degradation of the material due to the long exposure time. Our extracted values do not lead to unphysical values of the band gap as seen in some experiments.[179,180] An alternative fit based on an assumed Gaussian form for

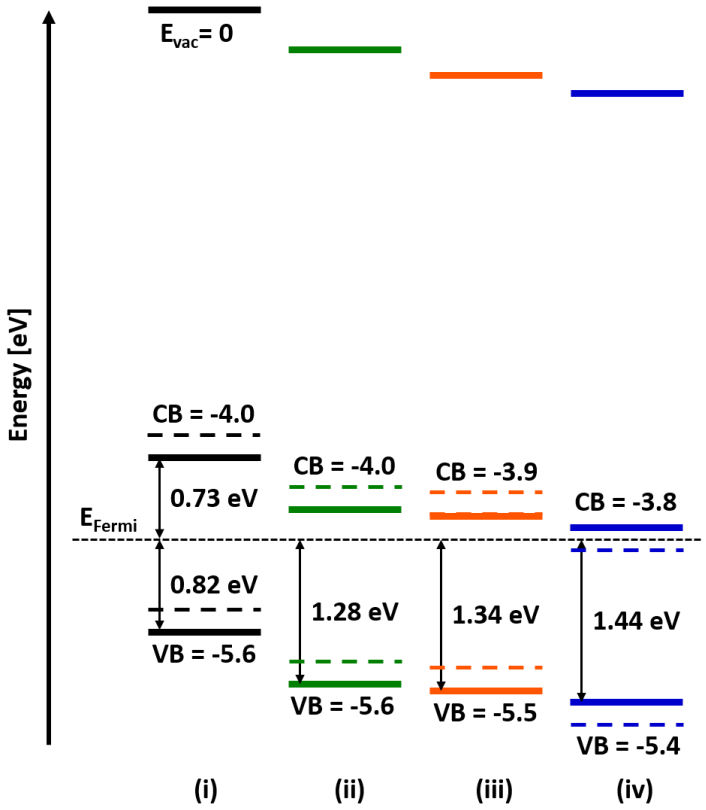

Figure 4.3 Energy level diagram experimentally determined by UPS for (i) neat $MAPbI_3$, (ii) 0.1 mg/mL doped $MAPbI_3$, (iii) 0.2 mg/mL doped $MAPbI_3$, and (iv) 1 mg/mL doped $MAPbI_3$. Diagrams depict the position of the valence band (VBM), and the conduction band (CBM) in units of eV, assuming a band gap of 1.55 eV. The solid line represents values from a linear fit to the UPS data while the dashed line represents potential error in assigning the VBE by using a Gaussian edge fit on a logarithmic scale.

the VBE and a constant noise floor is shown on a semi-logarithmic scale in the Supporting Information (Figure S4.13). This type of fit also is imperfect due to question of whether this shape adequately fits the DOS. At higher dopant concentration, the shape of the spectrum changes near the edge; such features have been assigned to surface defects in some studies,[8,185] but it is difficult to unambiguously assign them. This shape change makes assigning a fit more challenging (two versions are shown in Figure S4.13), leading to the inversion in trend seen at 1 mg/mL between logarithmic and linear scale assignment of the

VBE. Despite the difficulty of the assignment of the edge, the two approaches agree within ≈0.2 eV and show the same trend with dopant concentration (Figure 4.3). For our analysis we choose the linear fit using data close to the edge for simplicity.

Using the UPS data, we can estimate the electron concentration as a function of the concentration of cobaltocene. Neat $MAPbI_3$ was calculated to have an electron concentration of ~10^6 carriers/cm^3 using reported values for the band gap and effective masses,[186,187] which is low as a result of the Fermi level being close to mid-gap i.e. a nearly intrinsic semiconductor. Previous studies reported that $MAPbI_3$ displayed *n*-type behavior when cast on oxide surfaces such as TiO_2, ZnO and Al_2O_3 due to Fermi level pinning.[8,123,180,188] The mid-gap position of the Fermi level seen here by using an underlying gold coated substrate is similar to other studies performed on gold[189,190] and p-type substrates such as PEDOT:PSS, NiO_x, and Cu_2O.[7,180] Due to the low intrinsic carrier density of $MAPbI_3$, the Fermi level will be tuned by the underlying substrate as a result of charge transfer.[191] The choice of substrate here was advantageous because intrinsic $MAPbI_3$ was conducive to observing the increase in charge carriers upon doping. In the doped $MAPbI_3$ films, the electron concentration increases to ~10^{13}, ~10^{14}, and ~10^{16} carriers/cm^3 for casting concentrations of 0.1, 0.2, and 1 mg/mL dopant concentration respectively. It should be noted that there may be chemical damage to the surface of $MAPbI_3$ at 1 mg/mL dopant concentration as indicated by XPS as a result of the high dopant concentration causing iodide diffusion towards the surface. Because of the dopant cation at the surface, the majority of charge carriers should be confined to a thickness of a few nm below the surface (See Supporting Information), which is consistent with other studies of surface doping on materials such as diamond and silicon.[66]

UPS is a surface sensitive technique which probes the top ~8 nm, making it important to consider the effects of the coverage of the molecular dopant. Given the atomic ratio of Co:I determined from XPS, the surface of the perovskite can be observed. This can be confirmed by looking at the shape of the DOS of the falling VBE (Figure S4.14), which maintains the same form as $MAPbI_3$ with slight changes with increasing dopant concentration. Another consideration of dopant coverage is the creation of interface dipoles as a result reacted cobaltocene cation, which is seen in other studies of charge transfer doping at interfaces.[66] The change in the work function upon doping includes the effects of both band bending and interface dipoles. Neat $MAPbI_3$ has a work function of 4.7 eV w.r.t E_F. Upon deposition of the dopant, the work function decreases relative to the neat film by 0.35, 0.58, and 0.74 eV for 0.1, 0.2, and 1 mg/mL dopant concentration respectively. The band bending component can be observed in shifts in the XPS core level spectra. Previous studies have tracked band bending in $MAPbI_3$ by the binding energy of the Pb 4f level.[8] Slight shifts in peak position of Pb 4f (~0.25 to 0.35 eV) toward higher binding energy upon doping indicate downward band bending (See Figure S4.15). Therefore, the interface dipole contribution to the work function change would be around ~0.1, 0.3 and 0.5 eV for 0.1, 0.2 and 1 mg/mL dopant concentration respectively. In previous studies of surface doping, sharp changes in work function versus dopant thickness have been used to identify sub monolayer coverage, which is consistent with our observations of surface texturing of AFM micrographs.[192] Figure S4.16 shows the relationship of Co:I ratio over the dopant concentration range studied versus work function.

4.3.3 Surface Conductance and Evidence of Trap Passivation

The increased concentration of electrons results in a substantial increase in the lateral electrical conductivity of the films (Figure 4.4(a)). The electrical conductivity was measured using a two-point probe geometry due to the high absolute resistance of the films. The electrical conductivity was calculated using the full thin film thickness (~120nm) for each concentration, but we note that the charge should be confined to a thin region near the surface making the surface region substantially more conductive than the bulk.[66] The range of dark conductivity for the neat samples (~10^{-7} S/cm) can be compared to the conductivity of ~10^{-7} S/cm reported by Peng et al for a $MAPbI_3$ single crystal[193] and to the conductivity of ~10^{-8} S/cm for a $MAPbI_3$ thin film reported by Levine et al.[194] The conductivity of neat samples on quartz is inconsistent with the charge carrier concentration of films on gold substrates

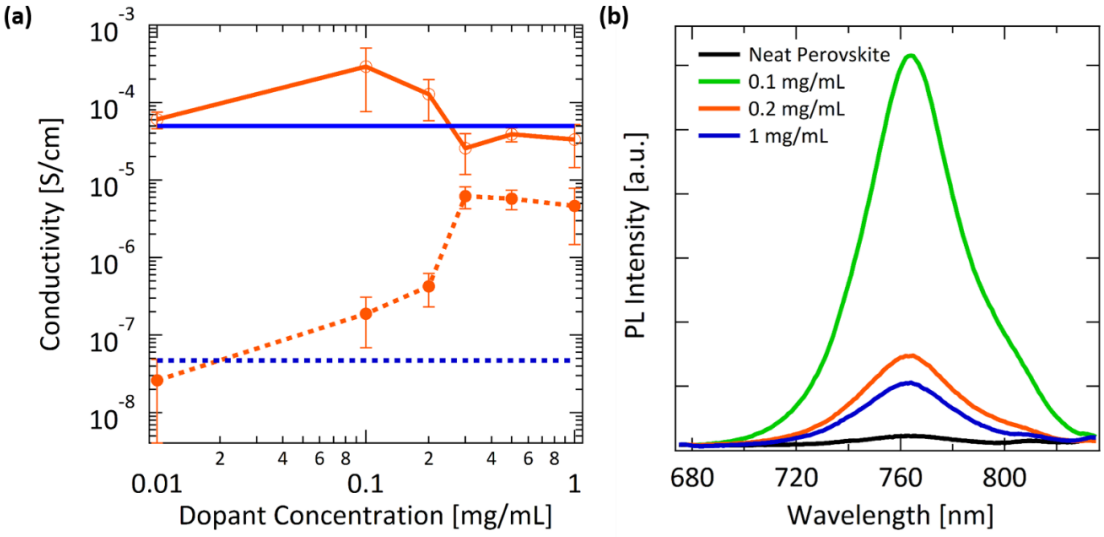

Figure 4.4 (a) Photoconductivity and dark conductivity of $MAPbI_3$ films as a function of dopant concentration (Orange Solid: Photoconductivity of doped samples, Orange Dashed: Dark conductivity of doped samples, Blue Solid: Average photoconductivity of neat films, Blue dashed: Average dark conductivity of neat films). Photoconductivity was performed by illuminating $MAPbI_3$ films with a 525 nm LED with a photon flux of 5.81 $\times 10^{17}$ photons cm^{-2} s^{-1}. Error bars are determined from three devices each from three separate films. (b) Steady-state photoluminescence of neat and doped $MAPbI_3$ films. A substantial enhancement in PL intensity occurs for the 0.1 mg/mL doped $MAPbI_3$, consistent with passivation of surface traps.

determined by UPS given n~10^6 carriers/cm^3 with a mobility of 1 cm^{2}V^{-1}s^{-1} implies a conductivity of ~10^{-13} S/cm. This difference, however, can be explained by charge transfer from the underlying gold coated substrate reducing the charge carrier concentration in $MAPbI_3$.[191]

Evidence of surface conductance is provided by the trend of the dark conductivity of the doped samples in Figures 4.4(a) and S4.17. This trend follows a rise by orders of magnitude, a peak and fall in dark conductivity with the dopant concentration. The rise in dark conductivity with increasing dopant concentration can be explained by the apparent partial coverage of the dopant cast from solution with concentration of 0.1 and 0.2 mg/mL as seen in SEM micrographs (Figure 4.1(b)). The peak in dark conductivity occurs once full coverage of the dopant has been reached. This is inferred by the uniform appearance of the surface in SEM and AFM images (Figures 4.1(b) and S4.1). The measured conductivity of surface doped samples was stable over the period of several days when stored in a nitrogen glove box (Figure S4.18).

Temperature dependent measurements of the conductivity was performed in order to determine the transport mechanism for conduction in doped samples (Figure S4.19). An Arrhenius plot of temperature-dependent electrical conductivity measurements confirm that the conductivity of these polycrystalline films is thermally activated below 300 K, with activation energies determined by the Arrhenius expression for activated transport: $\sigma = \sigma_0 \times exp\left[\frac{-E_A}{k_B T}\right]$. For the neat $MAPbI_3$ film, a fit from 300 to 260 K gives an activation energy of E_A=290 meV. For the 1 mg/mL doped $MAPbI_3$ film, a fit from 300 to 230 K gives an activation energy of E_A=320 meV. Determining the relationship between conductivity and temperature over a wider range is prohibited by the high resistances of $MAPbI_3$ films. In

addition, the lower limit that would be possible would be near 160 K as a result of the tetragonal to orthorhombic phase transition of $MAPbI_3$.[195] The temperature range over which conductivity was measured is reasonable for understanding the conductivity close to operating conditions of solar cells. A similar measurement on neat $MAPbI_3$ was made by Pisoni et al, which showed an activation energy of E_A=185 meV between 320 to 250 K and E_A=70 meV below 250 K.[196] At higher temperatures, they attribute the barrier to thermal activation from impurity levels, and at lower temperatures to hopping conduction within the impurity level. We further expect differences in the activation energies based on grain size for in-plane measurements of films. Here, doping of $MAPbI_3$ results in a small, ~30 meV increase in activation energy. There are a variety of potential causes for this; one reason could be coulombic repulsion between electrons due to the high density of charge creating barriers to hopping at grain boundaries.[197]

We measured the photoconductivity to determine if the surface doped samples would show evidence of trap filling (Figure 4.4(a)). The photoconductivity was measured as a function of incidence fluence in our neat $MAPbI_3$ films using above band-gap light (525 nm) to vary the generation rate, *G*, to gain information about the recombination mechanism (Figure S4.20). We then measured the lateral photoconductivity of our doped samples at a *G* of ~10^{22} photons/cm^3s (comparable to solar generation rate), where the neat sample exhibits a combination of monomolecular (trapping) and bimolecular decay (electron-hole recombination). Trap-filling as a result of charge transfer at the surface should be observable since not all traps are filled by photo generated carriers at this fluence. We also examined the impact of light soaking and whether the samples exhibited persistent photoconductivity as controls to verify that the changes were not caused by non-idealities in the samples (Figure

S4.21 and Table S4.9). At moderate doping levels, such as samples doped by solutions with a dopant concentration of 0.1 mg/mL, the photoconductivity increases by an order of magnitude. At dopant concentrations above 0.2 mg/mL, the photoconductivity starts to decrease, causing it to be comparable and then below the neat photoconductivity. This decrease in photoconductivity begins as the dark conductivity begins to substantially increase. This suggests that the increase of the carrier concentration at the surface leads to additional recombination pathways after the surface traps are passivated. Steady-state photoluminescence (PL) is consistent with the explanation for the trend in photoconductivity (Figure 4.4(b)) where an increase in PL at a dopant concentration of 0.1 mg/mL is followed by a decrease at higher surface doping. The initial PL increase is similar to observations of the passivation of surface traps by treating with the Lewis base pyridine.[59] The fact that *n*-type doping passivates the surface suggests that moving the Fermi level towards the CBM fills trap states. In many computational and experimental studies, electron traps near the center of the band gap have been implicated as recombination centers.[10–14] We expect that surface doping could be a route to further elucidate the nature of these sites.

4.4 Conclusions

In summary, we have studied how electron transfer from the small molecule cobaltocene to the surface of $MAPbI_3$ changes its electronic properties. This results in surface conductance within the top few nm which can be tuned by the dopant surface coverage. Surface doping results in a gradual shift of the VBM away from the Fermi level illustrating that charge transfer doping allows for control over the interfacial energy levels. We find evidence for increased recombination at higher surface doping through photoconductivity and PL measurements.

These results can provide a basis for understanding the role of doping at more complex interfaces, e.g. those of $MAPbI_3$ and organic semiconductors, used in device applications.

Chapter 5

Systematic Study of the Impact of Doping Concentration of the Electron Transport Layer on Perovskite Solar Cell Performance

This concluding study investigates the effect of doping the electron transport layer (ETL) on perovskite solar cell performance. The doping concentration of the (ETL) was varied over three orders of magnitude (0.1 wt%, 1 wt% and 10 wt%) in order to understand the potential impacts of doping. Design considerations for achieving good polymer: dopant miscibility developed in Chapter 3 was utilized in the choice of PDI-2T as the ETL. This resulted in tunable electrical properties of PDI-2T. Solar cell performance showed an improvement upon doping followed by a deterioration, with a maximum at 1 wt% dopant. Observations about solar cell performance, such as the trend in V_{OC} and hysteresis, were consistent with the surface doping study, which indicated that surface passivation occurs at intermediate doping levels and degradation of the surface occurs at high doping levels. Further

evidence was present for charge transfer between doped PDI-2T to $MAPbI_3$ based on changes in electrical conductivity, energy levels and carrier lifetimes. These results suggest that the impacts of interfacial charge transfer should be considered when optimizing the doping concentration of the ETL.

5.1 Introduction

Perovskite solar cells (PSCs) have captured the focus of the photovoltaic research community due to their ease of fabrication and high power conversion efficiencies, now in excess of ~22%.[18] Electron transport layers (ETLs) play an important role in high performing PSCs by extracting photogenerated electrons from the perovskite and transporting these charges to electrodes.[5] There is a variety of factors that determine the final performance of an ETL, such as carrier mobility, resistance mismatch, energy level alignment, morphology, and ability to passivate the perovskite surface.[5] The remarkable performance of PSCs is not limited to any specific device architecture (conventional *n-i-p* or inverted *p-i-n*) or choice of material of the transport layers.[5] There is a wide range of potential ETLs that can be utilized, including inorganic materials such as ITO, FTO, TiO_2, and ZnO.[20] However, use of metal oxides as the ETL typically requires annealing at high temperatures,[198,199] which can be a hindrance to commercialization and prohibits use in flexible devices.[20] Alternatively, organic semiconductors are ideal candidates because of their low temperature processing (<150°C) and scalable fabrication.[5]

The major obstacle to the use of organic semiconductors as transport layers in PSCs is their low carrier mobility that may cause a parasitic series resistance that reduces the fill factor.[200] Carrier mobility is particularly important as the thickness of the ETLs increases,

which is an essential feature for low-cost fabrication. In inverted device architectures, where it is most common to use organic ETLs, it is essential to have sufficiently thick organic layers to avoid direct contact between the perovskite layer and the metal contact in order to prevent degradation.[2–4] In addition, industrial roll-to-roll processing is limited to organic layers of 100 to 300 nm.[6] In order to overcome transport issues, doping of organic transport layers is performed to passivate trap sites and increase the concentration of free carriers.[107,201] In addition to altering carrier mobility and electrical conductivity, doping of the organic semiconductor has been reported to impact several other factors that influence ETL performance, such as molecular contact at interfaces due to disrupted morphology from dopant aggregates,[49,50] and interfacial energetic alignment as a result of doping induced shifts.[15]

To date there has been little work on understanding how the presence of small molecule dopants can directly influence the perovskite active layer. Our group recently explored the impact of charge transfer doping on the surface properties of the hybrid halide perovskite methylammonium lead iodide ($MAPbI_3$).[201] In this study, we performed a surface doping study where the *n*-type small molecule dopant cobaltocene ($Co(C_5H_5)_2$) was deposited directly onto the surface of $MAPbI_3$.[201] This model system provides a means to understand the more complex heterointerface of doped organic blends at the perovskite surface. The major conclusion of this study was that the lack of surface states of $MAPbI_3$ enables charge transfer between small molecule dopants and the perovskite surface. This introduces additional considerations for the optimization of dopant concentration: intermediate degrees of charge transfer can be used to passivate deep electron traps, while high degrees of charge transfer introduce excess carriers that increase bimolecular recombination and cause degradation of

the $MAPbI_3$ surface.[201] The suggestion of surface passivation occurring as a result of doping the ETL was also made by Wang *et. al.*, who observed a decreased defect density in mixed halide perovskites measured with the trap density of states (tDOS).[106] Given this evidence of interfacial charge transfer, many studies of the effects of doping the ETL are providing an interpretation that may be an over simplification of the complexity of the ETL/$MAPbI_3$ interface.

There is a variety of *n*-type organic semiconductors that have been reportedly utilized as ETLs in PSCs. Fullerene derivatives such as PCBM ([6,6]-phenyl-C_{61}-butyric acid methyl ester), C_{60}, and $IC_{60}BA$ (Indene C_{60} Bis Adduct) are commonly employed because of their electron affinity, solvent processability and ability to passivate the perovskite surface.[48,63,64] Additionally, non-fullerene electron acceptors have been developed because of their unique advantages such as high absorption in visible range, tunable energy levels, and ease of synthesis.[105,202] There have been numerous studies on the effects of electrical doping of ETLs on the photovoltaic performance. Several of these doping studies have focused on fullerenes such as PCBM[15,21,49,50,203] and C_{60},[106] while others have investigated less common ETLs such as di-perylene diimide (diPDI),[105] or *c*-HATNA ((3,9,14-trifluorodiquinoxalino[2,3-a:2′,3′-c]phenazine −2,8, 15-trisulfinyl)tris(propane-3,1-diyl) tris(2-methylacrylate)).[107] Optimum power conversion efficiencies (PCEs) have been reported at doping compositions of 0.1 wt% to 1 wt%,[15,49,50,105,106] which we estimate to be a ratio of dopant to acceptor (or monomeric unit) of 10^{-2} to 10^{-3}. The improvements in performance upon doping were attributed to be the result of increased fill factor (FF) and short circuit current density (J_{SC}), and, in some cases, an increased open circuit voltage (V_{OC}). In all of these studies, the figures of merit (FF, J_{SC}, and V_{OC}) first increase and then decrease

with increasing dopant concentration.[15,49,50,105,106] The increase is attributed to improved electron mobility and conductivity, leading to better carrier transport in the ETL. The decrease is attributed to dopant aggregate formation the can decrease carrier mobility and disrupt molecular contact at the ETL/perovskite and ETL/electrode interfaces.[105,203]

In this report, we present a systematic study of how the doping concentration in an ETL affects the performance of $MAPbI_3$ solar cells. Doping concentrations of neat (0 wt%), 0.1 wt%, 1 wt% and 10 wt% were chosen because we believed orders of magnitude variations would best illustrate the potential impacts of doping. For our study we choose an ETL with the following characteristics: (1) a non-fullerene electron acceptor in order to make passivation effects as a result of charge transfer more easily observable and (2) a glassy polymer with good dopant/polymer miscibility in order to avoid dopant solubility limitations that occur in highly crystalline polymers such as P(NDI2OD-T2) **(**Poly{[*N*,*N*′-bis(2-octyldodecyl)-naphthalene-1,4,5,8-bis(dicarboximide) -2,6-diyl]-*alt*-5,5′-(2,2′-bithiophene)**)** .[101,204] For these reasons, we employ the polymer PDI-2T (Poly{[*N*,*N*′-bis-(10-nonadecyl)-perylene-3,4,9,10-tetracarboxylic diimide-1,7-diyl]-alt-(2,2′: 5′,2"-terthiophene-5,5′-yl)}), which has long sidechains that prevent crystallization and a high EA (Figure 5.1) (Supporting

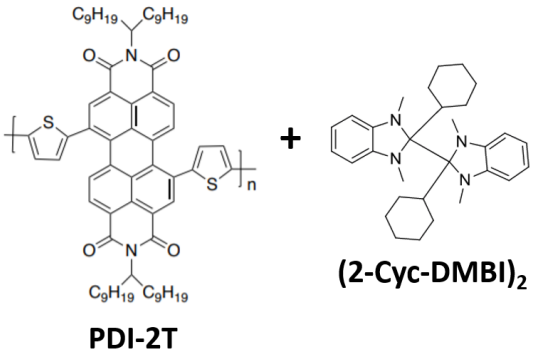

Figure 5.1 Chemical structure of PDI-2T and $(2\text{-Cyc-DMBI})_2$. The long sidechains of PDI-2T leads to glassy structuring. $(2\text{-Cyc-DMBI})_2$ is a dimer dopant that undergoes a charge transfer reaction.

Information Figure S5.1). We chose an *n*-type dopant with high solubility and efficient charge transfer to PDI-2T. The dimeric dopant, $(2\text{-Cyc-DMBI})_2$ (Figure 5.1), fit these requirements with the additional benefit of air stability prior to central bond cleavage.[205,206] Our results show tunable electrical properties of PDI-2T upon doping with (2-Cyc-DMBI_2), indicating good miscibility of the polymer and dopant.

5.2 Results and Discussion

5.2.1 Electronic Properties of Electrically Doped PDI-2T

In order to understand the characteristics of the PDI-2T/$MAPbI_3$ interface, it is helpful to consider the doping mechanism of PDI-2T by $(2\text{-Cyc-DMBI})_2$. PDI-2T was doped in solution by $(2\text{-Cyc-DMBI})_2$ prior to casting on the surface of thin films of $MAPbI_3$ (See Supporting Information for Experimental Details). Small molecules dopants can either undergo charge transfer with organic semiconductors in solution or upon incorporation into thin films. The latter mechanism could also enable direct charge transfer from small molecules dopants to the perovskite surface. The possibility of direct charge transfer between $(2\text{-Cyc-DMBI})_2$ and $MAPbI_3$ was confirmed with surface doping. However, steady-state photoluminescence shows that $(2\text{-Cyc-DMBI})_2$ splits and undergoes charge transfer with PDI-2T in solution (Supporting Information Figure S5.2-S5.3), similar to the doping mechanism reported for organometallic dimers.[98] Because the reaction in solution will prevent direct doping of $MAPbI_3$ by (2-Cyc-DMBI_2), we expect that charge transfer between the ETL and $MAPbI_3$ would occur via Fermi level equilibration with the doped organic semiconductor.

The electrical conductivity and carrier concentration of neat films of PDI-2T was tunable by changing the concentration of $(2\text{-Cyc-DMBI})_2$ in the casting solution. The

conductivity of neat PDI-2T (<10^{-6} S/cm) increases upon doping to ~10^{-5}, ~10^{-4} and ~10^{-3} S/cm for 0.1 wt%, 1 wt% and 10 wt% concentrations of $(2\text{-Cyc-DMBI})_2$ respectively. The spin concentration detected by EPR in the solid state was $9\pm3\times10^{19}$ and $1\pm0.1\times10^{21}$ spins/cm^3 respectively for 1 wt% and 10 wt% dopant films, (Supporting Information). Consistent with studies on other heavily doped systems, the carrier concentrations of 1 wt% and 10 wt% dopant films equates to a ~1:10 and ~1:1 spins: monomer unit ratio (Supporting Information), respectivly.[104,204] The carrier concentration of neat and 0.1 wt% dopant films were below the threshold of the EPR apparatus of ~10^{18} spins/cm^3.

The impact of doping on the energy levels of PDI-2T was investigated with Ultraviolet and Inverse Photoelectron Spectroscopy (UPS & IPES). UPS measurements were performed using a H Lyman-α source (10.2 eV) that limits degradation of organic materials during spectra collection.[117] We assigned neat PDI-2T an ionization energy (IE) and electron affinity (EA) of ≈6.1 eV and ≈4.0 eV respectively assigned based on features related to the HOMO

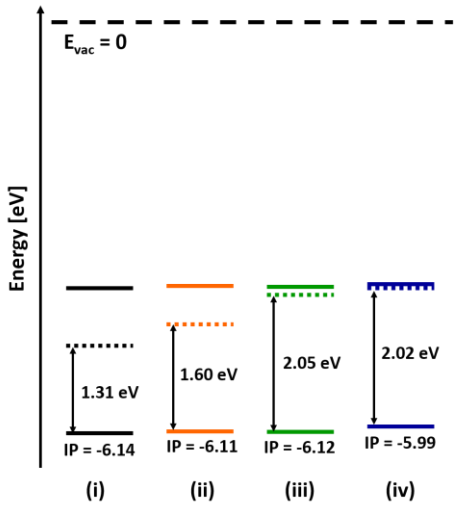

Figure 5.2 Energy levels of PDI-2T measured using UPS, which shows a gradual shift of the Fermi level towards the LUMO level with increasing dopant concentration. The dopant concentrations studied are denoted as: (i) neat PDI-2T, (ii) 0.1 wt% dopant, (iii) 1 wt% dopant, and (iv)10 wt% dopant.

and LUMO levels (Figure 5.2)(Supporting Information). The Fermi level shows a gradual shift toward the LUMO level with increasing dopant concentration. By 10 wt% dopant, the Fermi level shift is large enough that PDI-2T is a degenerate semiconductor and sub-gap states are observed by UPS (Supporting Information). These shifts are consistent with the high carrier concentrations observed by EPR.

High doping concentrations were observed to alter the morphology of PDI-2T films. Atomic force micrographs (AFM) (Figure 5.3(a)) of PDI-2T films on quartz suggest that while there is good miscibility for PDI-2T with 0.1 wt% and 1 wt% dopant, the morphology of the film with 10 wt% dopant appears to have undergone a phase separation, similar to that of other

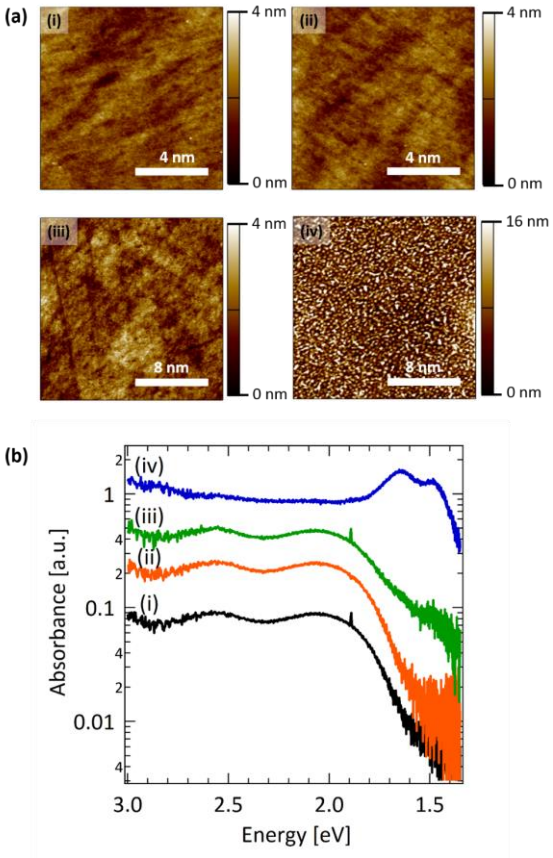

Figure 5.3 (a) AFM micrographs of PDI-2T films, indicating phase separation of the dopant at high concentrations. (b) Optical absorption of PDI-2T films, confirming heavy doping at 10 wt%. The dopant concentrations studied are denoted as: (i) neat PDI-2T, (ii) 0.1 wt% dopant, (iii) 1 wt% dopant, and (iv) 10 wt% dopant.

polymers.[101] This observation is consistent with optical absorption spectra of PDI-2T films given in Figure 5.3(b) (and Supporting Information S5.4). At low doping concentration there is a neutral polymer transition at ~2.0 eV with limited bleaching upon doping for the 0.1 wt% and 1 wt% dopant films. For the 10 wt% dopant film, the neutral polymer peak has been completely bleached and a new transition has emerged at 1.6 eV. This corresponds to heavy doping on the polymer. Based on AFM, it is apparent that there is a large amount of dopant that has infiltrated the polymer matrix at this doping concentration. The emergence of this transition may also be present at 1 wt% dopant. The phase separation of the dopant and polymer is important because it can impede contact of PDI-2T with the metal electrode and/or $MAPbI_3$.

5.2.2 Solar Cell Device Characteristics

The use of PDI-2T as the ETL in inverted PSCs showed distinct performance differences with varying dopant concentration, which is illustrated in the *J-V* characteristics (Figure 5.4) (Supporting Information Figures S5.5-5.8). A schematic of the solar cell device is given in Figure 5.5(a). For doping concentrations of the ETL solution of 0 wt% (neat), 0.1 wt%, 1 wt% and 10 wt%, the power conversion efficiencies (PCEs) were 0.6, 3.8, 8.3, and 3.2 % respectively (Table 5.1). The low PCEs obtained for these devices is attributed to relatively thick ETL layers (~190 nm) leading to low FFs. The thick layers were employed to ensure surface coverage over $MAPbI_3$ films with surface roughness of ~± 20 nm and to imitate thicknesses compatible with roll-to-roll processing[6] (Figure 5.5(b) and Supporting Information Figure S5.5). In contrast, high performance devices with inverted architecture with PCEs >17% typically have organic ETLs with thicknesses of less than 40 nm.[207–209]

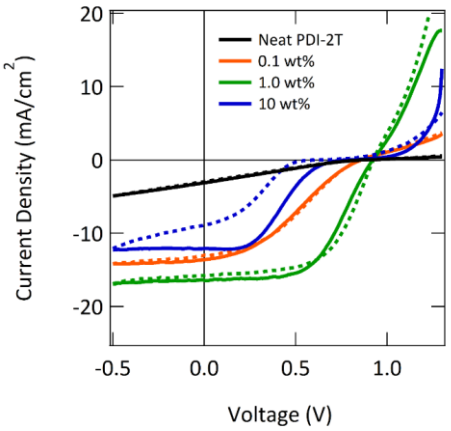

Figure 5.4 Current density-Voltage (J-V) characteristics of $MAPbI_3$ solar cells with ETLs of PDI-2T with varying doping concentration. See Supporting Information Figure S6 for zoomed in plots around the J_{SC} and V_{OC}.

Table 5.1 Extracted performance parameters including V_{OC}, J_{SC}, FF and PCE of the *J-V* curve from the reverse scan (1.3 to -0.5 V) denoted as solid lines.

ETL	Voc (V)	Jsc (mA/cm^2)	FF (%)	PCE %
Neat	0.85	2.1	24	0.6
0.1 wt%	0.85	13.6	36	3.8
1 wt%	0.91	16.4	55	8.3
10 wt%	0.77	12.1	34	3.2

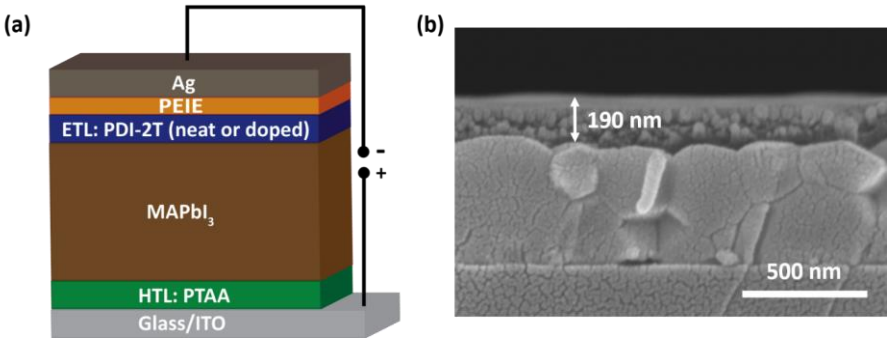

Figure 5.5 (a) Solar cell device with inverted architecture of Glass/ITO/PTAA/$MAPbI_3$/PDI-2T (neat or doped with $(2\text{-Cyc-DMBI})_2$)/PEIE/Ag (b) Cross sectional SEM of PDI-2T:$MAPbI_3$ bilayer on quartz showing the thickness of the ETL layer used in solar cell devices.

All of the figures of merit, including short circuit current density (J_{SC}), open circuit voltage (V_{OC}), and fill factor (FF), show a roll over in performance with a maximum at 1 wt% dopant. The changes in performance upon doping can be attributed to a combination of changes that arise as a result of a non-ideal contacts: charge transport losses, charge injection losses, interfacial recombination, and degradation of the interface.[210] We examine the impact on doping for each component of the *J-V* curve in turn.

Because doping of PDI-2T increases its electrical conductivity, we expected that doping would decrease the series resistance of the thick ETL layer. The solar cell with an ETL of neat PDI-2T shows very low J_{SC} and FF, which we attribute to the high resistance of neat PDI-2T ($\sigma < 10^{-6}$ S/cm). Upon doping, the performance of the J_{SC} and V_{OC} dramatically improves, as shown in Table 5.1 indicating an improvement with doping followed by a deterioration. For doping concentrations of 0.1 wt% and 10 wt%, the *J-V* curve shows a 'global' S-shaped behavior. Such features can be attributed to charge accumulation as a result of energy barriers or poor charge transport in the ETL. Because the electrical conductivity of PDI-2T is still $\sim 5\times10^{-4}$ S/cm at 10 wt% dopant, we attribute the lower performance to dopant aggregate formation (as observed by AFM in Figure 5.3(a)). This is expected to impede charge transfer at the PDI-2T/$MAPbI_3$ or PDI-2T/Ag interfaces.

The V_{OC} also shows improvement with doping followed by a deterioration with a maximum at 1 wt%. Control over V_{OC} involves considerations of both energy level alignment and surface recombination.[210] Theoretical calculations suggest that the band offset between the ETL and perovskite should be 0.0-0.3 eV in order to achieve high FF and V_{OC}.[211] The EA of PDI-2T of ~ 4.0 eV suggests that the ETL should provide efficient extraction of photogenerated electrons from $MAPbI_3$, which also had a measured EA of ~ 4.0 eV. If the

primary cause for the change in V_{OC} is a consequence of surface recombination, the results are consistent with our previous surface doping study of $MAPbI_3$ that showed that a small amount of added electrons could passivate trap levels, while increasing concentration resulted in degradation of the surface and bimolecular recombination.[201]

Hysteresis of the *J-V* characteristics is observable at 10 wt%. Hysteresis has previously been attributed to redistribution of mobile ionic charge and recombination near the ETL/$MAPbI_3$ interface.[212–215] Structural damage as a result of the high concentrations of additional charge was seen in the surface doping study, which was likely a result of mobile I^- ions that were released by chemical damage to the $MAPbI_3$ surface.[201]

5.2.3 Interfacial Charge Transfer between PDI-2T and $MAPbI_3$

The performance of solar cells using thick layers of doped PDI-2T as an ETL shows that the series resistance is reduced upon doping, but there are effects related to charge transfer from the ETL to the $MAPbI_3$ surface. In our surface doping study of $MAPbI_3$, we found that charge transfer doping can be used to passivate surface traps. However, at very high surface concentrations of dopants, the surplus charge introduced an additional pathway for recombination of photogenerated carriers. Here, we examine how equilibration of charge between the ETL and $MAPbI_3$ produces similar effects.

As a measure of charge transfer between PDI-2T and $MAPbI_3$, we examined the lateral electrical conductivity of PDI-2T/$MAPbI_3$ bilayers (Figure 5.6) (Supporting Information). Because transport in polymers is frequently anisotropic, measurement of the electrical conductivity in the direction of transport is desirable. However, we were unable to carry out transport measurements in-plane, as the electrical conductivity was below measurable limits

using our 4-probe system. In a lateral measurement, the conductivity of the layers can be considered to be electrically in parallel. Therefore, we can examine the net conductivity in the limit that only the PDI-2T is conductive, as well as the limit that charge is evenly distributed across the bilayer. We estimate the thickness of the PDI-2T films from cross-sectional SEM and calculate the conductivity based on the two assumptions (Supporting Information Figure S5.9). Regardless of model, there is a drop in conductivity of PDI-2T on $MAPbI_3$ compared to quartz. This change could potentially be a result of the underlying roughness of the perovskite surface (Supporting Information Figure S5.9-S5.10) causing scattering of carriers in the PDI-2T layer.[216,217] We found that surface doping with $MAPbI_3$ films with $(2\text{-CYC-DMBI})_2$ gave an electrical conductivity of $\sim 10^{-6}$ S/cm which is similar to the bilayer of 1 wt% PDI-2T/$MAPbI_3$ (Supporting Information S5.11). This gives a bound for the electrical conductivity of films of MAPbI3.

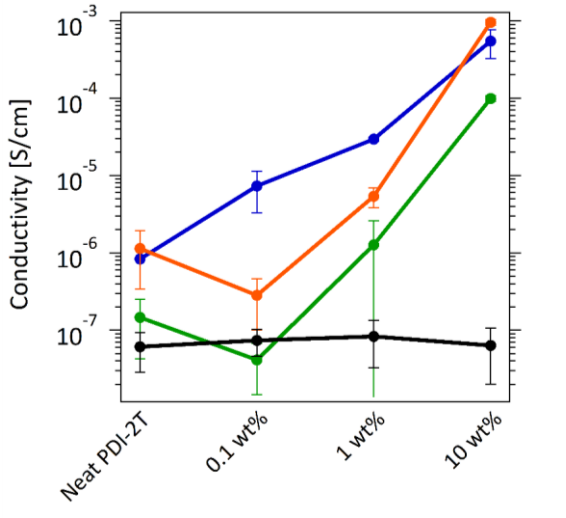

Figure 5.6 Lateral conductivity of PDI-2T and for varying doping concentrations. Curves correspond to (blue) PDI-2T on quartz, (orange) PDI-2T on $MAPbI_3$ calculated assuming thickness of the PDI-2T layer, (green) PDI-2T on $MAPbI_3$ calculated assuming thickness of the bilayer, (black) $MAPbI_3$ prior to ETL deposition to control for film-to-film variation. For comparison, conductivity values from the surface doping study were $\sim 10^{-6}$ S/cm for full dopant coverage.

Charge transfer between the ETL and $MAPbI_3$ will occur due to Fermi level equilibration between the semiconductors. Consequently, the Fermi level of PDI-2T measured using UPS should vary when assessed on top of $MAPbI_3$ versus in single layer films (Figure 5.7(a)) (Supporting Information Figure S5.12-S5.15). The energy levels of bare $MAPbI_3$ are also provided for comparison of the Fermi level position (VBE= -0.83 for both linear and semi-logarithmic fits) (Supporting Information Figure S5.16-S5.18). When measured in isolation, PDI-2T showed a gradual shift of the Fermi level towards the LUMO level with increasing dopant concentration, consistent with *n*-type doping. Whereas in the PDI-2T/$MAPbI_3$ bilayer, measurement of the Fermi level of neat, 0.1 wt%, and 1 wt% dopant PDI-2T occurs at roughly the same position in the bandgap (VBEs are -1.86, -1.83 and -1.76 eV respectively) within the margin of error for the UPS apparatus (±0.05 eV). In the surface doping study, the Fermi level

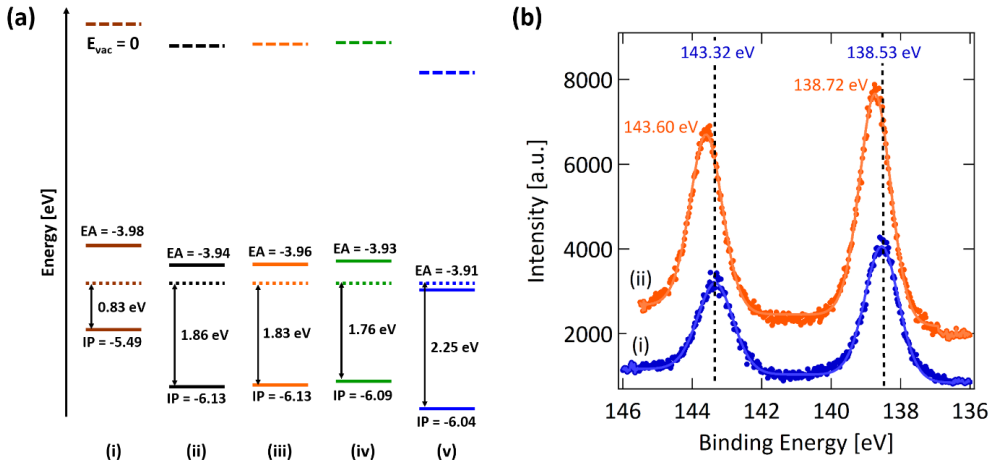

Figure 5.7 (a) Energy levels of PDI-2T in the ETL/$MAPbI_3$ bilayer measured using UPS and IPES. Films are denoted in the figure according to (i) bare $MAPbI_3$, (ii) PDI-2T (neat)/$MAPbI_3$, (iii) PDI-2T (0.1 wt% dopant)/$MAPbI_3$, (iv) PDI-2T (1 wt% dopant)/$MAPbI_3$, and (v) PDI-2T (10 wt% dopant)/$MAPbI_3$. (b) Binding energy positions of Pb 4f peaks measured using XPS of (i) bare $MAPbI_3$ versus (ii) $MAPbI_3$ with partial coverage of PDI-2T (1 wt% dopant), which shows a shift towards higher binding energy upon deposition of the doped ETL that indicates downward band bending of $MAPbI_3$ at the interface.

change of $MAPbI_3$ between dopant coverages that resulted in trap passivation and increased bimolecular recombination also occurred within a narrow range of 0.16 eV.[201]

It was challenging to develop an understanding of band bending and dipole formation at the interface; Control over the thickness of PDI-2T layers for which band bending occurs (0 to 30 nm) was not possible due to the $MAPbI_3$ surface roughness of ± 20 nm (Supporting Information Figure S5.10). To confirm charge transfer via Fermi level equilibration, it was important to find an alternative means of probing interfacial energy levels. For a doping concentration of 1 wt%, PDI-2T was deposited onto the $MAPbI_3$ surface at low concentration (0.5 mg/mL) that resulted in partial coverage of the surface (Supporting Information Figure S5.19), which allowed the perovskite surface to still be accessible via X-ray photoelectron spectroscopy (XPS). XPS shows shifts in the peak positions of Pb 4f and I 3d orbitals by ~0.2 eV towards higher binding energy, indicating downward band bending of the $MAPbI_3$ surface (Figure 5.7(b) and Supporting Information Figure S5.20). This result was similar to the shift of the Pb 4f peak by ~0.3 eV for direct doping of the surface by cobaltocene,[201] suggesting the shift seen here is not likely due to degradation of the surface leading to PbI_2 formation. To put this observation into context for how band bending would alter interfacial energy levels, a shift in Fermi level of $MAPbI_3$ by ~0.2 eV (from a VBE =0.83 eV to 1.03 eV) would be within the range of that seen in the surface doping study between the neat $MAPbI_3$ (VBE = 0.82 eV) and $MAPbI_3$ with partial dopant surface coverage (VBE = 1.28 eV),[218] indicating that this doping concentration leads to a degree of charge transfer that passivates deep electron traps that occur roughly around mid-gap.

Carrier lifetimes extracted from time-resolved photoluminescence (TR-PL) of the PDI-2T/$MAPbI_3$ bilayers (Figure 5.8 and Supporting Information Figure S5.21-S5.23) can provide information simultaneously about the degree of recombination occurring in perovskite, and the ability of the ETL to extract photogenerated electrons. The ability of the ETL to extract photogenerated electrons from $MAPbI_3$ is influenced by several factors, including interfacial energy alignment, molecular contact of $MAPbI_3$ and the ETL, and the ability of PDI-2T to accept additional charge. The alignment of LUMO level of PDI-2T to the conduction band of $MAPbI_3$ suggests efficient electron transfer across the interface. For high doping concentrations, disruption of molecular contact may be relevant as a result of dopant aggregates that hinder extraction of photogenerated charge carriers by being electrically insulating. The ability of PDI-2T to accept photogenerated charge carriers is determined by the fraction of monomers that are already accommodating charge created upon doping.[23,27]

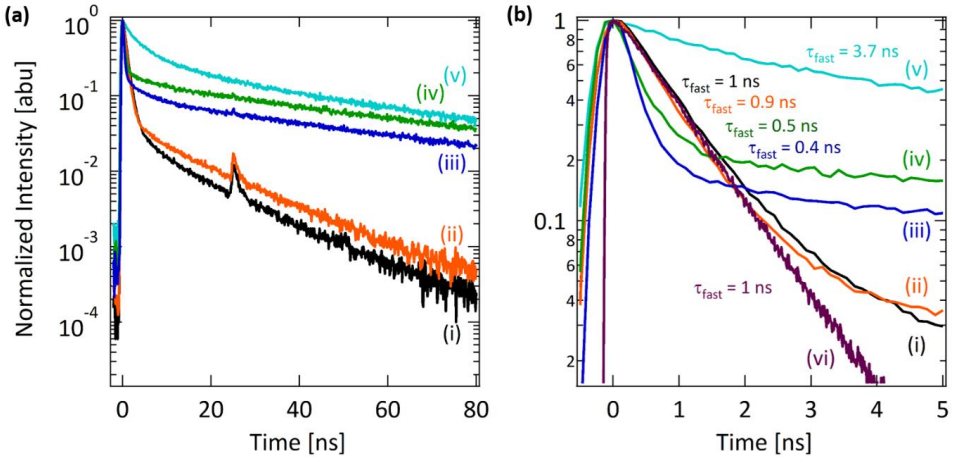

Figure 5.8 (a) Time resolved photoluminescence (TR-PL) of PDI-2T films on MAPbI3 denoted as (i) PDI-2T (neat)/$MAPbI_3$, (ii) PDI-2T (0.1 wt% dopant)/$MAPbI_3$, (iii) PDI-2T (1 wt% dopant)/$MAPbI_3$, and (iv) PDI-2T (10 wt% dopant)/$MAPbI_3$, (v) bare $MAPbI_3$ and (vi) neat PDI-2T on quartz. Spectra were measured using a 410 nm excitation and 770 nm collection light at energy density of 0.15 uJ/cm^2, which assuming an absorption coefficient of ~1.5×10^5 at 410 nm corresponds to a charge density of 6.9×10^{15} cm^{-3}. Spectra were collected such that light entered the film from the PDI-2T layer.

The trend in carrier lifetime with increasing doping concentration of PDI-2T on $MAPbI_3$ can be explained by the competing influence of these factors. All PDI-2T/$MAPbI_3$ bilayers demonstrate lower carriers lifetimes than pristine $MAPbI_3$, indicating extraction of photogenerated carriers. Low doping concentrations of neat and 0.1 wt% dopant result in fast extraction of photogenerated electrons from $MAPbI_3$. This result is reasonable given UPS suggests favorable energy level alignment and only a small fraction of PDI-2T monomer units are already accommodating additional electrons. High doping concentrations of 1 wt% and 10 wt% dopant exhibit a separate trend with longer carrier lifetimes. Electron paramagnetic spectroscopy (EPR) indicates that PDI-2T is heavily doped at 1 wt% and 10 wt% dopant with carrier concentrations of ~10^{20} and ~10^{21} spins/cm^3 respectively, which correspond to between a 1:1 and 1:10 spin: monomer unit ratio.[104,204] Given that most monomers units already contain charge, they are less able to accept photogenerated electrons from $MAPbI_3$. Challenges to extraction of photogenerated carriers that become more prevalent with higher doping concentration, such as an inability to accept additional charge and the presence of dopant aggregates, would suggest that the carrier lifetime of 10 wt% dopant should be the higher than 1 wt% dopant. This is not the case, suggesting the differences in carrier lifetime between 1 wt% and 10 wt% dopant are also influenced by recombination in $MAPbI_3$. The observed trend can be explained by either reduced trap assisted recombination in 1 wt% dopant or increased bimolecular recombination in 10 wt% dopant. This observation is consistent with the surface doping study which showed that intermediate degrees of charge transfer can be used to passivate deep electron traps, while high degrees of charge transfer introduce excess carriers that increase bimolecular recombination and cause degradation of the $MAPbI_3$ surface.

Direct quantification of the surface recombination of 1 wt% and 10 wt% dopant in the PDI-2T/$MAPbI_3$ bilayer can be made using carrier lifetimes. The TR-PL spectra were fit using a biexponential decay, which incorporates a fast decay time component associated with recombination behavior at the surface, and a slow decay time component associated with recombination in the bulk (Supporting Information Figure S5.21). Steady-state photoluminescence (SS-PL) of PDI-2T films showed signal due to the perylenediimide unit[219] which is quenched upon doping with $(2\text{-Cyc-DMBI})_2$ (Supporting Information Figure S5.2). Consequently, the short decay component of neat and 1 wt% dopant in the PDI-2T/$MAPbI_3$ bilayer is dominated by photoluminscent decay of PDI-2T, resulting in a mono exponential fit of 1 ns. By 1 wt% dopant, this signal is quenched, allowing the fast component of PL decay attributed to surface recombination to be directly quantified. The fast decay lifetimes for 1 wt% and 10 wt% dopant in the PDI-2T/$MAPbI_3$ bilayer are 0.5 ns and 0.4 ns respectively, suggesting that the degree of charge transfer has altered recombination at the $MAPbI_3$ surface.

In other studies that investigated charge extraction of doped ETL/perovskite bilayers, the factor with the greatest influence on carrier lifetimes varied based on the characteristics of the ETL.[15,106,203] Consistently, lower carrier lifetimes were reported for optimally doped ETLs as a result of faster extraction.[15,203] For bis-PCBM, this is attributed to doping induced shifts that create improved energetic alignment to $MAPbI_3$.[15] Whereas for mono-PCBM, which does not experience improved energetic alignment upon doping due to its deeper LUMO, faster extraction upon doping is attributed to improved electron transport and smoother films.[203] Wang et al. reported a trend in carrier lifetime with increasing doping concentration of C_{60}, showing the fastest quench for the optimal doping concentration of 1 wt% dopant, with

slower extraction for 5 wt% and 10 wt% dopant due to the either the formation of dopant aggregates or the ETLs diminished ability to accept additional electrons.[106] Here, neat PDI-2T is able to show more efficient extraction because of its favorable energy level alignment to $MAPbI_3$ and high ability to accept photogenerated charge. This illustrates how other factors, such as carrier transport and surface passivation, are important for solar cell performance. In contrast to other studies, the longest carrier lifetime was observed for the optimal doping concentration of 1 wt%, which we attributed to passivation of surface traps. This may play an important role in its improved solar cell performance as trap-assisted recombination at material interfaces is the dominant recombination channel limiting device performance.

5.3 Conclusions

In summary, we performed a systematic study of doping concentration of an organic electron transport layer on the performance of perovskite solar cells. We previously developed several design considerations based on a surface doping study, which indicated that intermediate degrees of charge transfer can be used to passivate deep electron traps, while high degrees of charge transfer introduce excess carriers that increase bimolecular recombination and cause degradation of the $MAPbI_3$ surface.[201] The performance of solar cells and the electronic behavior of the PDI-2T/$MAPbI_3$ bilayer was consistent with these observations, which was illustrated by increased V_{OC}, downward band bending of the $MAPbI_3$ surface, and the trend in carrier lifetime with ETL doping concentration. A more broad consequence of studying the impact of doping the ETL (PDI-2T), is that if initially a low PCE is observed despite reasonable energy alignment to $MAPbI_3$, then doping should be utilized to further gauge an organic semiconductor's potential performance.

Appendix A

Supporting Information for

Chapter 3: *N*-doping of a Non-Planar Ambipolar Semiconducting Polymer Illustrating Improved Polymer: Dopant Miscibility

Table of Contents

I. General Procedure for the Synthesis of P(BTP-DPP)

The monomer and polymer synthesis followed a similar procedure reported by the authors.[1] In brief, the polymer was synthesized using a mixture of stannylated biindeno[2,1-b]thiophenylidene (BTP-Sn) (80 mg, 0.12 mmol), 3,6-bis(5-bromothiophen-2-yl)-2,5-diicosylpyrrolo[3,4-c]pyrrole-1,4(2*H*,5*H*)-dione (122 mg, 0.12 mmol), Pd_2dba_3 (7 mg, 0.006 mmol) and P(*o*-tol)$_3$ (7.4 mg, 0.024 mmol) The mixture was then flushed with Ar for 5 min and sealed before 2 ml of degassed anhydrous chlorobenzene was added using a syringe. The reaction mixture was then stirred at 145 °C for 24 h. At the end of reaction, the mixture was allowed to cool down to room temperature and was then added dropwise to methanol (20 ml) with stirring. The solid was collected through filtration and subjected to Soxhlet extraction. After being thoroughly washed by acetone and hexane, respectively, the purified polymer was extracted by hot chloroform in the same setup and collected in a round bottom flask. The solution was concentrated and added slowly to methanol to form a dark-purple to black solid. P(BTP-DPP) was then dried in vacuum overnight (105 mg, 72% yield).

Three batches of P(BTP-DPP) were used in this study. GPC at room temperature with chloroform as the eluent and polystyrene as the reference gave the following characteristics for each batch:

- Batch 1: M_n = 62.0 kDa, M_w = 130 kDa, PDI = 2.11
- Batch 2: M_n = 42.3 kDa, M_w = 114 kDa, PDI = 2.70
- Batch 3: M_n = 27.0 kDa, M_w = 49.5 kDa, and PDI = 1.83

II. Substrate Preparation

Several types of substrates, measuring 1.5 cm × 1.5 cm, were used for these experiments: quartz, sapphire, and intrinsic silicon wafers with native oxide or a 200 nm thermal SiO_2. All substrates were cleaned in an ultrasonic bath in water, acetone and isopropanol for 20 minutes then treated with an oxygen plasma for 120 seconds.

III. Electrical Conductivity Measurements

Conductivity values were measured using a four-point probe method. Gold contact pads were deposited onto films using a shadow mask in a thermal evaporator in a collinear geometry with 100 µm spacing between electrodes that were 500 µm wide. Conductivity values reported were calculated using the following equation for conductivity of thin layer samples measured using a four point measurement where *I* is the current, *V* is the measured voltage and *d* is the film thickness:[220]

$$\sigma = \frac{I}{V}\frac{1}{d}\frac{\ln[2]}{\pi} \qquad \text{S3.1}$$

This approximation is accurate if the film thickness is less than one half the needle distances which is satisfied because of the thickness of films (≈40 nm) and the distance between probes (500 µm).

The electrical conductivity of doped samples of P(BTP-DPP) was dependent on the molecular weight of the polymer. The electrical conductivity of sequentially processed samples was measured using Batch 1 (M_n = 62.0 K) and the values are given in Figure 3.2 and Table S3.2. Conductivity measurements performed with batches with lower molecular weight showed lower conductivity. The difference in performance of electrical conductivity of sequentially cast versus blend casted films was performed using Batch 2 (M_n = 42.3 K).

Conductivity of sequential and blend casted films were compared at the optimal dopant concentration of 0.55 monomeric dopants to repeat unit, and produced values of $9.45 \times 10^{-2} \pm 2 \times 10^{-6}$ S/cm and $1.41 \times 10^{-2} \pm 3 \times 10^{-6}$ S/cm respectively. These conductivity values are reported for a single sample taken at three different film locations.

Table S3.1 Electrical conductivity of P(BTP-DPP) sequentially doped with $(RuCp^*mes)_2$. Conductivity values are reported for three separate regions on the same film. However, if a device's conductivity was below measurable limits, then its value was not included in the calculation. Thus a standard deviation of N/A means that only one device was measured at that concentration.

Monomeric Dopant per Repeat Unit determined by XPS	Conductivity [S/cm]	Standard Deviation [S/cm]
0.15	0.023	2×10^{-4}
0.37	0.43	.1
0.55	0.45	0
0.77	0.34	0.07
0.92	0.0016	3×10^{-4}
1.19	0.007	9×10^{-4}
1.43	0.0012	N/A

IV. Roughness of Films from Atomic Force Microscopy

An Asylum MFP-3D atomic force microscope was used to measure the topography of films cast on X substrates.

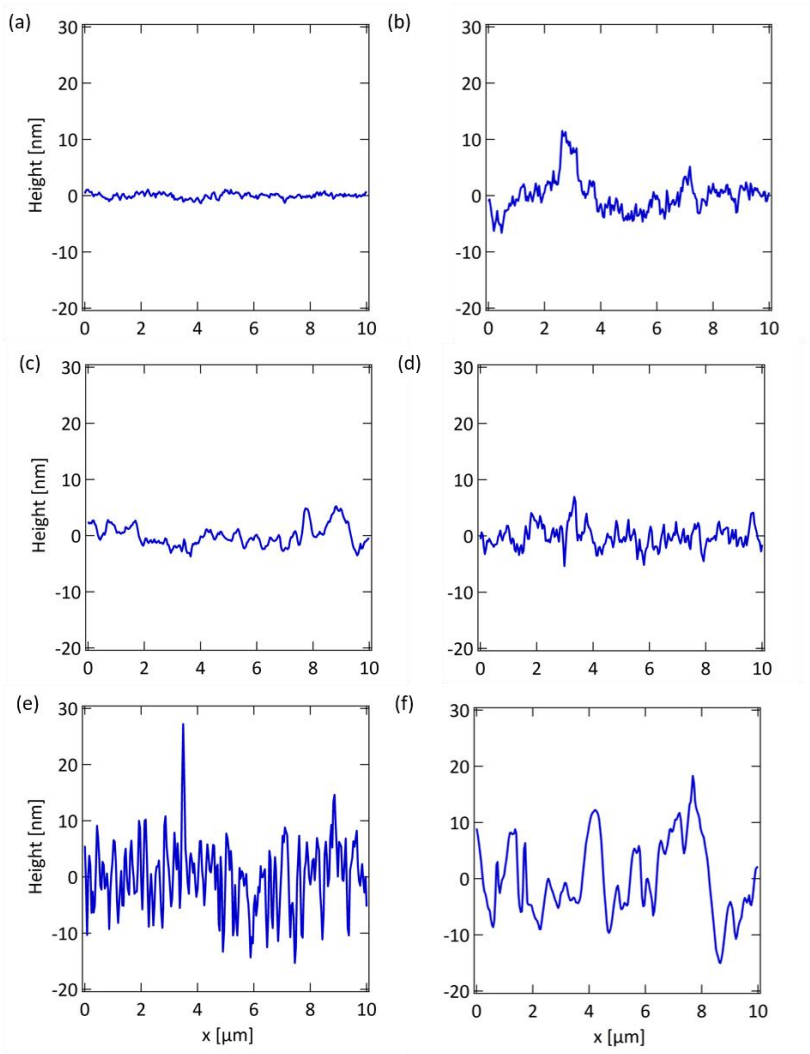

Figure S3.1 Example cross-sectional height profile extracted from AFM images indicating film roughness. (a) neat film, (b) 0.15 monomeric dopants per repeat unit, (c) 0.37 monomeric dopants per repeat unit, (d) 0.55 monomeric dopants per repeat unit, (e) 0.77 monomeric dopants per repeat unit and (f) 0.92 monomeric dopants per repeat unit.

V. Characterization by X-Ray Photoemission Spectroscopy

X-ray and ultraviolet photoelectron spectroscopy (XPS and UPS) was carried out on a Kratos Axis Ultra XPS/UPS instrument. The films were cast on a gold coated 10 × 10 mm crystalline silicon substrate (80 nm of gold with a 20 nm of chromium adhesion layer deposited by thermal evaporation). Films of P(BTP-DPP) were then spin-cast onto the substrates. The semiconducting film was removed from one edge of the sample by swabbing with chlorobenzene to expose the underlying gold layer. Nickel tape was used to electrically connect the exposed gold on the top of the substrates to the airtight sample holder in order to prevent charging. For XPS, a monochromated Al-Kα source (180 W) was used under ultrahigh vacuum conditions (10^{-7} Torr). Survey scans were collected with a step size of 0.5 eV, a pass energy of 160 eV, and a dwell time of 100 ms.

XPS was performed in order to evaluate the concentration of $(RuCp^*mes)_2$ that was incorporated into the film within approximately the top 10 nm of the film (total film thickness is ~40 nm). There is finite roughness on the surface due to dopant aggregates. Therefore, there is some uncertainty in the bulk concentration. XPS was performed on samples of 0.15, 0.37, 0.77 and 0.92 monomeric dopants per repeat unit. The weight percentage of the dopant incorporated into the film was determined by comparing the ratio of the atomic percent of the Ru $3d_{5/2}$ peak to the S 2p peak. This calculation assumes that the concentrations present at the top 8 nm of the film surface (i.e. the XPS penetration depth) are similar to those in the bulk.

The following equation was used to calculate monomeric dopant per repeat unit given the atomic percent of Ru and S determined from the integrated intensity (I) of Ru $3d_{5/2}$ peak and the S 2p peak and corrected for the stoichiometry of 4 S atoms per P(BTP-DPP) monomer and 1 Ru atom per RuCp*mes unit.

$$\frac{I_{Ru\ 3d_{5/2}}}{I_{S\ 2p}} \times \frac{4\text{ S atoms}}{1\text{ monomer of P(BTP-DPP)}} = \frac{\#\text{ of RuCp*mes}}{\text{monomers of P(BTP-DPP)}} \equiv \frac{\#\text{ carriers}}{\text{monomer of P(BTP-DPP)}}$$

Given monomeric dopants per repeat unit it is also possible to calculate the weight percent RuCp*mes in the film using the following equation.

$$\frac{\text{Molar Mass of RuCp*mes}}{\left(\text{Molar mass of P(BTP-DPP) monomer} \times \frac{\#\text{ monomers P(BTP-DPP)}}{\#\text{ of RuCp*mes}}\right) + \text{Molar Mass of RuCp*mes}}$$

$$= \text{Weight Percent of RuCp*mes}$$

Monomeric dopant per repeat unit and Weight percent RuCp*mes is summarized in Table S3.2.

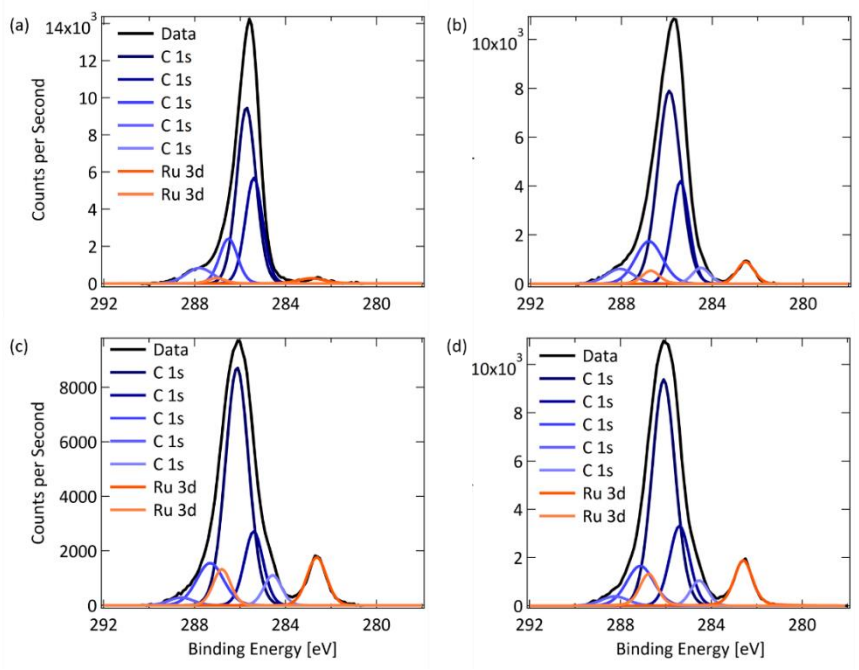

Figure S3.2 XPS spectrum of P(BTP-DPP) doped at a) 0.15 monomeric dopant per repeat unit, b) 0.37 monomeric dopant per repeat unit, c) 0.77 monomeric dopant per repeat unit, and d) 0.92 monomeric dopants per repeat unit. Ruthenium $3d_{5/2}$ peaks are symmetrically shaped, and at a BE which is consistent with where $[RuCp^*mes]^+$ has previously been observed. This suggests that the doping efficiency, defined here as the efficiency of electron transfer to the host semiconductor, of $(RuCp^*mes)_2$ is near 100%.

Table S3.2 Atomic percent Sulfur and Ruthenium as determined by XPS and corresponding monomeric dopant per repeat unit and weight percent RuCp*mes in films. For dopant solution concentrations not measured using XPS denoted by *, the natural logarithm relationship given in the last section was used to approximate weight percent.

Dopant Solution Concentration [mg/ml]	Sulfur Atomic %	Ruthenium Atomic %	Monomeric dopants per repeat unit	Weight Percent RuCp*mes
Neat	5.83	0	--	0
0.05	4.88	0.18	0.15	4.2
0.1	4.48	0.41	0.37	9.8
0.25	*	*	0.55	14.1
0.5	3.96	0.76	0.77	18.6
1	3.62	0.83	0.92	21.4
2	*	*	1.19	25.9
4	*	*	1.43	29.9

The number of monomeric dopants per repeat unit as a function of the concentration of dopant in solution used for sequential casting fit well to an empirical logarithmic relationship (Figure S3.2). This relationship was used to determine the number of monomeric dopants per repeat unit of the polymer for concentrations not measured by XPS.

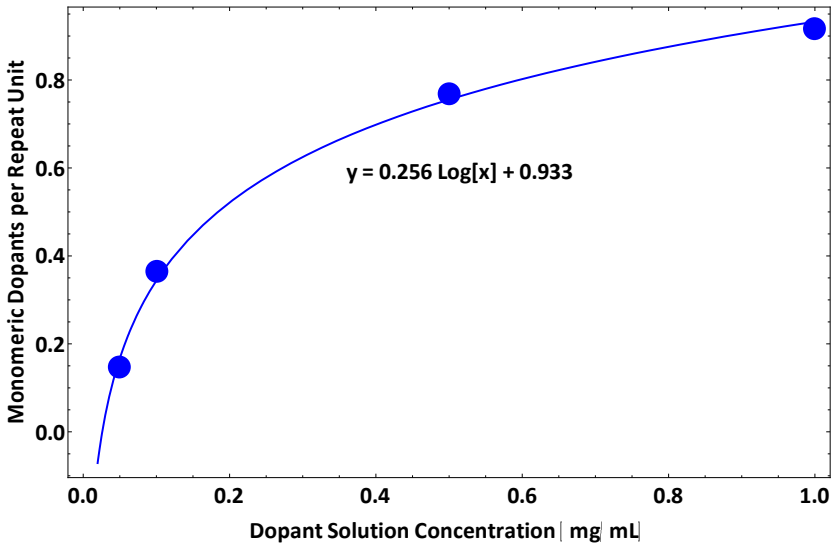

Figure S3.3 Relationship between dopant solution concentration and monomeric dopant per repeat unit incorporated into the film. This can be described using the following equation: Dopant Weight Percent = 0.256 × log[Dopant Solution Concentration] + 0.933

Given the number of monomeric dopants per repeat unit and value of the number density of monomers, it is possible to calculate carrier concentration using the following equation:

$$\frac{\#\ of\ RuCp * mes}{monomers\ of\ P(BTP-DPP)} \times \frac{carriers}{\#\ of\ RuCp * mes} \times \frac{monomers}{cm^3} = \frac{carriers}{cm^3}$$

For samples that showed detectable EPR signal (0.1 and 0.5 mg/ml loading or 0.37 and 0.77 monomeric dopant per repeat unit respectively) this would predict a carrier concentration of:

$$0.37 \times 1 \times 5.15\times10^{20}\,\frac{\text{monomers}}{\text{cm}^3} = 1.9\times10^{20}\ \frac{\text{carriers}}{\text{cm}^3}$$

$$0.77 \times 1 \times 5.15\times10^{20}\,\frac{\text{monomers}}{\text{cm}^3} = 4\times10^{20}\ \frac{\text{carriers}}{\text{cm}^3}$$

The density of monomeric units was approximated by an orthorhombic unit cell given with the repeat length of the monomer backbone and data from GIWAXS, which displays a peak at q ~ 1.5 $Å^{-1}$ that is attributed to an inter-chain separation distance of 4.2 Å and the peak at q ~ 0.3 $Å^{-1}$ that is attributed to an alkyl stacking distance of 2.1 nm.

Unit Cell Volume =

Interchain Separation Distance × Alkyl Stacking Distance × Repeat Length of Backbone

$$4.2\ Å \times 21\ Å \times 22.8\ Å = 2\times10^{-21}\text{cm}^3$$

$$\text{number density} = 5\times10^{20}\,\frac{\text{monomers}}{\text{cm}^3}$$

VI. Field-Effect Measurements of Mobility

The carrier mobility of P(BTP-DPP) was evaluated using thin film transistors (TFTs). TFTs were formed using spin-coated films of P(BTP-DPP) without a post-annealing step on a gate dielectric of a 10 nm cross-linked polymer benzocyclobutene (BCB) layer on top of a SiO_2 layer (200 nm) supported by a doped silicon wafer.

We fabricated field effect transistors with both Batch 2 (M_n = 42.3 kDa) and Batch 3 (M_n = 27.0 kDa), which resulted in similar hole and electron mobilities (electrons ≈ 1 x 10^{-3} cm^2V^{-1} s^{-1} & holes ≈ 3 x 10^{-3} cm^2V^{-1} s^{-1}. The field-effect mobilities were determined by a fit to the output characteristics at gate voltages such that the device was well into the *n*- or *p*-type regime of operation. The *n*-type region showed the existence of a clear contact resistance at low V_{ds} which likely affects the magnitude of the extracted mobility. Output characteristics of TFTs made with Batch 2 are shown in Figure S3.4.

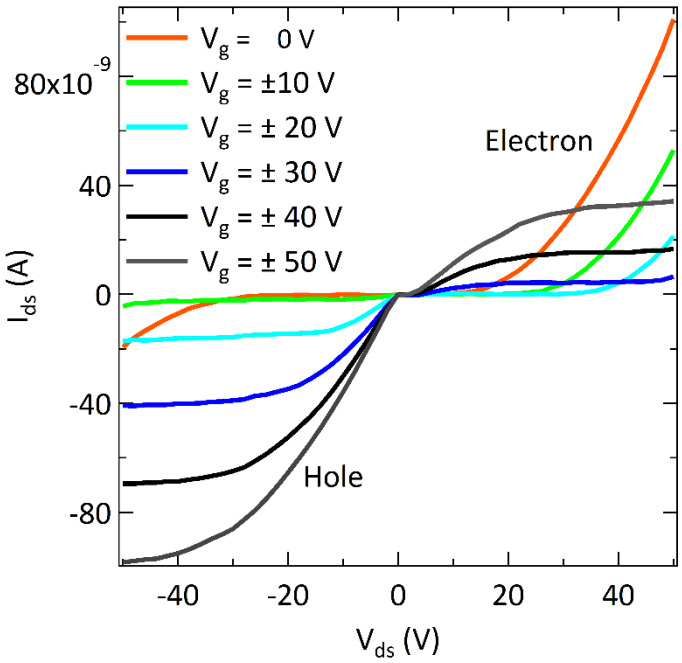

Figure S3.4 Output characteristics (drain current measured as a function of drain voltage) of example ambipolar P(BTP-DPP) field effect transistor. The drain current was measured for both negative and positive gate bias, corresponding to typical hole and electron accumulation regimes. Ambipolar behavior can be seen at gate voltages more negative than -20 V for *p*-type devices and greater than 30 V for *n*-type devices.

In contrast to the ~10^{-3} cm^2 V^{-1} s^{-1} mobility that we measured, the previously reported electron and hole mobilites were 1.21 × 10^{-1} and 8.9 × 10^{-2} cm^2 V^{-1} s^{-1}.[221] Differences in extracted mobility could be due to different processing (Chiu, et. al. used decyltricholosilane (DTS) as the dielectric and post-annealed at 150 ºC for 8 min) or the choice of fitting method.

VII. Electron Paramagnetic Resonance Measurement of Carrier Concentration

Electron Paramagnetic Resonance (EPR) measurements were performed with a Bruker EMX X-Band EPR. EPR samples were prepared by depositing films onto quartz microscope cover slides with dimensions 2 × 2 cm using spin conditions described previously in the Experimental Section. Samples were cleaved using a diamond scribe into approximately 1.5 cm × 3 mm wide pieces, prior to being inserted into low pressure/vac Suprasil® EPR sample tubes that were used in order to maintain nitrogen atmosphere. Samples were then transferred outside the glove box and the EPR spectra was measured immediately. Quantitative determination of the spin concentration was obtained by comparing samples to a reference sample of 2,2-diphenyl-1-picrylhydrazyl (DPPH) with a known spin concentration. This required both the integrated spin intensity, quality factor, power and volume of both samples and DPPH reference. Sample volumes were found by taking the area of the substrate determined using a micrometer and film thickness determined by AFM (films were ca. 40 nm thick).

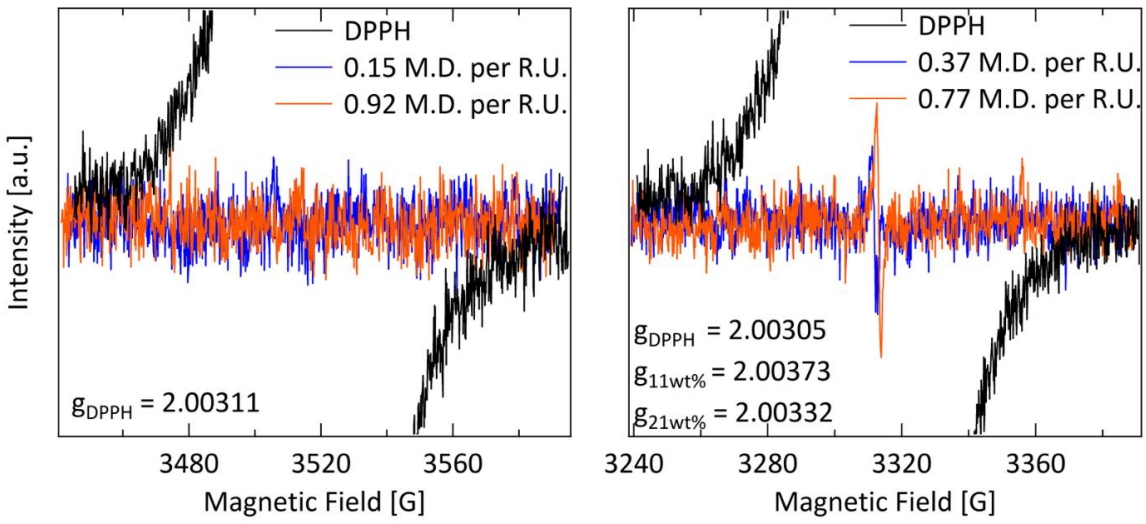

Figure S3.5 Raw EPR signals of an example sample of 0.15, 0.37, 0.77 and 0.92 monomeric dopants per repeat unit. The g values are reported in the figure corner.

EPR spectra were for several ratios of monomeric dopant to polymer repeat unit are show in Figure S3.5 along with the g-factor observed for DPPH and samples with detectable signal. The observed spin concentrations are reported in Figure S3.6, which show error bars representing the standard deviation of spin concentrations from three separate samples. In addition to room-temperature measurements, low-temperature EPR was also performed. No change in the EPR spectra was observed in the range of 100-300 K. EPR spectra of samples were measured on different days, and due to tuning of the cavity the magnetic field over which spectra was obtained varies. However, DPPH reference spectra confirms that the magnetic field range over which the samples were measured would be sufficient to show signal if it should exist.

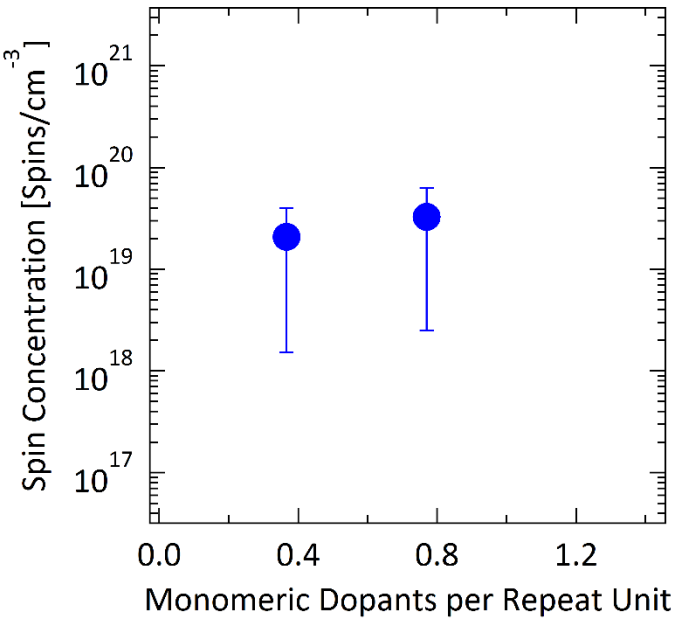

Figure S3.6 Spin concentration values for 0.15, 0.37, 0.77 and 0.92 monomeric dopants per repeat unit. Error bars are determined by the standard deviation of spin concentrations for a given dopant concentration from three separate samples. Values below measurement threshold (10^{14} spins/cm^3) are not plotted.

VIII. Optical Absorption Spectra

Thin film absorption measurements were conducted with a Shimadzu UV 3600 UV-VIS spectrometer. Samples were cast on sapphire substrates and measured in a specially made holder composed of flanges with sapphire windows, O-ring and clamp that was used in order to keep the sample under inert gas [nitrogen] in order to prevent dedoping of the sample.

IX. Density Functional Theory Calculations of Electronic Levels and Optical Transitions

Density functional calculations were carried out with Gaussian09(REF) to model the electronic structure of P(BTP-DPP). Due to the size of the compound, a model compound comprising the BTP unit flanked by two DPP units without the full alkyl sidechains was chosen (Fig. S7). The geometry of the neutral, anion and dianion were optimized at the B3LYP/6-311+G* level of theory and TD-DFT calculations were performed using this geometry. Images of the HOMO and LUMO levels and molecular geometries of the neutral, anion and dianion are given in Figure S3.7. A substantial narrowing of the gap between the HOMO and LUMO is observed in the dianion (0.8 eV) relative to the neutral compound (1.6 eV). This difference is ~0.3 eV larger than the difference in the LUMO and LUMO+1 of the neutral compound and is comparable to values expected for polaronic shifts of gap states in polymers. The single electron levels of the anion are complex because the compound has an open shell allowing splitting of the spin up and down electrons and we do not discuss the particular shifts here. Table S3.3 shows the first three optical transitions and associated orbitals. Note that the anion is an open-shelled species and the transitions involve both alpha and beta spin orbitals.

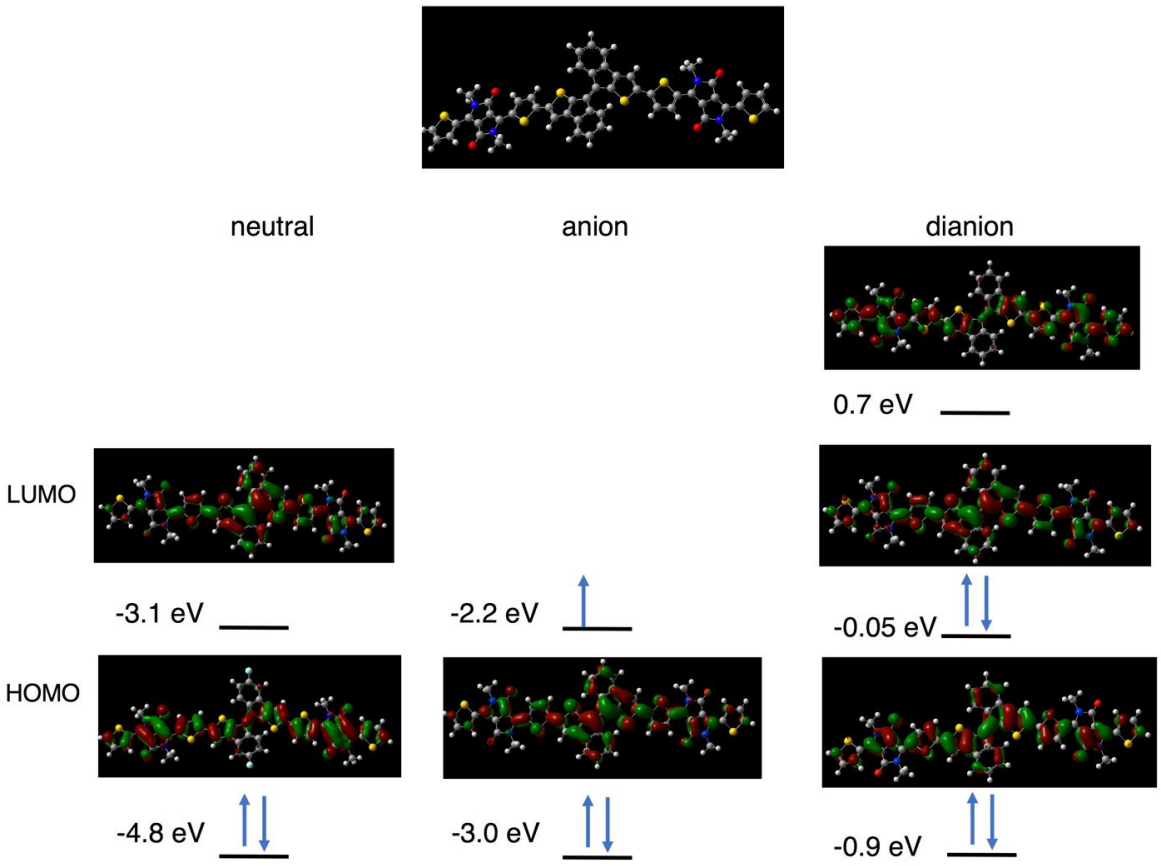

Figure S3.7 Model structures, images of the electron probability density of the HOMO and LUMO orbitals and their energies.

Table S3.3 First three optical transitions from TD-DFT theory (B3LYP/6-311+G*) for BTPDPP models.

Species	**Dominant Orbitals in Transition (A and B refers to spin & the numberical value is the contribution to transition)**	**Energy (eV)**	**Oscillator Strength**
Neutral	HOMO to LUMO	1.42	1.59
	HOMO-1 to LUMO (0.67) HOMO to LUMO+1 (0.19)	1.59	0.03
	HOMO-2 to LUMO (0.57) HOMO-1 to LUMO+1 (0.21)	2.0	0.51
Anion	HOMO-2:A to LUMO+1:A (-0.12) HOMO-1:A to LUMO+1:A (0.15) HOMO:A to LUMO:A (0.83) HOMO-2:B to LUMO:B (0.17) HOMO-1:B to HOMO:B (0.50)	0.66	0.15
	HOMO-2:A -> LUMO+1:A (-0.13) HOMO-1:A -> LUMO:A (0.27) HOMO:A to LUMO+1:A (0.76) HOMO-2:B -> HOMO:B (-0.37) HOMO-1:B -> LUMO:B (-0.41)	0.83	1.36
	HOMO-3:A to LUMO+1:A (-0.12) HOMO-3:A to LUMO:A (-0.22) HOMO:A to LUMO:A (0.55) HOMO-3:A to LUMO+1:A (0.13) HOMO-2:B to LUMO:B (0.24) HOMO-1:B to HOMO:B (0.74) HOMO:B to LUMO:B (0.12)	1.04	1.82
Dianion	HOMO to LUMO	0.94	2.3
	HOMO-1 to LUMO (-0.30) HOMO to LUMO+1 (0.64)	1.03	0.040
	HOMO-2 to LUMO (-0.14) HOMO-1 to LUMO+1 (0.40) HOMO to LUMO+2 (0.55)	1.70	0.19

X. Determination of Energy Levels from Ultraviolet Photoemission Spectroscopy

Ultraviolet photoemission spectroscopy was performed on the same setup and samples as XPS. Samples were transported using an airtight sample holder from the nitrogen glovebox used for film fabrication to the XPS/UPS instrument. For UPS, a helium I radiation source was used with a gate bias voltage of −9 V. Photoelectrons at the 0◦ takeoff angle were collected at 600 W (6 kV, 10 mA) with a pass energy of 5 eV and a step size of 0.025 eV. Survey scans were collected once with a dwell time of 100 ms. Finer scans near the valence band maximum (VBM) were collected with a dwell time of 600 ms.

The equations used to determine the energy levels in Figure 3.7 are given by the following: the Ionization Potential is defined as $IP = h\nu - |E_{SEE} - E_{VBE}|$, the Work Function is defined as $\varphi = h\nu$ [21.22] - E_{SEE} , and the Electron Affinity EA= φ – (Band Gap- $|E_{VBE}|$). The following figures S3.8-3.12 show how the E_{SEE} (secondary electron edge) and E_{VBE} (valence band edge) were defined. Note: samples with high doping concentrations contain a sub-gap feature that is near the E_{VBE}.

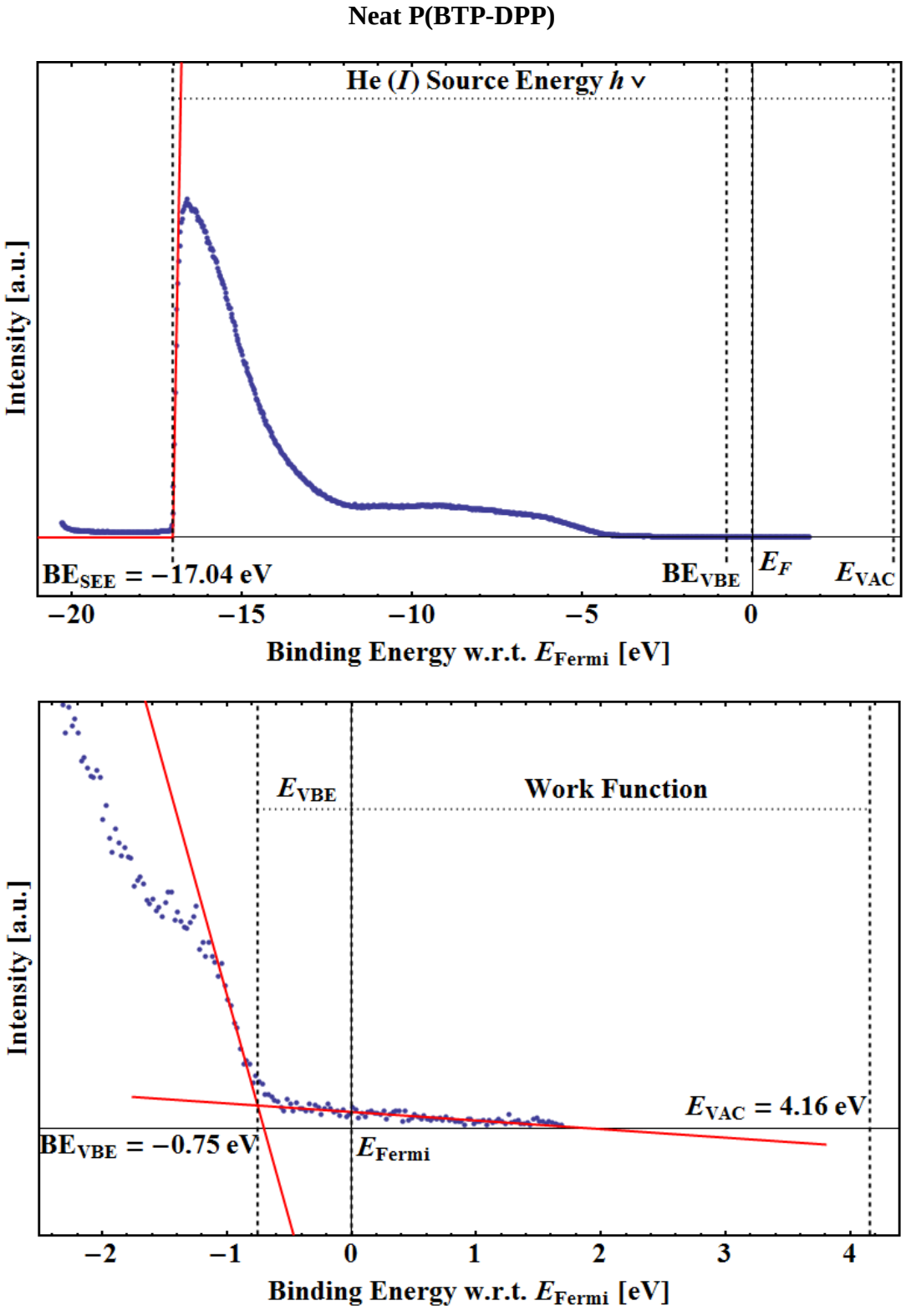

Figure S3.8 Example of He(I) UPS spectrum of neat P(BTP-DPP) showing how the secondary electron edge (Top) and the valence band edge (Bottom) were defined.

0.15 Monomeric Dopant per Repeat Unit

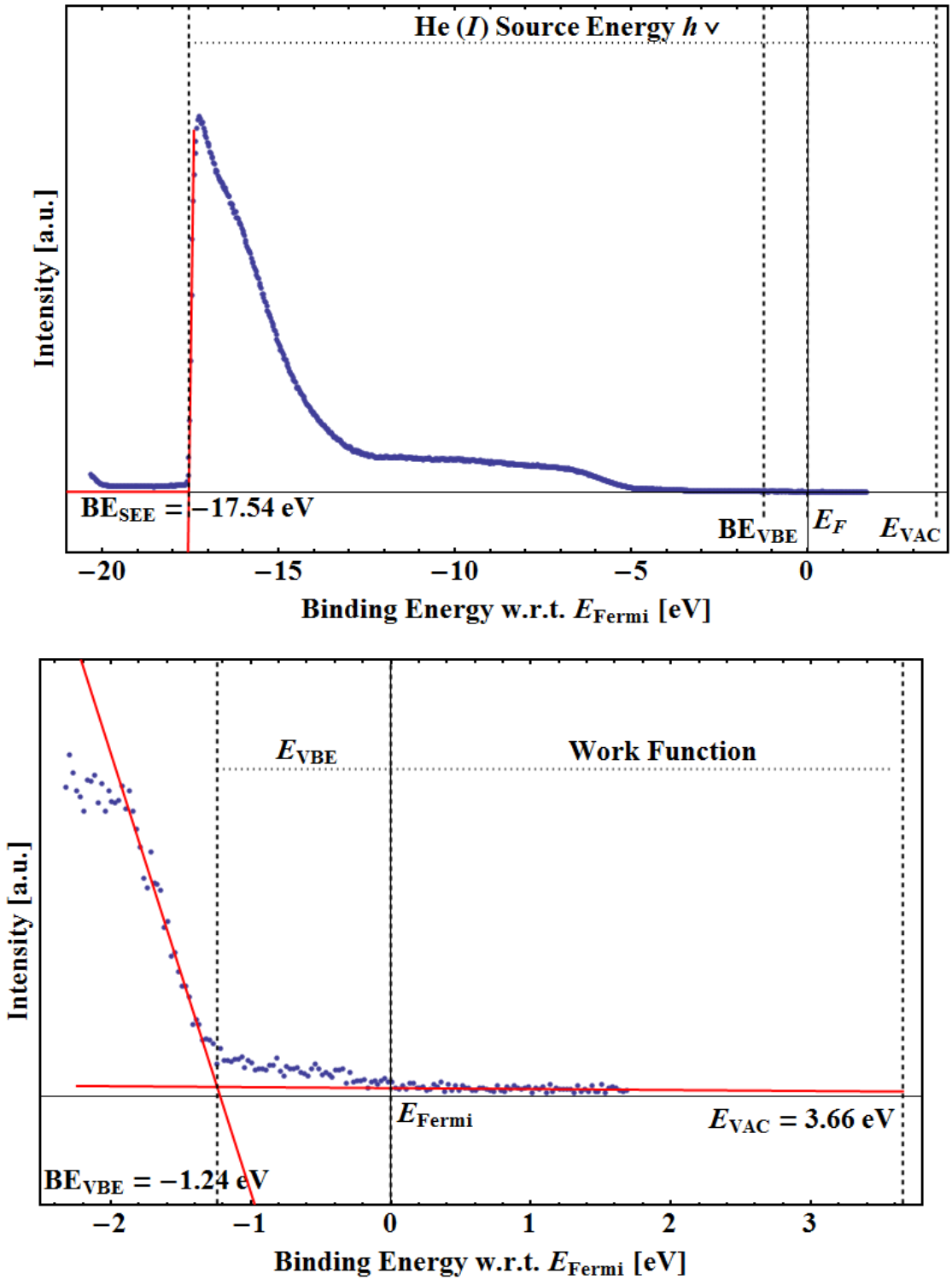

Figure S3.9 Example of He(I) UPS spectrum of P(BTP-DPP) doped at 0.15 monomeric dopant per repeat unit showing how the secondary electron edge (Top) and the valence band edge (Bottom) were defined.

0.37 Monomeric Dopant per Repeat Unit

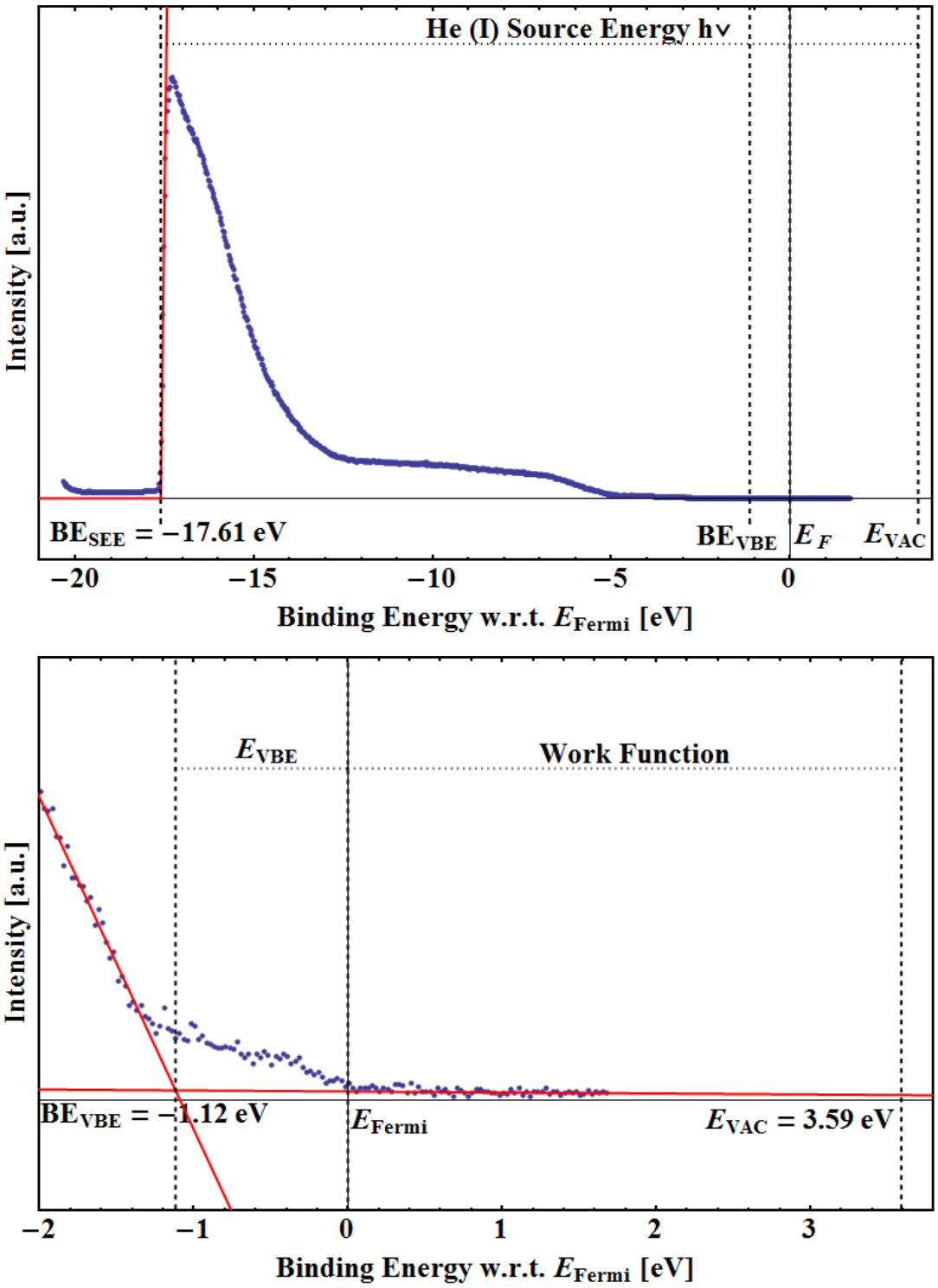

Figure S3.10 Example of He(I) UPS spectrum of P(BTP-DPP) doped at 0.37 monomeric dopant per repeat unit showing how the secondary electron edge (Top) and the valence band edge (Bottom) were defined.

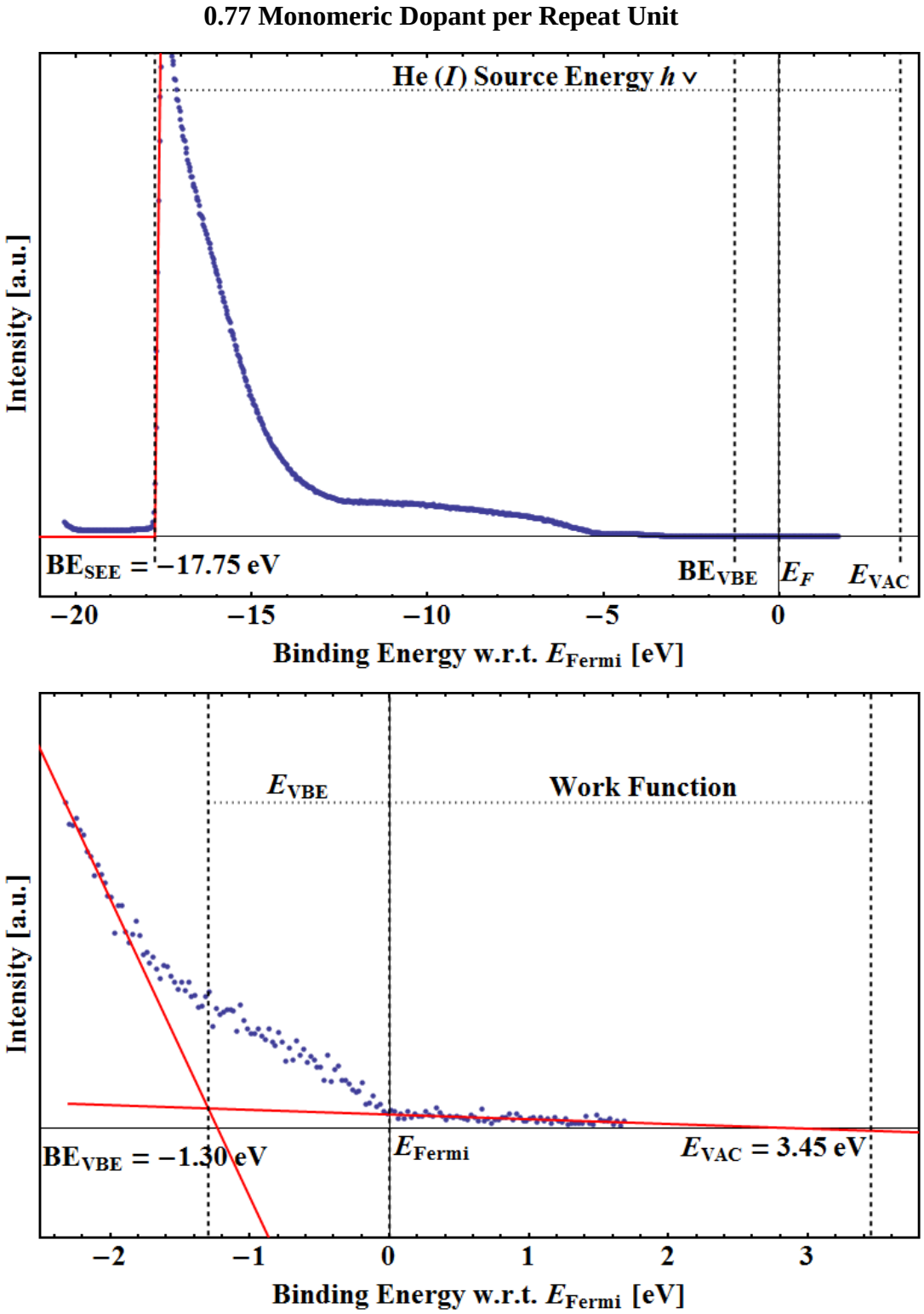

Figure S3.11 Example of He(I) UPS spectrum of P(BTP-DPP) doped at 0.77 monomeric dopant per repeat unit showing how the secondary electron edge (Top) and the valence band edge (Bottom) were defined.

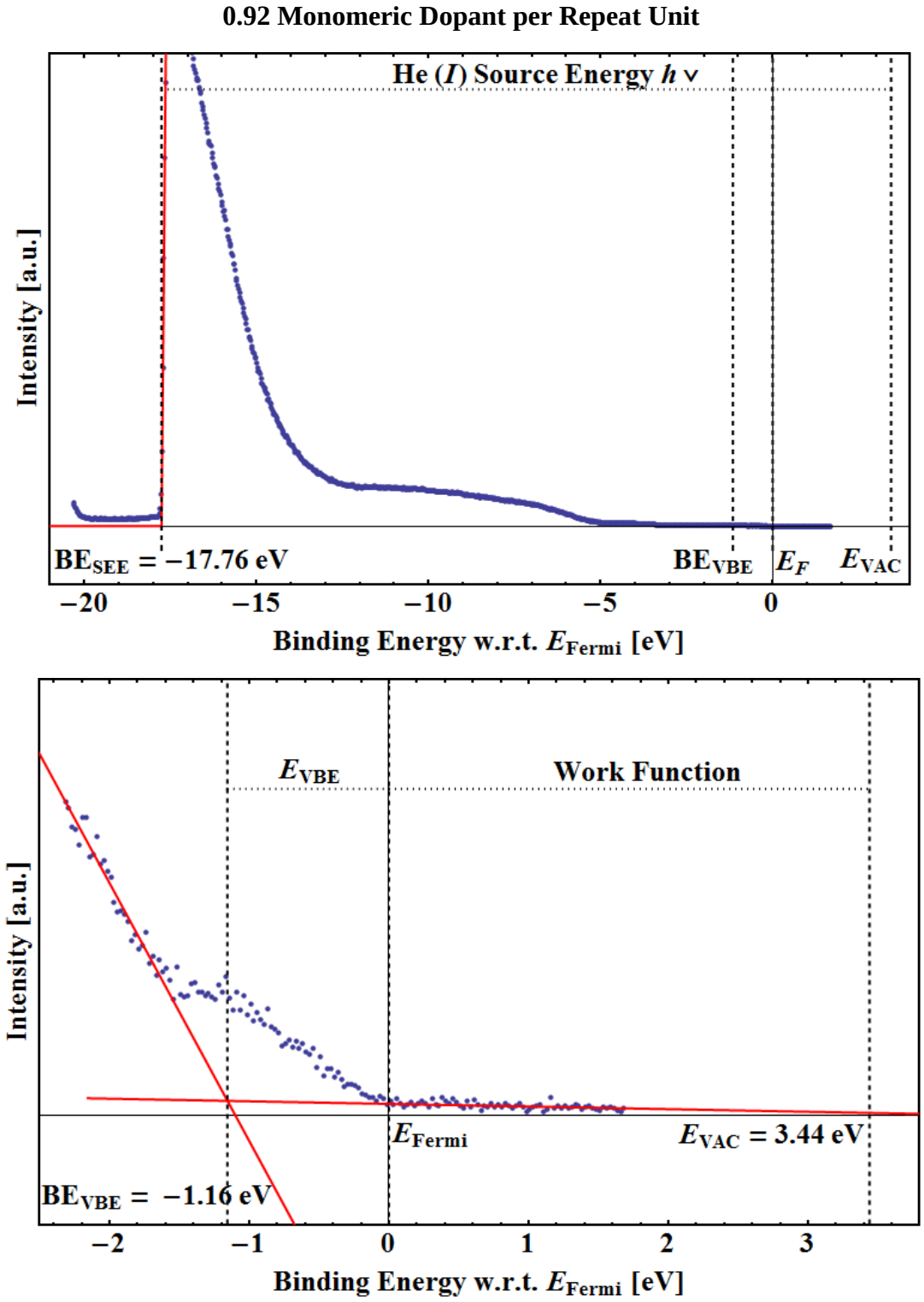

Figure S3.12 Example of He(I) UPS spectrum of P(BTP-DPP) doped at 0.92 monomeric dopant per repeat unit showing how the secondary electron edge (Top) and the valence band edge (Bottom) were defined.

Table S3.4 Ionization potential (IP), separation of HOMO and fermi lelel and work funciton as a function of RuCp*mes measured by Ultraviolet photoemission spectroscopy (UPS). See Figure 3.6 for graphical depiction of Table S3.4.

Monomeric Dopant per Repeat Unit	Ionization Energy (eV)	Separation of HOMO and Fermi Level (eV)	Work Function (eV)
Neat	4.9	0.8	4.2
0.15	4.9	1.2	3.7
0.37	4.7	1.1	3.6
0.77	4.8	1.3	3.5
0.92	4.6	1.2	3.5

XI. Grazing Incidence Wide-Angle Scattering

Grazing incidence X-ray scattering (GIWAXS) was performed at the Stanford Synchotron Radiation Lightsource (SSRL) on beam line 11–3. 2D scattering data was processed and reduced using the WxDiff software developed at SSRL. The beamline energy was 12.7 keV and an incident angle of 0.1° was used.

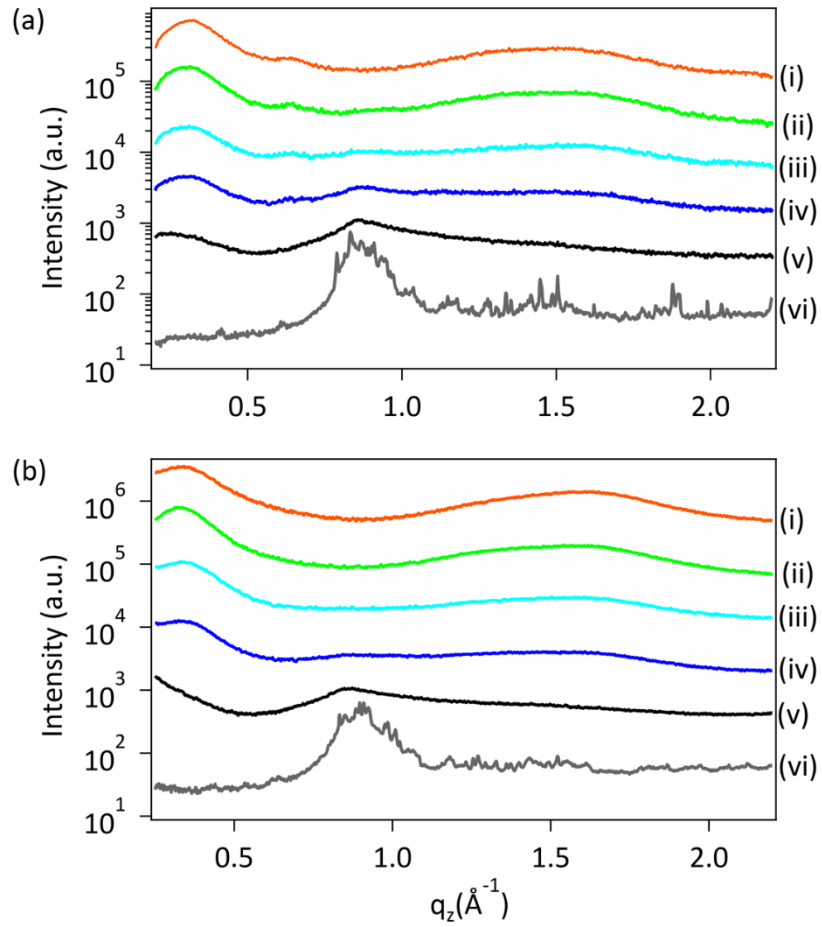

Figure S3.13 Line Cuts from the 2D scattering image in the (a) in-plane and (b) out-of-plane direction of P(BTP-DPP) films with increased dopant concentration (i) neat P(BTP-DPP), (ii) 0.15 monomeric dopant per repeat unit, (iii) 0.37 monomeric dopant per repeat unit, (iv) 0.55 monomeric dopant per repeat unit, (v) 0.92 monomeric dopant per repeat unit, (vi) neat $(RuCp^*mes)_2$. Features corresponding to significant scattering by the dopant emerge at 0.55 monomeric dopant per repeat unit.

Appendix B:

Supporting Information for

Chapter 4: N-Type Surface Doping of $MAPbI_3$ via Charge Transfer from a Small Molecule

Table of Contents

I. Atomic Force Microscopy of Film Surface

An Asylum MFP-3D atomic force microscope was used to measure the topography of films cast on quartz substrates.

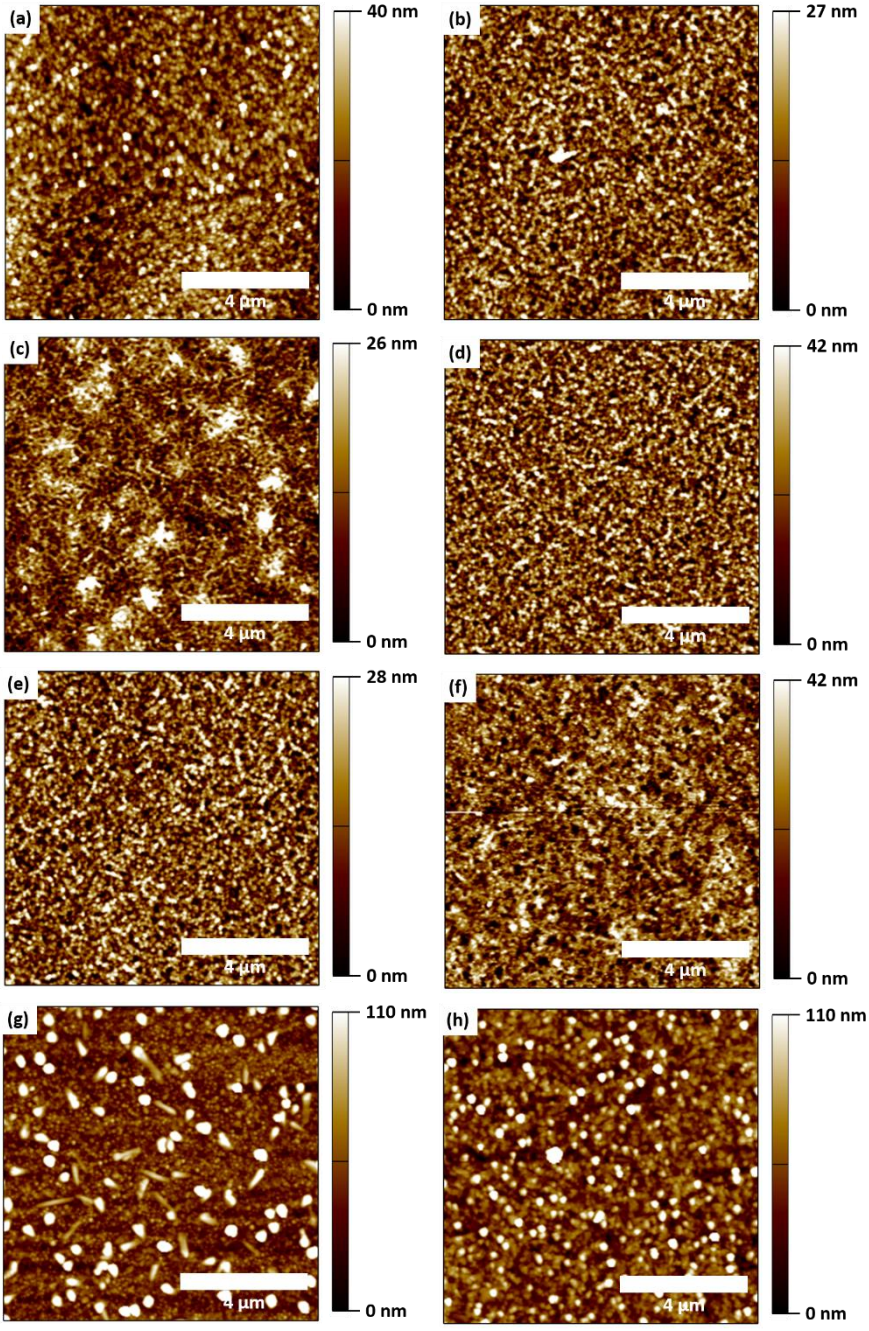

Figure S4.1 Atomic force microscopy (AFM) micrographs of $MAPbI_3$ surface with increasing dopant concentration: (a) neat perovskite, (b) 0.1 mg/mL, (c) 0.2 mg/mL, (d) 0.3 mg/mL, (e) 0.5 mg/mL, (f) 1 mg/mL, (g) 5 mg/mL, and (h) 10 mg/mL.

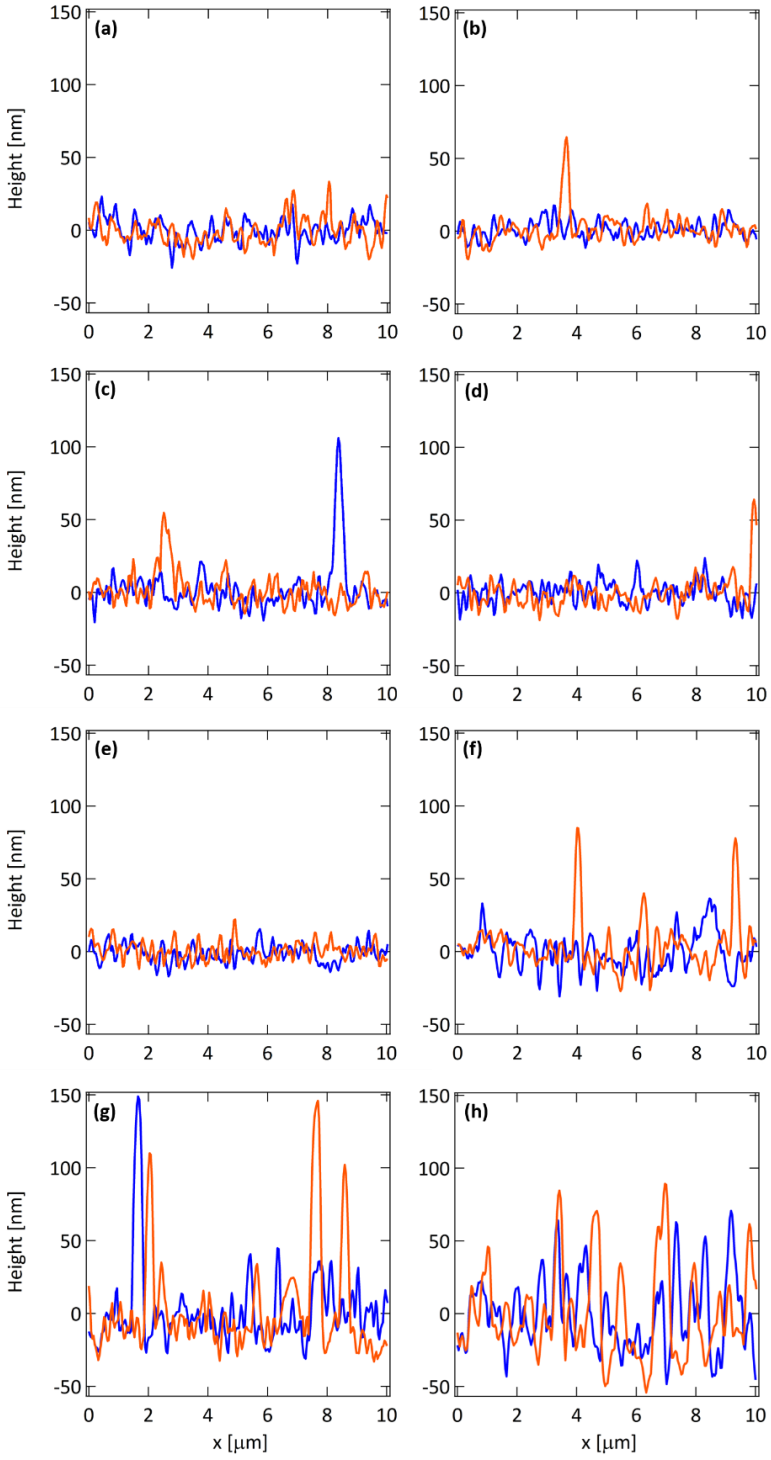

Figure S4.2 Example cross-sectional height profile extracted from AFM images indicating film roughness. Two example linecuts (orange and blue) are given for each sample with increasing dopant concentration: (a) neat perovskite, (b) 0.1 mg/mL, (c) 0.2 mg/mL, (d) 0.3 mg/mL, (e) 0.5 mg/mL, (f) 1 mg/mL, (g) 5 mg/mL, and (h) 10 mg/mL.

II. X-Ray Photoemission Spectroscopy: Degradation at the Surface

X-ray and Ultraviolet Photoemission Spectroscopy (XPS and UPS) was carried out on a Kratos Axis Ultra XPS/UPS instrument. The films were cast on a gold coated 10 × 10 mm crystalline silicon substrate (80 nm of gold with an underlying 20 nm of chromium adhesion layer deposited by thermal evaporation). Substrates were transported in a nitrogen environment. Films of $MAPbI_3$ were spin-cast onto the substrates within 1 hour to minimize fouling of the gold. The cobaltocene dopant solution was cast onto the sample immediately before transferring them to the instrument in an air tight sample holder. Nickel tape was used to electrically connect the $MAPbI_3$ to the sample holder in order to prevent charging. For XPS, a monochromatic Al-Kα source (180 W) was used under ultra-high vacuum conditions (10^{-7} Torr). Survey scans were collected with a step size of 0.5 eV, a pass energy of 20 eV, and a dwell time of 100 ms. In order to determine if these conditions damaged $MAPbI_3$, we performed a looped measurement (16×) of binding energies between 144 and 132 eV around the Pb 4f peaks on a neat $MAPbI_3$ film. The results of this loop, along with the position of the Pb $4f_{5/2}$ peak are given in Figure S4.3. Several conclusions were drawn using the atomic ratios of Pb, I and Co. The atomic percentages of Pb, I and Co are given in Table S4.1.

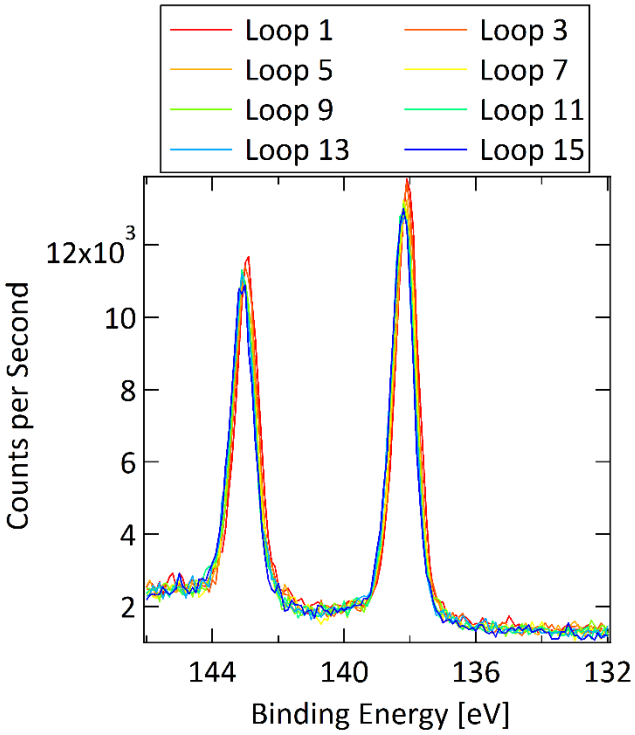

Loop #	Binding Energy of Pb 4f Peak [eV]
1	138.08
2	138.11
3	138.13
4	138.14
5	138.14
6	138.16
7	138.16
8	138.17
9	138.19
10	139.19
11	138.21
12	138.21
13	138.23
14	138.23
15	138.23
16	138.25

Figure S4.3 (Left) Looped XPS measurement of binding energies between 132 and 146 eV around the Pb 4f peak. (Right) The position of the $4f_{5/2}$ peak is given in the accompanying table. This measurement was performed in order to characterize the amount of damage to $MAPbI_3$ during a dwell time of 100 ms, which resulted in negligible shifts in binding energy over 16×.

Table S4.1 Atomic ratios determined by XPS survey scans of the perovskite surface with increasing dopant concentration. Orbitals used for comparison were Co 2p, I 3d and Pb 4f. Ratios of elements were used to infer conclusions about degradation (Pb:I) and dopant coverage (Co:I).

Sample Dopant Concentration	Atomic % Co	Atomic % I	Atomic % Pb	Ratio Pb:I	Ratio Co:I
Neat	0.00	75.09	24.91	.33	0
0.1 mg/mL	12.34	64.29	23.37	.36	.19
0.2 mg/mL	12.58	63.99	23.43	.37	.20
1 mg/mL	18.76	66.01	15.23	.23	.28
5 mg/mL	41.36	54.02	4.62	.09	.77

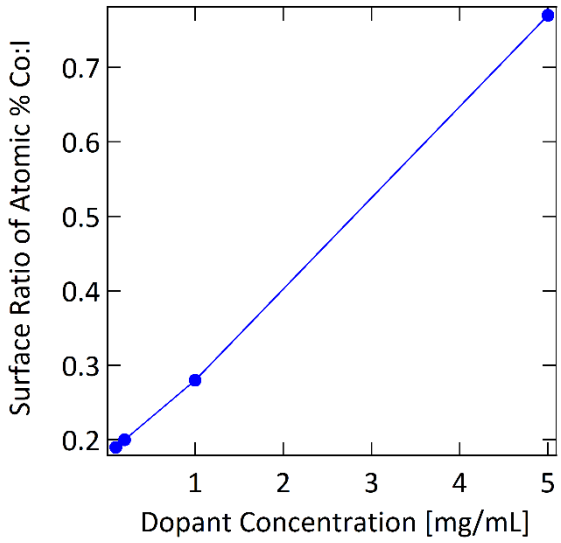

Figure S4.4 Surface Ratio of atomic percentages of Co:I appears to follow a linear relationship with dopant concentration deposited via spin casting.

III. Optical Absorption Spectroscopy

Thin film absorption measurements were conducted with an Ocean Optics HR2000+ High resolution spectrometer with a DH-2000 UV-VIS-NIR Light Source. Samples were cast on quartz substrates. The measurement was made in a nitrogen glovebox in order to prevent potential de-doping reactions of the films with air and moisture.

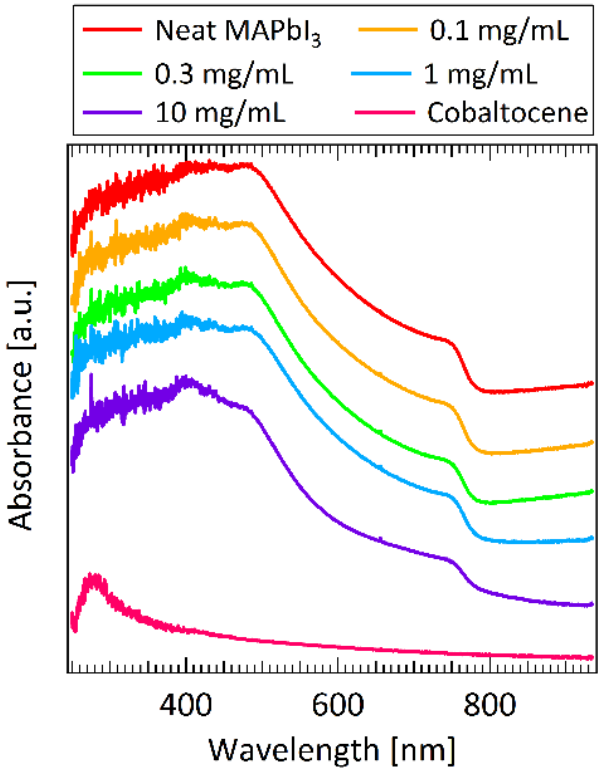

Figure S4.5 Absorbance of $MAPbI_3$ in neat form and with increasing dopant concentration. The spectra show no signs of bleaching of the main features. Cobaltocene absorbs around ~275 nm.

IV. X-Ray Diffraction

X-ray diffraction (XRD) patterns (Figure S4.6) were measured using a PANalytical Empyrean powder diffractometer with a Cu-Kα source, measured in reflection mode with an accelerating voltage of 45 kV and a beam current of 45 mA. Powder XRD patterns were simulated using the General Structure Analysis System (GSAS), with a calibration file specific to our instrument. The cobaltocene diffraction spectrum was simulated from a previously reported crystal structure.[222] Figure S4.6 shows that $MAPbI_3$ shows no signs of degradation upon doping and that cobaltocene crystallizes at high concentration. In addition, XRD spectra measured two weeks after dopant deposition also show no evidence of degradation. As diffraction is a bulk technique, information in spectra represent the average structure of the entire thin-film; degradation measured by XPS and conductivity are likely surface phenomena.

Films were deposited onto glass substrates which cause an amorphous hump in spectra. In addition, higher cobaltocene concentrations may lead this amorphous hump to become more pronounced. In doped $MAPbI_3$ samples, peaks corresponding to cobaltocene are denoted by blue dots. Peaks not seen in either the $MAPbI_3$ or cobaltocene simulated spectra are denoted by a black asterisks. We cannot account for these peaks; they are not consistent with PbI_2 impurities and may be a result of a cobaltocene polymorph as they increase with dopant concentration.

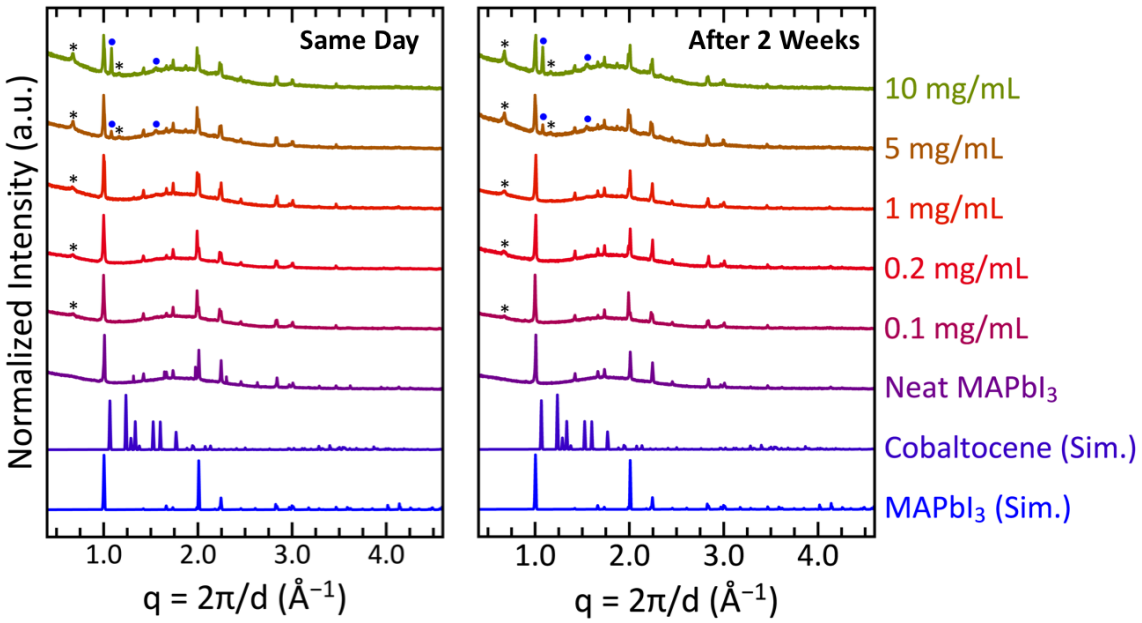

Figure S4.6 X-ray diffraction patterns of doped films (right) on the same day as cobaltocene doping and (left) two weeks later (14 days). Peaks corresponding to cobaltocene are denoted by blue dots. Peaks not seen in either the $MAPbI_3$ or cobaltocene simulated spectra are denoted by a black asterisks.

V. Determination of Energy Levels with Ultraviolet Photoemission Spectroscopy

Ultraviolet photoemission spectroscopy (UPS) was performed on the same setup and samples as those used in XPS. The UPS setup utilized a Helium I radiation source (21.22 eV). The UPS measurement was performed prior to XPS. Samples were transported using an airtight sample holder from the nitrogen glovebox used for film fabrication to the XPS/UPS instrument. Photoelectrons at the 0˚ takeoff angle were collected at a pass energy of 5 eV and a step size of 0.05 eV. Survey scans were collected once with a dwell time of 100 ms.

Figure S4.7 shows UPS spectra around the secondary electron edge (SEE) and valence band edge (VBE) of neat and doped $MAPbI_3$ films. A dashed line indicates where the SEE and VBE have been defined. Figures S4.8-S4.12 provide further detail of fitting the VBE and SEE of each sample.

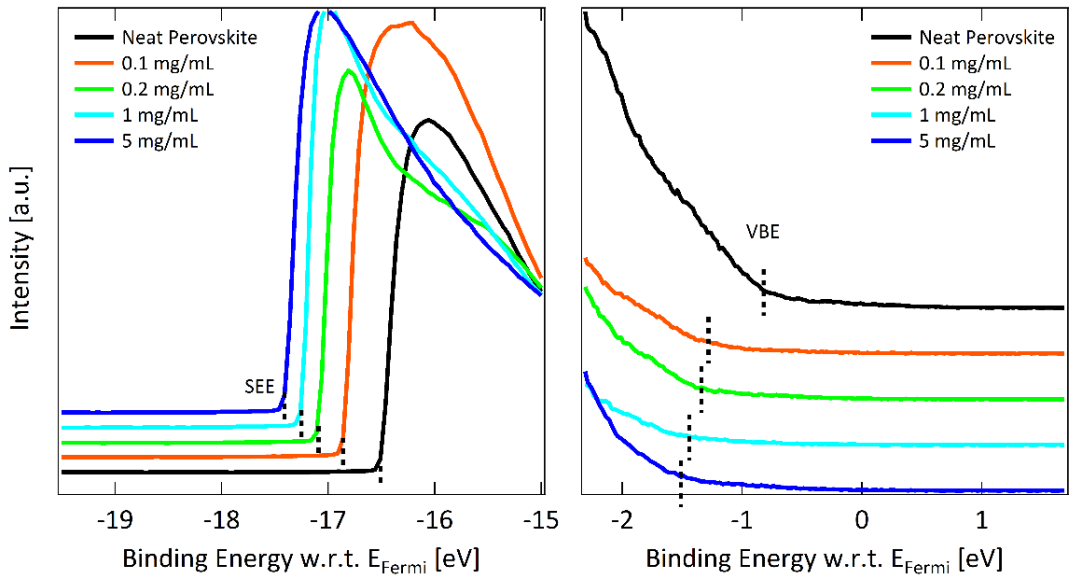

Figure S4.7 Ultraviolet photoemission spectroscopy around the (left) secondary electron edge and (right) valence band edge.

Neat Perovskite Surface

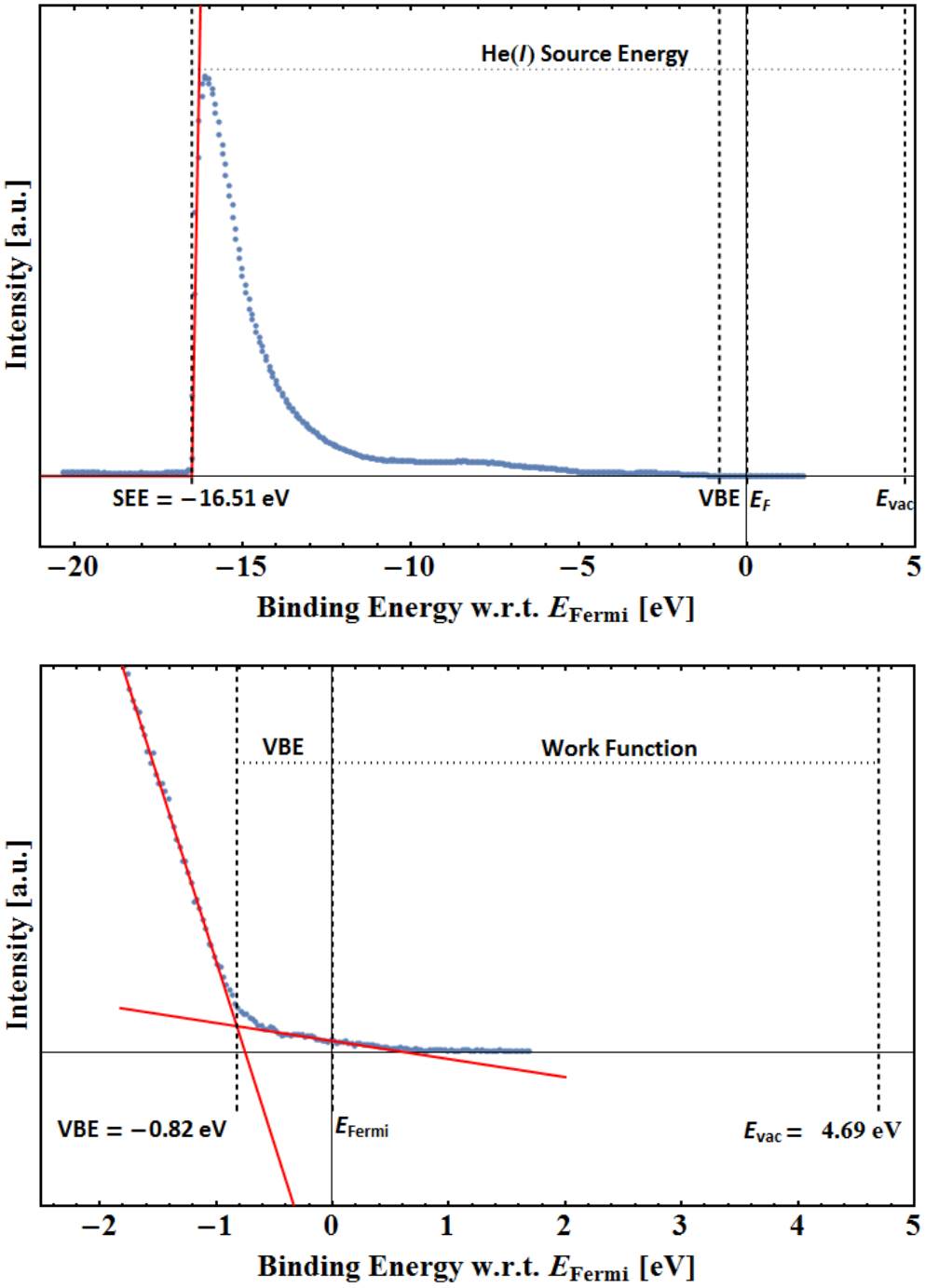

Figure S4.8 Example of UPS spectrum of neat $MAPbI_3$ showing how the secondary electron edge (top) and the valence band edge (bottom) were defined.

Surface Doping 0.1 mg/mL

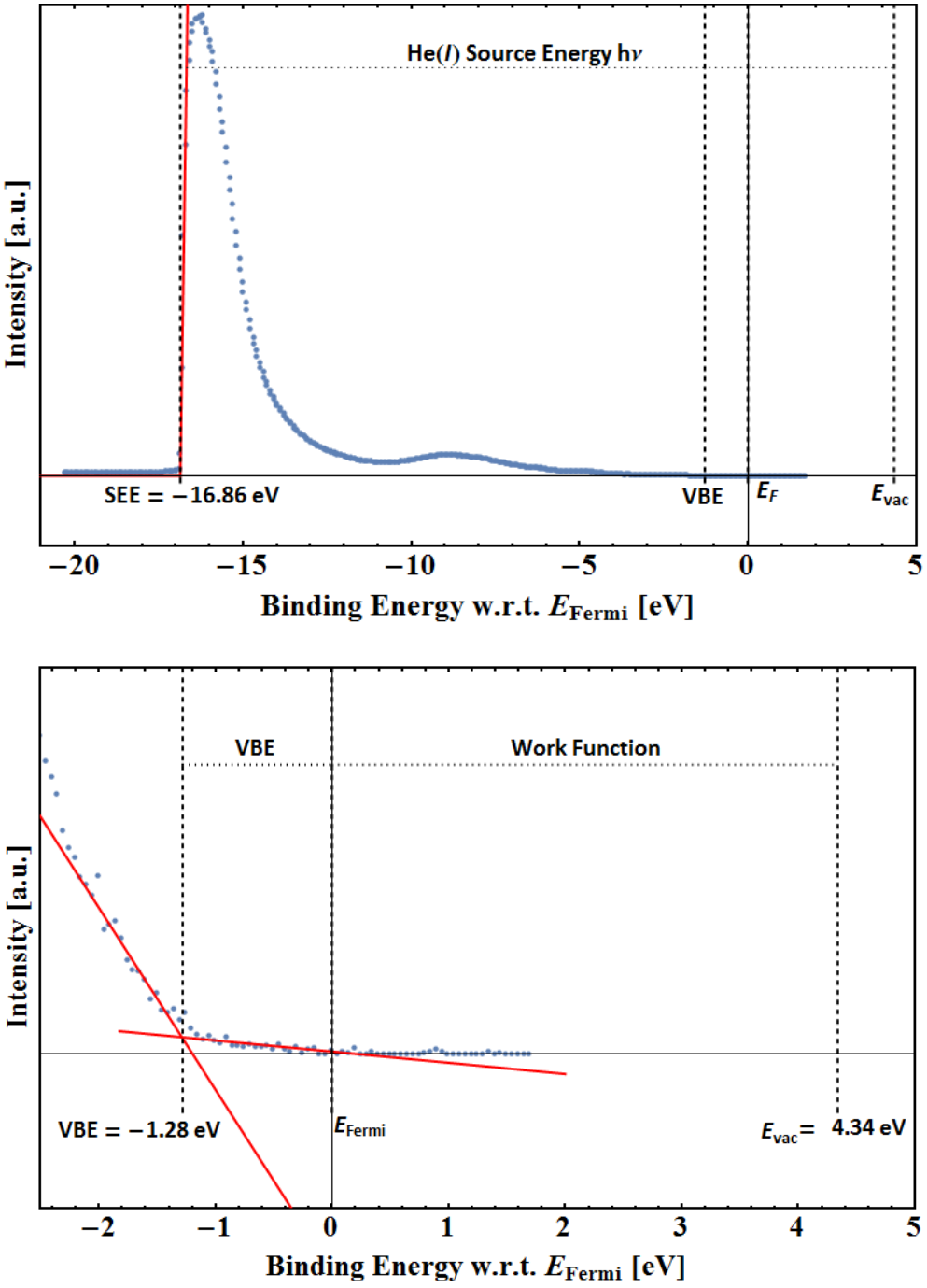

Figure S4.9 Example of UPS spectrum of 0.1 mg/mL doped $MAPbI_3$ film showing how the secondary electron edge (top) and the valence band edge (bottom) were defined.

Surface Doping 0.2 mg/mL

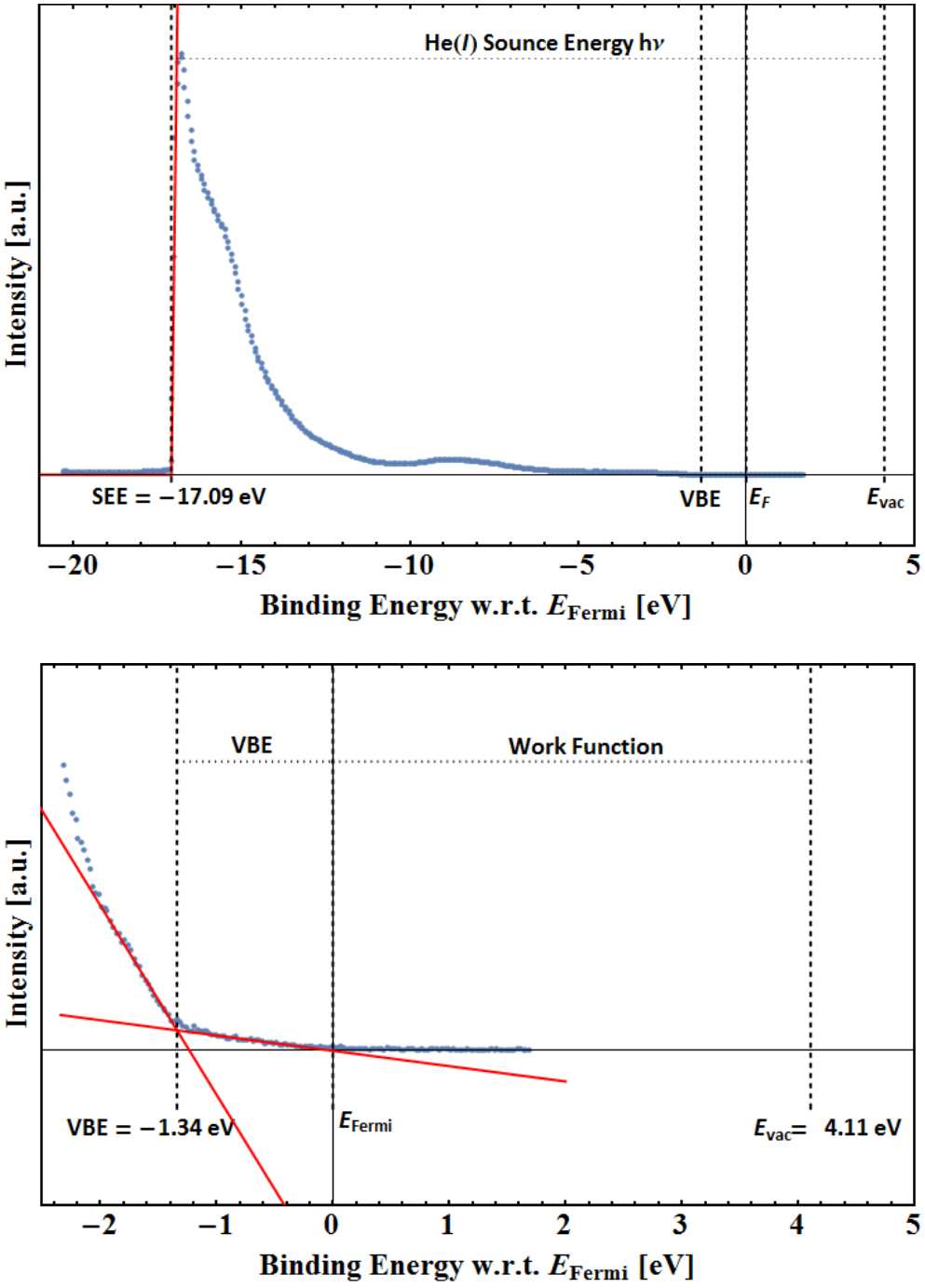

Figure S4.10 Example of UPS spectrum of 0.2 mg/mL doped $MAPbI_3$ film showing how the secondary electron edge (top) and the valence band edge (bottom) were defined.

Surface Doping 1 mg/mL

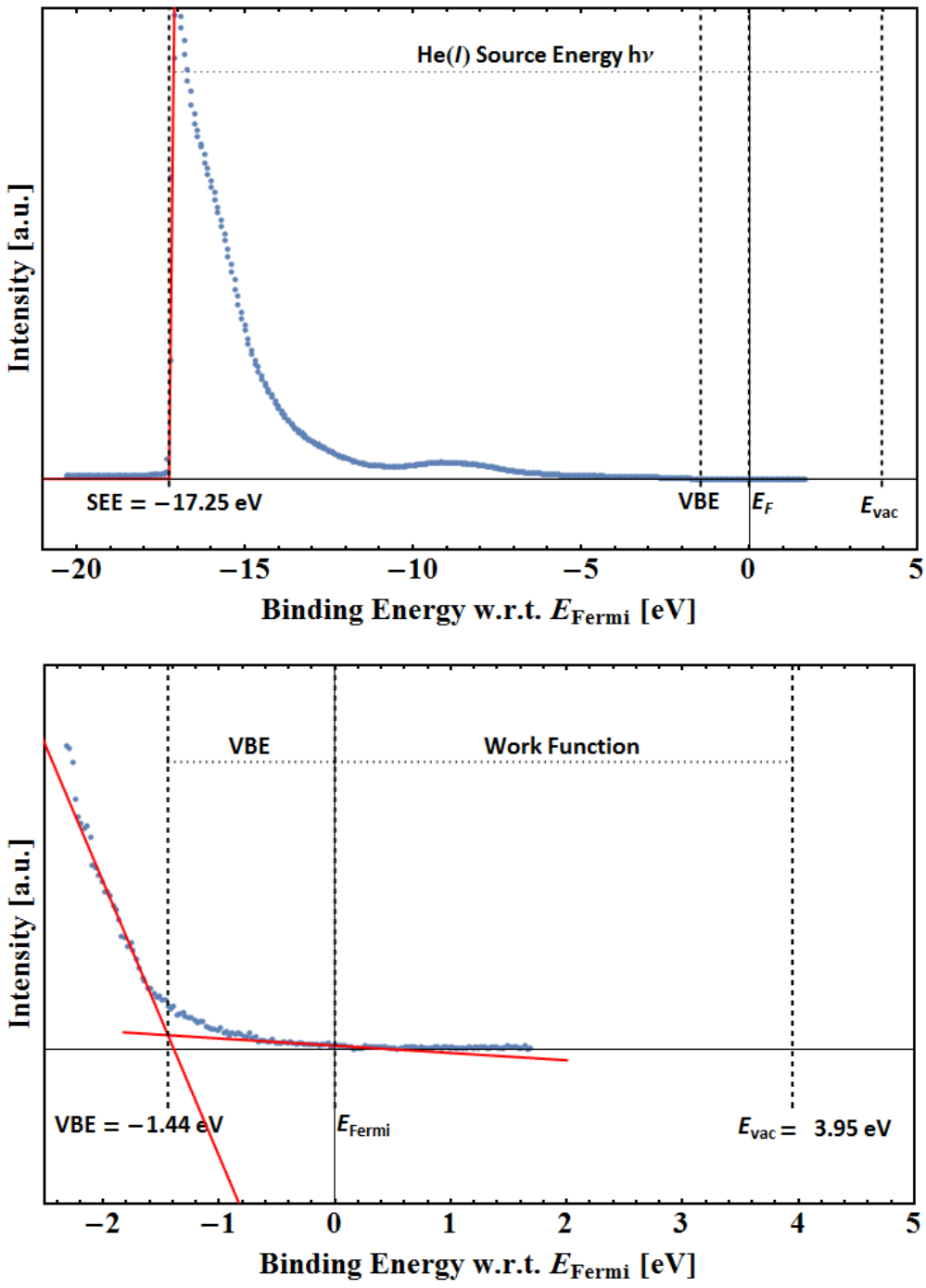

Figure S4.11 Example of UPS spectrum of 1 mg/mL doped $MAPbI_3$ film showing how the secondary electron edge (top) and the valence band edge (bottom) were defined.

Surface Doping 5 mg/mL

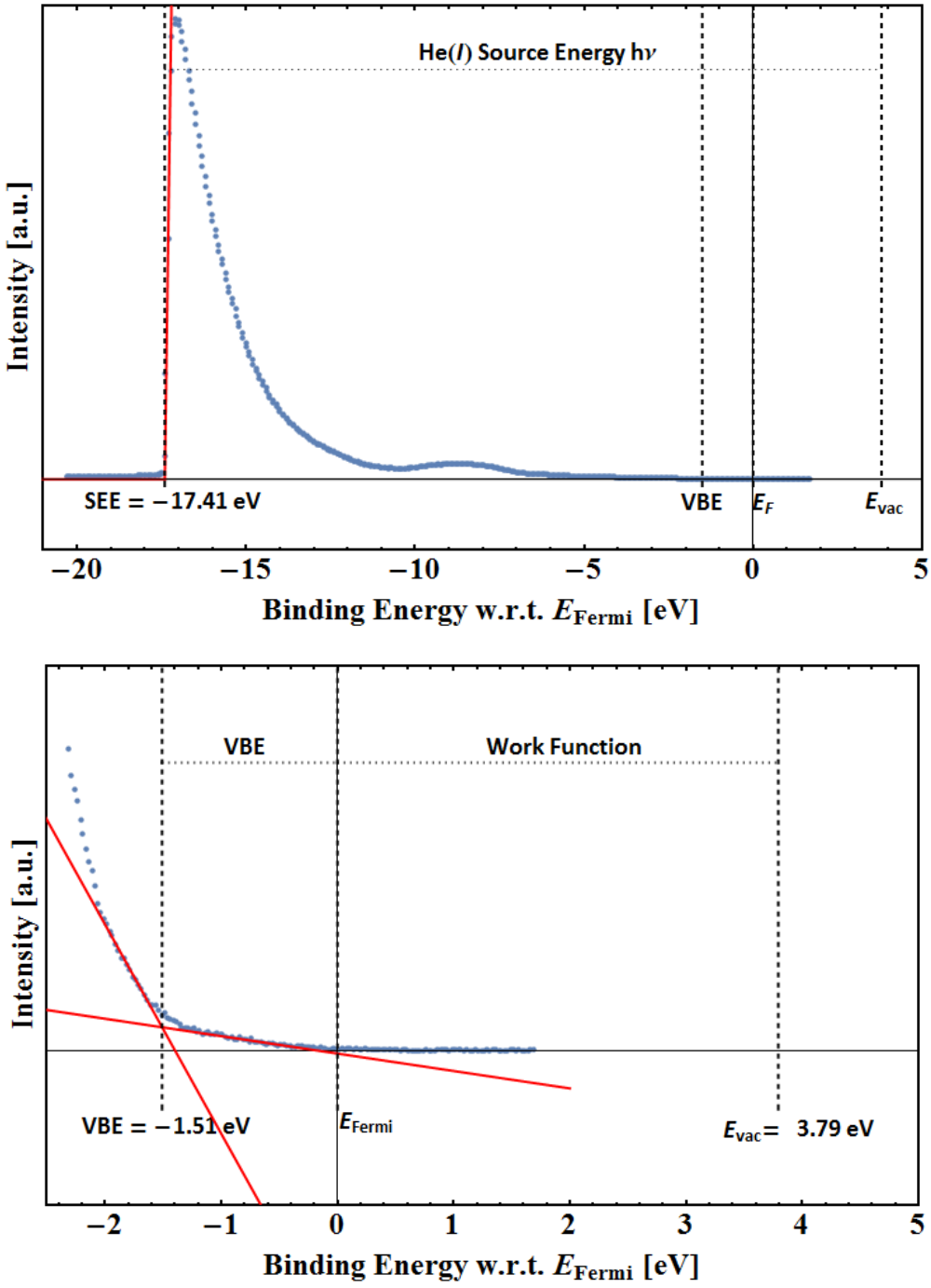

Figure S4.12 Example of UPS spectrum of 5 mg/mL doped $MAPbI_3$ film showing how the secondary electron edge (top) and the valence band edge (bottom) were defined.

The equations used to determine the energy levels in Figure 4.3 are given by the following: the Ionization Potential is defined as $IP = h\nu - |E_{SEE} - E_{VBE}|$, the Work Function is defined as $\varphi = h\nu$ [21.22 eV] - E_{SEE} , and the Electron Affinity $EA = \varphi - (\text{Band Gap} - |E_{VBE}|)$. The values of these quantities for various dopant concentrations (taken from linear intensity scale analysis) are given below in Table S4.2. The band gap here was assumed to be 1.55 [eV].

Table S4.2 Summary of values for secondary electron edge (SEE), valence band edge (VBE), ionization potential (IP), work function (WF) and electron affinity (EA) extracted from UPS.

Sample	SEE [eV w.r.t E_F]	VBE [eV w.r.t E_F]	IP [eV]	WF [eV w.r.t E_F]	EA [eV]
(a) Neat $MAPbI_3$	-16.5	-0.8	5.5	4.7	4.0
(b) 0.1mg/mL	-16.9	-1.3	5.6	4.4	4.1
(c) 0.2 mg/mL	-17.1	-1.3	5.5	4.1	3.9
(d) 1 mg/mL	-17.3	-1.4	5.4	4.0	3.9
(e) 5 mg/mL	-17.4	-1.5	5.3	3.8	3.8

Assignment of the VBE on a Logarithmic Intensity Scale

Figures S4.8-S4.12 show assignment of the SEE and VBE using a linear intensity scale. Several studies report a low density of states near the VBE in $MAPbI_3$, suggesting a logarithmic intensity scale can provide improved assignment of the VBE.[8,131,223] Assignment of the VBE using a logarithmic intensity scale is given in Figure S4.13 for comparison to Figures S4.8-S4.12. Similar to a study by Endres et al.,[223] we used a Gaussian fit to replicate the falling edge of the valence band. One of the issues using this fit is that a lack of a well-defined shoulder in the valence band adds some subjectivity to where a Gaussian is fit. It appears that with increasing dopant concentration, the Gaussian fit deviates from the data close the VBE. We suspect this could be a result of surface states in the gap of the material.[8] The VBE was assigned at the intersection of the Gaussian fit and a noise floor for the UPS apparatus that was designated as 100 counts per second. The difference in the VBE assigned on the linear vs logarithmic intensity scale is between ~0.1 and ~0.2 eV. This difference is given as the error bar in Figure 4.3.

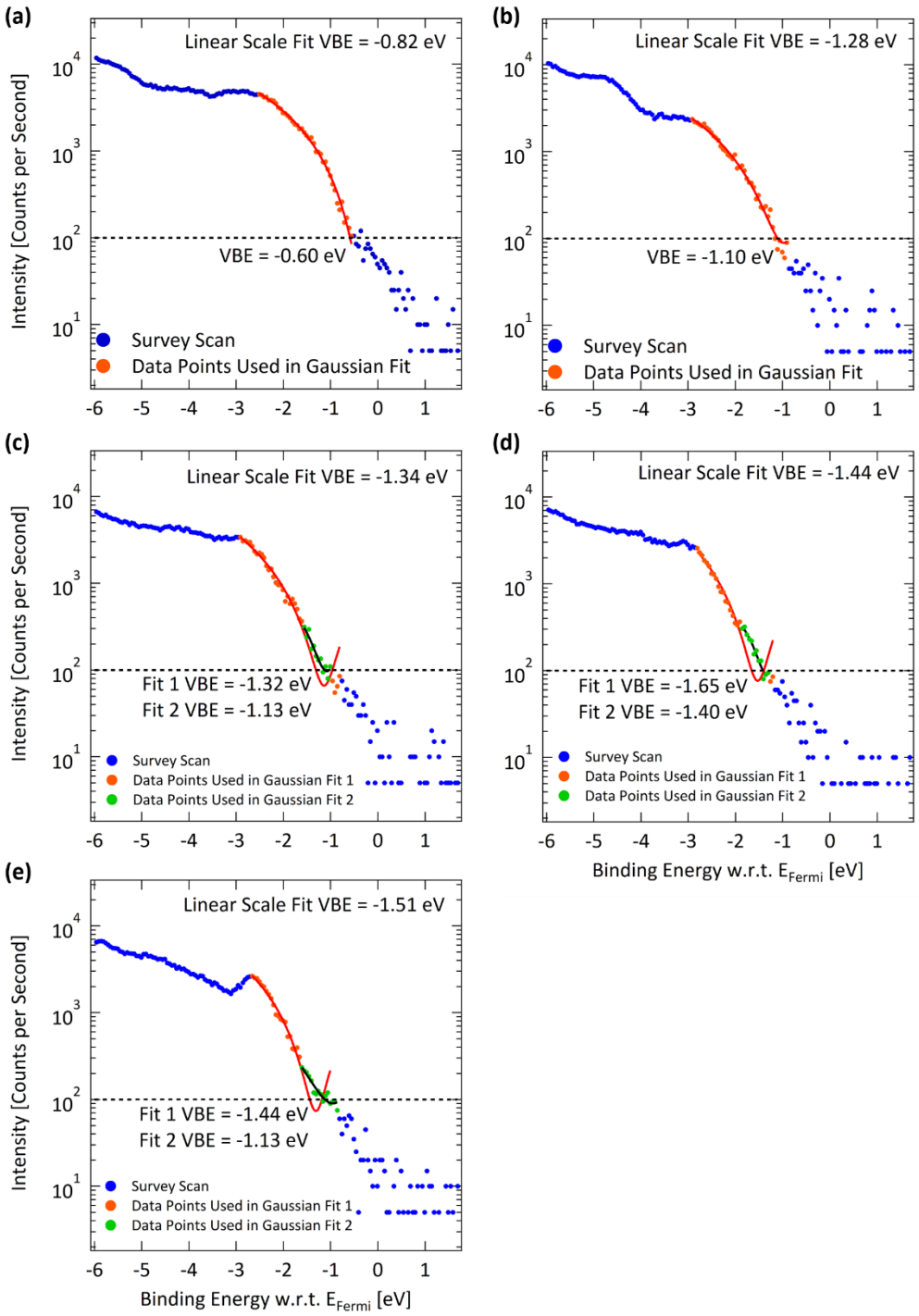

Figure S4.13 UPS spectra plotted on a logarithmic intensity scale of $MAPbI_3$ films with increasing dopant concentrations: (a) neat $MAPbI_3$, (b) 0.1 mg/mL dopant concentration, (c) 0.2 mg/mL dopant concentration, (d) 1 mg/mL dopant concentration, and (e) 5 mg/mL dopant concentration. The VBE was determined by the intersection of a Gaussian fit and a noise floor of 100 CPS. Minimal variance of the VBE value between linear and logarithmic intensity scale analysis is seen.

Characterization of Surface Effects: Surface Dipole and Band Bending

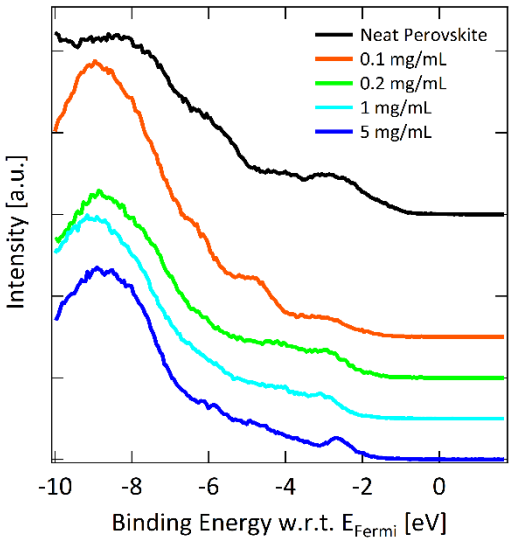

Figure S4.14 Ultraviolet photoemission spectroscopy showing the falling edge of the valence band. Slight changes in the density of states occur upon doping, but overall the shape is the same. This suggests that even though there is a dopant layer on the surface, UPS is still probing the surface of $MAPbI_3$.

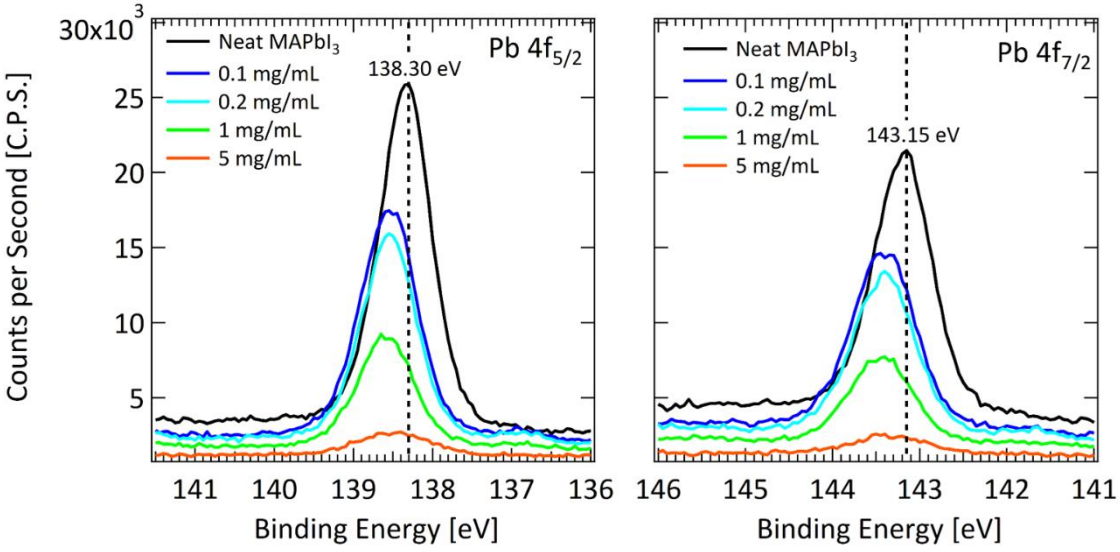

Figure S4.15 XPS core level shifts of (left) Pb $4f_{5/2}$ and (right) Pb $4f_{7/2}$ orbital peak positions. Upon doping, a shift of ~0.3 eV toward high binding energy occurs, indicating downward band bending at the surface.

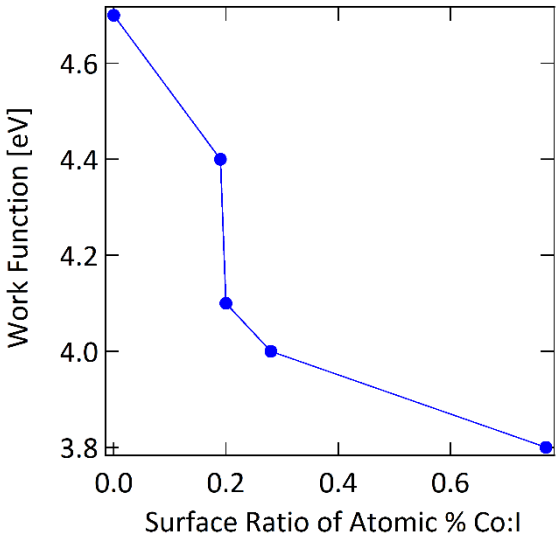

Figure S4.16 Relationship between Work function and the surface ratio of Atomic % Co:I. Changes in work function encompass both the effects of interface dipole formation and band bending.

VI. Calculation of Carrier Concentration based on Fermi Level

Several of the following calculations will require an estimate of the carrier concentration based on the position of the Fermi level as determined by UPS. Initially, it is necessary to determine a value for the quantum concentration of conduction electrons (Equation S4.1). This was determined by using a value for the effective electron mass to be m*≈ 0.2. [224,225]

$$n_c \equiv N_c/V = 2(m_e^* k_b T/2\pi\hbar^2)^{3/2} \quad \text{S4.1}$$

This produces a value for the quantum concentration of conduction electrons $n_c = 2.2 \times 10^{24}\ m^{-3}$. Using this term for the quantum concentration of conduction electrons, the conduction electron concentration is given by the following equation:

$$n_e = n_c \times \mathrm{Exp}\left[\frac{-(\varepsilon_c - \mu)}{k_b T}\right] \quad \text{S4.2}$$

The difference in energy levels between the conduction band ε_c and the Fermi level μ is determined experimentally using the Valence Band Edge (VBE) from UPS and by assuming a band gap. Since these values are used within the exponential term of Equation S4.2, small degrees of error can lead to significant variation in conduction electron concentrations. The resolution of UPS is roughly ±0.15 eV, making it difficult to be accurate with this estimation. Given the VBE value evaluated via UPS, we have calculated the conduction electron concentration for a range of band gaps: 1.55, to 1.6 eV (Table S4.3).

Table S4.3 Conduction electron concentrations calculated using data from UPS. UPS does not measure the band gap, which was assumed here to be 1.55 eV. However, in literature the band gap of $MAPbI_3$ has been reported over the range of 1.55 to 1.60 eV. The concentration of conduction electrons is calculated using these two values to illustrate how small uncertainties in the energy levels can alter estimates for carrier concentrations.

SAMPLE	VBE [eV]	n_e [m^{-3}] if BG=1.55 eV	n_e [m^{-3}] if BG=1.6 eV
Neat $MAPbI_3$	-0.8	9.9×10^{11}	1.4×10^{11}
0.1 mg/mL	-1.3	6.0×10^{19}	8.6×10^{18}
0.2 mg/mL	-1.3	6.2×10^{20}	8.9×10^{19}
1 mg/ml	-1.4	3.1×10^{22}	4.4×10^{21}
5 mg/mL	-1.5	4.7×10^{23}	6.7×10^{22}

VII. Estimates of Surface Conductivity and Thickness of Doped Layer

Surface doping of this kind results in charge carriers that are confined to the top few nm of the surface by the electric field created by the interfacial charge separation.[66] The conductivity reported in Figure 4.4(a) was calculated using the total film thickness rather than accounting for the thickness of the region where carriers are accumulated. In order to estimate the thickness of the doped layer and its corresponding conductivity, we used an approximation explained below. Given the number of assumptions made, this estimate in some cases predict that the thickness of the doped surface layer is unphysically low. However, it does confirm that the thickness of the surface layer is small and that this is not a bulk doping technique.

Estimate 1: System of Equations Using Conductance

Here the film is modeled like resistors in parallel, with the two resistors corresponding to the top surface doped layer and the neat bulk. The resistance of the entire film R_{Total} can be described using Equation S4.3. Similarly, the conductance of the entire film G_{Total}, which is the inverse of R_{Total}, is given by Equation S4.4.

$$\frac{I}{R_{Total}} = \frac{1}{R_{SurfaceDoped}} + \frac{1}{R_{Bulk}} \quad \text{S4.3}$$

$$G_{Total} = G_{SurfaceDoped} + G_{Bulk} \quad \text{S4.4}$$

Where $R_{SurfaceDoped}$ and $G_{SurfaceDoped}$ are the resistance and conductance of the top, thin surface doped region respectively and R_{Bulk} and G_{Bulk} are the resistance and conductance of the neat bulk region respectively. Conductance G is given by Equation S4.5.

$$G = \sigma \frac{A}{L} \quad \text{S4.5}$$

In this equation, σ is conductivity, A is area i.e. contact length × film thickness, and L is length i.e. contact spacing. For the two resistor components, the contact length and spacing are the same. The total thickness T of $MAPbI_3$ films is 120 nm. Conductance of doped films can be described using Equation S4.6.

$$\sigma_{AfterDope}\left(\frac{CL\times T}{CS}\right)=\sigma_{SurfaceDope}\left(\frac{CL\times t}{CS}\right)+\sigma_{Bulk}\left(\frac{CL\times(T-t)}{CS}\right) \quad \text{S4.6}$$

From Figure 4.4(a), values for total conductivity $\sigma_{AfterDope}$ and bulk conductivity σ_{Bulk} have been reported. Leaving the quantities of surface conductivity $\sigma_{SurfaceDope}$ and surface thickness t unknown. In order to find $\sigma_{SurfaceeDope}$ we can use the conductivity equation $\sigma = n\times q\times\mu$. This will require taking n to be the value for the concentration of conduction electrons solved for in the section on the calculation of carrier concentration based on Fermi level. There is likely some degree of error in the carrier concentration assumption, given the Fermi levels of the gold substrate and $MAPbI_3$ equilibrated in the UPS measurement. Whereas conductivity measurements were performed on quartz and Fermi level equilibration likely did not result in the same degree of charge transfer. Taking methods that measure mobility across grains such as a thin film transistor measurement (TFT), we used a mobility value of $\mu \approx 1\ cm^2V^{-1}s^{-1}$.[226,227] We estimate that a potential upper bound to this value could be $\mu \approx 10\ cm^2V^{-1}s^{-1}$.

Estimates for the surface conductivity are given in Table S4.4. In addition to considering two different mobility values, Table S4.4 also includes two different band gap values which will determine the concentration of conduction electrons. These values are given to illustrate the potential amount of error in this calculation, which is why in Figure 4.4(a) conductivity values were reported using the total film thickness.

Table S4.4 Estimates for surface conductivity. This calculation was performed for two mobility values and two band-gap values to illustrate the range over which surface conductivity is reasonable.

Sample	**Mobility [cm^2/V s]**	**Surface Conductivity [S/cm]**	
		BG=1.55 [eV]	BG=1.6 [eV]
Neat	1	1.6×10^{-13}	2.3×10^{-14}
	10	1.6×10^{-12}	2.3×10^{-13}
0.1 mg/mL	1	9.6×10^{-6}	1.4×10^{-6}
	10	9.6×10^{-5}	1.4×10^{-5}
0.2 mg/ML	1	1.0×10^{-6}	1.4×10^{-5}
	10	1.0×10^{-5}	1.4×10^{-4}
1 mg/mL	1	4.9×10^{-3}	7.0×10^{-4}
	10	4.9×10^{-2}	7.0×10^{-3}
5 mg/mL	1	7.5×10^{-2}	1.1×10^{-2}
	10	7.5×10^{-1}	1.1×10^{-1}

Using the values for $\sigma_{SurfaceDoped}$ given in Table S4.4 above, Equation S4.6 produces estimates for the surface thickness t given in Table S4.5. For intermediately doped samples (0.1 & 0.2 mg/mL dopant concentration), this calculation predicts a surface thickness of a few nm. At high doping concentrations, estimates for the thickness of surface doped layer become less physically reasonable, as they become increasingly small.

Table S4.5 Estimate for thickness of surface doped layer. This calculation was performed for two mobility values and two band-gap values to illustrate the range over which the thickness of the doped layer is reasonable.

Sample	**Mobility [cm^2/V s]**	**Thickness [Nanometers]**	
		BG=1.55 [eV]	BG=1.6 [eV]
0.1 mg/mL	1	5.7	41.3
	10	5.6×10^{-1}	4.0
0.2 mg/ML	1	1.3	9.2
	10	1.3×10^{-1}	9.2×10^{-1}
1 mg/mL	1	1.9×10^{-1}	1.3
	10	1.9×10^{-2}	1.3×10^{-1}
5 mg/mL	1	5.4×10^{-3}	3.8×10^{-2}
	10	5.4×10^{-4}	3.8×10^{-3}

VIII. Electrical Conductivity Measurements: General

Conductivity values were measured using a two-point probe method using a picoammeter due to the resistance of the $MAPbI_3$ films. Gold contact pads 80 nm tick were deposited onto films using a shadow mask in a thermal evaporator in a collinear geometry with 160 µm spacing between electrodes that were 3200 µm long. Conductivity values reported were calculated using the following equation for conductivity of thin layer samples measured using a two-point measurement where *I* is the current, *V* is the measured voltage and *d* is the layer thickness:[220]

$$\sigma = \frac{I}{V}\frac{1}{d}\frac{\ln[2]}{\pi} \qquad \text{S4.}$$

This approximation is accurate if the film thickness is less than one half the needle distances which is satisfied because of the thickness of films (≈120 nm) and the distance between probes (160 µm).

Error bars in Figure 4.4(a) are determined from three devices each on three separate films (9× total measurements). The conductivity was measured for each sample both prior to and

after doping. Conductivity measurements done prior to doping were made in order to account for film to film variation. The neat conductivity given in Figure 4.4(a) is an average of the values given in Figure S4.17.

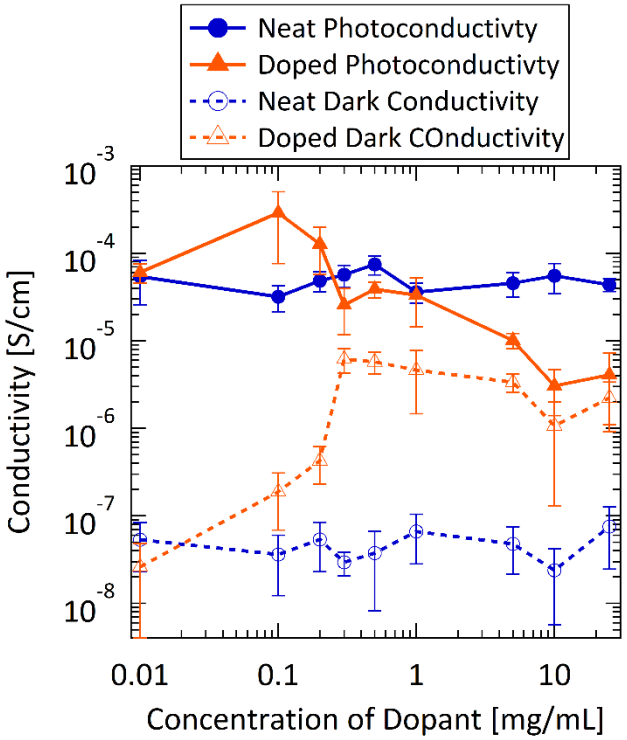

Figure S4.17 Photoconductivity and dark conductivity of $MAPbI_3$ films as a function of dopant concentration. Neat conductivity gives the actual device averages of films prior to dopant deposition. Error bars are determined from three devices each from three separate films.

Stability Under Air Exposure, Time, and Ultra High Vacuum

The stability of doping using small molecules has proved challenging. In *n*-type organic semiconductors, high LUMOs result in de-doping if films are exposed to the ambient.[228] The conduction band of $MAPbI_3$ has similar energy levels to the LUMOs of *n*-type organic semiconductors, making de-doping a concern. Table S4.6 gives the conductivity of $MAPbI_3$ film doped with 1 mg/mL solution before and after being exposed to air for 1 minute. There is a small drop in dark conductivity. However, we chose to employ a nitrogen environment or encapsulation via Cytop amorphous fluoropolymer resin solution in all measurements of this study.

Table S4.6 Photoconductivity and dark conductivity of a 1 mg/mL doped film before and after it has been exposed to air for 1 minute. Photoconductivity measurements were performed with illumination from a 525 nm LED with a photon flux of 5.8×10^{17} photons cm^{-2} s^{-1}.

	LED Initial [S/cm]	Dark Initial [S/cm]	LED After [S/cm]	Dark After [S/cm]
Air (1 Minutes)	7.60×10^{-6}	2.50×10^{-6}	1.07×10^{-5}	7.80×10^{-7}

In addition to ambient stability, we also investigated if doping was stable over a period of ~2 days when stored in a nitrogen glovebox. Figure S4.18 gives the conductivity of a 1 mg/mL doped film as a function of time. There does not appear to be any drop in conductivity over the time period measured.

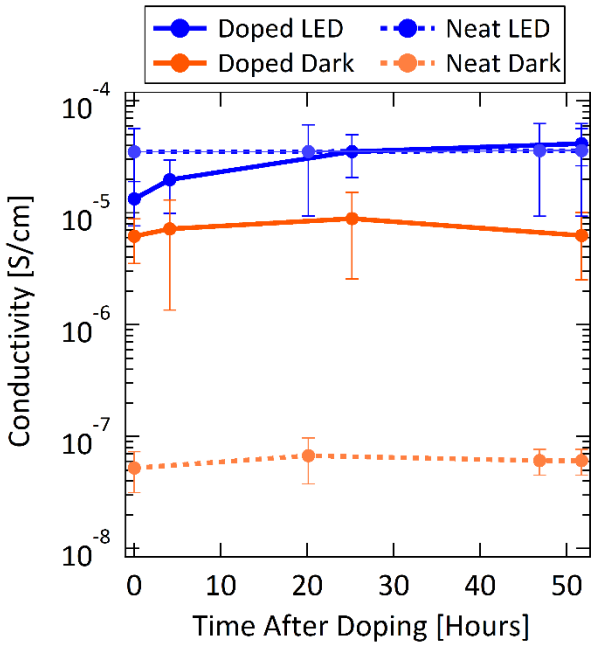

Figure S4.18 Conductivity of a 1 mg/mL doped $MAPbI_3$ film as a function of time. Photoconductivity measurements were performed with illumination from a 525 nm LED with a photon flux of 5.8×10^{17} photons cm^{-2} s^{-1}.

The volatility of small molecule dopants is also important since in several measurements (XPS/UPS and temperature dependent conductivity) were performed under Ultra-high vacuum (UHV). Cobaltocene has a relatively small molecule weight (189.12 g/mol) compared to other *n*-type dopants (examples: decamethylcobaltocene 329.39 g/mol, $[RuCp^*mes]_2$ 712.98 g/mol, N-DMBI 267.37 g/mol), making it a concern that cobaltocene would sublime and undergo reverse charge transfer.[167] In order to determine if cobaltocene is removed from the surface under UHV, we placed a 1 mg/mL doped $MAPbI_3$ film in a thermal evaporator (~10^{-7} Torr) for 40 minutes. Because this required films to be transferred between gloveboxes and the container used to transport them may not have been perfectly air tight, we also include a control of another 1 mg/mL doped $MAPbI_3$ film that was not placed in the thermal evaporator, but was moved with the other film between locations. The photoconductivity and

dark conductivity of this test are given in Table S4.7, which indicates that cobaltocene did not sublime from the surface.

Table S4.7 Photoconductivity and dark conductivity of a film exposed to UHV (~10^{-7} Torr) for 40 minutes. A control is provided since films were moved between gloveboxes and the container used to transport them was not completely air tight. Photoconductivity measurements were performed with illumination from a 525 nm LED with a photon flux of 5.8×10^{17} photons $cm^{-2}\,s^{-1}$.

	LED Initial [S/cm]	Dark Initial [S/cm]	LED After [S/cm]	Dark After [S/cm]
UHV (40 Minutes)	1.1×10^{-5}	5.2×10^{-6}	6.2×10^{-6}	1.6×10^{-6}
UHV Control	1.1×10^{-5}	5.9×10^{-6}	7.6×10^{-6}	2.5×10^{-6}

IX. Electrical Conductivity Measurements: Temperature Dependent Conductivity

The electrical conductivity was measured below 300 K under high vacuum (10^{-5} Torr) to determine the activation energy for both neat $MAPbI_3$ and 1 mg/mL doped $MAPbI_3$ (Figure S4.19). This measurement was performed using two-point probe with a picoammeter. Activation energy was found via fitting the curves to the Arrhenius expression for activated transport: $\sigma = \sigma_0 \times Exp\left[\frac{-E_A}{k_B T}\right]$ from 300 to 260 K (neat $MAPbI_3$) and from 300 to 230°K (1 mg/mL doped $MAPbI_3$).

In order to avoid de-doping due to exposure to air, the 1 mg/mL doped $MAPbI_3$ was encapsulated by spin-coating a layer of Cytop amorphous fluoropolymer resin solution on the film surface following dopant deposition. Cytop spin-coating conditions are as follows: 10 seconds at 1000 rpm with 200 rpm acceleration, followed by 20 seconds at 5000 rpm with a 1000 rpm acceleration. Cytop was subsequently annealed by leaving the film under vacuum in a nitrogen glovebox antechamber for 3 hours. Table S4.8 gives conductivity values of the 1 mg/mL doped $MAPbI_3$ film with Cytop encapsulation both before and after exposure to air. Once the 1 mg/mL doped $MAPbI_3$ sample was under vacuum in the temperature-dependent probe station, the Cytop layer was peeled off in order to ensure good contact between probe needles and gold contact pads.

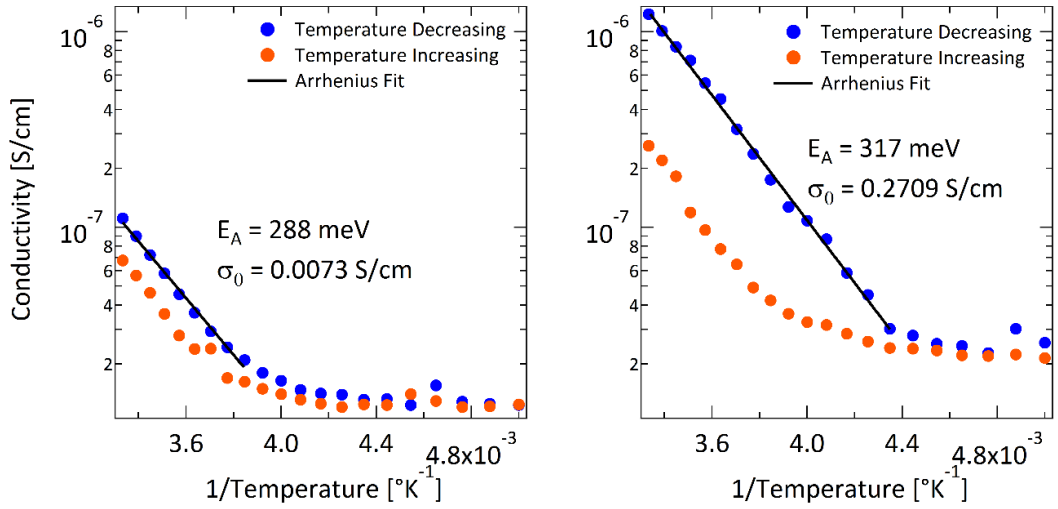

Figure S4.19 Temperature dependent conductivity of (left) neat $MAPbI_3$ and (right) 1 mg/mL doped $MAPbI_3$ films. Fitted parameters from the Arrhenius expression for activated transport are given in each figure. Temperature was measured both in increasing and decreasing directions in order to characterize reversibility of temperature.

Table S4.8 Conductivity values of 1 mg/mL doped $MAPbI_3$ films that have been encapsulated using Cytop using differing annealing methods before and after exposure to air for 1 min. Simple exposure to vacuum after deposition of Cytop successfully encapsulated the doped film. This method was used for transporting doped films to the temperature dependent probe station.

	Nitrogen Environment		1 min Exposure to Air	
Sample	Photoconductivity [S/cm]	Dark Conductivity [S/cm]	Photoconductivity [S/cm]	Dark Conductivity [S/cm]
Doped Film Unencapsulated	$1.3 \times 10^{-5} \pm 4 \times 10^{-6}$	$4.3 \times 10^{-6} \pm 3 \times 10^{-7}$	--	--
Doped Film: Cytop Dried in Antechamber for 3 hours	$1.3 \times 10^{-5} \pm 3\times 10^{-6}$	$2.1 \times 10^{-6} \pm 6 \times 10^{-7}$	$1.9 \times 10^{-5} \pm 5 \times 10^{-6}$	$2.2 \times 10^{-6} \pm 8 \times 10^{-7}$

X. Electrical Conductivity Measurements: Photoconductivity

Photoconductivity Dependence on LED Intensity

A photoconductivity intensity sweep was performed on a neat $MAPbI_3$ film using a 525 nm LED in order to determine what recombination mechanism might dominate at varying photon fluxes (Figure S4.20). Photoexcitation density G was calculated from photon flux using Equation S4.8.

$$G = \frac{1}{120\ \text{nm}} \int_0^{120\ \text{nm}} \alpha N_0 \text{Exp}[-\alpha x]\, dx \qquad \text{S4.8}$$

Where α is the absorption coefficient (here taken to be ~0.5×10^5 at 525 nm light),[4] N_0 is the photon flux at the surface (5.8×10^{17} photons $cm^{-2}\ s^{-1}$), x is the distance into the film, and the total film thickness is 120 nm.

In order to extract information about the recombination mechanism, photoconductivity versus photoexcitation density is fitted to a power law: $\sigma_{PC} \propto G^{\alpha}$ (Figure S4.20). The exponent α= 1, ½ or 1/3 indicates monomolecular, bimolecular and trimolecular decay in the simplest case. Intermediate values indicate a combination of mechanisms. Here α≈0.8 likely indicates a combination of monomolecular and bimolecular decay, thus not all trap states have been completely filled by photo generated carriers. For comparison, studies in literature show varying exponents. Chen et al reported that at G≈10^{19} $cm^{-3}s^{-1}$ α transitioned from α≈½ [below] to α≈1 [above] for a solution grown $MAPbI_3$ thin film.[229] In contrast, Igal et al. reported α≈0.4 for $MAPbI_3$, but determined that this was the result of the presence of a recombination center a few k_BT above the Fermi level by incorporating information about the minority carrier lifetime.[194].

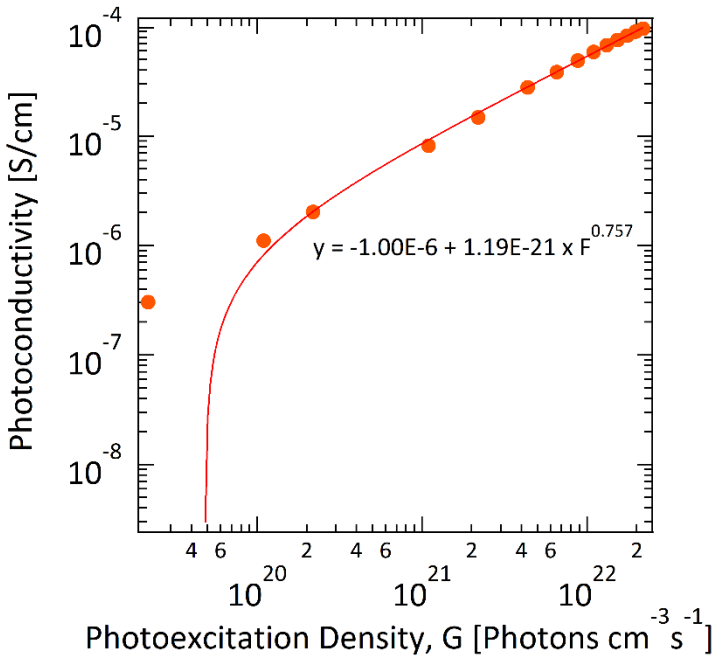

Figure S4.20 Power law ($\sigma_{PC} \propto G^{\alpha}$) fits to extract the light exponent factor α from photoconductivity versus photoexcitation density G of neat $MAPbI_3$. The extracted light exponent factor α is ≈0.8, indicating bimolecular and monomolecular decay.

Light Soaking

A light soaking experiment was performed in order to establish the stability of doped $MAPbI_3$ films under constant irradiation. In this experiment $MAPbI_3$ films were illuminated with a 525 nm LED with a photon flux of 5.8 $\times 10^{17}$ photons cm^{-2} s^{-1} for 90 minutes with photoconductivity measured every 5 minutes. Both neat $MAPbI_3$ and 0.5 mg/mL doped $MAPbI_3$ films show a decrease in photoconductivity by ~12% and 17% respectively over the course of this time (the contact appears to have moved for the neat $MAPbI_3$ film, which was taken into account). Light-soaking has been suggested as an effect of trap-assisted recombination.[230] There does not appear to be evidence for surface doping reducing this process at 0.5 mg/mL doped $MAPbI_3$ film.

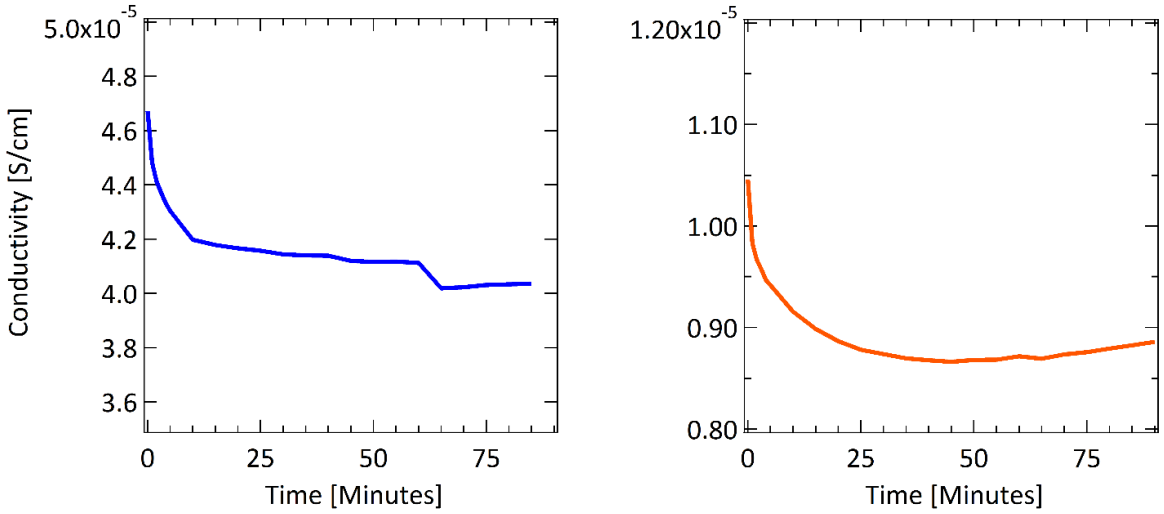

Figure S4.21 Photoconductivity of (left) neat $MAPbI_3$ and (right) 0.5 mg/mL doped $MAPbI_3$ over a period of 90 min constant illumination of 525 nm light with a photon flux of 5.8×10^{17} photons $cm^{-2}\ s^{-1}$.

Persistent Photoconductivity

Persistent photoconductivity is caused by internal and surface deep-level defects and can result in photodetectors that suffer from slow responses of several seconds or longer.[231] Organic metal halide are dominated by shallow defects, typically resulting in photodetectors with a response time of less than 20 µs.[231] Despite this low number, we still checked to ensure that persistent photoconductivity does not cause artifacts that resemble doping. Conductivity of a 1 mg/mL doped $MAPbI_3$ film was measured in the dark, then under illumination (525 nm LED with a photon flux of 5.8×10^{17} photons $cm^{-2}\ s^{-1}$), then in the dark once more. The results of this test are given in Table S4.9. There is very little variation between dark conductivity before and after illumination, suggesting that persistent photoconductivity is not responsible for the increases in conductivity we see upon deposition of cobaltocene.

Table S4.9 Dark conductivity before and after photoconductivity measurement.

	Dark Initial	LED Illumination	Dark After
Conductivity [S/cm]	2.1×10^{-6}	4.8×10^{-6}	2.3×10^{-6}

XI. Photoluminescence Measurements

Photoluminescence (PL) measurements were carried out on a Horiba FluoroMax 4 spectrometer calibrated using Milli-Q water. Films were deposited on z-cut quartz as described and encapsulated using Cytop amorphous fluoropolymer resin that was dried under vacuum for 3 hours. Films were loaded into a thin-film sample stage angled at 60° between the excitation and emission port. All measurements were performed with an excitation wavelength of 450 nm using a consistent slit size. In order to limit effects of Rayleigh scattering at long wavelengths, a long-pass filter slightly above the excitation wavelength (455 nm) was placed in front of the emission port.

Appendix C

Supporting Information for

Systematic Study of Doping Concentration of the Electron Transport Layer on the Performance of Perovskite Solar Cells

Table of Contents

I. GIWAXS of Neat PDI-2T Showing Glassy Characteristics

X-ray scattering was conducted on beamline 7.3.3 at the Advanced Light Source (ALS). Silver behenate was used as a calibration for the beam center and sample-to-detector distance. 2D GIWAXS scattering images were collected using a Pilatus 2 M area detector at an incidence angle of 0.20°.The samples were kept under a helium environment during X-ray exposure to minimize sample degradation and scattering from O_2. The collected data were processed using Nika, a 2D data reduction macro on IgorPro using established procedures.1D profiles along the in-plane direction were created by plotting intensities along line cuts near q_{xy}= 0. To correct for the grazing incidence geometry, scattering intensity was integrated along a small sector near the missing wedge to obtain 1D profiles near q_Z=0.

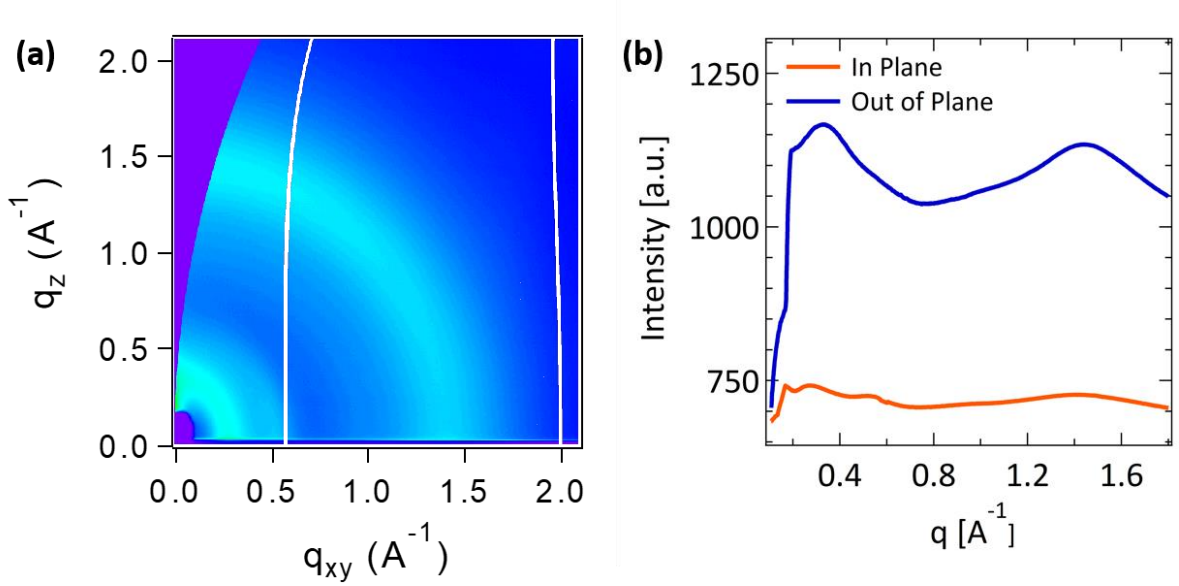

Figure S5.1 The 2D GIWAXS of neat PDI-2T indicates that it is a glassy polymer due to the diffuse scattering features. GIWAXS patterns given include (a) 2D images and (b) 1D linecuts.

II. General Film Preparation

Several types of substrates (quartz, ITO coated glass and silicon with either native oxide or thermally grown 200 nm SiO_2), measuring 1.5 cm × 1.5 cm, were used for these experiments. All substrates were cleaned in an ultrasonic bath in soapy water, water, acetone and isopropanol for 20 minutes then treated with an oxygen plasma for 180 seconds.

Films of $MAPbI_3$ were fabricated using a 1 Molar solution of 1:1 ratio of PbI_2: MAI in a 1:10.4 ratio (by volume) of DMSO: DMF. Precursors were purchased according from the following list: methylammonium iodide (Dysol), lead iodide (Aldrich) and DMSO (Aldrich) and anhydrous DMF (Aldrich). The solution was spin-coated onto substrates with the following conditions: (1) 2 seconds at 1000 rpm with 1000/s rpm acceleration (dust spin off step), (2) 5 seconds at 0 rpm with 4000/s rpm acceleration, (3) 13 seconds at 2000 rpm with 330/s rpm acceleration, followed by (4) 30 seconds at 4000 rpm with a 3000/s rpm acceleration. $MAPbI_3$ precursor solution is dropped on the substrate surface once 1000 rpm has been achieved in step (3). An anti-solvent of 200 μL of chlorobenzene is dropped on the film surface during step (4) between 23 and 21 seconds prior to completion. The film immediately undergoes annealing at 100°C for 10 min. This results in $MAPbI_3$ films that are ~450 nm thick.

PDI-2T (1-Material Inc.) was dissolved in a chlorobenzene solution at 9 mg/mL loading (solar measurements were made with 2× loading) with dopant concentrations of 0 wt%, 0.1 wt%, 1 wt% and 10 wt%. The solution was spin-coated onto substrates with the following conditions: (1) 6 seconds at 200 rpm with 1000/s rpm acceleration, (2) 60 seconds at 1000 rpm with 1000/s rpm acceleration, followed by (3) 3 seconds at 3000 rpm with 1000/s rpm acceleration.

III. Steady-State Photoluminescence of PDI-2T & PDI-2T/$MAPbI_3$ Bilayers

A. Description of Experimental Setup

Steady-state photoluminescence (SS-PL) measurements were carried out on a Horiba FluoroMax 4 spectrometer calibrated using Milli-Q water. Films were deposited on z-cut quartz and encapsulated using Cytop amorphous fluoropolymer resin that was dried under vacuum for 3 hours. Films were loaded into a thin-film sample stage angled at 60° between the excitation and emission port. All measurements were performed with an excitation wavelength of 450 nm using a consistent slit size. In order to limit effects of Rayleigh scattering at long wavelengths, a long-pass filter slightly above the excitation wavelength (455 nm) was placed in front of the emission port.

B. Steady-State Photoluminescence in Thin Films

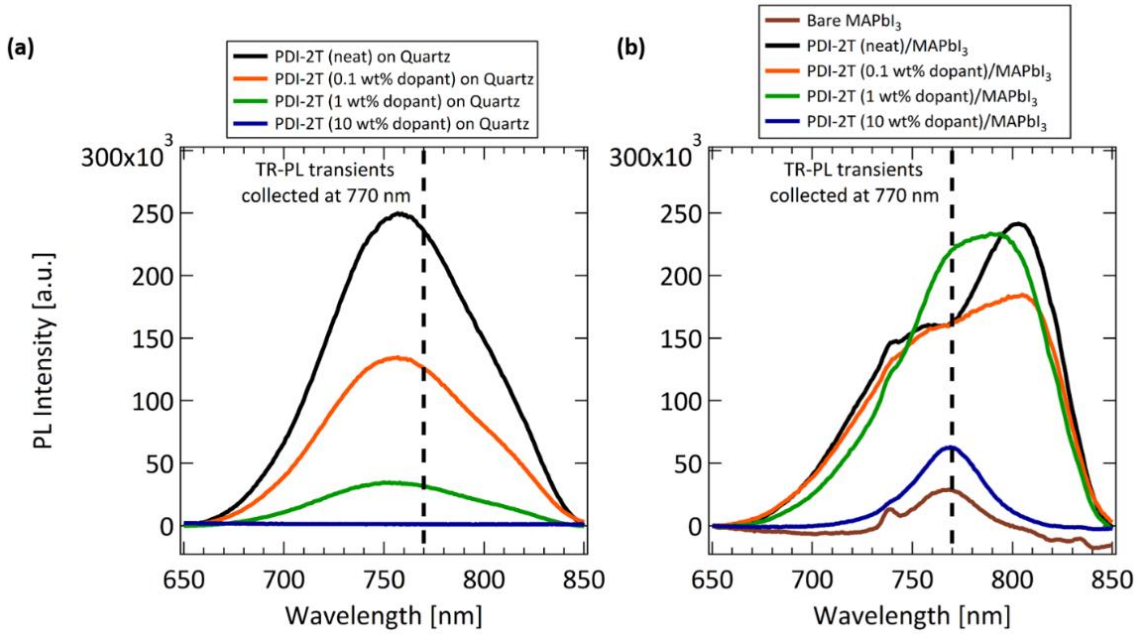

Figure S5.2 Steady-state photoluminescence (SS-PL) of thin film samples, including (a) PDI-2T on quartz and (b) PDI-2T/$MAPbI_3$ bilayers. PDI-2T on quartz shows PL intensity due to the perylene diimide unit, which is quenched upon doping. For PDI-2T/$MAPbI_3$ bilayers, there is a red-shift relative to $MAPbI_3$ for neat/low doping concentrations. Other studies on the passivation effect of PCBM on $MAPbI_3$ reported a blue-shift (from 782 to 775) that was attributed to passivation of trap states the lead to radiative recombination.[48,232] In contrast, no shift was observed in $MAPbI_3$ films passivated with the Lewis base pyridine.[59] This inconsistency may be a result of the mechanism for surface passivation: PCBM is believed to be adsorbing onto Pb-I antistite defective grain boundary, and Lewis bases are passivating dangling Pb atoms through coordination or bond formation. The black dashed line indicates the wavelength (770 nm) that transients were collected at in time-resolved photoluminescence (TR-PL). There is PL signal for PDI-2T that is quenched upon doping at this wavelength, which was relevant to analysis of the fast decay component of TR-PL.

C. Steady-State Photoluminescence in Solution

The charge transfer mechanism could have two potential routes: (1) charge transfer is occurring directly from the small molecule dopant to the perovskite surface (which is a possible reaction given the increase in conductance seen upon surface doping or (2) the dopant charge transfers to PDI-2T which subsequently Fermi equilibrates with the $MAPbI_3$ surface. In order to determine the mechanism, solution steady-state photoluminescence (SS-PL) was performed to compare the intensity of PDI-2T (neat) versus PDI-2T (1 wt% dopant) in chlorobenzene. SS-PL of PDI-2T thin films showed a dramatic decrease in peak intensity upon doping, which was also observed in solution. This confirms that the doping process is completed in solution prior to spin casting. This result is consistent with that seen by the Marder group for a similar class of organometallic dimer dopants.[98]

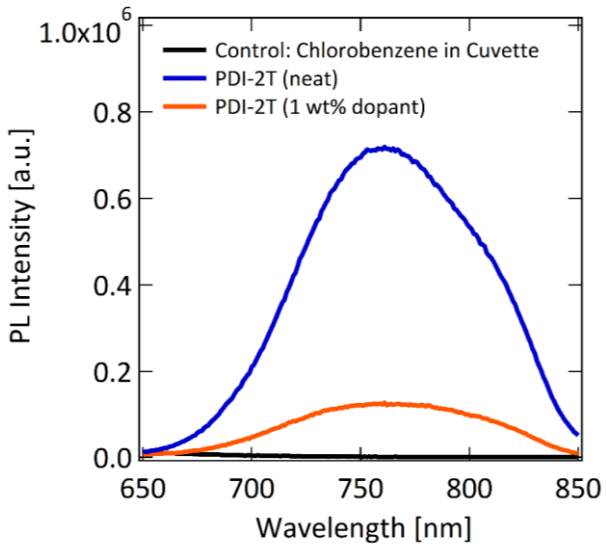

Figure S5.3 Solution steady-state photoluminescence of PDI-2T (neat) versus PDI-2T (1 wt% dopant). The lower PL intensity of PDI-2T (1 wt% dopant) indicates that the charge transfer mechanism of $(2\text{-Cyc-DMBI})_2$ to PDI-2T occurs in solution.

IV. Electron Paramagnetic Resonance Measurement of Carrier Concentration

Electron Paramagnetic Resonance (EPR) measurements were performed with a Bruker EMX X-Band EPR. EPR samples were prepared by depositing films onto quartz microscope cover slides with dimensions 2 × 2 cm. Samples were cleaved using a diamond scribe into approximately 1.5 cm × 3 mm wide pieces, prior to being inserted into low pressure/vac Suprasil® EPR sample tubes that were used in order to maintain nitrogen atmosphere. Samples were then transferred outside the glove box and the EPR spectra was measured immediately. Quantitative determination of the spin concentration was obtained by comparing samples to a reference sample of 2,2-diphenyl-1-picrylhydrazyl (DPPH) with a known spin concentration. This required both the integrated spin intensity, quality factor, power and volume of both samples and DPPH reference. Sample volumes were found by taking the area of the substrate determined using a micrometer and film thickness determined by AFM (films were 69, 75, 57 and 67 nm thick respectively for PDI-2T (neat), PDI-2T (0.1 wt% dopant), PDI-2T (1 wt% dopant) and PDI-2T (10 wt% dopant) respectively). Only doping concentrations of PDI-2T (1 wt% dopant) and PDI-2T (10 wt% dopant) had carrier concentrations that were above the measurement threshold of our EPR apparatus ~10^{18} carriers/cm^3. Their carrier concentrations are given in Table S5.1. Reported values were obtained from the average of two samples.

Table S5.1 Carrier concentrations obtained from EPR for PDI-2T samples cast on quartz substrates.

Sample	Carriers/cm^3
PDI-2T (1 wt% dopant)	$9.85\times10^{19} \pm 3.77\times10^{19}$
PDI-2T (10 wt% dopant)	$1.23\times10^{21} \pm 1.16\times10^{20}$

Spin to Monomer Unit Ratio Estimation

To approximate the spin to monomer unit ratio, an estimation was made for the monomer density of PDI-2T. This was made assuming a mass density of 1.1 to 1.2 g/cm^3, which is typical of polymers. A better estimate was difficult based on the structural ordering of PDI-2T as the GIWAXS indicated a glassy polymer. The molecular mass of PDI-2T of 1085 g/mol and Avagadro's number is 6.022×10^{23} mol^{-1}. Monomer density approximations are as follows:

$$\frac{1.1\frac{\text{g}}{\text{cm}^3}}{1085.6\frac{\text{g}}{\text{mol}}}\times 6.022\times10^{23}\,\frac{\text{monomers}}{\text{mol}} = 6.1\times10^{20}\,\frac{monomers}{cm^3}$$

$$\frac{1.2\frac{\text{g}}{\text{cm}^3}}{1085.6\frac{\text{g}}{\text{mol}}}\times 6.022\times10^{23}\,\frac{\text{monomers}}{\text{mol}} = 6.6\times10^{20}\,\frac{monomers}{cm^3}$$

Using this approximation for monomer density and the spin density obtained from EPR, the spin per monomer unit ratio are estimated in the range of 0.15:1 and 0.16:1 for 1 wt% and 1.86:1 and 2.0:1 for 10 wt%.

V. Optical Absorption

Thin film absorption measurements were conducted with an Ocean Optics HR2000+ High resolution spectrometer with a DH-2000 UV-VIS-NIR Light Source. Samples were cast on z-cut quartz substrates (University Wafer). The measurement was made in a nitrogen glovebox in order to prevent potential de-doping reactions of the films with air.

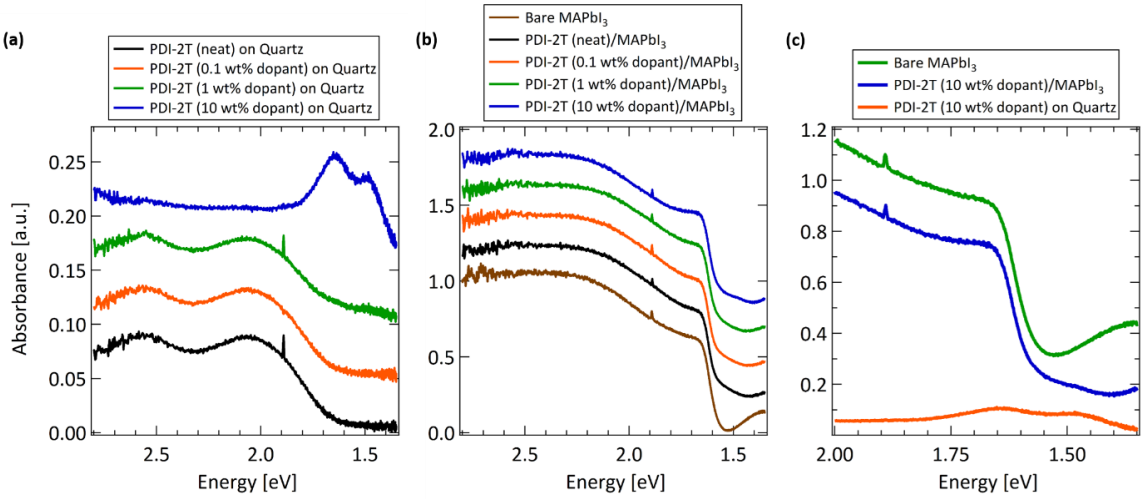

Figure S5.4 Optical absorption of (a) PDI-2T on quartz and (b) on $MAPbI_3$ and (c) an overlay of PDI-2T (10 wt% dopant) on quartz and $MAPbI_3$. For PDI-2T on quartz, the optical gap is around ~1.6 eV. At low doping concentration there a neutral polymer transition at ~2.0 eV with limited bleaching upon doping for 0.1 wt% and 1 wt%. For 10 wt%, the neutral polymer peak has been completely bleached and a new transition has emerged at ~1.6 eV, which is the result of heavy doping. The emergence of this transition may also be present at 1 wt%. For PDI-2T/$MAPbI_3$ bilayers, optical absorption indicates that there is no degradation of the bulk with ETL deposition. This observation is most relevant for PDI-2T (10 wt% dopant) as it is the likeliest to experience degradation due to heavy doping.

VI. Additional Details of Solar Cell Performance

A. Solar Cell Device Preparation

Solar cells were made using inverted architectures of Glass/ITO/PTAA/$MAPbI_3$/PDI-2T (neat or doped with $(2\text{-Cyc-DMBI})_2$)/PEIE/Ag. Photovoltaic devices were prepared according to the following procedure. ITO coated glass substrates (University Wafer) were sequentially cleaned in an ultrasonic bath of soapy water, water, acetone and isopropanol for 20 minutes then treated with an oxygen plasma for 180 seconds. Substrates were then transferred into a nitrogen environment. The hole transport layer (HTL) was deposited using a solution of 2 mg/mL polytriarylamine (PTAA, Aldrich) in chlorobenzene (Aldrich) that was spun-cast onto the substrates at 6000 rpm. The $MAPbI_3$ layer was deposited according to the description in the previous section on general film preparation. The electron transport layer was deposited using a solution of 18 mg/mL PDI-2T in chlorobenzene that was spun-cast onto the substrates at 1000 rpm. PEIE in isopropyl alcohol (0.02 wt%, diluted from 37% aqueous solution of PEIE from Aldrich) was deposited at 6000 rpm. The devices were finally capped with Ag (80 nm) by thermal evaporator deposition.

In order to illustrate the importance of doping in thicker ETLs layers, solution loadings of 18 mg/mL were used in this measurement. This is in contrast to other measurements in this study that were performed using a 9 mg/mL solution. An example cross-sectional SEM of PDI-2T (18 mg/mL loading) on $MAPbI_3$ is given in Figure S5.5, which indicates an ETL thickness of ~170 to 190 nm.

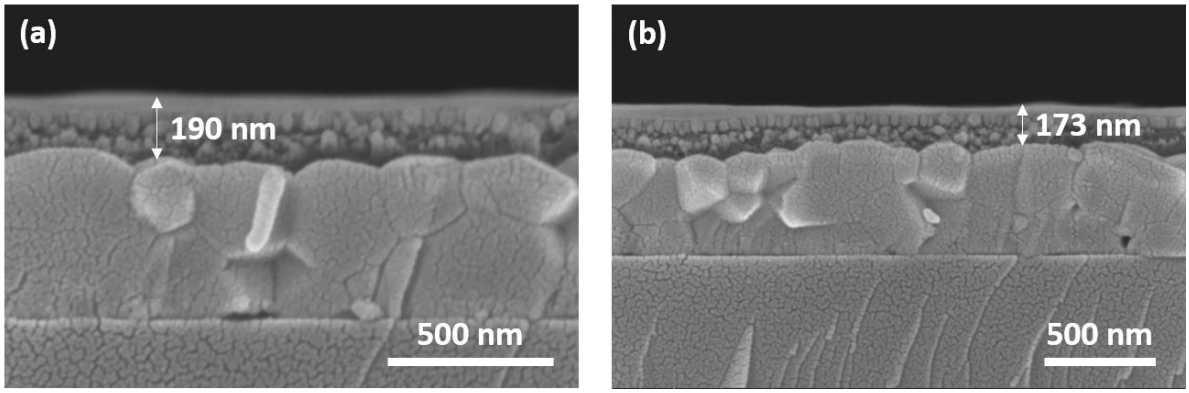

Figure S5.5 Cross-sectional SEM of the PDI-2T/$MAPbI_3$ bilayer at the PDI-2T loading (18 mg/mL) used in solar cell devices. This loading produces ETLs that are 170 to 190 nm thick, which is similar to thickness that would be used in commercial devices.

B. Solar Cell Performance Characterization

The *J–V* characteristics were measured at 1 sun illumination (AM 1.5G, 100mW/cm^2) in a N_2-filled glovebox with a solar simulator equipped with a Xenon lamp (Newport), a Keithley 2602 Source Meter and a calibrated silicon reference cell. The power conversion efficiency (PCE) was calculated with the following equation: PCE (%) = 100 × V_{OC} × J_{SC} × FF / P_{inc} from the open circuit voltage, V_{OC}, the short circuit current, J_{SC}, the fill factor FF and the incident powder P_{inc}.

The external quantum efficiency (EQE) was analyzed using a fully computerized measurement system consisting of a 300-W xenon lamp (Newport), a monochromator (Newport CS130), a chopper controller (Newport), two current preamplifiers (SRS SR570), and two lock-in amplifiers (SRS SR810).

C. V_{OC} and J_{SC} in Greater Detail

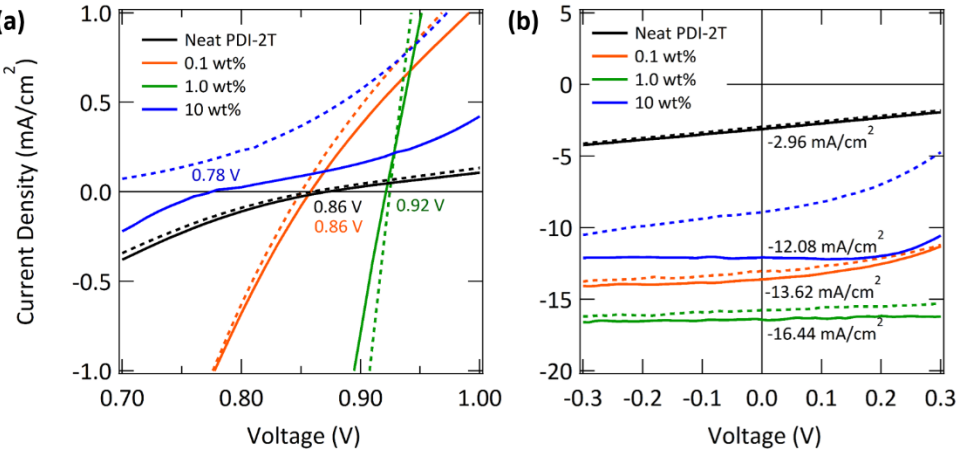

Figure S5.6 Greater resolution plots of J-V curve in Figure 5.4 around the (a) V_{OC} and (b) J_{SC}. The reverse scan (1.3 to -0.5 V) is denoted as solid lines.

D. External Quantum Efficiency (EQE)

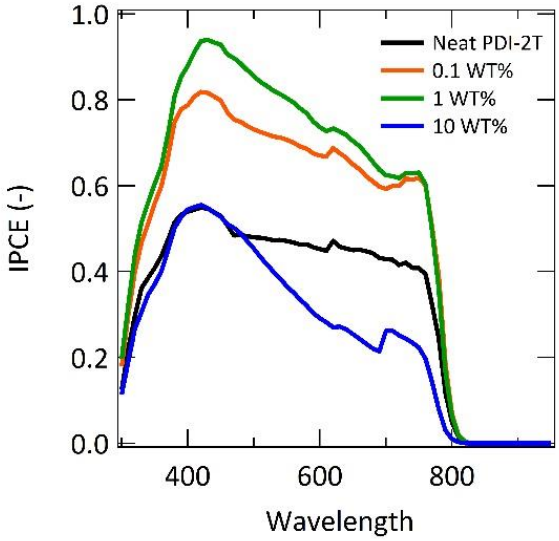

Figure S5.7 External Quantum Efficiency (EQE) of the same solar cell devices as the measurement of the J-V curve in Figure 5.4. The EQE has some inconsistencies with the J-V curve, notably the EQE for PDI-2T (1 wt% dopant) is near 90% despite a moderate PCE of 8.3%. This is a result of our setup measuring EQE at lower light intensities. There appears to be a gap state emerge around 710 nm for ETL of doped PDI-2T.

E. Light Intensity of V_{OC}

Light intensity of V_{OC} was measured using a 525 nm (or 2.36 eV) LED with a maximum power resulting in a photon flux at the surface of 5.8 $\times 10^{17}$ photons cm^{-2} s^{-1}. V_{OC} measurements were performed on the same devices used for the J-V characteristics in Figure 5.4, albeit were measured ~1 week later. The light dependence of the V_{OC} is fit to a model used to extract the diode ideality factor n_{id} according to $\frac{d\,V_{oc}}{d\,\ln(\Phi)} = \frac{k\,T}{q} n_{id}$. The magnitude of the diode ideality factor does not directly correlate to the quality of the solar cell, instead it is used to identify what surface or bulk recombination processes are dominant. Diode ideality factors of $n_{id} = 1$ indicate bulk bimolecular recombination, whereas $n_{id} = 2$ indicate recombination via trap sites in the band gap. Diode ideality factors < 1 indicate that surface recombination is dominant.

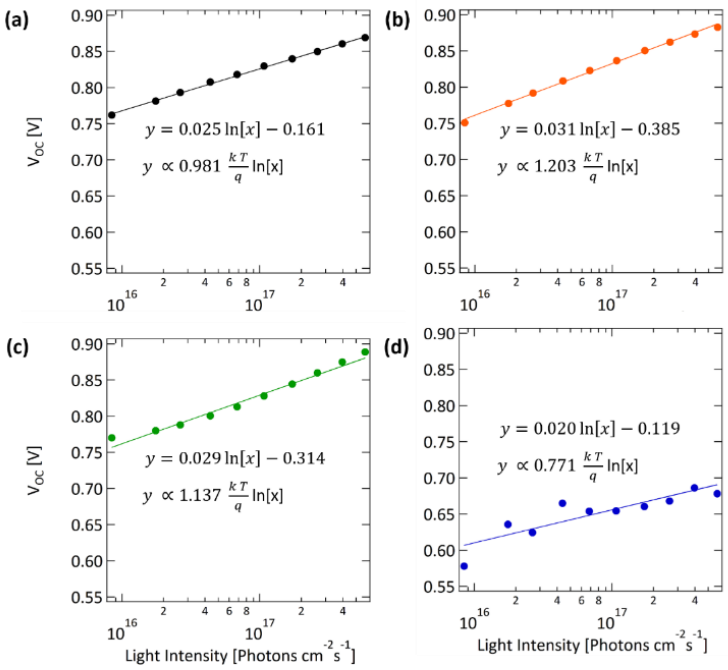

Figure S5.8 Light intensity of the V_{oc} for solar cells with ETLs of (a) PDI-2T (neat), (b) PDI-2T (0.1 wt% dopant), (c) PDI-2T (1 wt% dopant) and (d) PDI-2T (10 wt% dopant). The diode ideality factors for neat, 0.1 wt%, 1 wt% and 10 wt% are 0.98, 1.20, 1.14, and 0.77 respectively. As there is hysteresis for the PDI-2T (10 wt% dopant) ETL solar cell, extraction of the diode ideality factor will likely vary with sweep conditions.

VII. Lateral Conductivity Measurements

A. Details of Experimental Setup

Conductivity values were measured using a two-point probe method using a picoammeter due to the high resistance of the $MAPbI_3$ films. For PDI-2T on quartz, contact pads were evaporated onto the PDI-2T surface. Whereas for PDI-2T on $MAPbI_3$, contact pads were deposited onto the $MAPbI_3$ surface prior to PDI-2T deposition. Gold contact pads of 80 nm thicknesses were deposited onto films using a shadow mask in a thermal evaporator in a collinear geometry with spacings of 200 μm between electrodes that were 1000 μm long. In order to correct for effects of contact resistance, two-point probe conductivity was measured for three contact spacings: 200, 500, and 800 μm. Conductivity values are reported according to $\sigma = \frac{Sheet\ Conductance}{Film\ thickness}$, where sheet conductance is determined by the slope of individual device conductance versus ratio of distance: width of contacts. Film thickness was obtained using AFM for PDI-2T on quartz and cross-sectional SEM for PDI-2T on $MAPbI_3$.

Error bars in Figure 5.6 are determined from three devices each on two separate films (6× total measurements). The conductivity was measured for each $MAPbI_3$ device both prior to and after ETL deposition. Conductivity measurements done prior to ETL deposition were made in order to account for film-to-film variation.

B. X-sectional SEM of PDI-2T on $MAPbI_3$

A FEI Nova Nano 650 FEG SEM scanning electron microscope was used to image the cross section of PDI-2T/$MAPbI_3$ bilayers on silicon substrates. Images are of 9 mg/mL loading, which was the concentration used for all measurements used besides solar cell performance (18 mg/mL) and XPS of patchy coverage (0.5 mg/mL).

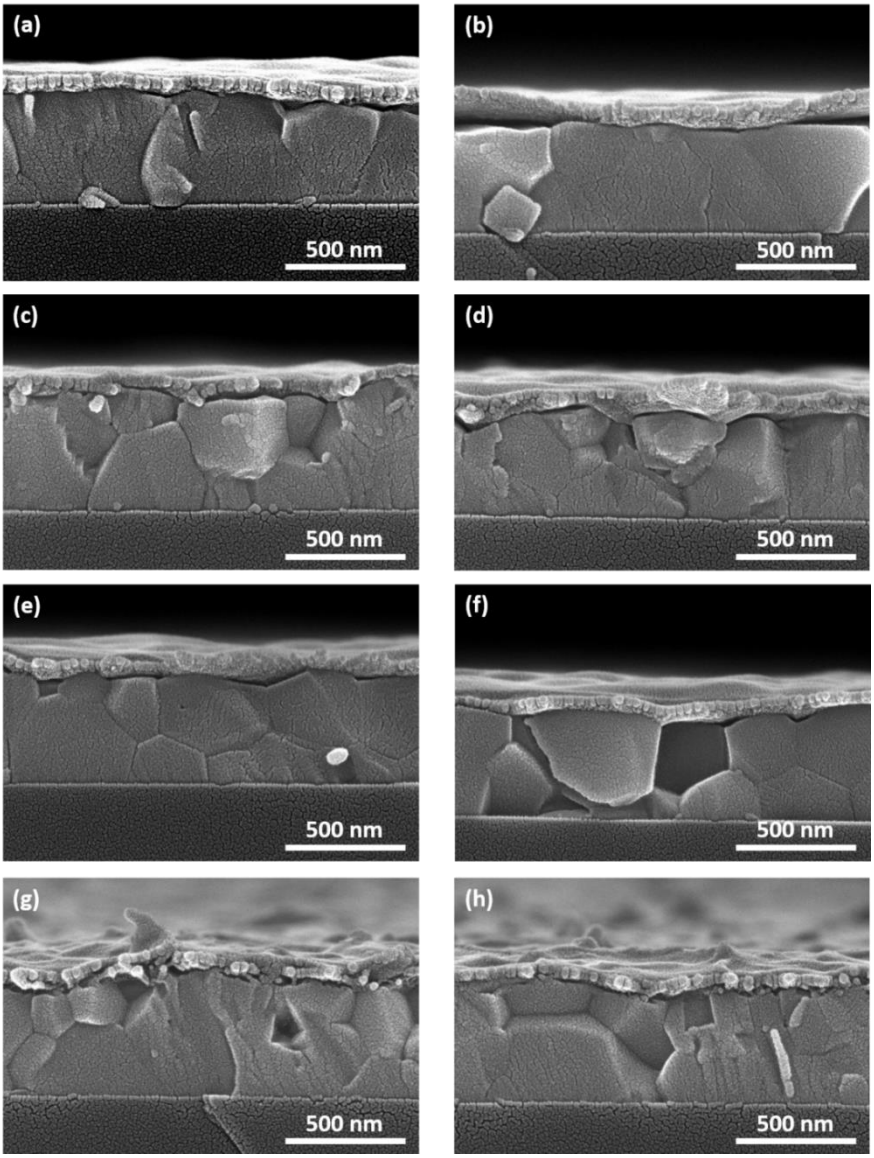

Figure S5.9 Cross-sectional SEM images of PDI-2T/ $MAPbI_3$ bilayers with doping levels of (a) & (b) PDI-2T (neat), (c) & (d) PDI-2T (0.1 wt% dopant), (e) & (f) PDI-2T (1 wt% dopant), and (g) and (h) PDI-2T (10 wt%. dopant). SEM images provide information about planarization and roughness of PDI-2T on $MAPbI_3$. Planarization is relevant to whether the underlying roughness of $MAPbI_3$ is causing scattering of charge carriers in the conductivity measurement. Roughness, which appears present at PDI-2T (10 wt% dopant) due to heavy doping, is relevant to the quality of contact at PDI-2T/$MAPbI_3$ and PDI-2T/Ag interfaces, which impacts charge transfer ability.

C. Roughness of $MAPbI_3$ Surface

An Asylum MFP-3D atomic force microscope was used to measure the topography of a $MAPbI_3$ film cast on a quartz substrate. Line cuts were taken of these images to provide example cross-sectional height profiles indicating film roughness.

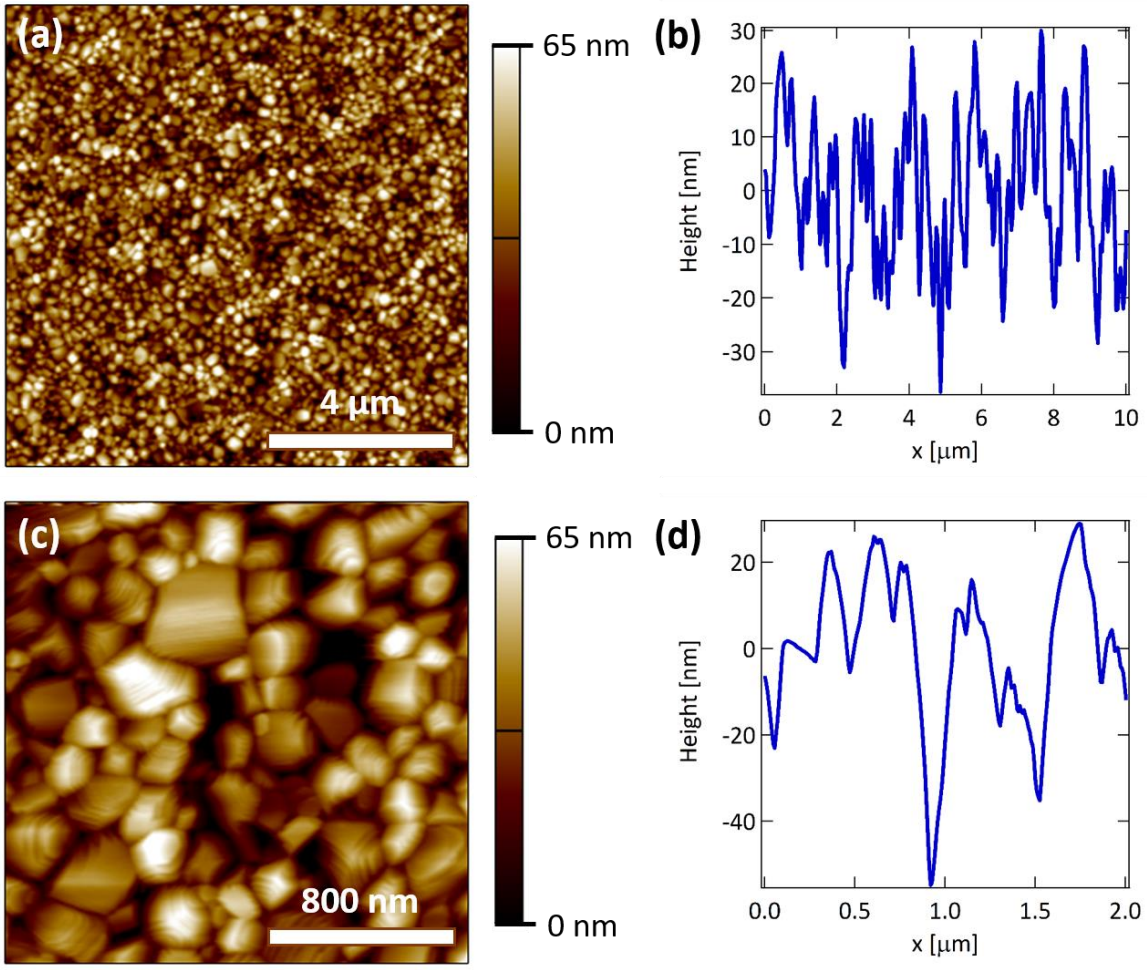

Figure S5.10 Atomic force microscopy of $MAPbI_3$ (a) & (c) and accompanying cross-sectional height profile (b) & (d). Images were taken from a good quality film (no cloudiness) in two different locations. Image (c) was taken over a small length scale so that roughness can be more easily compared to cross-sectional SEM images of PDI-2T/$MAPbI_3$ bilayers (Figure S5.9).

D. Surface doping $MAPbI_3$ with $(2\text{-Cyc-DMBI})_2$

In our previous surface doping study, thinner $MAPbI_3$ films of ~120 nm were used as they were conducive to seeing changes in surface conductance upon doping. The films used in this study are thicker ~450 nm in order to improve solar cell performance. Consequently if conductivity values from the surface doping study are to be compared, different values would be seen given that only the top few nanometers are doped. Below, we show that the dopant used in this study $(2\text{-Cyc-DMBI})_2$ can also dope the surface of $MAPbI_3$ via a charge transfer reaction. The conductivity value of surface doping with 1 mg/mL cobaltocene from our previous study is depicted using a black dashed line. If it were assumed that the films used in that study were instead 450 nm thick, then a lower conductivity value would be obtained, which is depicted by the red dashed line. This value is similar to that obtained for the dopant/film thickness used in this study.

Recently there have been studies suggesting that additional energy activation (most often in the form of light or heat) is sometimes needed for the charge transfer reaction to occur.[73] We show that the charge transfer reaction here can proceed without requiring extra energy (we used annealing at 60°C for 10 minutes).

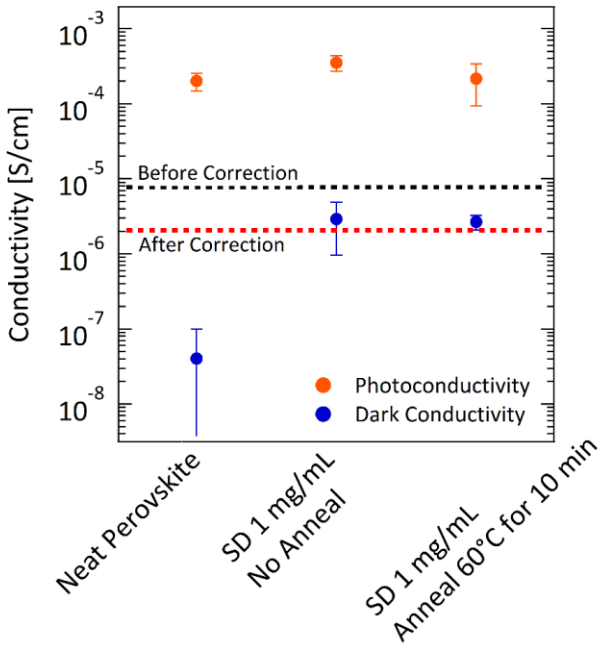

Figure S5.11 Conductivity of $MAPbI_3$ surface doped with 1 mg/mL $(2\text{-Cyc-DMBI})_2$. For reference, the conductivity values from our previous surface doping study are depicted as dashed lines, including both the value reported using a 120 nm thick film (black) and the value if a correction were to be made assuming a thicker film of 450 nm (red).

VIII. Photoelectron Spectroscopy (UPS, IPES, XPS)

A. Details of Experimental Setup

UPS measurements were performed by the Graham Group at University of Kentucky. Films were cast on gold coated 10 × 10 mm crystalline silicon substrate. Transport of samples between the spin coater and UPS/XPS/IPES apparatus was done entirely under nitrogen atmosphere. ETL layers were cast on $MAPbI_3$ immediately before transferring to the Ultra High Vacuum (UHV) chamber. UPS measurements were conducted in a PHI 5600 UHV system with an 11 inch diameter hemispherical electron energy analyzer with multichannel detector. The photon source for the UPS measurements was an Excitech H Lyman-α lamp (E-LUXTM121) coupled with a 900 ellipsoidal mirror (E-LUXTM EEM Optical Module) with a dry oxygen purge of the beam path at 7.5 - 8.5 Torr.[117] All UPS measurements were recorded with -5 V sample bias and a pass energy of 5 eV. IPES measurements were performed using the Bremsstrahlung isochromat mode with electron kinetic energies below 5 eV to minimize sample damage. The low energy electron beam was generated using a Kimball Physics ELG-2 electron gun equipped with a low temperature (1150K) BaO cathode. Emitted photons were collected and focused with a fused silica bi-convex lens into the photon detector that consisted of an optical bandpass filter (214 nm, Andover Corporation) and a photomultipler tube (R585, Hamamatsu Photonics). The IPES measurement was performed with a custom LabVIEW program. During all IPES measurements the UHV chamber was blacked-out to exclude external light and samples were held under a -20 V bias.

The equations used to determine the energy levels in Figure 5.2 and 5.7 are given by the following: the Ionization Potential is defined as $IP = h\nu - |E_{SEE} - E_{VBE}|$, the Work Function is defined as $WF = h\nu - E_{SEE}$, and the Electron Affinity EA is determined directly from IPES.

For IPES, a correction must be applied to the collected spectra according to 4.428 eV- Intercept = EA, where 4.428 eV is the center energy of the band pass filter used in the IPES apparatus.

B. UPS of PDI-2T (single layer)

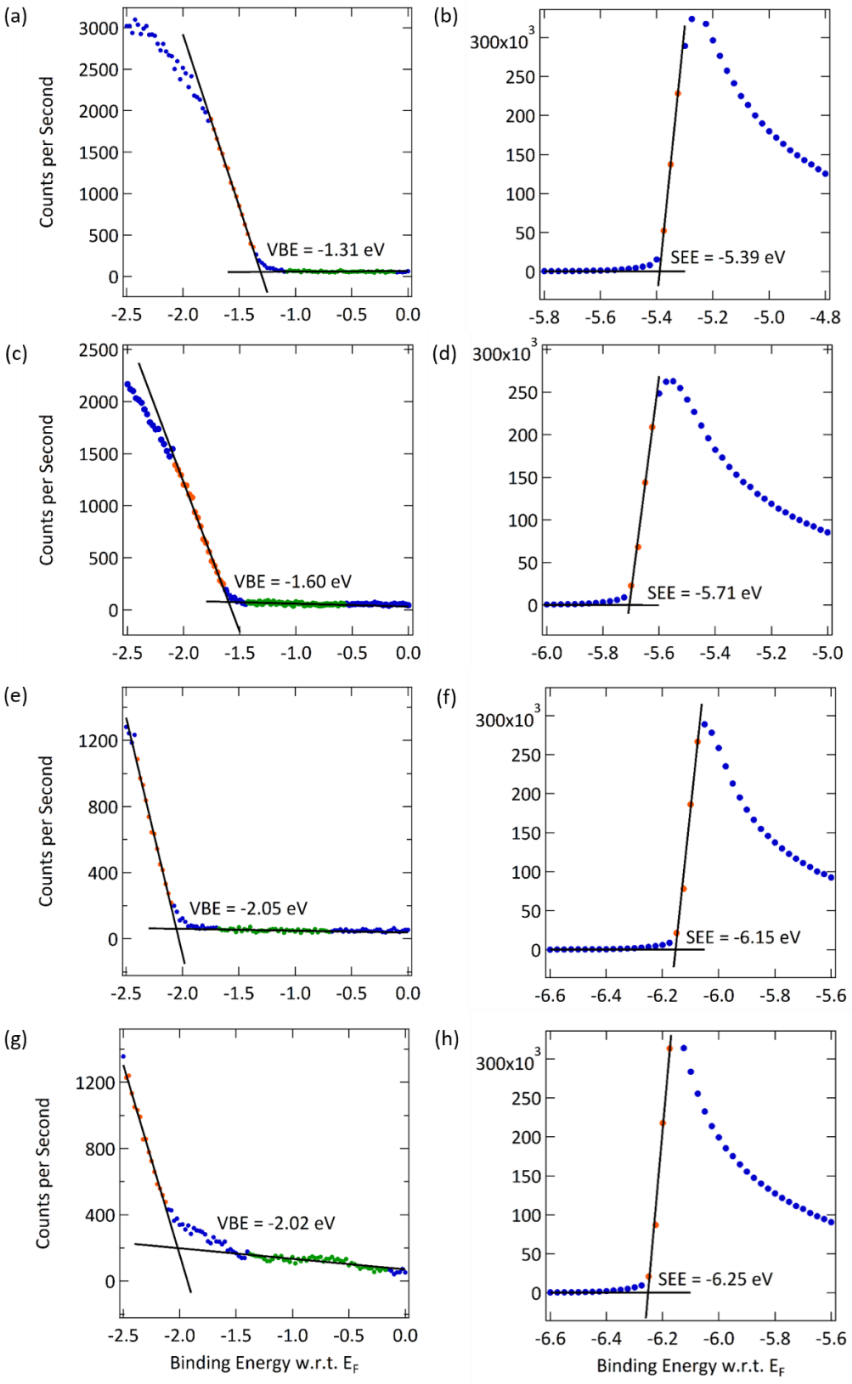

Figure S5.12 UPS spectrums of PDI-2T (single layer) (underlying Au substrate) showing how the valence band edge (VBE) and secondary electron edge (SEE) were defined: (a) PDI-2T (neat) VBE, (b) PDI-2T (neat) SEE, (c) PDI-2T (0.1 wt% dopant) VBE, (d) PDI-2T (0.1 wt% dopant) SEE, (e) PDI-2T (1 wt% dopant) VBE, (f) PDI-2T (1 wt% dopant) SEE, (g) PDI-2T (10 wt% dopant) VBE, and (h) PDI-2T (10 wt% dopant) SEE.

Table S5.2 Summary of extracted energy levels for PDI-2T (single layer) including: valence band edge (VBE), secondary electron edge (SEE), work function (WF), and ionization potential (IP).

Sample	VBE (eV)	SEE (eV)	WF (eV w.r.t. Vac)	IP (eV w.r.t Vac)
Neat	-1.31	-5.39	-4.83	-6.14
0.1 wt%	-1.60	-5.71	-4.51	-6.11
1 wt%	-2.05	-6.15	-4.07	-6.12
10 wt%	-2.02	-6.25	-3.97	-5.99

C. UPS/IPES Fits of PDI-2T/$MAPbI_3$ Bilayer

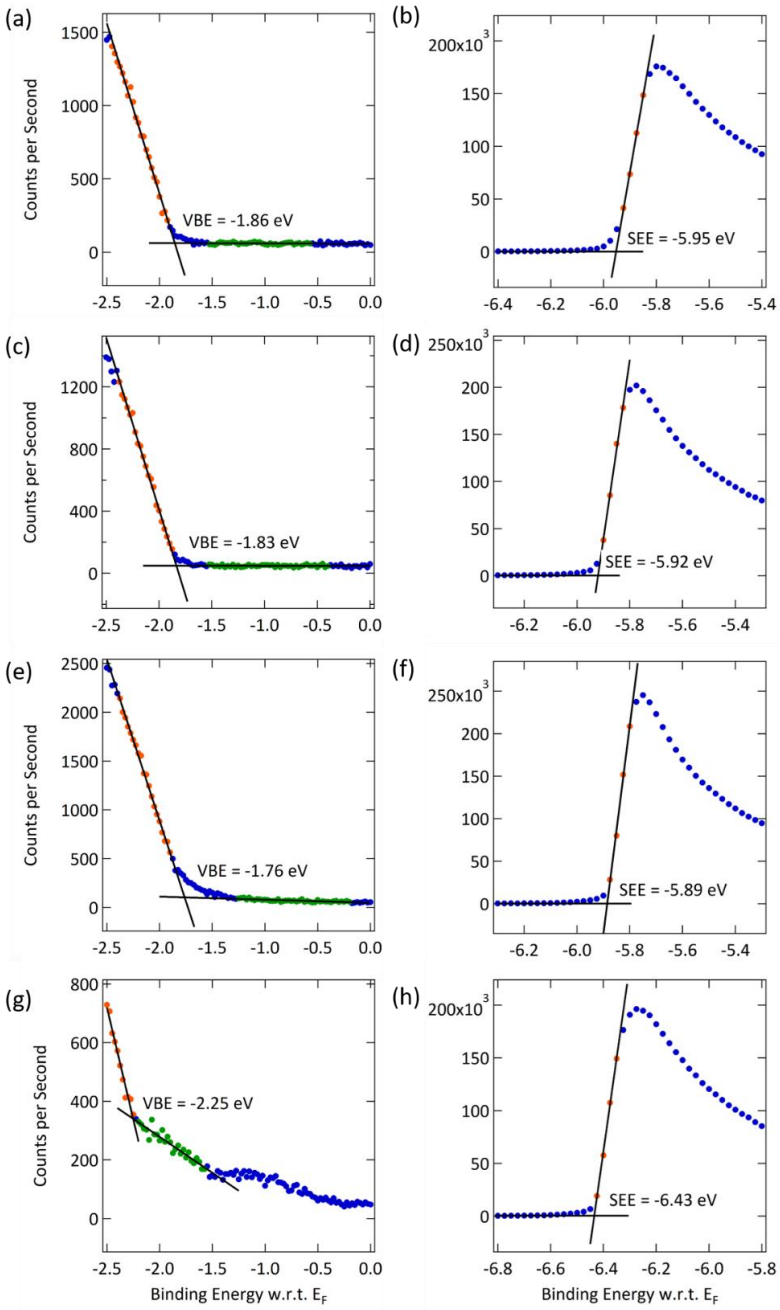

Figure S5.13 UPS spectrums of the PDI-2T/$MAPbI_3$ bilayer (PDI-2T surface) showing how the valence band edge and secondary electron edges were defined: (a) PDI-2T (neat) VBE, (b) PDI-2T (neat) SEE, (c) PDI-2T (0.1 wt% dopant) VBE, (d) PDI-2T (0.1 wt% dopant) SEE, (e) PDI-2T (1 wt% dopant) VBE, (f) PDI-2T (1 wt% dopant) SEE, (g) PDI-2T (10 wt% dopant) VBE, and (h) PDI-2T (10 wt% dopant) SEE. The PDI-2T layers were between 57 to 75 nm thick, consequently the effects of band bending should not be observable in this measurement.

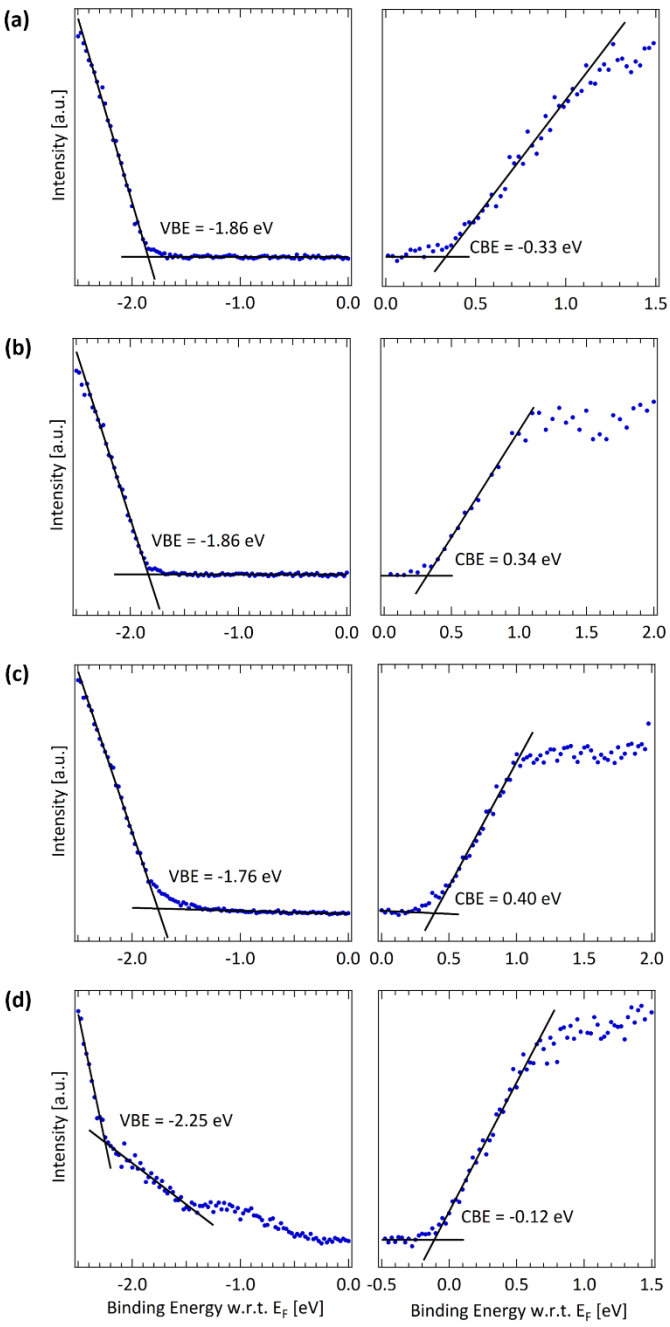

Figure S5.14 UPS of VBE and IPES of CBE of the PDI-2T/$MAPbI_3$ bilayer: (a) PDI-2T (neat), (b) PDI-2T (0.1 wt% dopant), (c) PDI-2T (1 wt% dopant), and (d) PDI-2T (10 wt% dopant). IPES spectra are originally measured in units of kinetic energy, which allows extraction of the EA. Here, the spectra has been shifted such that it is in units of binding energy relative to the Fermi level, allowing the band gap of the material to be more easily observed.

Table S5.3 Summary of extracted energy levels for the PDI-2T/$MAPbI_3$ bilayer (PDI-2T surface) including: valence band edge (VBE), secondary electron edge (SEE), electron affinity (EA), work function (WF), ionization potential (IP) and band gap (BG).

Sample	VBE (eV)	SEE (eV)	EA (eV w.r.t Vac)	WF (eV w.r.t. Vac)	IP (eV w.r.t Vac)	BG (eV)
Neat	-1.86	-5.95	-3.94	-4.27	-6.13	2.19
0.1	-1.83	-5.92	-3.96	-4.30	-6.13	2.17
1	-1.76	-5.89	-3.93	-4.33	-6.09	2.16
10	-2.25	-6.43	-3.91	-3.79	-6.04	2.13

E. XPS of PDI-2T/$MAPbI_3$ Bilayer with Full Coverage

The uniformity of coverage of PDI-2T on $MAPbI_3$ was assessed using XPS a control to ensure that the difference in VBEs of PDI-2T measured in isolation versus in the bilayer (Figure 5.2 and 5.7) was not just a result of patchy coverage. There was an absence of peaks around the binding energy of Pb 4f, which showed that $MAPbI_3$ was not contributing to the UPS measurement of the VBE.

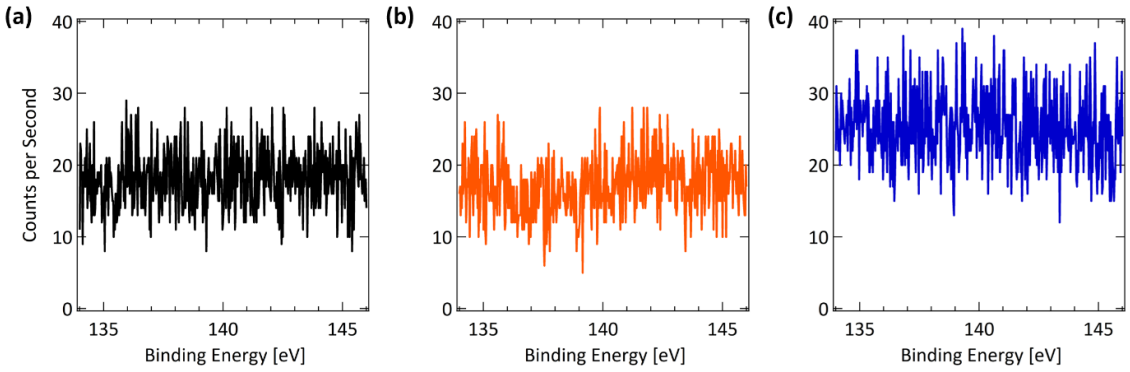

Figure S5.15 XPS spectra of the PDI-2T/$MAPbI_3$ bilayer with (a) PDI-2T (neat), (b) PDI-2T (0.1 wt% dopant) and (c) PDI-2T (10 wt% dopant). Binding energies are shown around the position of the Pb 4f peak in order to determine if $MAPbI_3$ could be contributing to the UPS measurement of the VBE. The presence of Pb is absent for these scans, indicating good coverage of PDI-2T on the $MAPbI_3$ surface. The XPS spectra of the PDI-2T/$MAPbI_3$ bilayer with PDI-2T (1 wt% dopant) is not included because as an oversight the film location for which UPS was collected was not also measured using XPS.

D. UPS/IEPS of $MAPbI_3$

The position of energy levels extracted for $MAPbI_3$ can vary depending on the surface composition, which can easily be altered based on precursor ratio or annealing time (MA and I are more volatile and can be lost from the surface).[179,233,234] In order to ensure that we were measuring the correct stoichiometry of $MAPbI_3$ on the surface, XPS was used to determine the atomic ratio of Pb:I, which was found to be ~0.30 (or 23.4% to 76.6%).

The Fermi level of $MAPbI_3$ is roughly around mid-gap, i.e. a nearly intrinsic semiconductor. The mid-gap position occurs as a result of using an underlying gold coated substrate, which is seen in other similar studies performed on gold and p-type substrates.[180,191] The following section will show the fits used to find the VBE, SEE and EA. For several of these values, multiple fits may be possible based on the interpretation of the data. Figure S5.16 shows assignment of the VBE using both linear and logarithmic intensity scales. While assignment using a linear scale is typical in organic semiconductors, several studies report a low density of states near the VBE in $MAPbI_3$, suggesting a logarithmic intensity scale can provide improved assignment of the VBE.[8,131,223] Endres et al. suggested using a Gaussian fit to replicate the falling edge of the valence band.[131] One of the issues using this fit is that a lack of a well-defined shoulder in the valence band adds some subjectivity to where a Gaussian is fit. The VBE was assigned at the intersection of the Gaussian fit and a noise floor for the UPS apparatus that was designated as 85 counts per second. When fit as close to edge as possible, there is not difference in the VBE assigned on the linear vs semi-logarithmic intensity scale.

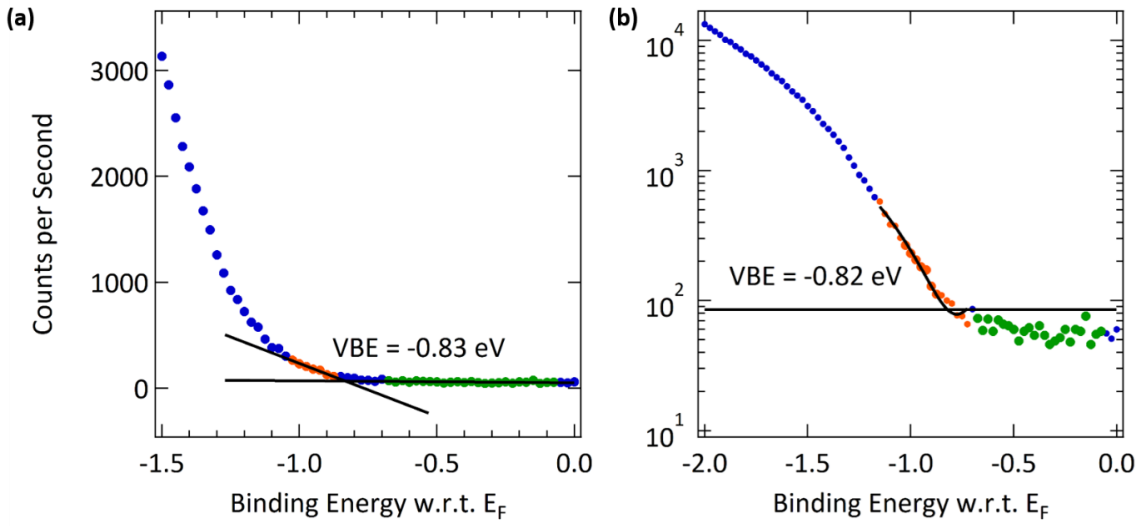

Figure S5.16 Potential fits of the valence band edge (VBE) of $MAPbI_3$ on both a (a) linear and (b) semi-logarithmic intensity scale. When fit nearest the edge as possible, there is no difference in linear and semi-logarithmic intensity scale fits (-0.82 versus -0.83 eV).

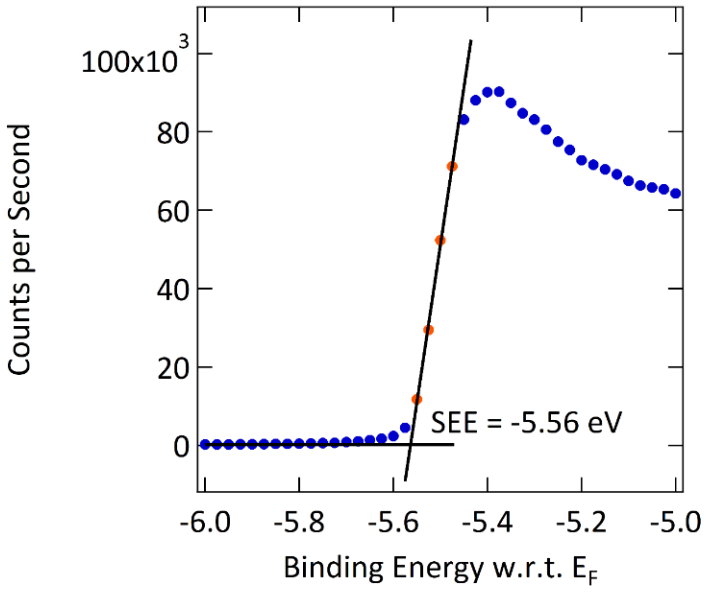

Figure S5.17 Fit of the secondary electron edge (SEE) of $MAPbI_3$.

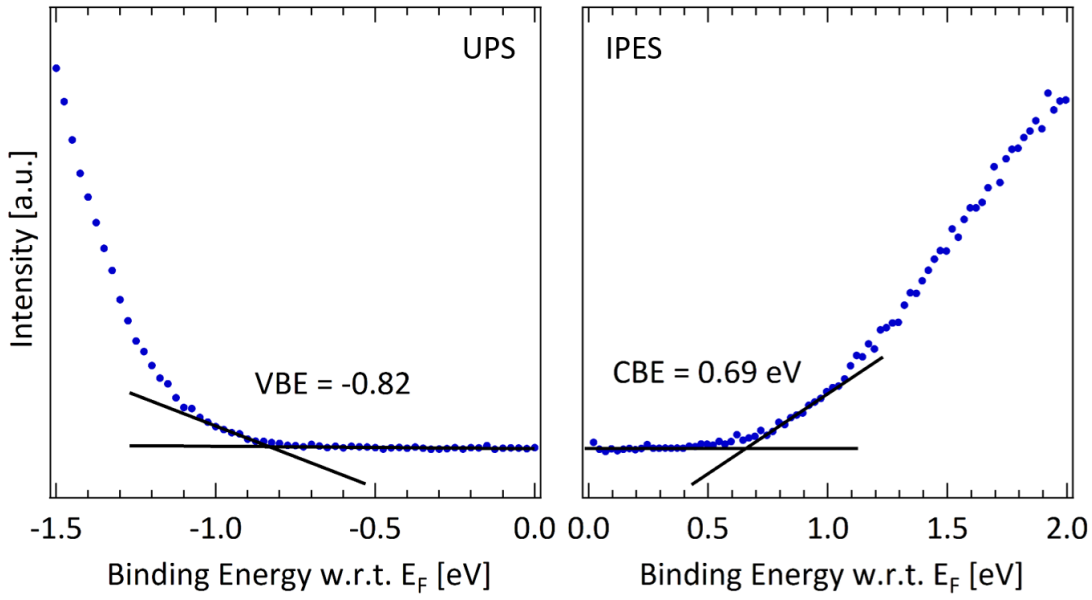

Figure S5.18 UPS of the VBE and IPES of the CBE of $MAPbI_3$ (underlying gold substrate). IPES spectra are originally measured in units of kinetic energy, which allows extraction of the EA. Here, the spectra has been shifted such that it is in units of binding energy relative to the Fermi level, allowing the band gap of the material to be more easily observed. The IPES spectra was not ideal because it lacked a sharp onset, leaving some interpretation open to assignment of the edge.

Table S5.4 Summary of extracted energy levels for $MAPbI_3$ including: valence band edge (VBE), secondary electron edge (SEE), electron affinity (EA), work function (WF), ionization potential (IP), and band gap (BG). The position of the ionization potential relative to vacuum (-5.5 eV) is consistent with that most often reported in literature,[235] although there has been a reported range of -5.2 to -6.6 eV.[7,8,123,179,188–190,233,234,236–248]

Fit	VBE (eV)	SEE (eV)	EA (eV w.r.t Vac)	WF (eV w.r.t. Vac)	IP (eV w.r.t Vac)	BG (eV)
VBE Linear Fit	-0.83	-5.56	-3.98	-4.66	-5.49	1.51
VBE Logarithmic Fit	-0.82	-5.56	-3.98	-4.66	-5.48	1.50

F. XPS Shits of Pb 4f and I 3d of Bare $MAPbI_3$ versus $MAPbI_3$ with Intentional Patchy Coverage of PDI-2T (1 wt% dopant)

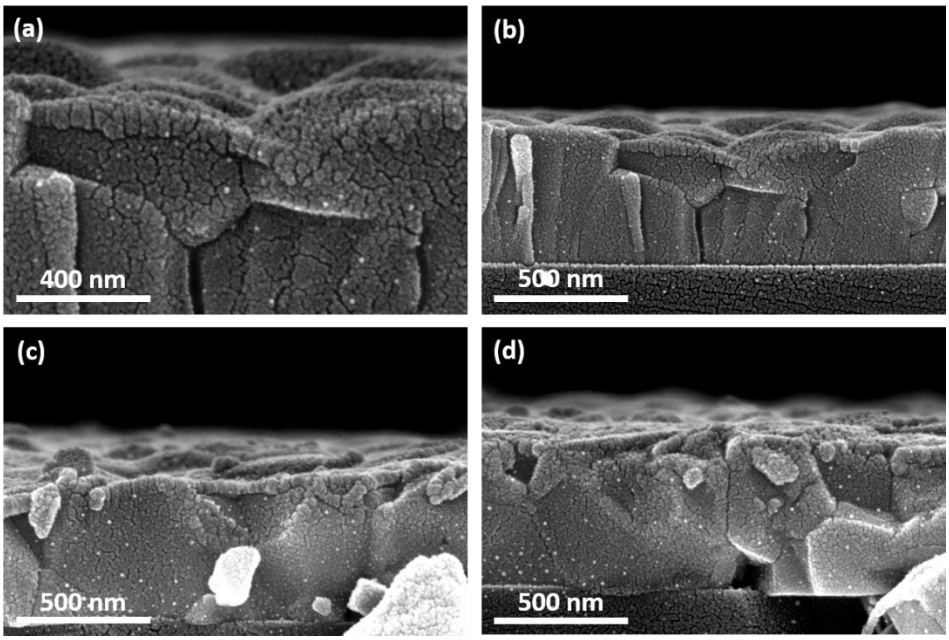

Figure S5.19 Cross-sectional SEM images of 0.5 mg/mL loading of PDI-2T (1 wt% dopant) on the $MAPbI_3$ surface. Low solution loadings result in patchy coverage of the perovskite surface, allowing Pb and I orbitals still be accessible to XPS (probes top ~10 nm of the film) in some areas of the film.

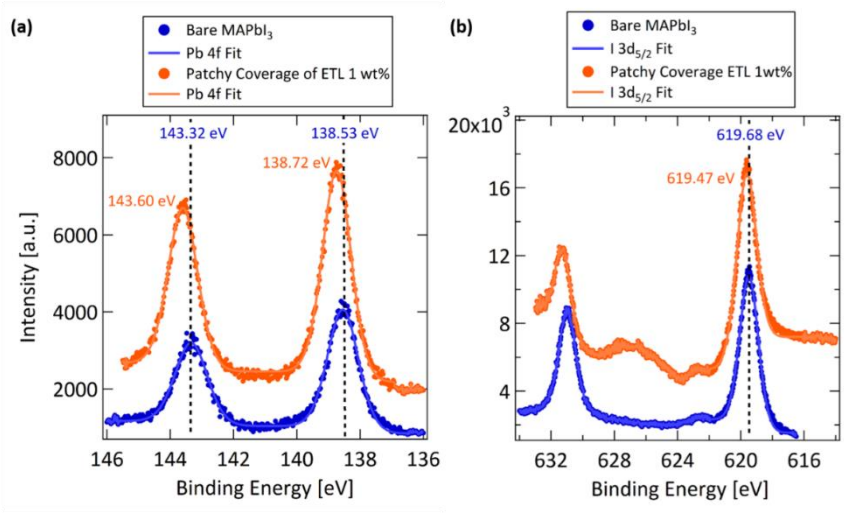

Figure S5.20 XPS core level shifts of (a) Pb 4f and (b) I 3d orbital peak positions. Upon doping, a shift of ~0.2 eV toward high binding energy occurs, indicating downward band bending at the $MAPbI_3$ surface.

XI. Time-Resolved Photoluminescence

A. Description of Setup and Fitting Procedure

Time-resolved PL (TR-PL) decays were acquired using a time-correlated single photon counting (TCSPC) technique. (TR-PL) decays were measured using 410 nm excitation and the transients were collected at 770 nm. Samples were contained in a chamber that maintained a nitrogen environment. Pulse energy densities of 0.15 uJ/cm^2, 0.05 uJ/cm^2, and 0.015 uJ/cm^2 were used, which assuming an absorption coefficient of ~1.5×10^5 at 410 nm, corresponds to charge densities of 6.9×10^{15}, 2.3×10^{15}, and 6.9×10^{14} cm^{-3} respectively.

Spectra for $MAPbI_3$ samples (either in a bilayer or by itself) was fit using a biexponential decay in order to extract carrier lifetimes.[249–251] Similarly, PDI-2T on quartz was fit using a monoexponential decay. A biexponential decay has the form:

$$I(t) = I_1 e^{-\left(\frac{t}{\tau_1}\right)} + I_2 e^{-\left(\frac{t}{\tau_2}\right)}$$

B. Biexponential Fits of TR-PL Spectra Collected at a Charge Density 6.87×10^{15} cm^{-3}

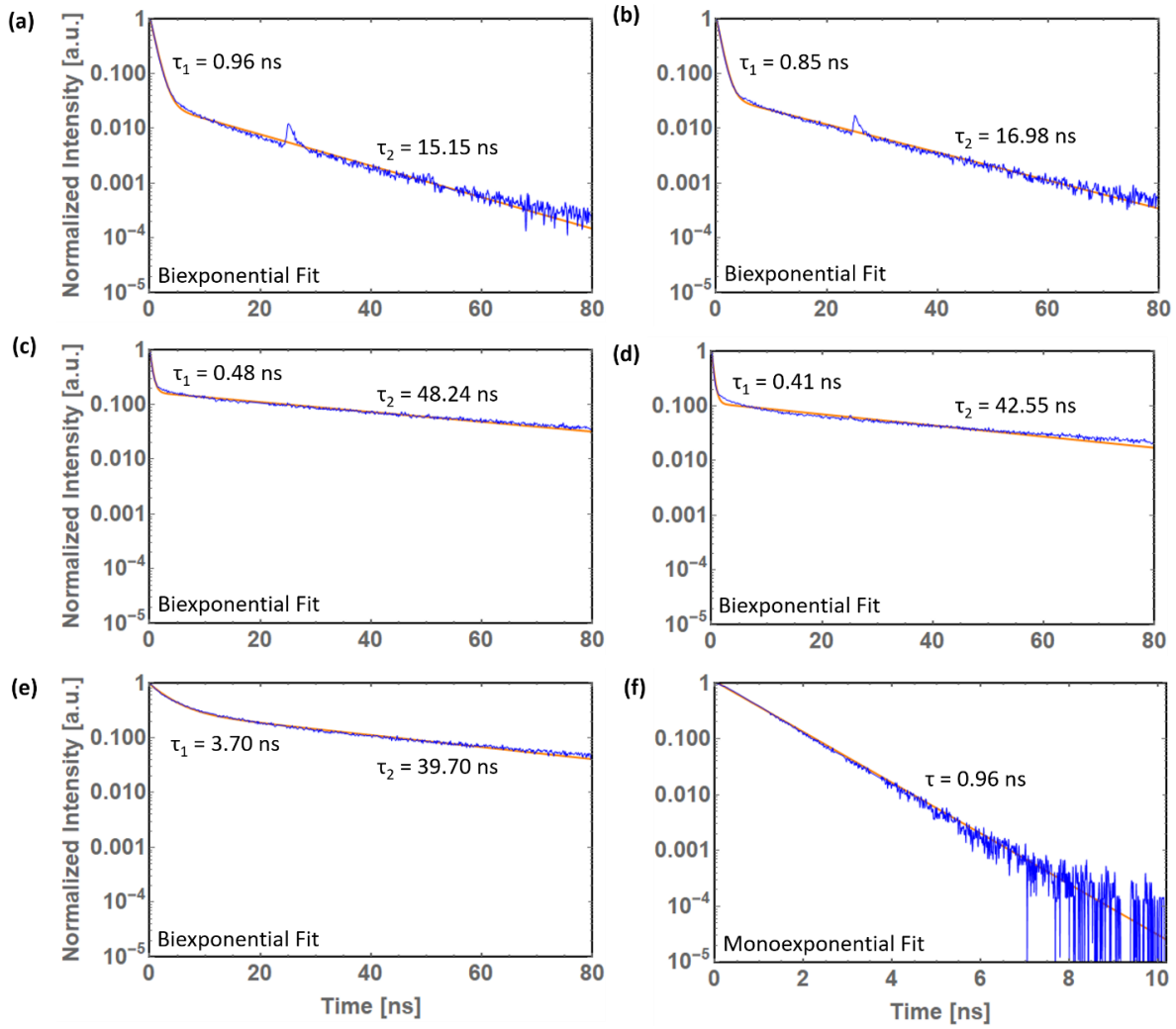

Figure S5.21 Biexponential fits of the time-resolved photoluminescence decay of (a) PDI-2T (neat)/$MAPbI_3$, (b) PDI-2T (0.1 wt% dopant)/$MAPbI_3$, (c) PDI-2T (1 wt% dopant)/$MAPbI_3$, (d) PDI-2T (10 wt% dopant)/$MAPbI_3$, (e) bare $MAPbI_3$, and (f) PDI-2T (neat) on quartz. Biexponential fitting incorporates a fast decay time lifetime τ_1 associated with recombination behavior at the surface, and a slow decay lifetime τ_2 associated with recombination in the bulk. The fast decay component of PDI-2T (neat)/$MAPbI_3$ and PDI-2T (0.1 wt% dopant)/$MAPbI_3$ is dominated by the decay of PDI-2T, consequently information about surface recombination lifetimes in $MAPbI_3$ for these samples are masked. TR-PL spectra were collected using a pulse energy density of 0.15 uJ/cm^2, which corresponds to a charge density of 6.9×10^{15} cm^{-3}.

C. Overlay of TR-PL Spectra of PDI-2T/$MAPbI_3$ bilayers, $MAPbI_3$ (single layer) and PDI-2T (single layer) for Varying Charge Densities

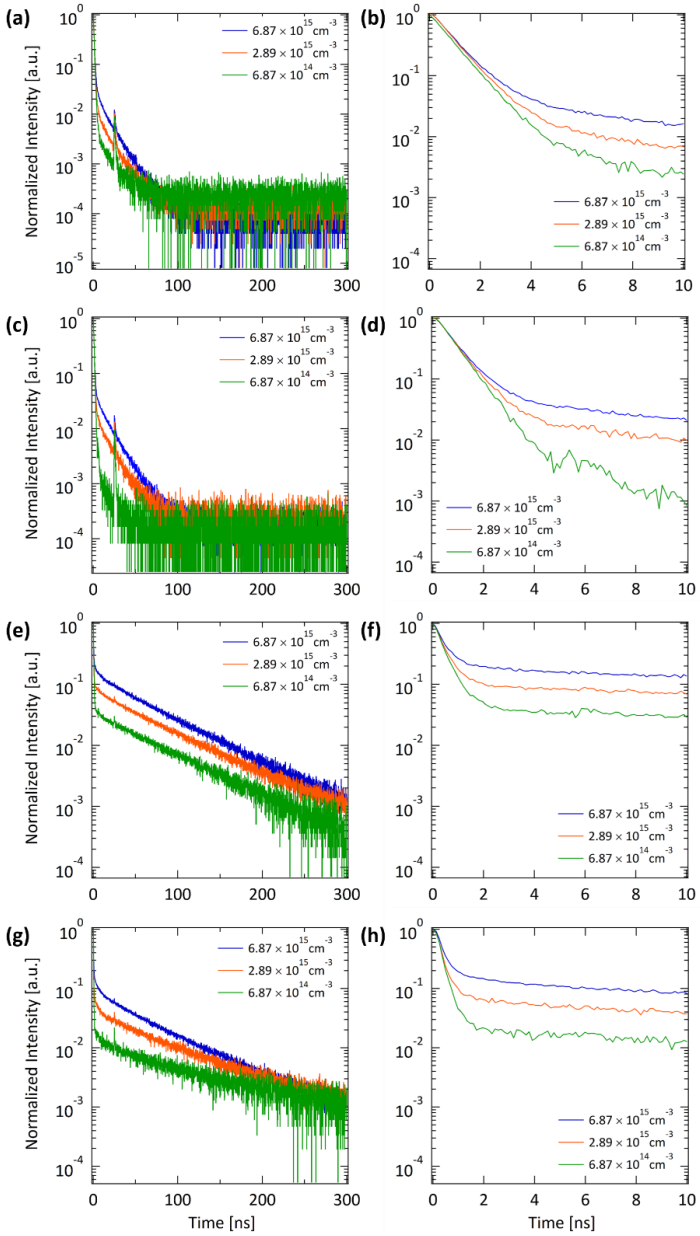

Figure S5.22 Time-resolved photoluminescence spectra of PDI-2T/$MAPbI_3$ bilayers, showing (left) the full TR-PL spectra and (right) the spectra around the fast decay component. Spectra correspond to bilayers according to: (a) & (b) PDI-2T (neat)/$MAPbI_3$, (c) & (d) PDI-2T (0.1 wt% dopant)/$MAPbI_3$, (e) & (f) PDI-2T (1 wt% dopant)/$MAPbI_3$, and (g) & (h) PDI-2T (10 wt% dopant)/$MAPbI_3$. Time-resolved PL decays were measured using a 410 nm excitation and three pulse energy densities: 0.15 uJ/cm^2, 0.05 uJ/cm^2, and 0.015 uJ/cm^2, which correspond to charge densities of 6.9×10^{15}, 2.3×10^{15}, and 6.9×10^{14} cm^{-3}.

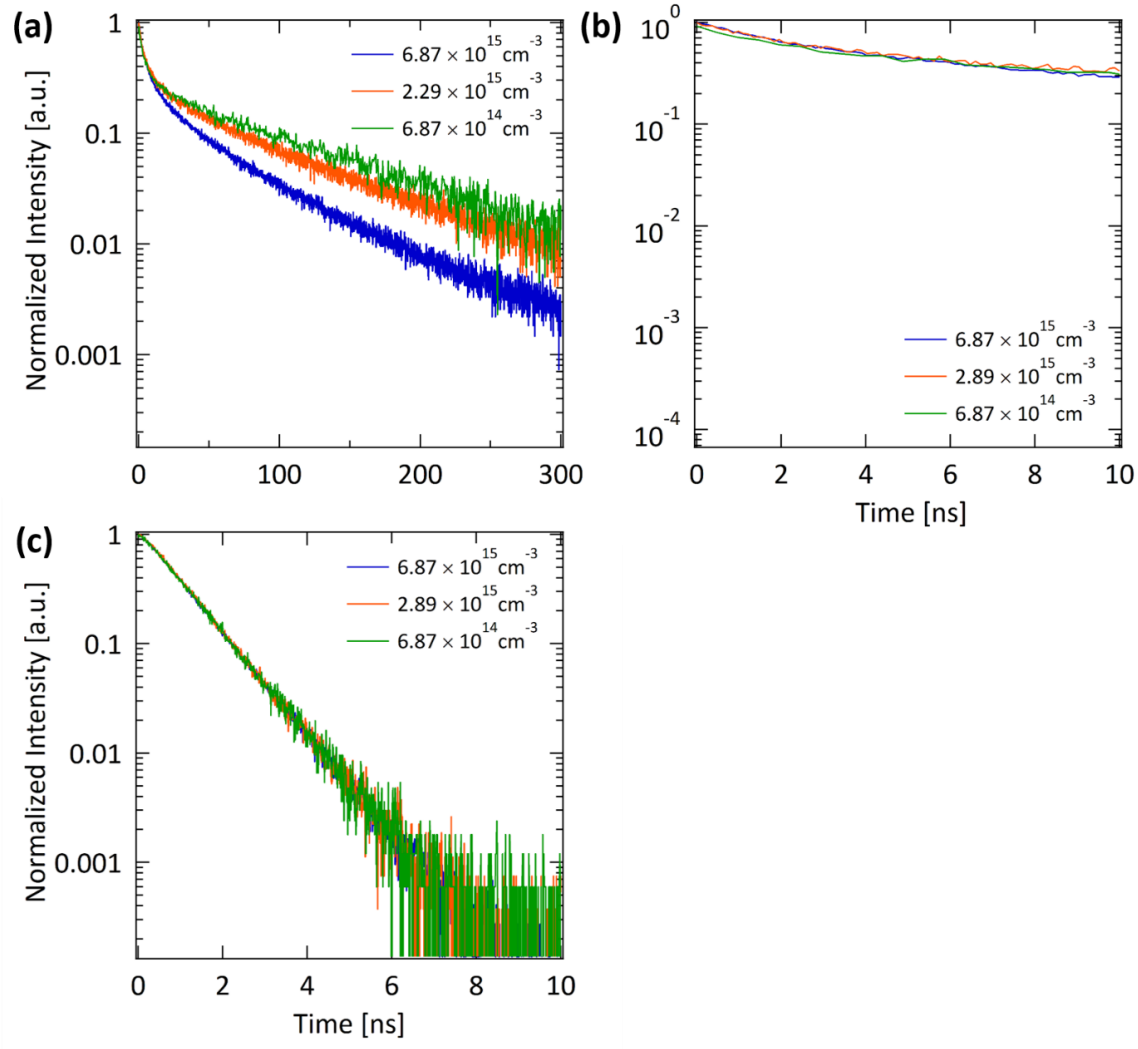

Figure S5.23 Time-resolved photoluminescence spectra of (a) & (b) bare $MAPbI_3$ on quartz and (c) PDI-2T (neat) on quartz, showing (left) the full TR-PL spectra and (right) the spectra around the fast decay component. PDI-2T on quartz was measured as a control to account for the photoluminescence of PDI-2T (perylene diimide unit) in bilayer samples such as PDI-2T (neat)/$MAPbI_3$ and PDI-2T (0.1 wt% dopant)/$MAPbI_3$. By PDI-2T (1 wt% dopant) the time-resolved photoluminescence no longer has intensity. Time-resolved PL decays were measured using a 410 nm excitation and three pulse energy densities: 0.15 uJ/cm^2, 0.05 uJ/cm^2, and 0.015 uJ/cm^2, which correspond to charge densities of 6.9×10^{15}, 2.3×10^{15}, and 6.9×10^{14} cm^{-3}.

7 References

[1] M. A. Green, Y. Hishikawa, E. D. Dunlop, D. H. Levi, J. Hohl-Ebinger, A. W. Y. Ho-Baillie, *Progress in Photovoltaics: Research and Applications* **n.d.**, *26*, 427.

[2] L. Zhao, R. A. Kerner, Z. Xiao, Y. L. Lin, K. M. Lee, J. Schwartz, B. P. Rand, *ACS Energy Lett.* **2016**, *1*, 595.

[3] K. Domanski, J.-P. Correa-Baena, N. Mine, M. K. Nazeeruddin, A. Abate, M. Saliba, W. Tress, A. Hagfeldt, M. Grätzel, *ACS Nano* **2016**, *10*, 6306.

[4] W. Ming, D. Yang, T. Li, L. Zhang, M.-H. Du, *Advanced Science* **n.d.**, *5*, 1700662.

[5] G. Yang, H. Tao, P. Qin, W. Ke, G. Fang, *Journal of Materials Chemistry A* **2016**, *4*, 3970.

[6] S. Razza, S. Castro-Hermosa, A. Di Carlo, T. M. Brown, *APL Materials* **2016**, *4*, 091508.

[7] P. Schulz, L. L. Whittaker-Brooks, B. A. MacLeod, D. C. Olson, Y.-L. Loo, A. Kahn, *Advanced Materials Interfaces* **2015**, *2*, 1400532.

[8] P. Schulz, E. Edri, S. Kirmayer, G. Hodes, D. Cahen, A. Kahn, *Energy & Environmental Science* **2014**, *7*, 1377.

[9] M. Yang, Y. Zeng, Z. Li, D. H. Kim, C.-S. Jiang, J. van de Lagemaat, K. Zhu, *Phys. Chem. Chem. Phys.* **2017**, *19*, 5043.

[10] M. H. Du, *J. Mater. Chem. A* **2014**, *2*, 9091.

[11] M.-H. Du, *J. Phys. Chem. Lett.* **2015**, *6*, 1461.

[12] T. Leijtens, G. E. Eperon, A. J. Barker, G. Grancini, W. Zhang, J. M. Ball, A. R. Srimath Kandada, H. J. Snaith, A. Petrozza, *Energy & Environmental Science* **2016**, *9*, 3472.

[13] A. Baumann, S. Väth, P. Rieder, M. C. Heiber, K. Tvingstedt, V. Dyakonov, *J. Phys. Chem. Lett.* **2015**, *6*, 2350.

[14] G.-J. A. H. Wetzelaer, M. Scheepers, A. M. Sempere, C. Momblona, J. Ávila, H. J. Bolink, *Adv. Mater.* **2015**, *27*, 1837.

[15] Q.-Q. Ye, Z.-K. Wang, M. Li, C.-C. Zhang, K.-H. Hu, L.-S. Liao, *ACS Energy Lett.* **2018**, *3*, 875.

[16] R. Schlesinger, F. Bianchi, S. Blumstengel, C. Christodoulou, R. Ovsyannikov, B. Kobin, K. Moudgil, S. Barlow, S. Hecht, S. R. Marder, F. Henneberger, N. Koch, *Nat Commun* **2015**, *6*, 6754.

[17] J. Goldemberg, United Nations Development Programme, United Nations, World Energy Council, Eds. , *World Energy Assessment: Energy and the Challenge of Sustainability*, United Nations Development Programme, New York, NY, **2000**.

[18] M. A. Green, Y. Hishikawa, E. D. Dunlop, D. H. Levi, J. Hohl-Ebinger, A. W. Y. Ho-Baillie, *Progress in Photovoltaics: Research and Applications* **n.d.**, *26*, 3.

[19] L. Calió, S. Kazim, M. Grätzel, S. Ahmad, *Angewandte Chemie International Edition* **n.d.**, *55*, 14522.

[20] K. Mahmood, S. Sarwar, M. Taqi Mehran, *RSC Advances* **2017**, *7*, 17044.

[21] Y. Zhou, Z. Zhou, M. Chen, Y. Zong, J. Huang, S. Pang, N. P. Padture, *J. Mater. Chem. A* **2016**, *4*, 17623.

[22] J. L. Gray, in *Handbook of Photovoltaic Science and Engineering*, Wiley-Blackwell, **2005**, pp. 61–112.

[23] S. C. Bhattacharyya, D. Palit, *Energy Policy* **2016**, *94*, 166.
[24] S. Hubbard, in *Photovoltaic Solar Energy*, Wiley-Blackwell, **2017**, pp. 39–46.
[25] J. Boyd, "Efficiency of Silicon Solar Cells Climbs," can be found under https://spectrum.ieee.org/energywise/energy/renewables/efficiency-of-solar-cells-continues-to-climb, **2017**.
[26] "What Is the Lifespan of a Solar Panel?," can be found under https://www.engineering.com/DesignerEdge/DesignerEdgeArticles/ArticleID/7475/What-Is-the-Lifespan-of-a-Solar-Panel.aspx, **n.d.**
[27] K. Bullis, "A Price Drop for Solar Panels," can be found under https://www.technologyreview.com/s/410064/a-price-drop-for-solar-panels/, **n.d.**
[28] V. M. Fthenakis, S. C. Morris, P. D. Moskowitz, D. L. Morgan, *Progress in Photovoltaics: Research and Applications* **n.d.**, *7*, 489.
[29] C. C. Stoumpos, M. G. Kanatzidis, *Advanced Materials* **n.d.**, *28*, 5778.
[30] A. Kojima, K. Teshima, Y. Shirai, T. Miyasaka, *J. Am. Chem. Soc.* **2009**, *131*, 6050.
[31] Y. Wu, D. Yan, J. Peng, T. Duong, Y. Wan, S. P. Phang, H. Shen, N. Wu, C. Barugkin, X. Fu, S. Surve, D. Grant, D. Walter, T. P. White, K. R. Catchpole, K. J. Weber, *Energy Environ. Sci.* **2017**, *10*, 2472.
[32] C. Eames, J. M. Frost, P. R. F. Barnes, B. C. O'Regan, A. Walsh, M. S. Islam, *Nat Commun* **2015**, *6*, DOI 10.1038/ncomms8497.
[33] L. Glasser, *Inorg. Chem.* **2012**, *51*, 2420.
[34] D. Shi, V. Adinolfi, R. Comin, M. Yuan, E. Alarousu, A. Buin, Y. Chen, S. Hoogland, A. Rothenberger, K. Katsiev, Y. Losovyj, X. Zhang, P. A. Dowben, O. F. Mohammed, E. H. Sargent, O. M. Bakr, *Science* **2015**, *347*, 519.
[35] Q. Dong, Y. Fang, Y. Shao, P. Mulligan, J. Qiu, L. Cao, J. Huang, *Science* **2015**, *347*, 967.
[36] C. Motta, F. El-Mellouhi, S. Sanvito, *Scientific Reports* **2015**, *5*, 12746.
[37] L. M. Pazos-Outón, M. Szumilo, R. Lamboll, J. M. Richter, M. Crespo-Quesada, M. Abdi-Jalebi, H. J. Beeson, M. Vrućinić, M. Alsari, H. J. Snaith, B. Ehrler, R. H. Friend, F. Deschler, *Science* **2016**, *351*, 1430.
[38] L. A. Frolova, N. N. Dremova, P. A. Troshin, *Chem. Commun.* **2015**, *51*, 14917.
[39] A. Walsh, D. O. Scanlon, S. Chen, X. G. Gong, S.-H. Wei, *Angew Chem Int Ed Engl* **2015**, *54*, 1791.
[40] W.-J. Yin, T. Shi, Y. Yan, *Applied Physics Letters* **2014**, *104*, 063903.
[41] T. Li, Y. Pan, Z. Wang, Y. Xia, Y. Chen, W. Huang, *J. Mater. Chem. A* **2017**, *5*, 12602.
[42] A. L. Abdelhady, M. I. Saidaminov, B. Murali, V. Adinolfi, O. Voznyy, K. Katsiev, E. Alarousu, R. Comin, I. Dursun, L. Sinatra, E. H. Sargent, O. F. Mohammed, O. M. Bakr, *J. Phys. Chem. Lett.* **2016**, *7*, 295.
[43] J. Chen, Y. Rong, A. Mei, Y. Xiong, T. Liu, Y. Sheng, P. Jiang, L. Hong, Y. Guan, X. Zhu, X. Hou, M. Duan, J. Zhao, X. Li, H. Han, *Adv. Energy Mater.* **2016**, *6*, n/a.
[44] M. Abdi-Jalebi, M. I. Dar, A. Sadhanala, S. P. Senanayak, M. Franckevičius, N. Arora, Y. Hu, M. K. Nazeeruddin, S. M. Zakeeruddin, M. Grätzel, R. H. Friend, *Adv. Energy Mater.* **2016**, *6*, n/a.
[45] J. L. Boland, S. Conesa-Boj, P. Parkinson, G. Tütüncüoglu, F. Matteini, D. Rüffer, A. Casadei, F. Amaduzzi, F. Jabeen, C. L. Davies, H. J. Joyce, L. M. Herz, A. Fontcuberta i Morral, M. B. Johnston, *Nano Lett.* **2015**, *15*, 1336.

[46] K. Wojciechowski, S. D. Stranks, A. Abate, G. Sadoughi, A. Sadhanala, N. Kopidakis, G. Rumbles, C.-Z. Li, R. H. Friend, A. K.-Y. Jen, H. J. Snaith, *ACS Nano* **2014**, *8*, 12701.
[47] G. Xing, B. Wu, S. Chen, J. Chua, N. Yantara, S. Mhaisalkar, N. Mathews, T. C. Sum, *Small* **n.d.**, *11*, 3606.
[48] Y. Shao, Z. Xiao, C. Bi, Y. Yuan, J. Huang, *Nature Communications* **2014**, *5*, 5784.
[49] S. S. Kim, S. Bae, W. H. Jo, *Chem. Commun.* **2015**, *51*, 17413.
[50] J.-H. Bae, Y.-J. Noh, M. Kang, D.-Y. Kim, H.-B. Kim, S.-H. Oh, J.-M. Yun, S.-I. Na, *RSC Adv.* **2016**, *6*, 64962.
[51] P. Zhao, B. J. Kim, H. S. Jung, *Materials Today Energy* **2018**, *7*, 267.
[52] A. H. Ip, L. N. Quan, M. M. Adachi, J. J. McDowell, J. Xu, D. H. Kim, E. H. Sargent, *Appl. Phys. Lett.* **2015**, *106*, 143902.
[53] Y. Li, Y. Zhao, Q. Chen, Y. (Michael) Yang, Y. Liu, Z. Hong, Z. Liu, Y.-T. Hsieh, L. Meng, Y. Li, Y. Yang, *J. Am. Chem. Soc.* **2015**, *137*, 15540.
[54] G. Xing, N. Mathews, S. S. Lim, N. Yantara, X. Liu, D. Sabba, M. Grätzel, S. Mhaisalkar, T. C. Sum, *Nature Materials* **2014**, *13*, 476.
[55] D. Baek, S. Rouvimov, B. Kim, T.-C. Jo, D. K. Schroder, *Appl. Phys. Lett.* **2005**, *86*, 112110.
[56] Y. Yang, F. Gao, S. Gao, S.-H. Wei, *J. Mater. Chem. A* **2018**, DOI 10.1039/C8TA01496E.
[57] Z. Fan, H. Xiao, Y. Wang, Z. Zhao, Z. Lin, H.-C. Cheng, S.-J. Lee, G. Wang, Z. Feng, W. A. Goddard, Y. Huang, X. Duan, *Joule* **2017**, *1*, 548.
[58] N.-K. Kim, Y. H. Min, S. Noh, E. Cho, G. Jeong, M. Joo, S.-W. Ahn, J. S. Lee, S. Kim, K. Ihm, H. Ahn, Y. Kang, H.-S. Lee, D. Kim, *Scientific Reports* **2017**, *7*, 4645.
[59] N. K. Noel, A. Abate, S. D. Stranks, E. S. Parrott, V. M. Burlakov, A. Goriely, H. J. Snaith, *ACS Nano* **2014**, *8*, 9815.
[60] I. A. Shkrob, T. W. Marin, *The Journal of Physical Chemistry Letters* **2014**, *5*, 1066.
[61] J.-W. Lee, H.-S. Kim, N.-G. Park, *Acc. Chem. Res.* **2016**, *49*, 311.
[62] Y. Lin, L. Shen, J. Dai, Y. Deng, Y. Wu, Y. Bai, X. Zheng, J. Wang, Y. Fang, H. Wei, W. Ma, X. C. Zeng, X. Zhan, J. Huang, *Advanced Materials* **n.d.**, *29*, 1604545.
[63] P.-W. Liang, C.-C. Chueh, S. T. Williams, A. K.-Y. Jen, *Advanced Energy Materials* **n.d.**, *5*, 1402321.
[64] J. Xu, A. Buin, A. H. Ip, W. Li, O. Voznyy, R. Comin, M. Yuan, S. Jeon, Z. Ning, J. J. McDowell, P. Kanjanaboos, J.-P. Sun, X. Lan, L. N. Quan, D. H. Kim, I. G. Hill, P. Maksymovych, E. H. Sargent, *Nature Communications* **2015**, *6*, 7081.
[65] A. Abate, M. Saliba, D. J. Hollman, S. D. Stranks, K. Wojciechowski, R. Avolio, G. Grancini, A. Petrozza, H. J. Snaith, *Nano Lett.* **2014**, *14*, 3247.
[66] W. Chen, D. Qi, X. Gao, A. T. S. Wee, *Progress in Surface Science* **2009**, *84*, 279.
[67] S. Esconjauregui, L. D'Arsié, Y. Guo, J. Yang, H. Sugime, S. Caneva, C. Cepek, J. Robertson, *ACS Nano* **2015**, *9*, 10422.
[68] P. Strobel, M. Riedel, J. Ristein, L. Ley, *Nature* **2004**, *430*, 439.
[69] K. J. Rietwyk, Y. Smets, M. Bashouti, S. H. Christiansen, A. Schenk, A. Tadich, M. T. Edmonds, J. Ristein, L. Ley, C. I. Pakes, *Physical Review Letters* **2014**, *112*, DOI 10.1103/PhysRevLett.112.155502.
[70] Z. Zhang, J. T. Yates, *Chem. Rev.* **2012**, *112*, 5520.
[71] B. Lüssem, M. Riede, K. Leo, *Phys. Status Solidi A* **2013**, *210*, 9.

[72] B. Lüssem, C.-M. Keum, D. Kasemann, B. Naab, Z. Bao, K. Leo, *Chem. Rev.* **2016**, *116*, 13714.
[73] X. Lin, B. Wegner, K. M. Lee, M. A. Fusella, F. Zhang, K. Moudgil, B. P. Rand, S. Barlow, S. R. Marder, N. Koch, A. Kahn, *Nature Materials* **2017**, *16*, 1209.
[74] C. Y. Kao, B. Lee, L. S. Wielunski, M. Heeney, I. McCulloch, E. Garfunkel, L. C. Feldman, V. Podzorov, *Adv. Funct. Mater.* **2009**, *19*, 1906.
[75] S. N. Patel, A. M. Glaudell, D. Kiefer, M. L. Chabinyc, *ACS Macro Lett.* **2016**, 268.
[76] R. D. McCullough, S. Tristram-Nagle, S. P. Williams, R. D. Lowe, M. Jayaraman, *J. Am. Chem. Soc.* **1993**, *115*, 4910.
[77] Y. Xia, K. Sun, J. Ouyang, *Adv. Mater.* **2012**, *24*, 2436.
[78] Y. Wang, M. Nakano, T. Michinobu, Y. Kiyota, T. Mori, K. Takimiya, *Macromolecules* **2017**, *50*, 857.
[79] S. Wang, H. Sun, U. Ail, M. Vagin, P. O. Å. Persson, J. W. Andreasen, W. Thiel, M. Berggren, X. Crispin, D. Fazzi, S. Fabiano, *Adv. Mater.* **2016**, *28*, 10764.
[80] K. Shi, F. Zhang, C.-A. Di, T.-W. Yan, Y. Zou, X. Zhou, D. Zhu, J.-Y. Wang, J. Pei, *J. Am. Chem. Soc.* **2015**, *137*, 6979.
[81] M. R. Andersson, K. Väkiparta, M. Reghu, Y. Cao, D. Moses, *Phys. Rev. B* **1993**, *47*, 9238.
[82] M. Bendikov, F. Wudl, D. F. Perepichka, *Chem. Rev.* **2004**, *104*, 4891.
[83] S. Tanaka, K. Kanai, E. Kawabe, T. Iwahashi, T. Nishi, Y. Ouchi, K. Seki, *Jpn. J. Appl. Phys.* **2005**, *44*, 3760.
[84] K. Harada, A. G. Werner, M. Pfeiffer, C. J. Bloom, C. M. Elliott, K. Leo, *Phys. Rev. Lett.* **2005**, *94*, 036601.
[85] M. L. Tietze, F. Wölzl, T. Menke, A. Fischer, M. Riede, K. Leo, B. Lüssem, *physica status solidi (a)* **n.d.**, *210*, 2188.
[86] T. Menke, D. Ray, J. Meiss, K. Leo, M. Riede, *Applied Physics Letters* **2012**, *100*, 093304.
[87] F. A. Cotton, N. E. Gruhn, J. Gu, P. Huang, D. L. Lichtenberger, C. A. Murillo, L. O. V. Dorn, C. C. Wilkinson, *Science* **2002**, *298*, 1971.
[88] C. K. Chan, A. Kahn, Q. Zhang, S. Barlow, S. R. Marder, *Journal of Applied Physics* **2007**, *102*, 014906.
[89] J.-L. Xu, R.-X. Dai, Y. Xin, Y.-L. Sun, X. Li, Y.-X. Yu, L. Xiang, D. Xie, S.-D. Wang, T.-L. Ren, *Scientific Reports* **2017**, *7*, 6751.
[90] P. Wei, J. H. Oh, G. Dong, Z. Bao, *J. Am. Chem. Soc.* **2010**, *132*, 8852.
[91] B. L. Schottel, H. T. Chifotides, K. R. Dunbar, *Chem. Soc. Rev.* **2007**, *37*, 68.
[92] C.-Z. Li, C.-C. Chueh, F. Ding, H.-L. Yip, P.-W. Liang, X. Li, A. K.-Y. Jen, *Advanced Materials* **n.d.**, *25*, 4425.
[93] A. G. Werner, F. Li, K. Harada, M. Pfeiffer, T. Fritz, K. Leo, *Appl. Phys. Lett.* **2003**, *82*, 4495.
[94] F. Li, A. Werner, M. Pfeiffer, K. Leo, X. Liu, *J. Phys. Chem. B* **2004**, *108*, 17076.
[95] P. Wei, T. Menke, B. D. Naab, K. Leo, M. Riede, Z. Bao, *J. Am. Chem. Soc.* **2012**, *134*, 3999.
[96] T. Menke, P. Wei, D. Ray, H. Kleemann, B. D. Naab, Z. Bao, K. Leo, M. Riede, *Organic Electronics* **2012**, *13*, 3319.
[97] K. Walzer, B. Maennig, M. Pfeiffer, K. Leo, *Chem. Rev.* **2007**, *107*, 1233.

[98] S. Guo, S. K. Mohapatra, A. Romanov, T. V. Timofeeva, K. I. Hardcastle, K. Yesudas, C. Risko, J.-L. Brédas, S. R. Marder, S. Barlow, *Chem. Eur. J.* **2012**, *18*, 14760.
[99] Y. Qi, S. K. Mohapatra, S. B. Kim, S. Barlow, S. R. Marder, A. Kahn, *Applied Physics Letters* **2012**, *100*, 083305.
[100] B. D. Naab, S. Zhang, K. Vandewal, A. Salleo, S. Barlow, S. R. Marder, Z. Bao, *Adv. Mater.* **2014**, *26*, 4268.
[101] R. A. Schlitz, F. G. Brunetti, A. M. Glaudell, P. L. Miller, M. A. Brady, C. J. Takacs, C. J. Hawker, M. L. Chabinyc, *Adv. Mater.* **2014**, *26*, 2825.
[102] H. Yan, Z. Chen, Y. Zheng, C. Newman, J. R. Quinn, F. Dötz, M. Kastler, A. Facchetti, *Nature* **2009**, *457*, 679.
[103] Z. Chen, Y. Zheng, H. Yan, A. Facchetti, *J. Am. Chem. Soc.* **2009**, *131*, 8.
[104] B. Russ, M. J. Robb, F. G. Brunetti, P. L. Miller, E. E. Perry, S. N. Patel, V. Ho, W. B. Chang, J. J. Urban, M. L. Chabinyc, C. J. Hawker, R. A. Segalman, *Adv. Mater.* **2014**, *26*, 3473.
[105] S. S. Kim, S. Bae, W. H. Jo, *RSC Adv.* **2016**, *6*, 19923.
[106] Z. Wang, D. P. McMeekin, N. Sakai, S. van Reenen, K. Wojciechowski, J. B. Patel, M. B. Johnston, H. J. Snaith, *Advanced Materials* **n.d.**, *29*, 1604186.
[107] Z. Zhu, D. Zhao, C.-C. Chueh, X. Shi, Z. Li, A. K.-Y. Jen, *Joule* **2018**, *2*, 168.
[108] R. Weber, J. Jiang, D. Barr, **1998**.
[109] "EPR: Theory," can be found under https://chem.libretexts.org/Textbook_Maps/Physical_and_Theoretical_Chemistry_Textbook_Maps/Supplemental_Modules_(Physical_and_Theoretical_Chemistry)/Spectroscopy/Magnetic_Resonance_Spectroscopies/Electron_Paramagnetic_Resonance/EPR%3A_Theory, **2013**.
[110] "EPR: Interpretation," can be found under https://chem.libretexts.org/Textbook_Maps/Physical_and_Theoretical_Chemistry_Textbook_Maps/Supplemental_Modules_(Physical_and_Theoretical_Chemistry)/Spectroscopy/Magnetic_Resonance_Spectroscopies/Electron_Paramagnetic_Resonance/EPR%3A_Interpretation, **2013**.
[111] J. W. Robinson, E. S. Frame, G. M. F. II, *Undergraduate Instrumental Analysis, Seventh Edition*, CRC Press, **2014**.
[112] I. A. Shkrob, T. W. Marin, *J. Phys. Chem. Lett.* **2014**, *5*, 1066.
[113] M. M. Dorio, Ed. , *Multiple Electron Resonance Spectroscopy*, Springer US, **1979**.
[114] S. Suga, A. Sekiyama, in *Photoelectron Spectroscopy*, Springer, Berlin, Heidelberg, **2014**, pp. 1–6.
[115] S. Suga, A. Sekiyama, in *Photoelectron Spectroscopy*, Springer, Berlin, Heidelberg, **2014**, pp. 7–31.
[116] S. Suga, A. Sekiyama, in *Photoelectron Spectroscopy*, Springer, Berlin, Heidelberg, **2014**, pp. 33–89.
[117] A. M. Boehm, J. Wieser, K. Butrouna, K. R. Graham, *Organic Electronics* **2017**, *41*, 9.
[118] D. W. Turner, M. I. A. Jobory, *The Journal of Chemical Physics* **1962**, *37*, 3007.
[119] In *X-Ray Photoelectron Spectroscopy*, Wiley-Blackwell, **2011**, pp. 27–60.
[120] D. Cahen, A. Kahn, E. Umbach, *Materials Today* **2005**, *8*, 32.
[121] A. Kahn, *Materials Horizons* **2016**, *3*, 7.

[122] D. Cahen, A. Kahn, *Advanced Materials* **n.d.**, *15*, 271.
[123] S. Chen, T. W. Goh, D. Sabba, J. Chua, N. Mathews, C. H. A. Huan, T. C. Sum, *APL Materials* **2014**, *2*, 081512.
[124] A. Opitz, J. Frisch, R. Schlesinger, A. Wilke, N. Koch, *Journal of Electron Spectroscopy and Related Phenomena* **2013**, *190*, 12.
[125] N. Koch, D. Pop, R. L. Weber, N. Böwering, B. Winter, M. Wick, G. Leising, I. V. Hertel, W. Braun, *Thin Solid Films* **2001**, *391*, 81.
[126] P. Bröms, N. Johansson, R. W. Gymer, S. C. Graham, R. H. Friend, W. R. Salaneck, *Advanced Materials* **n.d.**, *11*, 826.
[127] M. R. M. Chagas, W. G. Quirino, A. M. J. C. Neto, E. A. de Sousa, M. Cremona, M. L. M. Rocco, G. V. S. Mota, *Thin Solid Films* **2009**, *517*, 4461.
[128] S. Gardonio, L. Gregoratti, P. Melpignano, L. Aballe, V. Biondo, R. Zamboni, M. Murgia, S. Caria, M. Kiskinova, *Organic Electronics* **2007**, *8*, 37.
[129] Q. L. Song, M. L. Wang, E. G. Obbard, X. Y. Sun, X. M. Ding, X. Y. Hou, C. M. Li, *Appl. Phys. Lett.* **2006**, *89*, 251118.
[130] S. Olthof, *APL Materials* **2016**, *4*, 091502.
[131] J. Endres, D. A. Egger, M. Kulbak, R. A. Kerner, L. Zhao, S. H. Silver, G. Hodes, B. P. Rand, D. Cahen, L. Kronik, A. Kahn, *J. Phys. Chem. Lett.* **2016**, *7*, 2722.
[132] E. E. Perry, C.-Y. Chiu, K. Moudgil, R. A. Schlitz, C. J. Takacs, K. A. O'Hara, J. G. Labram, A. M. Glaudell, J. B. Sherman, S. Barlow, C. J. Hawker, S. R. Marder, M. L. Chabinyc, *Chem. Mater.* **2017**, *29*, 9742.
[133] Z. Zhu, D. Zhao, C.-C. Chueh, X. Shi, Z. Li, A. K.-Y. Jen, *Joule* **2018**, *2*, 168.
[134] S. Reineke, M. Thomschke, B. Lüssem, K. Leo, *Rev. Mod. Phys.* **2013**, *85*, 1245.
[135] D. Gaspar, E. Polikarpov, *OLED Fundamentals: Materials, Devices, and Processing of Organic Light-Emitting Diodes*, CRC Press, Boca Raton, FL, **2015**.
[136] H. Sirringhaus, *Adv. Mater.* **2014**, *26*, 1319.
[137] Y. Lin, Y. Li, X. Zhan, *Chem. Soc. Rev.* **2012**, *41*, 4245.
[138] G. Li, R. Zhu, Y. Yang, *Nat Photon* **2012**, *6*, 153.
[139] O. Bubnova, X. Crispin, *Energy Environ. Sci.* **2012**, *5*, 9345.
[140] B. Russ, M. J. Robb, B. C. Popere, E. E. Perry, C.-K. Mai, S. L. Fronk, S. N. Patel, T. E. Mates, G. C. Bazan, J. J. Urban, M. L. Chabinyc, C. J. Hawker, R. A. Segalman, *Chem. Sci.* **2016**, DOI 10.1039/C5SC04217H.
[141] C. Yu, A. Murali, K. Choi, Y. Ryu, *Energy Environ. Sci.* **2012**, *5*, 9481.
[142] Q. Zhang, Y. Sun, W. Xu, D. Zhu, *Adv. Mater.* **2014**, *26*, 6829.
[143] S. Olthof, S. Mehraeen, S. K. Mohapatra, S. Barlow, V. Coropceanu, J.-L. Brédas, S. R. Marder, A. Kahn, *Phys. Rev. Lett.* **2012**, *109*, 176601.
[144] J. Li, Y. Zhao, H. S. Tan, Y. Guo, C.-A. Di, G. Yu, Y. Liu, M. Lin, S. H. Lim, Y. Zhou, H. Su, B. S. Ong, *Scientific Reports* **2012**, *2*, DOI 10.1038/srep00754.
[145] J. Lee, A.-R. Han, H. Yu, T. J. Shin, C. Yang, J. H. Oh, *J. Am. Chem. Soc.* **2013**, *135*, 9540.
[146] B. Sun, W. Hong, Z. Yan, H. Aziz, Y. Li, *Adv. Mater.* **2014**, *26*, 2636.
[147] S. Guo, S. B. Kim, S. K. Mohapatra, Y. Qi, T. Sajoto, A. Kahn, S. R. Marder, S. Barlow, *Adv. Mater.* **2012**, *24*, 699.
[148] P. Wei, J. H. Oh, G. Dong, Z. Bao, *J. Am. Chem. Soc.* **2010**, *132*, 8852.
[149] C.-Z. Li, C.-C. Chueh, F. Ding, H.-L. Yip, P.-W. Liang, X. Li, A. K.-Y. Jen, *Adv. Mater.* **2013**, *25*, 4425.

[150] Y. Zhang, H. Phan, H. Zhou, X. Zhang, J. Zhou, K. Moudgil, S. Barlow, S. R. Marder, A. Facchetti, T.-Q. Nguyen, *Adv. Electron. Mater.* **2017**, n/a.
[151] A. Higgins, S. Mohapatra, S. Barlow, S. Marder, K. Antoine, *Appl. Phys. Lett.* **2015**, *106*, 163301.
[152] C.-Y. Chiu, H. Wang, F. G. Brunetti, F. Wudl, C. J. Hawker, *Angew. Chem. Int. Ed.* **2014**, *53*, 3996.
[153] J. B. Sherman, C.-Y. Chiu, R. Fagenson, G. Wu, C. J. Hawker, M. L. Chabinyc, *MRS Communications* **2015**, *5*, 447.
[154] C.-Y. Chiu, H. Wang, H. Phan, K. Shiratori, T.-Q. Nguyen, C. J. Hawker, *J. Polym. Sci. Part A: Polym. Chem.* **2016**, *54*, 889.
[155] O. V. Gusev, M. A. Ievlev, M. G. Peterleitner, S. M. Peregudova, L. I. Denisovich, P. V. Petrovskii, N. A. Ustynyuk, *Journal of Organometallic Chemistry* **1997**, *534*, 57.
[156] S. K. Mohapatra, A. Fonari, C. Risko, K. Yesudas, K. Moudgil, J. H. Delcamp, T. V. Timofeeva, J.-L. Brédas, S. R. Marder, S. Barlow, *Chem. Eur. J.* **2014**, *20*, 15385.
[157] D. T. Scholes, S. A. Hawks, P. Y. Yee, H. Wu, J. R. Lindemuth, S. H. Tolbert, B. J. Schwartz, *J. Phys. Chem. Lett.* **2015**, *6*, 4786.
[158] I. E. Jacobs, E. W. Aasen, J. L. Oliveira, T. N. Fonseca, J. D. Roehling, J. Li, G. Zhang, M. P. Augustine, M. Mascal, A. J. Moulé, *J. Mater. Chem. C* **2016**, *4*, 3454.
[159] I. D. V. Ingram, D. J. Tate, A. V. S. Parry, R. S. Sprick, M. L. Turner, *Applied Physics Letters* **2014**, *104*, 153304.
[160] J. C. Aguirre, S. A. Hawks, A. S. Ferreira, P. Yee, S. Subramaniyan, S. A. Jenekhe, S. H. Tolbert, B. J. Schwartz, *Adv. Energy Mater.* **2015**, *5*, n/a.
[161] A. J. Heeger, S. Kivelson, J. R. Schrieffer, W.-P. Su, *Rev. Mod. Phys.* **1988**, *60*, 781.
[162] W. R. Salaneck, R. H. Friend, J. L. Brédas, *Physics Reports* **1999**, *319*, 231.
[163] L. Zaikowski, P. Kaur, C. Gelfond, E. Selvaggio, S. Asaoka, Q. Wu, H.-C. Chen, N. Takeda, A. R. Cook, A. Yang, J. Rosanelli, J. R. Miller, *J. Am. Chem. Soc.* **2012**, *134*, 10852.
[164] J. L. Bredas, G. B. Street, *Acc. Chem. Res.* **1985**, *18*, 309.
[165] G. Heimel, *ACS Cent. Sci.* **2016**, *2*, 309.
[166] R.-Q. Png, M. C. Y. Ang, M.-H. Teo, K.-K. Choo, C. G. Tang, D. Belaineh, L.-L. Chua, P. K. H. Ho, *Nature Communications* **2016**, *7*, 11948.
[167] C. K. Chan, F. Amy, Q. Zhang, S. Barlow, S. Marder, A. Kahn, *Chemical Physics Letters* **2006**, *431*, 67.
[168] M. Vosgueritchian, D. J. Lipomi, Z. Bao, *Adv. Funct. Mater.* **2012**, *22*, 421.
[169] C. K. Chan, W. Zhao, S. Barlow, S. Marder, A. Kahn, *Organic Electronics* **2008**, *9*, 575.
[170] G. Iucci, K. Xing, M. Lögdlund, M. Fahlman, W. R. Salaneck, *Chemical Physics Letters* **1995**, *244*, 139.
[171] M. Fahlman, D. Beljonne, M. Lögdlund, R. H. Friend, A. B. Holmes, J. L. Brédas, W. R. Salaneck, *Chemical Physics Letters* **1993**, *214*, 327.
[172] E. E. Perry, J. G. Labram, N. R. Venkatesan, H. Nakayama, M. L. Chabinyc, *Advanced Electronic Materials* **n.d.**, *4*, 1800087.
[173] A. Kojima, K. Teshima, Y. Shirai, T. Miyasaka, *J. Am. Chem. Soc.* **2009**, *131*, 6050.
[174] M. A. Green, K. Emery, Y. Hishikawa, W. Warta, E. D. Dunlop, D. H. Levi, A. W. Y. Ho-Baillie, *Prog. Photovolt: Res. Appl.* **2017**, *25*, 3.
[175] L. K. Ono, Y. Qi, *J. Phys. Chem. Lett.* **2016**, *7*, 4764.

[176] B. Chandra, A. Afzali, N. Khare, M. M. El-Ashry, G. S. Tulevski, *Chem. Mater.* **2010**, *22*, 5179.
[177] W. Chen, S. Chen, D. C. Qi, X. Y. Gao, A. T. S. Wee, *J. Am. Chem. Soc.* **2007**, *129*, 10418.
[178] Y. He, F. Xia, Z. Shao, J. Zhao, J. Jie, *J. Phys. Chem. Lett.* **2015**, *6*, 4701.
[179] J. Emara, T. Schnier, N. Pourdavoud, T. Riedl, K. Meerholz, S. Olthof, *Adv. Mater.* **2016**, *28*, 553.
[180] E. M. Miller, Y. Zhao, C. C. Mercado, S. K. Saha, J. M. Luther, K. Zhu, V. Stevanović, C. L. Perkins, J. van de Lagemaat, *Phys. Chem. Chem. Phys.* **2014**, *16*, 22122.
[181] B. Lüssem, C.-M. Keum, D. Kasemann, B. Naab, Z. Bao, K. Leo, *Chem. Rev.* **2016**, *116*, 13714.
[182] H. Uratani, K. Yamashita, *J. Phys. Chem. Lett.* **2017**, *8*, 742.
[183] L.-M. Chen, Z. Xu, Z. Hong, Y. Yang, *J. Mater. Chem.* **2010**, *20*, 2575.
[184] W. Koh, A. Y. Koposov, J. T. Stewart, B. N. Pal, I. Robel, J. M. Pietryga, V. I. Klimov, *Scientific Reports* **2013**, *3*, 2004.
[185] C. M. Sutter-Fella, D. W. Miller, Q. P. Ngo, E. T. Roe, F. M. Toma, I. D. Sharp, M. C. Lonergan, A. Javey, *ACS Energy Lett.* **2017**, *2*, 709.
[186] A. M. A. Leguy, P. Azarhoosh, M. Isabel Alonso, M. Campoy-Quiles, O. J. Weber, J. Yao, D. Bryant, M. T. Weller, J. Nelson, A. Walsh, M. van Schilfgaarde, P. R. F. Barnes, *Nanoscale* **2016**, *8*, 6317.
[187] K. Galkowski, A. Mitioglu, A. Miyata, P. Plochocka, O. Portugall, G. E. Eperon, J. T.-W. Wang, T. Stergiopoulos, S. D. Stranks, H. J. Snaith, R. J. Nicholas, *Energy Environ. Sci.* **2016**, *9*, 962.
[188] E. S. Thibau, A. Llanos, Z. H. Lu, *Appl. Phys. Lett.* **2016**, *108*, 021602.
[189] C. Wang, X. Liu, C. Wang, Z. Xiao, C. Bi, Y. Shao, J. Huang, Y. Gao, *Journal of Vacuum Science & Technology B, Nanotechnology and Microelectronics: Materials, Processing, Measurement, and Phenomena* **2015**, *33*, 032401.
[190] X. Liu, C. Wang, L. Lyu, C. Wang, Z. Xiao, C. Bi, J. Huang, Y. Gao, *Phys. Chem. Chem. Phys.* **2014**, *17*, 896.
[191] S. Olthof, K. Meerholz, *Scientific Reports* **2017**, *7*, 40267.
[192] D. Qi, W. Chen, X. Gao, L. Wang, S. Chen, K. P. Loh, A. T. S. Wee, *J. Am. Chem. Soc.* **2007**, *129*, 8084.
[193] W. Peng, J. Yin, K.-T. Ho, O. Ouellette, M. De Bastiani, B. Murali, O. El Tall, C. Shen, X. Miao, J. Pan, E. Alarousu, J.-H. He, B. S. Ooi, O. F. Mohammed, E. Sargent, O. M. Bakr, *Nano Lett.* **2017**, *17*, 4759.
[194] I. Levine, S. Gupta, T. M. Brenner, D. Azulay, O. Millo, G. Hodes, D. Cahen, I. Balberg, *J. Phys. Chem. Lett.* **2016**, *7*, 5219.
[195] P. S. Whitfield, N. Herron, W. E. Guise, K. Page, Y. Q. Cheng, I. Milas, M. K. Crawford, *Scientific Reports* **2016**, *6*, 35685.
[196] A. Pisoni, J. Jaćimović, O. S. Barišić, M. Spina, R. Gaál, L. Forró, E. Horváth, *J. Phys. Chem. Lett.* **2014**, *5*, 2488.
[197] J. Y. W. Seto, *Journal of Applied Physics* **1975**, *46*, 5247.
[198] N. J. Jeon, J. H. Noh, W. S. Yang, Y. C. Kim, S. Ryu, J. Seo, S. I. Seok, *Nature* **2015**, *517*, 476.

[199] W. S. Yang, J. H. Noh, N. J. Jeon, Y. C. Kim, S. Ryu, J. Seo, S. I. Seok, *Science* **2015**, *348*, 1234.
[200] J. You, Z. Hong, Y. (Michael) Yang, Q. Chen, M. Cai, T.-B. Song, C.-C. Chen, S. Lu, Y. Liu, H. Zhou, Y. Yang, *ACS Nano* **2014**, *8*, 1674.
[201] Q. Wang, C. Bi, J. Huang, *Nano Energy* **2015**, *15*, 275.
[202] F. Wu, W. Gao, H. Yu, L. Zhu, L. Li, C. Yang, *J. Mater. Chem. A* **2018**, *6*, 4443.
[203] Z. Bin, J. Li, L. Wang, L. Duan, *Energy & Environmental Science* **2016**, *9*, 3424.
[204] E. E. Perry, C.-Y. Chiu, K. Moudgil, R. A. Schlitz, C. J. Takacs, K. A. O'Hara, J. G. Labram, A. M. Glaudell, J. B. Sherman, S. Barlow, C. J. Hawker, S. R. Marder, M. L. Chabinyc, *Chem. Mater.* **2017**, DOI 10.1021/acs.chemmater.7b03516.
[205] D. Yuan, D. Huang, C. Zhang, Y. Zou, C. Di, X. Zhu, D. Zhu, *ACS Appl. Mater. Interfaces* **2017**, *9*, 28795.
[206] S. Zhang, B. D. Naab, E. V. Jucov, S. Parkin, E. G. B. Evans, G. L. Millhauser, T. V. Timofeeva, C. Risko, J.-L. Brédas, Z. Bao, S. Barlow, S. R. Marder, *Chemistry* **2015**, *21*, 10878.
[207] M. Saliba, J.-P. Correa-Baena, C. M. Wolff, M. Stolterfoht, N. Phung, S. Albrecht, D. Neher, A. Abate, *Chemistry of Materials* **2018**, *30*, 4193.
[208] J. H. Heo, H. J. Han, D. Kim, T. K. Ahn, S. H. Im, *Energy Environ. Sci.* **2015**, *8*, 1602.
[209] W. Sun, Y. Li, S. Ye, H. Rao, W. Yan, H. Peng, Y. Li, Z. Liu, S. Wang, Z. Chen, L. Xiao, Z. Bian, C. Huang, *Nanoscale* **2016**, *8*, 10806.
[210] A. Fakharuddin, L. Schmidt-Mende, G. Garcia-Belmonte, R. Jose, I. Mora-Sero, *Advanced Energy Materials* **n.d.**, *7*, 1700623.
[211] T. Minemoto, M. Murata, *Solar Energy Materials and Solar Cells* **2015**, *133*, 8.
[212] P. Calado, A. M. Telford, D. Bryant, X. Li, J. Nelson, B. C. O'Regan, P. R. F. Barnes, *Nature Communications* **2016**, *7*, 13831.
[213] S. van Reenen, M. Kemerink, H. J. Snaith, *J. Phys. Chem. Lett.* **2015**, *6*, 3808.
[214] A. Pockett, M. J. Carnie, *ACS Energy Lett.* **2017**, *2*, 1683.
[215] M. T. Neukom, S. Züfle, E. Knapp, M. Makha, R. Hany, B. Ruhstaller, *Solar Energy Materials and Solar Cells* **2017**, *169*, 159.
[216] S. M. Rossnagel, T. S. Kuan, *Journal of Vacuum Science & Technology B: Microelectronics and Nanometer Structures Processing, Measurement, and Phenomena* **2004**, *22*, 240.
[217] V. Timoshevskii, Y. Ke, H. Guo, D. Gall, *Journal of Applied Physics* **2008**, *103*, 113705.
[218] E. E. Perry, J. G. Labram, N. R. Venkatesan, H. Nakayama, M. L. Chabinyc, *Advanced Electronic Materials* **n.d.**, *0*, 1800087.
[219] Z. Chen, V. Stepanenko, V. Dehm, P. Prins, L. D. A. Siebbeles, J. Seibt, P. Marquetand, V. Engel, F. Würthner, *Chemistry – A European Journal* **n.d.**, *13*, 436.
[220] B. Schumacher, H.-G. Bach, P. Spitzer, J. Obrzut, in *Springer Handbook of Materials Measurement Methods* (Eds.: H.C. Prof, T. Saito, L. Smith), Springer Berlin Heidelberg, **2006**, pp. 431–484.
[221] C.-Y. Chiu, H. Wang, H. Phan, K. Shiratori, T.-Q. Nguyen, C. J. Hawker, *J. Polym. Sci. Part A: Polym. Chem.* **2015**, n/a.
[222] M. Y. Antipin, R. Boese, N. Augart, G. Schmid, *Structural Chemistry* **1993**, *4*, 91.

[223] J. Endres, M. Kulbak, L. Zhao, B. P. Rand, D. Cahen, G. Hodes, A. Kahn, *Journal of Applied Physics* **2017**, *121*, 035304.
[224] P. Umari, E. Mosconi, F. D. Angelis, *Scientific Reports* **2014**, *4*, 4467.
[225] J. Feng, B. Xiao, *J. Phys. Chem. Lett.* **2014**, *5*, 1278.
[226] S. P. Senanayak, B. Yang, T. H. Thomas, N. Giesbrecht, W. Huang, E. Gann, B. Nair, K. Goedel, S. Guha, X. Moya, C. R. McNeill, P. Docampo, A. Sadhanala, R. H. Friend, H. Sirringhaus, *Science Advances* **2017**, *3*, e1601935.
[227] J. G. Labram, D. H. Fabini, E. E. Perry, A. J. Lehner, H. Wang, A. M. Glaudell, G. Wu, H. Evans, D. Buck, R. Cotta, L. Echegoyen, F. Wudl, R. Seshadri, M. L. Chabinyc, *J. Phys. Chem. Lett.* **2015**, *6*, 3565.
[228] C.-Z. Li, C.-C. Chueh, F. Ding, H.-L. Yip, P.-W. Liang, X. Li, A. K.-Y. Jen, *Adv. Mater.* **2013**, *25*, 4425.
[229] Y. Chen, H. T. Yi, X. Wu, R. Haroldson, Y. N. Gartstein, Y. I. Rodionov, K. S. Tikhonov, A. Zakhidov, X.-Y. Zhu, V. Podzorov, **2016**, *7*, 12253.
[230] S. Shao, M. Abdu-Aguye, L. Qiu, L.-H. Lai, J. Liu, S. Adjokatse, F. Jahani, M. E. Kamminga, G. H. ten Brink, T. T. M. Palstra, B. J. Kooi, J. C. Hummelen, M. A. Loi, *Energy & Environmental Science* **2016**, *9*, 2444.
[231] F. Wang, J. Mei, Y. Wang, L. Zhang, H. Zhao, D. Zhao, *ACS Applied Materials & Interfaces* **2016**, *8*, 2840.
[232] C. Park, H. Ko, D. H. Sin, K. C. Song, K. Cho, *Advanced Functional Materials* **2017**, *27*, 1703546.
[233] T. G. Kim, S. W. Seo, H. Kwon, J. Hahn, J. W. Kim, *Phys. Chem. Chem. Phys.* **2015**, *17*, 24342.
[234] H. Xie, X. Liu, L. Lyu, D. Niu, Q. Wang, J. Huang, Y. Gao, *J. Phys. Chem. C* **2016**, *120*, 215.
[235] S. Olthof, *APL Materials* **2016**, *4*, 091502.
[236] A. Calloni, A. Abate, G. Bussetti, G. Berti, R. Yivlialin, F. Ciccacci, L. Duò, *J. Phys. Chem. C* **2015**, *119*, 21329.
[237] J. Chang, H. Zhu, B. Li, F. H. Isikgor, Y. Hao, Q. Xu, J. Ouyang, *J. Mater. Chem. A* **2016**, *4*, 887.
[238] J. Chang, H. Zhu, J. Xiao, F. H. Isikgor, Z. Lin, Y. Hao, K. Zeng, Q.-H. Xu, J. Ouyang, *J. Mater. Chem. A* **2016**, *4*, 7943.
[239] J. P. C. Baena, L. Steier, W. Tress, M. Saliba, S. Neutzner, T. Matsui, F. Giordano, T. J. Jacobsson, A. R. S. Kandada, S. M. Zakeeruddin, A. Petrozza, A. Abate, M. K. Nazeeruddin, M. Grätzel, A. Hagfeldt, *Energy Environ. Sci.* **2015**, *8*, 2928.
[240] B. J. Foley, D. L. Marlowe, K. Sun, W. A. Saidi, L. Scudiero, M. C. Gupta, J. J. Choi, *Appl. Phys. Lett.* **2015**, *106*, 243904.
[241] H.-S. Kim, C.-R. Lee, J.-H. Im, K.-B. Lee, T. Moehl, A. Marchioro, S.-J. Moon, R. Humphry-Baker, J.-H. Yum, J. E. Moser, M. Grätzel, N.-G. Park, *Scientific Reports* **2012**, *2*, 591.
[242] C. Li, J. Wei, M. Sato, H. Koike, Z.-Z. Xie, Y.-Q. Li, K. Kanai, S. Kera, N. Ueno, J.-X. Tang, *ACS Appl. Mater. Interfaces* **2016**, *8*, 11526.
[243] K.-G. Lim, S. Ahn, Y.-H. Kim, Y. Qi, T.-W. Lee, *Energy Environ. Sci.* **2016**, *9*, 932.
[244] P. Liu, X. Liu, L. Lyu, H. Xie, H. Zhang, D. Niu, H. Huang, C. Bi, Z. Xiao, J. Huang, Y. Gao, *Appl. Phys. Lett.* **2015**, *106*, 193903.

[245] M.-F. Lo, Z.-Q. Guan, T.-W. Ng, C.-Y. Chan, C.-S. Lee, *Adv. Funct. Mater.* **2015**, *25*, 1213.
[246] Q. Wang, Y. Shao, H. Xie, L. Lyu, X. Liu, Y. Gao, J. Huang, *Appl. Phys. Lett.* **2014**, *105*, 163508.
[247] X. Zhou, X. Li, Y. Liu, F. Huang, D. Zhong, *Appl. Phys. Lett.* **2016**, *108*, 121601.
[248] S. M. Park, S. M. Mazza, Z. Liang, A. Abtahi, A. M. Boehm, S. R. Parkin, J. E. Anthony, K. R. Graham, *ACS Appl. Mater. Interfaces* **2018**, *10*, 15548.
[249] A. D. Wright, R. L. Milot, G. E. Eperon, H. J. Snaith, M. B. Johnston, L. M. Herz, *Advanced Functional Materials* **n.d.**, *27*, 1700860.
[250] D. W. de Quilettes, S. M. Vorpahl, S. D. Stranks, H. Nagaoka, G. E. Eperon, M. E. Ziffer, H. J. Snaith, D. S. Ginger, *Science* **2015**, *348*, 683.
[251] S. D. Stranks, G. E. Eperon, G. Grancini, C. Menelaou, M. J. P. Alcocer, T. Leijtens, L. M. Herz, A. Petrozza, H. J. Snaith, *Science* **2013**, *342*, 341.